

NEMATIC MATERIALS IN CURVED SPACES

A Dissertation
Presented to
The Academic Faculty

By

Perry W. Ellis

In Partial Fulfillment
of the Requirements for the Degree
Doctor of Philosophy in the
School of Physics

Georgia Institute of Technology

May 2018

Copyright © Perry W. Ellis 2018

NEMATIC MATERIALS IN CURVED SPACES

Approved by:

Dr. Alberto Fernández-Nieves,
Advisor
School of Physics
Georgia Institute of Technology

Dr. Paul Goldbart
School of Physics
Georgia Institute of Technology

Dr. Peter Yunker
School of Physics
Georgia Institute of Technology

Dr. Brian Kennedy
School of Physics
Georgia Institute of Technology

Dr. Eric Weeks
Department of Physics
Emory University

Date Approved: December 18,
2017

Geometry, which should always follow physics when used to describe nature,
sometimes commands it.

Jean Le Rond d'Alembert

To my family.

ACKNOWLEDGEMENTS

First, I would like to thank my advisor, Professor Alberto Fernández-Nieves; it has been an incredible experience working with him over these past six years. Alberto is a truly fantastic mentor and has been a constant source of guidance and inspiration. He continuously pushes me and the rest of the group to be the best versions of ourselves possible, and his influence is the main reason I have become the scientist that I am. I would also like to thank the rest of faculty members who have agreed to serve on my committee: Professor Paul Goldbart, Professor Peter Yunker, Professor Brian Kennedy, and Professor Eric Weeks. For the wonderful opportunity of being paid to learn and be a student, thank you to the Georgia Tech School of Physics and to the FLAMEL program.

This work was truly the product of collaboration, and I would especially like to thank those who directly contributed to this dissertation. Professor Luca Giomi and Daniel Pearce performed the numerical simulations on the active nematic toroids presented in Chapter 3. Karthick Nayani started the work on homeotropic nematic toroids and performed some of the experiments presented in Chapter 4. Jayalakshmi Vallamkondu started the work on the nematic bridges and performed some of the experiments presented in Chapter 5. Susannah Klaneček, an undergraduate in our group, performed many of the experiments on the nematic bridges; Chapter 5 would not exist without her. Professor Paul Goldbart and Shengnan Huang performed the numerical calculations for the nematic bridges.

To the Fernández-Nieves Lab, past and present, thank you for your inspiration, support, conversation, and so much more. Alexandros Fragkopoulos for helping me with homework in our first year, for serving as a sounding board for many ideas and thoughts over the years, and for being a wonderful friend. Karthik Nayani for many discussions about liquid crystals and unrelated tangents. Ya-wen (Winnie) Chang for

her help and wisdom both in and out of the lab. Mike Dimitriyev for his patience in teaching me math and so much more. The rest of my labmates, Ekapop, John, Miguel, Josefa, Mike T., Caleb, Jonas, Sam, and Boyang, thank you for more than you know. It has been a pleasure working with all of you.

Finally, to my family. Mama, Baba, Reilly, Clayton, and Kristine, thank you for your unending love and support. This one's for you.

TABLE OF CONTENTS

Acknowledgments	v
List of Tables	xiii
List of Figures	xiv
Chapter 1: Introduction	1
Chapter 2: Fundamentals of nematic liquid crystals	20
2.1 Local order and defects	20
2.1.1 The director and the order parameter	21
2.1.2 Defects in a nematic	24
2.2 Frank-Oseen free energy	33
2.2.1 A brief derivation	33
2.2.2 Nehring, Saupe, and second derivatives	37
2.2.3 Insights from microscopic calculations	39
2.2.4 Saddle-splay and curvature-coupling	41
2.3 Landau-de Gennes free energy	46
2.3.1 The isotropic-nematic phase transition	47
2.3.2 The distortion free energy	49

2.3.3	The scaling of the Frank elastic constants	52
2.4	Experimental characterization of nematic liquid crystals	53
2.4.1	Confinement and boundary conditions	53
2.4.2	Birefringence and optically polarized microscopy	58
Chapter 3:	Active nematics on the surface of a torus	63
3.1	Introduction	63
3.2	Making active nematic toroids	72
3.2.1	Active nematic formulation	72
3.2.2	Flat sample confirmation	77
3.2.3	Making toroidal droplets	79
3.3	Imaging active nematic toroids	84
3.3.1	Confocal fluorescence microscopy	85
3.3.2	Confocal setup and parameters	88
3.3.3	Inputting confocal data into MATLAB	94
3.4	Determining director and defects	96
3.4.1	Coherence-enhanced diffusion filtering	96
3.4.2	Calculating the director	100
3.4.3	Finding defect location and topological charge	101
3.4.4	Measuring defect charge in a specified region	101
3.4.5	Edge charge	105
3.5	Measuring surface curvature	109
3.5.1	The Weingarten matrix	109

3.5.2	Iteratively-reweighted least squares	110
3.5.3	Fitting the Weingarten matrix on a surface	116
3.5.4	Correcting the surface normal vectors	122
3.5.5	Finding the area element	122
3.5.6	Validation on test surfaces	122
3.5.7	Measuring the curvature of toroidal droplets	126
3.6	Defect charge and curvature	127
3.6.1	Finding regions of specific integrated Gaussian curvature . . .	128
3.6.2	Time-averaged defect charge as a function of integrated Gaussian curvature: curvature-induced defect unbinding	129
3.7	Defect number distributions	131
3.8	Comparison with numerical simulations	132
3.8.1	Simulation details	133
3.8.2	Matching simulation parameters to experiment	135
3.8.3	Estimates of material parameters	138
3.9	Conclusions	140
Chapter 4: Homeotropic nematics confined in toroids and bent capillaries	142
4.1	Introduction	142
4.2	Escaped radial and twisted escaped radial configurations in capillaries	149
4.2.1	Intensity profile and intensity ratio	150
4.3	Nematic liquid crystals in toroids	153
4.3.1	Measuring the intensity profile and aspect ratio	154

4.3.2	Large aspect ratio toroids	156
4.3.3	Small aspect ratio toroids	156
4.4	Simulating polarized optical microscopy textures for twisted escaped radial director configurations	157
4.4.1	Jones Calculus and simulation details	157
4.4.2	Validation using spherical droplets	163
4.4.3	Planar-anchored nematic toroids	165
4.4.4	Comparison with homeotropically-anchored nematic toroids .	177
4.4.5	Intensity ratio as a function of twist parameter	180
4.4.6	Intensity ratio as a function of escape rate	180
4.5	Nematic liquid crystals in bent capillaries	181
4.5.1	Making bent capillaries	181
4.5.2	Measuring planar curvature	182
4.5.3	Measuring the intensity profile	183
4.5.4	Comparison with toroids	184
4.6	Conclusions	184
Chapter 5: Homeotropic nematic bridges	186
5.1	Introduction	186
5.2	Making capillary bridges	188
5.3	Shape of capillary bridges	189
5.3.1	Measuring the shape	190
5.3.2	Constant mean curvature surfaces	191
5.4	Defect structure transitions	194

5.4.1	Defect transitions in a waist	194
5.4.2	Defect transitions in a barrel	196
5.5	Measuring defect conformation using fluorescence microscopy	200
5.5.1	Theoretical overview of polarized epifluorescent microscopy . .	200
5.5.2	Experimental realization	202
5.5.3	Validation in spherical droplets and cylindrical capillaries . . .	205
5.5.4	Radial and hyperbolic defects in waists and barrels	209
5.6	Comparison with numerical calculations: stable and metastable states	211
5.7	Conclusions	213
Chapter 6:	Summary, conclusions, and future work	215
6.1	Summary and conclusions	215
6.2	Defect orientation on curved surfaces: current status	218
6.2.1	Theory	218
6.2.2	Experiment	220
6.2.3	Future Work	227
6.3	Determining the saddle-splay elastic constant: current status	227
6.3.1	Prior estimates in tori	228
6.3.2	Results from spherical drops	229
6.3.3	Distinguishing K_{24} and surface contributions using twist angle and temperature	232
Appendix A:	Experimental protocol to bond polyacrylamide brushes to glass	236

References	237
Vita	257

LIST OF TABLES

2.1	Scalar invariants of powers of \mathcal{Q} in 3D	48
2.2	Basic group theory definitions [90, 91].	62
3.1	Stock solutions used to form an active nematic solution. The stock solutions in their given compositions are bolded	76
3.2	Recipe for 100 μL active nematic solution	78
3.3	Cost and weight functions of common M-estimators. x are the residuals and c is a tuning parameter.	115
3.4	Estimates of material parameters for an active nematic on a toroid for 144 μM and 36 μM ATP.	140
4.1	Jones calculus operators for common optical elements	158
6.1	Experimentally-obtained values for K_{24} using 5CB for four literature sources, both as reported and after recasting the saddle-splay distortion in the form: $-(1/2)(K_{22} + K_{24})\nabla \cdot (\mathbf{n}\nabla \cdot \mathbf{n} + \mathbf{n} \times \nabla \times \mathbf{n})$	228

LIST OF FIGURES

1.1 Smectic and nematic order. (A), A smectic phase breaks translational symmetry along one direction, leading to a layer-like structure. For the drawn Smectic-A phase, this direction is indicated by ν . (B), A uniaxial nematic phase has continuous translational symmetry in all directions and continuous rotational symmetry in one direction. This direction is indicated by the director, \mathbf{n} .	2
1.2 Schematic of the phase behavior for melting in 2D. T_{ch} and T_{hi} are the transition temperatures for the crystalline-hexatic transition and the hexatic-isotropic transition, respectively.	5
1.3 Packing rods in two dimensions. (A-C), Rod-like particles preferentially align along a common axis, given by the black lines. (A) On a plane, the alignment can be homogeneous everywhere. (B,C) On a sphere, there must be singularities (●) in the alignment directions, as shown for alignment directions along (B) the latitude or longitude lines on a globe and an alignment direction along (C) the stitching on a baseball. Note that while only one singularity is visible in (B,C), there are 2 singularities in (B) and 4 in (C).	6
1.4 Closed surfaces with the same Euler characteristic are homeomorphic. (A,B) Closed surfaces with no handle like a (A) sphere and (B) the surface of a cup can be continuously deformed into each other. (C,D) Closed surfaces with a single handle like a (C) torus and (D) the surface of a coffee mug can be continuously deformed into each other. However, the surfaces in (A,B) cannot be continuously deformed into the surfaces in (C,D) as the process of adding a handle breaks the surface.	7
1.5 Topological charge of disclinations. (A), The director rotates by 2π along the contour enclosing the singularity (●), giving $s = +1$ for both disclinations. (B) The director rotates by π along the contour enclosing the singularity (●), giving $s = +1/2$. (C) Attempting to construct an $s = +1/2$ disclination for a vector field results in a discontinuity in the vector field along the contour. This is seen by following the red contour as the vectors go from blue to cyan.	9

1.6 Shells of nematic liquid crystal. (A-C) Thin shells of NLC have four $s = +1/2$ defects, with an experimental crossed-polar image in (A), the tetrahedron highlighted in (B), and a cross-section schematically showing the director configuration in (C). The cross-section is of a great circle containing two $s = +1/2$ defects (●) on both the inner and outer surface of the shell, with a red singular line connecting corresponding disclinations. The disclinations occupy the vertices of a tetrahedron and thus are separated by 109° in the cross-section. (D) Cross-section of the director configuration in a thick shell. Here, the two $s = +1$ disclinations (●) on each surface are no longer connected by a singular line. (E,F) As $R^{in} \rightarrow 0$, the thick shell becomes a bipolar droplet, with a cross-section of the director field in (E) and a corresponding crossed-polar image in (F). Images/Schematics in (A,B) reproduced from Ref. [26] with permission from Macmillan Publishers Ltd: Nature Physics, copyright 2011.	10
1.7 Geometrical frustration in nematics and in magnetism. (A), A flat plane can support a homogeneous director field, indicated by the black lines. (B), Adding a hemisphere to the plane disrupts the homogeneous state, the Gaussian curvature of the hemisphere makes a distortion-free state impossible. (C), Modulating the surface with a sine wave adds mean curvature but not Gaussian curvature to the surface; the homogeneous state on the surface is still possible. (D), Geometrical frustration in magnetism. Perfect antiferromagnetic order cannot exist on a triangular lattice.	12
1.8 Planar and surface curvature. (A), A planar curve with unit tangent vector \mathbf{T} and unit normal vector \mathbf{k} . The osculating circles and associated radii of curvature are given for two points on the curve; the negative curvature is in blue and the positive curvature in red. (B), A normal section of a saddle-surface at a point corresponds to a planar curve, with the curve drawn in dark gray and the plane containing the curve indicated in transparent gray. The osculating circle and radius of curvature at the point of interest are drawn in blue. (C), The principal curvatures κ_1 and κ_2 at the point of interest on the surface from (B) are the maximum and minimum normal curvatures and are always in orthogonal directions. Here these directions are highlighted with the red and blue contours on the surface.	15
1.9 Doubly-twisted tori. (A,B), Schematics showing a (A) right-handed and (B) left-handed double-twist. (C), Schematic defining the central ring radius R_0 and tube radius a in a torus.	17

2.1 Symmetries in nematic phase. (A), A collection of rod-like particles in the isotropic phase. The orientation of the rod with index α is given by the angle \mathbf{u}^α , defined schematically in the image. (B), The rods from (A) in the nematic phase. The rods are preferentially but weakly aligned along the director \mathbf{n} , denoted in the panel. (C), The rods from (A,B) in the nematic phase. Here, the rods are strongly aligned along \mathbf{n} , denoted in the panel. (D), The positions of the center of mass of the rods in (A–C), highlighting the continuous translational symmetry of the rods.

21

2.2 Different types of defects in 3D and 2D. In 3D, there is the 2D wall defect, the 1D line defect, and the 0D point defect. Cross-sections of these three structures are shown schematically in the xy plane and the xz plane. The defects are marked with either a dot or a dashed line. The heads of the “nails” in the xz cross-section of the wall, point into the page. In 2D, a nematic can have 1D line defects and 0D point defects, where the singular region is highlighted with either a dashed line or a point. Note that the wall and line structures in 3D are invariant along the \hat{z} -direction. This invariance means that the xy cross-section of the wall and line structure in 3D map to the line and point structure in 2D, as shown by the arrows in the schematic. . . .

25

2.3 Examples of defect structures and the order parameter space in 2D. (A), An $s = +1/2$ defect with the singularity denoted with a red dot. The director along the red and purple contours is mapped to \mathbb{RP}^1 in (B). (B), A schematic showing \mathbb{RP}^1 (black line) as \mathbb{S}^1 (full circle) with antipodal points identified. The purple contour in \mathbb{RP}^1 corresponds to the purple contour in real space drawn schematically in (A). The purple contour can be continuously deformed to a point in \mathbb{RP}^1 . (C), A schematic showing \mathbb{RP}^1 (black line) as \mathbb{S}^1 (full circle) with antipodal points identified. The red contour in \mathbb{RP}^1 corresponds to the purple contour in real space drawn schematically in (A). The red contour spans \mathbb{RP}^1 , and thus has a winding number of $+1$ in \mathbb{RP}^1 and $+1/2$ in \mathbb{S}^1 . (D), An $S = -1/2$ defect with the singularity at the blue point. In \mathbb{RP}^1 , the blue contour would have the same winding as the red contour in (C), but would go the opposite direction. (E), An $s = +1$ defect (green dot) encircled by the green contour. In \mathbb{RP}^1 , the contour would have the same direction as the red contour in (C), but would cover \mathbb{RP}^1 twice and \mathbb{S}^1 once. (F), Two $s = +1/2$ defects (red dots) placed near to each other such that the green contour encircling both defects sees the same winding in order parameter space as the green contour in (E). Thus, far from the defects, we cannot distinguish between structures resulting from a single $s = +1$ defect and two $s = +1/2$ defects, reflecting the additivity of topological charge in 2D.

28

2.4	Singular line defects are topologically unstable in 2D. (A) a singular line defect in 2D, with the singular region denoted in red. (B) A nonsingular structure resulting from a continuous deformation of (A).	29
2.5	Contours in \mathbb{RP}^2 . (A–C), Schematics showing \mathbb{RP}^2 (blue hemisphere) as \mathbb{S}^2 (full sphere) with antipodal points identified. A (A) contour that wraps \mathbb{RP}^2 twice can be (B) slid off and is homotopic to a point. A (C) contour that starts and ends at antipodal points is not homotopic to a point and is the only nontrivial contour in \mathbb{RP}^2	30
2.6	Examples of defect structures in 3D. (A–D), Cross sections in the xz and xy planes of defect structures with $ q = 1$. Once we choose a reference point that defines the projection of \mathbf{n} onto the unit sphere, we can distinguish the structures in A,C from the structures in B,D. Without loss of generality, we take the convention that the structures in A,C have $q = +1$ such that the structures in B,D have $q = -1$. (A,B), schematics of a (A) radial and a (B) hyperbolic hedgehog defect. (C,D), schematics of a (C) radial ring and a (D) hyperbolic ring defect. Note that the ring defects in (C,D) are formed by an $s = +1/2$ and an $s = -1/2$ line defect that has closed in on itself.	32
2.7	Nematic distortions in the local frame. (A), A schematic showing a splay distortion corresponding to a nonzero s_2 . (B), A schematic showing a twist distortion corresponding to a nonzero t_2 . (C), A schematic showing a bend distortion corresponding to a nonzero b_2	36
2.8	Nematic liquid crystal confined to a spherical volume. (A), The classic radial director configuration found under homeotropic boundary conditions. The defect is indicated by \bullet . (B), The classic bipolar director configuration found under degenerate planar boundary conditions. The 2 defects are indicated by \bullet	54

2.9 Common anchoring schemes for nematic liquid crystals. (A), Homeotropic anchoring enforced by surfactant molecules. The polar heads of the molecules adsorb to the substrate, with the nonpolar tails extending into the NLC. The tails serve to align the nematic mesogens along the surface normal, making $\mathbf{k} \parallel \mathbf{n}$, as seen in the schematic. (B), Degenerate planar anchoring enforced by randomly oriented polymers on the substrate. The polymers only require that the mesogens lie in the plane of the interface such that $\mathbf{k} \perp \mathbf{n}$. Since there is no preferred direction in the plane of the substrate, the mesogens are free to choose any director in the plane, as depicted in the schematic. (C), Planar anchoring enforced via aligned polymers on the substrate. Here, the polymers have an alignment direction, setting the direction that the NLC mesogens also prefer to align along, such that $\mathbf{n} \parallel \boldsymbol{\sigma}$, where $\boldsymbol{\sigma}$ is a vector describing the polymer alignment direction, as defined in the schematic.

55

2.10 Schematic of the light path and polarization state for optically polarized microscopy (OPM). OPM places a linear polarizer called the “polarizer” before the condenser and another linear polarizer called the “analyzer” after the objective. The polarization states depicted in the figure assume the sample is birefringent and the pass axes of the polarizer and the analyzer are orthogonal.

59

2.11 Example OPM textures for a bipolar drop and a radial drop. (A–C), schematic and textures for a radial drop. The textures in (B,C) have the polarizer and analyzer directions specified on the images, with the drops oriented as depicted in (A). Note how the texture only changes orientation with the polarizer and analyzer orientation, but does not change character. (D–F), schematic and texture for a bipolar drop. The textures in (E,F) have the polarizer and analyzer directions specified on the images, with the drops oriented as depicted in (D). Note how the texture changes as the polarizer and analyzer rotate.

60

3.1 Interactions in extensile and contractile nematics. (A,C), Two-particle interaction for extensile (A) and contractile (C) mesogens. The arrows represent time. (B,D), Active stress exerted on a small area by the surroundings ($\boldsymbol{\sigma}$) and on the surroundings by the small area ($\boldsymbol{\sigma}'$) for (B) extensile and (D) contractile interactions.

64

3.2 Activity generates defect pairs. An (A) extensile and (B) contractile active nematic evolving over time. In both cases a $s = \pm 1/2$ defect pair is generated, with the defects indicated by (●), and (●), respectively. 65

3.3 Flow fields for active disclinations. (A,B) Flows generated by active (A) and $s = +1/2$ and (B) $s = -1/2$ disclinations, with the director lines drawn in white. Due to the polar structure of the active flow, $s = +1/2$ disclinations propel along their symmetry axis. The red arrow represents the propulsion direction for an extensile nematic; $s = +1/2$ disclinations will propel in the opposite direction for a contractile nematic.

68

3.4 Curvature-induced defect unbinding for a nematic on a torus. (A) A schematic of a torus with 4 pairs of unbound pairs of $s = \pm 1/2$ defects. The 3 visible $s = +1/2$ defects are indicated by \blacktriangle and the 3 visible $s = -1/2$ defects are indicated by \bullet . The red region on the torus has $K > 0$ and the blue region has $K < 0$. (B) A schematic of a cross-section of a torus defining the toroidal coordinate system $\{r, \theta, \varphi\}$. A given torus is specified by its central circle radius, R_0 and its tube radius, a , which combine to form the aspect ratio, $\xi = R_0/a$. (C) Plot of topological charge vs integrated Gaussian curvature as φ increases for the torus in (A). The red curve corresponds to integrating over the red region defined by $\theta \in [\pi/2, 3\pi/2]$ and the blue curve corresponds to integrating over the blue region defined by $\theta \in [-\pi/2, \pi/2]$. The positive slope indicates defect unbinding.

70

3.5 Microtubule-kinesin active nematic liquid crystal. (A) Schematic of tubulin polymerizing into a microtubule. The α/β -tubulin dimers polymerize end-to-end to form chains which then polymerize laterally to form microtubules. The microtubule polarity is indicated on the schematic, with (-) associated to free α -tubulin and (+) associated to free β -tubulin. (B) Kinesin (\bullet) walks along microtubules from the (-) end to the (+) end. When kinesin are bound to streptavidin (\bullet) to form clusters, these clusters can generate relative motion between two antiparallel microtubules. In contrast, parallel microtubules exhibit no relative motion, with the kinesin-streptavidin cluster simply translating itself in the shared (+) direction. (C) Microtubules and kinesin-streptavidin clusters bundles together by depletion form fibers that slide past each other. When the concentration of fibers is high enough to form a viscoelastic network, individual fibers cannot slide freely and instead will buckle and fracture. (D) In the presence of a liquid-liquid interface, the fibers will deplete to the interface and undergo an isotropic-nematic transition, with the fiber direction giving the nematic director. Pictured is a fluorescence microscopy snapshot of an active nematic, where the microtubules are fluorescently labeled such that the fiber direction is apparent. The director surrounding an $s = +1/2$ and $s = -1/2$ defect pair is highlighted by the dashed red and blue lines, respectively, with the fracture line connecting the pair highlighted with a yellow dashed line.

73

3.6	Schematic and assembly of a sample chamber for an active gel.	79
3.7	Making toroidal droplets. (A) Schematic of the apparatus used to make toroidal droplets. The inner fluid is injected into a cuvette on a rotating stage. The stage is driven by a DC motor and the entire process is imaged from below with a CCD camera. (B) A curved jet pulled from the needle by the viscous drag of the rotating bath. (C) A toroidal droplet formed when the curved jet in (B) closed upon itself. R_{tip} is the distance from the needle to the center of rotation.	81
3.8	Confocal microscopy. (A) Schematic showing the effect of the confocal aperture in front of the detector. Light from the red point is in focus at the aperture in the confocal plane, and thus can pass entirely through the aperture. In contrast, the blue light is emitted above the focal plane; the light is out of focus at the confocal plane and does not pass through the aperture. Similarly, the green light is in focus at the confocal plane, but it is not emitted from a conjugate point to the aperture and thus does not pass through the aperture. (B), Schematic of laser confocal fluorescence microscopy. There is a confocal aperture in front of the laser such that the laser is focused by the objective onto the focal plane in the sample. Thus, the maximum excitation will be at the conjugate point in the focal plane. As in (A), only the emitted light from the conjugate point in the focal plane is incident on the detector. A dichroic mirror allows the excited and emitted light to share the same path to and from the sample, but passes only the emitted light to the detector. Scanning mirrors (not drawn) between the dichroic mirror and the objective raster the conjugate point over the focal plane to construct a full image of the focal plane. (C) An example image stack of an active nematic torus, where the image stack has been reoriented to provide perspective and the data have been false-colored by height. This image stack was taken with a typical set of parameters: total size, 1.28 mm \times 1.28 mm \times 0.21 mm, pixel size, 2.5 $\mu\text{m}/\text{px} \times$ 2.5 $\mu\text{m}/\text{px} \times$ 7 $\mu\text{m}/\text{px}$. The scale bar is 250 μm	89
3.9	Fluorophore spectra and detector quantum efficiencies for our experimental system. (A), AlexaFluor 647 (red dashed line) excitation and (shaded red area) emission spectra. Spectra from Ref. [145]. (B), Quantum efficiency as a function of wavelength for a (green line) standard PMT and a (red line) GaAsP PMT as a function of wavelength. Plot from Ref. [146].	91

- 3.13 Time-averaged topological charge measured for different areas on a toroid with $\xi = 2.0$ and $a = 372 \mu\text{m}$. (A,C,E) The region outlined in white has (A) $(1/2\pi) \int K dA = 0$ and area $A = 0.795 \text{ mm}^{-2}$, (C) $(1/2\pi) \int K dA = 0$ and area $A = 0.211 \text{ mm}^{-2}$, (E) $(1/2\pi) \int K dA = 0$ and area $A = 0.064 \text{ mm}^{-2}$. (B,D,F) Plot of time-averaged topological charge vs averaging time for the region highlighted in (A,C,E), respectively. The error for each point is the standard error of the mean. 104
- 3.14 Schematic illustration of boundary and bulk charge. (A), The fixed frame is defined by the orthonormal basis $\{\hat{e}_1, \hat{e}_2\}$. The Frenet-Serret frame is a moving orthonormal frame defined by the unit tangent vector and unit normal vector, $\{\mathbf{T}, \mathbf{k}\}$. In the fixed frame, the director orientation and tangent vector orientation are given by ϕ and ψ , respectively. In the Frenet-Serret frame, the director orientation is ϕ' . (B–D) An example director field in a circular region drawn in a fixed frame and the director field at the boundary drawn in the Frenet-Serret frame. For the defect-free director field in (B), integrating $d\phi$ from $\Theta = 0$ to $\Theta = 2\pi$ yields a $s_{\text{bulk}} = 0$, while integrating $d\phi'$ from $\Theta = 0$ to $\Theta = 2\pi$ yields a $s_{\text{boundary}} = 1$, such that $s_{\text{bulk}} + s_{\text{boundary}} = 1$. Performing the same calculations for the director field containing the (C) $s = +1$ defect and (D) $s = -1/2$ defect yields $s_{\text{bulk}} + s_{\text{boundary}} = 1 + 0 = 1$, and $s_{\text{bulk}} + s_{\text{boundary}} = -1/2 + 3/2 = 1$, respectively. 106
- 3.15 Boundary charge and defect detection error on active nematic toroids. (A–D), Validation of the Frenet-Serret frame. For the example mask in (A), we find the (B) boundary, estimate the unit tangent vectors, and then rotate the tangent vectors by $-\pi/2$ to get the (C) unit normal vectors and complete the Frenet-Serret frame. The image in (C) is zoomed in on the highlighted portion of (B) to better show the arrows. (D), We check the Frenet-Serret frame in (C) by integrating the change in the unit normal vector along the boundary, $\int_0^\theta d(\psi - \pi/2) = \int_0^\theta d\psi = \int_0^\theta (\partial\psi/\partial\theta')d\theta'$, and see that the integral goes to 2π , as desired. (E), Circular region containing a director field from an active nematic toroid with $s = \pm 1/2$ defects found with our algorithm and labeled by (\times), (\circ), respectively, giving $s_{\text{bulk}} = \sum_i s_i = -1/2$. (F), $\int_{\theta=0}^{2\pi} d\phi'$ along the boundary yields $s_{\text{boundary}} = 3/2$ as $\theta \rightarrow 2\pi$. (G), $s_{\text{bulk}} + s_{\text{boundary}}$ for 262 frames evaluated using the region in (A) applied to a torus with $\xi = 2.4$ and $a = 268 \mu\text{m}$. There are 55 frames with $s_{\text{bulk}} + s_{\text{boundary}} \neq 1$ and 207 frames with $s_{\text{bulk}} + s_{\text{boundary}} = 1$, leading to $P(\text{error}) = 0.21$ and $\text{mean}(\text{error}) = 0.004$ 108

3.16 Plots of the cost functions and weight functions for common M-estimators. (A) The cost and weight function for a least-squares fit. (B-D) The cost and weight functions for a (B) Cauchy M-estimator, a (C) Fair M-estimator, and a (D) GMC M-Estimator, with the tuning parameter for the red curves set to yield 95% efficiency on a standard normal, and the tuning parameter for the blue curve set to twice the value in the red curve. The least-squares estimator in (A) and the Fair estimator in (C) have everywhere convex cost functions, in contrast to the Cauchy and the GMC M-estimators in (B,D), respectively. 115

3.17 Schematic of the quantities used to calculate the Gaussian curvature of a triangulated surface. $\mathbf{R}_{[0]}$ is the point of interest. $\mathbf{R}_{[1]}$ and $\mathbf{R}_{[2]}$ are an example pair of points close to the point of interest with $\Delta\mathbf{R}_{[1,2]} = \mathbf{R}_{[2]} - \mathbf{R}_{[1]}$ the displacement vector in the tangent plane of $\mathbf{R}_{[0]}$. $\mathbf{k}_{[1]}$ and $\mathbf{k}_{[2]}$ are the unit surface normal vectors associated to $\mathbf{R}_{[1]}$ and $\mathbf{R}_{[2]}$. 117

3.18 Example IRLS fit of the curvature at a point on a surface. (A,B) Residuals, weights, Λ , K , and cost for the (A) Fair M-estimator and (B) GMC M-estimator over multiple iterations, with the iteration number to the left of the residuals. The 0th iteration corresponds to the output from the initial least-squares fit. The dashed line in (A) is the outlier rejection criterion; residuals above the line have their weight set to 0. 121

3.19 Fitting the curvature of hemispheres with varying noise. (A-C) A hemisphere with $r = 30$ px and $K = 1.1 \times 10^{-3}$ px⁻² everywhere. The original triangulation is displayed in (A), the output of the initial least-squared fit with $d_1 = 2$ in (B), and the output of the IRLS fit with $d_2 = 4$ in (C), with the color scale for the curvature in (I). (D-H) The hemisphere in (A) with random noise from a distribution with mean 0 px and width 0.3 px added to the height at every point in the triangulation. The triangulation is displayed in (D), the output of the initial least-squared fit with $d_1 = 4$ in (E), and the output of the IRLS fit with $d_2 = 6, 8, 10$ in (F-H), respectively, with the color scale for the curvature in (I). 124

3.20 Fitting the curvature on a saddle surface with varying noise. (A-C) A saddle surface with $K = -0.4 \times 10^{-3} \text{ px}^{-2}$ in the center of the surface. The original triangulation is displayed in (A), the output of the initial least-squared fit with $d_1 = 2$ in (B), and the output of the IRLS fit with $d_2 = 4$ in (C), with the color scale for the curvature in (I). (D-H) The surface in (A) with random noise from a distribution with mean 0 px and width 0.3 px added to the height at every point in the triangulation. The triangulation is displayed in (D), the output of the initial least-squared fit with $d_1 = 4$ in (E), and the output of the IRLS fit with $d_2 = 6, 8, 10$ in (F-H), respectively, with the color scale for the curvature in (I).	125
3.21 Downsampling a surface. (A), Imaging the curved contour in gray leads to “step” artifacts in the black points. (B), We downsample the black points to get the red points. (C), The red points still represent the gray contour without so many step artifacts.	126
3.22 Measuring the Gaussian curvature and \sqrt{g} on a torus. (A) Triangula- tion colored by height formed from a downsampled $h(x, y)$. (B-D) The Gaussian curvature of the triangulation in (A) displayed as a (B,D) triangulation and an image, respectively, with the values given by the upper colorbar in (C). (E) The Gaussian curvature in (D), upsampled and with missing data filled in using linear interpolation to return the data to its original size. (F) The upsampled and filled in \sqrt{g} obtained from the corrected normal vectors with the values given by the lower colorbar in (C).	127
3.23 Defect unbinding in active nematic toroids. (A,B) Time-averaged topo- logical charge in an area vs the integrated Gaussian curvature of the area for toroids with (A) 144 μM ATP, (B) 36 μM ATP, and (C) both ATP concentrations with the data from (A) in red and the data from (B) in black. The lines in (A) and (B) are weighted averages of a linear fit to the data for each individual toroid in the plot and have slopes 4.3 ± 0.7 and 6.3 ± 0.5 , respectively with intercepts 0.01 ± 0.02 and 0.02 ± 0.03 , respectively. The toroids in (A) have: (●) $\xi = 1.6$ and $a = 275 \mu\text{m}$, (▲) $\xi = 2.0$ and $a = 372 \mu\text{m}$, (◆) $\xi = 2.4$ and $a = 268$ μm , (■) $\xi = 5.9$ and $a = 200 \mu\text{m}$, and (▼) $\xi = 6.6$ and $a = 167 \mu\text{m}$. The toroids in (B) have: (●) $\xi = 1.8$ and $a = 334 \mu\text{m}$, (▲) $\xi = 2.7$ and $a = 365 \mu\text{m}$, (◆) $\xi = 3.6$ and $a = 151 \mu\text{m}$, (■) $\xi = 4.7$ and $a = 200$ μm , and (▼) $\xi = 6.0$ and $a = 547 \mu\text{m}$	130

- 4.1 Spontaneous reflection symmetry breaking in twisted nematic cells and twisted bipolar droplets. (A), Schematic of a twisted nematic cell with a twist angle of $\pi/2$. The system could also satisfy the boundary conditions by twisting with the opposite handedness. (B), Schematic of a cross-section of the director in a twisted bipolar droplet. The nails represent the director going into the page. As with (A), the system could twist with the opposite handedness. 144
- 4.2 NLC in toroids with degenerate planar anchoring has a doubly-twisted ground state. (A-D), Director schematics for nematic toroids with degenerate planar anchoring. (A,B) Schematics for the twist-free state with (A) showing the director at the surface and (B) showing the director in a cross-section of the tube. (C,D) Schematics for doubly-twisted state with (C) showing the director at the surface and (D) showing the director in a cross-section of the tube. The nails represent the director going into the page. (E) Twist angle measured through the tube τ vs aspect ratio ξ for (●) 5CB and (■) SSY confined to toroidal droplets and cylindrical geometries. $\xi = \infty$ corresponds to measurements in a cylindrical geometry, and $\xi < \infty$ are previously published data in toroidal droplets from Ref. [37]. 146
- 4.3 Singular and escaped-radial distortions in cylindrical geometries. (A-C), Cross-sections showing the director fields for a (A) singular $s = +1$ distortion, a (B) escaped-radial distortion, and a (C) twisted escaped-radial distortion. The nails represent the director going into the page. (D), Director angle Ω measured off of the cylinder axis as a function of normalized radius, r/a , with a the cylinder radius. The blue curve corresponds the equilibrium solution for the 1-constant approximation, while the red curves correspond to $\Omega = (\pi/2)(r/a)^\phi$, with $\phi = 0.1, 0.5, 2, 5$. The curves with $\phi = 0.1, 0.5$ escape slower than the equilibrium solution, while the curves with $\phi = 2, 5$ escape faster than the equilibrium solution. 150
- 4.4 ER and TER capillaries and intensity profiles. (A,C), Bright field images of a capillary filled with (A) 5CB and (C) SSY with homeotropic anchoring. (B,D), corresponding OPM images showing that (A,B) 5CB has an ER configuration and (C,D) SSY has a TER configuration. (E,F), Intensity profiles measured across the capillary for (E) the 5CB texture in (B), and (F), the SSY texture in (D). The intensity scale is the grayscale intensity, with 1 corresponding to the white and 0 to black. 152

4.5 Images and intensity ratios for homeotropic nematic toroids. (A,B,D,E),
 (A,D) Bright-field and (B,E) associated OPM textures for toroids with
 (A,B) $\xi = 5$ and (D,E) $\xi = 5$. The central circle, defined by the radius
 R_0 , center \mathbf{p}_0 , and polar angle φ , as well as the local tube radius $a(\varphi)$
 are defined on the image in (A). The inner and outer circles, given by
 the radii R_{in} and R_{out} and centers \mathbf{p}_{in} and \mathbf{p}_{out} , respectively, are drawn
 on the OPM texture in (B). (C,F), OPM Intensity profiles across the
 tube of the toroid in (B,E), respectively. These profiles are taken at
 $\varphi = 0$, with $\phi \in [-1, 1]$ parameterizing the contour from the inner cir-
 cle to the outer circle for the given φ . Both profiles show two maxima
 surrounding a central minimum. We take I_{max} to be the average of
 the intensity values of the maxima and I_{min} to be the intensity at the
 central minimum. (G), I_{max}/I_{min} vs $\xi(\varphi) = R_0/a(\varphi)$ for a series of (○)
 homeotropic 5CB toroidal droplets, (▲) homeotropic 5CB bent and
 straight capillaries, and (■, □) homeotropic SSY straight capillaries.
 (■) corresponds to the transient ER state, while (□) corresponds to
 the equilibrium TER state. Scale bars in (A,D) are 250 μm 154

4.6 Symbols and coordinates used in simulating OPM droplet textures.
 (A), Relevant angles used in all simulations, where \mathbf{n}_d is the droplet
 director, \mathbf{n}_v is the local director, \mathbf{k}_0 is the incident wave vector, \mathbf{E}_P
 gives the orientation of the polarizer. \mathbf{n}_d is specified by θ_0 and α_0 ,
 while \mathbf{n}_v is specified by γ_v and α_v , where θ_0 and γ_v are measured from
 \hat{z} and \mathbf{k}_0 , respectively, and α is measured off of \hat{x} . (B), Breakdown
 of OPM simulation parameters in a spherical geometry, where $\boldsymbol{\rho}$ is
 the position vector in the final image and Δ is the thickness of the
 voxels used in the simulation. (C,D), Breakdown of OPM simulation
 parameters in a torus viewed from the (C) side and from the (D) top. 161

4.7 Director schematics and simulated and experimental OPM textures
 for (A–E) radial droplets, (F–M) bipolar droplets, and (N–U) twisted
 bipolar droplets. For the radial droplets, (A) is a director schematic,
 (B) is a our simulation, (C,E) are a grayscale and color experimental
 image, respectively, and (D) is a simulation image from Ref. [187]. For
 the bipolar and twisted bipolar droplets, (F–I) and (N–Q) are oriented
 with the bipolar axis aligned parallel to the analyzer direction while (J–
 M) and (R–U) have the bipolar axis rotated 15 degrees CCW from the
 analyzer direction. (F,J,N,R) are the schematics, (G,K,O,S) are our
 simulated images, (H,L,P,T) are experimental images, and (I,M,Q,U)
 are simulated textures from the literature. (I,M) are from Ref. [187],
 (P,T,Q,U) are from Ref. [177]. Scale bar is 20 μm in all images. Images
 from Ref. [187] reprinted with the permission of AIP Publishing. . . 162

4.8 Simulated OPM textures of nematic tori and experimental images of nematic toroids. (A,D–F), Experimental images of a tangentially-anchored nematic toroid with $\xi \approx 1.8$ from Ref. [37]. (A), OPM view from the top, (D), bright field view from the side, and (E,F), OPM views from the side with PA oriented at 0° and 45° , respectively. (B,G,H), Simulated OPM textures for a torus of $\xi = 1.8$ using the ansatz from Eq. 4.4 with $\omega = 0.420$ and $g = 0.750$ from minimizing the free energy. The OPM textures are viewed from the (B) top and from the side with P and A oriented at (G) 0° and (H) 45° . The intensity along the central ring for (A) (■) and (B) (▲) is plotted in (C). Scale bar is 100 μm in (E,F) and 200 μm in (A)	166
4.9 Values of (●) ω and (■) g as a function of ξ obtained by minimizing the Frank-Oseen free energy for the ansatz in Eq. 4.4.	167
4.10 Normalized weights as a function of wavelength to approximate the spectrum of a tungsten lamp. (A,B), the weights for 20 and 200 evenly-spaced wavelengths between 400 nm and 700 nm, respectively.	168
4.11 Relative response for the sensor in our color camera (DFK 41BU02). (A,B), the (A) individual R, G, and B channel and (B) total luminance relative response as a function of wavelength [189].	169
4.12 Intensity ratios for side-view and top-view simulated OPM textures of planar NLC toroids. (A), Schematic detailing the I_0 and I_{45} measurements from the side-view. (B,C), I_0/I_{45} versus ξ for (B) simulated and (C) experimental OPM textures from the side-view. (D) Schematic detailing the I_0 and I_{45} measurements from the top-view. (E,F), I_0/I_{45} versus ξ for (E) simulated and (F) experimental OPM textures from the top-view.	170
4.13 Predicted and measured twist angles for simulated OPM textures for planar NLC tori viewed from the top. (A) Simulated texture with the polarizer and analyzer aligned to extinguish both the e-mode (dark regions aligned vertically) and the o-mode (dark regions aligned horizontally). (B) Transmitted intensity as a function of analyzer angle with respect to the polarizer aligned along the entry director, with 1 corresponding to complete transmission and 0 to no transmission. The fit is to the theoretical transmitted intensity for a twisted nematic cell in the waveguiding limit [88].	171

4.14 The effect of averaging over multiple wavelengths in a simulated OPM texture. (A) Side-view simulated OPM texture of a planar NLC torus averaging over 200 wavelengths. The red square highlights the central region shown in (B–I). (B–E), The central region shown for the single wavelengths 400 nm, 500 nm, 600 nm, and 700 nm, respectively. (F–I), The central region shown for an average of 4, 8, 20, and 200 wavelengths, respectively, over the interval $\lambda \in [400, 700]$ nm.	174
4.15 Effect of voxel size on individual OPM textures and on I_0/I_{45} for planar NLC tori. (A–F), The central region of a simulated side-view OPM texture with $\xi = 1.8$ with PA at 0° (A–C) and PA at 45° (D–F) for (A,D) $\Delta/a = 0.04$, (B,E) $\Delta/a = 0.01$, and (C,F) $\Delta/a = 0.001$. All textures use a 200 wavelength average with $a = 100 \mu\text{m}$. (G) Intensity ratio I_0/I_{45} as a function of ξ for simulated side-view OPM textures as seen schematically in Figure 4.12(A) for (□) $\Delta/a = 0.04$, (□) $\Delta/a = 0.01$, and (■) $\Delta/a = 0.001$	175
4.16 Effect of refraction of top and side view images of toroids. (A,B,E,F), Experimental bright-field images of toroidal droplets of 5CB with (A,E) $n_{iso} \approx 1.6$, and (B,F) PDMS oil with $n \approx 1.4$ in a yield-stress outer medium with $n \approx 1.33$ viewed from the top (A,B) and from the side (E,F). Scale bar for experimental images is $200 \mu\text{m}$. (C,D,G,H), Simulated bright-field images of isotropic tori with (C,G) $n = 1.4$ and (D,H) $n = 1.2$ with outer index of refraction $n = 1$ viewed from the top (C,G) and from the side (D,H). Images simulated using Autodesk Maya.	176
4.17 Effect of shape on the star feature in simulated OPM textures of planar NLC tori. (A–C), Simulated OPM textures with $\xi = 1.8$ and $\Delta/a = 0.001$ for $a = 100 \mu\text{m}$ viewed from the side of truncated tori, as described schematically in (D). All simulations performed averaging over 200 wavelengths.	178
4.18 Simulated OPM textures, intensity profiles, and intensity ratios of TER configurations in tori and cylinders. (A–D), Simulated OPM textures of TER configurations in (A,B) tori and (C,D) cylinders. The textures are generated with twist angles (A,C) $\tau = 0^\circ$, (B,D) $\tau = 47.1^\circ$. (E), Intensity profiles from the simulated textures OPM textures in (A–D) corresponding to (□, ■, ○, ●), respectively. (F), Intensity ratio vs twist angle for simulated TER OPM textures.	179
4.19 Simulated OPM textures and intensity ratios of TER configurations in tori with varying escape rates. (A–C), Simulated OPM textures of TER configurations with $\tau = 34^\circ$ and $\Omega = (\pi/2)(r/a)^\phi$, where (A) $\phi = 1$, (B) $\phi = 10$, and (C) $\phi = 25$. (D), Intensity ratio vs ϕ for OPM textures with $\tau = 34.9^\circ$	181

- 4.20 Measuring curvature and intensity profile in homeotropic NLC confined to bent capillaries. (A), Bright-field image of a bend capillary with points selected along the left and right contour. The normal vectors at each point are plotted on the image. (B), The measured curvature along the (■) left contour and (●) right contour of the image in (A). (C), OPM image of the capillary in (A). (D), Intensity profile from the OPM texture in (C). For this profile, $I_{max}/I_{min} = 1.8$ and $\xi^{cap} = 6.8$ 182
- 5.1 Experimental set-up. (A,B) Schematic from the side of the setup to view a bridge from the (A) top and (B) side. The zoomed-in portion of (A,B) highlights the setup to make and manipulate the bridge on the microscope stage. 188
- 5.2 Measuring the shape of a bridge. (A,C), Bright-field images from the side of a (A) waist-shaped and a (C) barrel-shaped bridge, with the effective radius R and height H of each bridge defined in the image. The waist in (A) has $R = 180 \mu\text{m}$ and $H = 170 \mu\text{m}$, and the barrel in (C) has $R = 280 \mu\text{m}$ and $H = 300 \mu\text{m}$. (B,D), Contours of the bridge shown in (A,C), respectively, at different $\Gamma = 2R/H$, where the positions have been scaled by H and the (open symbols) lower contours have been reflected and shifted to line up with the (filled symbols) upper contours. The contours in (B) have (■, □) $\Gamma = 7.3$, (●, ○) $\Gamma = 4.6$, (▲, Δ) $\Gamma = 2.0$, (▼, ▽) $\Gamma = 1.0$, (◆, ◇) $\Gamma = 0.6$, and (★, ★) $\Gamma = 0.4$. The contours in (D) have (■, □) $\Gamma = 4.5$, (●, ○) $\Gamma = 3.9$, (▲, Δ) $\Gamma = 1.9$, (▼, ▽) $\Gamma = 1.5$, and (◆, ◇) $\Gamma = 1.3$ 190
- 5.3 Constant mean curvature surfaces. (A), The elevation angle θ and arclength parameter s defined for a surface of revolution in cylindrical coordinates, $\{r, \varphi, z\}$, with a contour of the surface displayed in cyan. θ is the angle between the tangent of the cyan curve at s and \hat{r} . $\theta(s=0) = \theta_0$, the contact angle, as shown in the magnified section in the blue circle. (B,C), Numerically calculated contours for a constant mean curvature surface of revolution plotted on experimentally measured contours for a (B) waist and a (C) barrel. The numerical solutions have contact angles (B) (black line) $\theta_0^{waist} = 37^\circ$, (cyan line) $\theta_0^{waist} = 35^\circ$ and (C) (black line) $\theta_0^{barrel} = 149^\circ$, (cyan line) $\theta_0^{barrel} = 120^\circ$. The measured contours in (B,C) are reproduced from Figure 5.2(B,D), respectively, and form the envelope of the measured contours in Figure 5.2(B,D). . . 193

5.6 Ring defects in barrel-shaped NLC bridges viewed from the top. (A), The ring defect diameter in a barrel-shaped bridge scaled by height of the bridge divided by 2, plotted as a function of the bridge aspect ratio, Γ . The experimental points include barrels made with the 5CB in the [open squares] nematic phase and the 5CB in the [filled squares] isotropic phase. We label the experimental points with their measurement number, with (■, □) corresponding to the first measurement, (■, □) the second measurement, (■, □) the third measurement, and (■, □) the fourth measurement, where we start at a large Γ and decrease Γ with each subsequent measurement in a single barrel. The (●) correspond to computations in a barrel structure using the elastic constants for 5CB. (B-E), First measurement of a barrel with (B,C) $\Gamma = 2.4$ and (D,E) $\Gamma = 2.8$ made with the 5CB in the isotropic phase and viewed from the top just after the (B,D) bright field and (C,E) corresponding crossed-polar image indicate the director field has stopped changing. We exclude this bridge in (B,C) from the plot in (A) due to the presence of micelles; we cannot say if the micelles are preventing the ring from collapsing to a point defect or if the measured $2R_{ring}/H = 0.2$ is the equilibrium state. The defect structure in (D,E) is a ring with $2R_{ring}/H = 0.1$ and is plotted in (A) as such. The scale bar in (B) is 250 μm .

199

5.7 Rotating the polarizer and analyzer for a waist-shaped bridge viewed with optical-polarized microscopy from the side. (A-C), A waist-shaped bridge with $\Gamma = 1.2$ viewed from the side under (A) bright field and (B,C) with crossed polarizer and analyzer (PA), where the PA orientations are specified in each image. (D-F), A waist-shaped bridge with $\Gamma = 6.6$ viewed from the side under (D) bright field and (E,F) with crossed PA, where the PA orientations are specified in each image. The scale bars in (A,D) are 250 μm .

201

5.8 Polarized epifluorescent microscopy on a planar NLC cell filled with a mixture of 5CB and Nile Red. (A), Schematic from the side of the setup for polarized epifluorescent microscopy (PFM). (B-D), PFM (B,C) images and (D) recorded intensity as a function of Φ_A of the planar NLC cell with rubbing direction along \hat{x} . Φ_A is indicated in the images in (B,C), and is measured in (D) with respect to \hat{y} . The blue curve is a fit of the data to Eq. 5.12, returning $\delta' = 89^\circ$. (E,F), Recorded intensity as a function of Φ_A of the planar NLC cell with rubbing direction (E) 25° CCW from \hat{y} and (F) 45° CCW from \hat{y} . The blue curves are fits of the data to Eq. 5.12 and have $\delta' = 2^\circ$ and $\delta' = 67^\circ$, respectively. The black dashed lines correspond to theoretical curves for $\delta' = 25^\circ$ and $\delta' = 45^\circ$, respectively.

202

5.9 The dichroic mirror is birefringent. (A,B), Optical-polarized microscopy images with no sample, P and A crossed, and the dichroic mirror in the light path. Φ_A is indicated by the white arrow in the bottom-right of each image. (C), Transmitted intensity as a function of Φ_A for the same setup as in (A,B), with Φ_A measured CCW off of \hat{y} . The maximum at $\Phi_A = 45^\circ$ and minima at $\Phi_A = 0^\circ, 90^\circ$ implies that the optic axis of the mirror is along either \hat{x} or \hat{y}	203
5.10 Recorded intensity as a function of Φ_A of a planar NLC cell filled with 5CB and melted to the isotropic. The rubbing direction is along 90° and the range in I is 6% of the mean.	205
5.11 PFM analysis for radial droplets. (A), Bright field image of radial droplets made from a mixture of 5CB and Nile red dispersed in water and 8 mM SDS. (B,C), Corresponding crossed-polar images of the droplets in (A) with the P and A orientation indicated in each image. The texture rotates with P and A, indicating the hedgehog in each droplet is radial. (D), Superposition of two PFM images of the droplets in (A), where the images have the same Φ_A but opposite analyzer wedge-angle orientations. Note how the two images are displaced due to the effect of the analyzer wedge-angle, making the superposition blurry. (E), Superposition of the same images in (D) after shifting each image to correct for the displacement due to the analyzer wedge-angle. Here, the two droplets are clear and the superposition is no longer blurry. The analyzer angle in (D,E) is indicated schematically. (F), Grayscale intensity of a PFM image of the droplets in (A) after blurring with a square Gaussian filter with side length 7 px. The analyzer orientation is indicated schematically. (G-I), Downsampled PFM images after blurring, with the analyzer angle in each image indicated schematically. (J), PFM intensity as a function of Φ_A from the highlighted pixel in (G-I). The blue curve is a fit to Eq 5.12, returning $\delta' = 88^\circ$. (K), The δ' from a PFM analysis of every pixel in (G-I) plotted on top of an epifluorescent image of the droplets. The droplets are clearly radial, matching our observations in (B,C). The scale bar in (A) is 25 μm	207
5.12 The analyzer shifts the image. (A), Schematic from the side showing how the wedge angle of the analyzer causes light from the sample to be translated by $\Delta\rho$ in the direction of the wedge, Φ_W . (B), The analyzer pass axis and the wedge angle are not parallel to each other. Rotating the analyzer by π will translate the image on the camera along a semicircle with radius $\Delta\rho$. Since $\Phi_A \in [0, \pi]$ while $\Phi_W \in [0, 2\pi]$, knowing Φ_A alone is not enough to know which direction the output image has been translated.	208

5.13 PFM in an escaped-radial capillary. (A), Crossed-polar image of a capillary filled with the Nile Red-Doped 5CB under homeotropic anchoring. (B), Bright-field image of the capillary in (A), with the director orientation from the PFM analysis plotted on top of the associated bright-field image. (C), δ' plotted versus the position across the capillary for the column indicated by the red arrow in (B). The blue curve is $2 \arctan(x/R)$, the theoretical director angles for an escaped-radial configuration in the one-constant approximation. Using the 5CB value of $K_{11}/K_{33} = 0.74$ would only slightly change the blue curve. The scale bar in (B) is 250 μm	209
5.14 (A-D), PFM analysis on waist-shaped bridges with (A,B) $\Gamma = 4.0$ and (C,D) $\Gamma = 0.8$. The δ' are plotted on the epifluorescent images in (B,D) with the associated bright-field images in (A,C). (E-H), PFM analysis on barrel-shaped bridges with (E,F) $\Gamma = 6.6$ and (G,H) $\Gamma = 1.5$. The δ' are plotted on the epifluorescent images in (F,H) with the associated bright-field images in (E,G). The scale bars in (A,B) are 250 μm , with the scale for all the (A,C,E,G) bright field images and all the (B,D,F,H) PFM images the same.	210
5.15 Results from the computational modeling of a nematic in a capillary bridge. (A), Phase diagram of the defect structure in a cylinder as a function of aspect ratio Γ and the ratio, K_{11}/K_{33} , of the splay and bend elastic constants. (B), Phase diagram of the defect structure in a waist-shaped bridge as a function of Γ and K_{11}/K_{33} . In (A,B), the minimum-energy state is indicated in each region, and the dashed line corresponds to K_{11}/K_{33} for 5CB. (C,D), Free energy of a director configuration in a waist-shaped bridge relative to the free energy in the presence of the point defect and normalized by HK_{33} , shown as a function of scaled ring radius R_{ring}/R_{bridge} . The curves correspond to (■) $\Gamma = 3.5$, (●) $\Gamma = 2.8$, (▲) $\Gamma = 2.5$, and (▼) $\Gamma = 2.0$	212
6.1 Example director fields and axes of symmetry for an (A) $s = +1/2$ and an (B) $s = -1/2$ defect. The axes of symmetry were calculated with Eqs. 6.2 and 6.3.	219
6.2 $s = \pm 1/2$ defect ordering on a toroid with $\xi = 2.4$, $a = 268 \mu\text{m}$, and an ATP concentration of 144 μM . Magnitude and direction of (A-C) polar and (D-F) nematic order calculated for the $s = +1/2$ defects and (G-I) three-fold bond angle order calculated for the $s = -1/2$ defects. The order in (A,D,G) and (B,E,H) is calculated for the $\{\theta, \varphi\}$ and the $\{\nabla K = \theta', \varphi'\}$ coordinate systems, respectively, with (C,F,I) indicating the color scales used to denote orientation.	224

6.3 $s = \pm 1/2$ defect order plotted as a function of the mean defect density and of the magnitude of the gradient of the Gaussian curvature. Magnitude and direction of the (A–D) polar order for the $s = +1/2$ defects and the (F–I) three-fold bond angle order for the $s = -1/2$ defects. (A,B) and (F,G) are calculated in the $\{\theta, \varphi\}$ coordinate system, while (C,D) and (H,I) are calculated in the $\{\nabla K = \theta', \varphi'\}$ coordinate system. The magnitude and direction of the order are plotted in (A,C,F,H) and (B,D,G,I) as a function of the mean defect density and of the mean magnitude of the gradient of the Gaussian curvature, respectively. The polar and three-fold bond angle color scales are displayed in (E,J), respectively.	226
6.4 OPM textures of an emulsion of 5CB undergoing a bipolar-to-radial transformation. (A–C), The outer medium consists of 99% w/w Millipore water with 1% w/w PVA. (D–F), The outer medium consists of 69% w/w Millipore water, 30% w/w Ethanol, and 1% w/w PVA. In all images the absolute and reduced temperature are displayed below the image. The scale bar is: 50 μm	231
6.5 The transition from bipolar-to-radial happens as the order parameter decreases. (A–E), Experimental images showing how a 40 μm diameter bipolar droplet transforms into a radial droplet. As the reduced temperature increases, the number of fringes in the (A–C) bipolar OPM textures decrease. The saturn ring mediated the bipolar-to-radial transformation is clearly visible under bright-field illumination in (D), with the final radial structure visible in the OPM texture in (E). (F–H), Simulated OPM textures of bipolar droplets with varying Δn ; the Δn were chosen to match the number of fringes in the experimental OPM textures in (A–C), respectively. (I), Plot of the scalar order parameter vs. the reduced temperature with data from Raman scattering measurements (\bullet) and from matching the simulated and experimental OPM textures (\blacktriangle)	233
6.6 Cylindrical structures of 5CB in a yield-stress material. (A), Bright-field image of a cylindrical structure of 5CB in a yield-stress medium consisting of 1% w/w PVA, 1.5% w/w carbopol, 3% w/w glycerol, 30% w/w ethanol, 64.5 w/w % Millipore water. (B–E), OPM textures of cylindrical structures of 5CB with (B,D) having aligned P and A, and (C,E) having P and A oriented for minimum transmission through the 5CB structure. (B,C) are a section of the structure in (A), while (D,E) are a section from a structure in an outer medium consisting of 1% w/w PVA, 1.8% w/w carbopol, 3% w/w glycerol, 94.2 w/w % Millipore water. Scale bar for (A–C) is 500 μm ; for (D,E) the scale bar is 250 μm	234

CHAPTER 1

INTRODUCTION

At high temperature, an isolated collection of molecules at a low enough volume fraction is a fluid and thus is a homogeneous system on average; the probability of finding any molecule at any specific position is a constant and only depends on the density of the particles. As this system is invariant under all possible rotations and translations, we say that the system has complete continuous translational and rotational symmetry. If we lower the temperature, the system will eventually develop order, where the individual molecules have a preferred local arrangement. For this example, lowering the temperature will eventually induce the system to transition from a fluid phase to a crystalline phase, characterized by an underlying periodic lattice. This order is *long-range*, such that knowing the position of one particle gives the position of every other particle in the system, regardless of the distance between the particles. Another way of stating this is that the correlation functions describing the ordered state do not decay. Thus, the system is now only invariant with respect to a discrete set of translations and rotations. Here, the system breaks the continuous symmetry of the isotropic phase in order to achieve the crystalline phase. Hence, the ordered phase has lower symmetry than the isotropic phase.

The advent of long range order as a result of the spontaneous breaking of continuous symmetry is general and is a hallmark of transitions between a multitude of different phases. In addition, the phases do not have to be formed by collections of molecules; they can be built from a variety of constituent units, from angstrom-scale atoms to micron-scale colloidal particles or even larger building blocks. Regardless of the nature of the constituent particles, the isotropic-to-crystalline phase transition in three dimensions (3D) breaks continuous translational and rotational symmetry in all

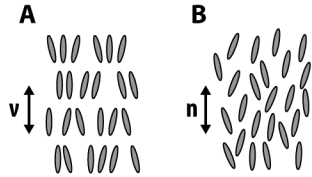


Figure 1.1: Smectic and nematic order. (A), A smectic phase breaks translational symmetry along one direction, leading to a layer-like structure. For the drawn Smectic-A phase, this direction is indicated by ν . (B), A uniaxial nematic phase has continuous translational symmetry in all directions and continuous rotational symmetry in one direction. This direction is indicated by the director, n .

directions. However, a system can also transition from an isotropic phase to a phase where the continuous translational and rotational symmetry is not broken in all directions. For example, an isotropic-to-smectic phase transition in 3D breaks continuous translation symmetry in only one direction and continuous rotational symmetry in two directions, while the isotropic-to-uniaxial nematic and isotropic-to-ferromagnetic transitions break no translational symmetries and only breaks rotational symmetry in two directions [1]. Breaking continuous translational symmetry results in positional order while breaking continuous rotational symmetry results in orientational order.

With the development of order as a result of breaking one or more continuous symmetries comes the rigidity needed to maintain that order. For example, due to their broken symmetries, crystalline, smectic, and nematic phases cannot be made to flow as easily as the isotropic phase of the material. However, since a nematic phase has no broken continuous translational symmetries, in contrast to smectic and crystalline phases, the nematic phase of a material will flow easier than the smectic and crystalline phases of that material. This is because the constituent particles in a nematic only need to maintain their orientation and not their position. In addition, systems with anisotropic order have a correspondingly anisotropic rigidity. Consider a smectic phase with its broken translational symmetry in one direction, defined by a unit vector ν , as drawn schematically in Figure 1.1(A). Along ν , the material will resist flow like a crystal, but will flow easily like an isotropic fluid

along directions orthogonal to ν . Similarly, even though a uniaxial nematic has continuous translational symmetry in all directions, it still has certain rigidity as the nematic must maintain its two-fold orientational order, defined by a unit vector \mathbf{n} [see Figure 1.1(B)]. A nematic phase resists torques that affect the orientations of \mathbf{n} . Since a force along \mathbf{n} imposes no torque, there is no rigidity along \mathbf{n} . In both of these examples, the rigidity depends on the direction of the deformation, and thus is anisotropic. This phenomenon is not limited to the rigidity; in general, properties of a phase will reflect the symmetries of the phase. For example, ordered materials often exhibit birefringence, where the index of refraction is anisotropic. Thus, the speed of light in a birefringent material depends on the direction and polarization of the light [1].

Ordered materials can also have defects, defined generally as locations in the material where the preferred arrangement is not satisfied. Belying the colloquial definition, defects in the order are not necessarily undesirable; in fact, they can have important consequences for the physics of the phase, and thus can be exploited to achieve specific properties. For example, joining two crystalline domains of incompatible orientations results in defects forming a border, or grain boundary, between the two domains. In a crystalline material, these grain boundaries affect the moduli of the material, and are even responsible for the phenomenon of “work hardening,” where the plastic deforming of the material increases the magnitude of the shear modulus. This is commonly done to create durable objects from copper and other ductile metals. The plastic deformations cause isolated defects and grain boundaries to proliferate within the material; however, as the defect density rises, so does the energy required to generate new defects and move existing defects. This results in an increased resistance to deformation that further reflects in the increase of the shear modulus.

In addition, defects can also directly mediate phase transitions, as in the celebrated Kosterlitz-Thouless-Halperin-Nelson-Young (KTHNY) theory of melting in 2D [2–

4]. In two or fewer dimensions, a system cannot spontaneously break continuous symmetry and establish LRO. This is known as the Mermin-Wagner theorem [1]. However, in 2D, a system can still have phases with quasi-long range order (QRLO). The QRLO and associated rigidity arise from correlations between the constituent particles in the material. However, the correlation functions in QRLO decay as a power law in the separation distance between the particles [1]. For this reason, phases with QLRO are also called *algebraically-ordered*. In this case, the increase in symmetry when an algebraically-ordered 2D crystalline phase melts to the isotropic phase is a two-step process. First, beginning in the crystalline phase, the crystalline phase will always possess pairs of thermally excited dislocations, or translational defects. While a single dislocation will always reduce the translational order of the crystal, a pair of dislocations can have no net effect on the order. Raising the temperature in the crystalline phase will eventually induce the dislocation pairs to *unbind*. The free dislocations reduce the translational order of the crystalline phase, but do not affect the orientational order of the system, inducing a transition from the crystalline phase to an intermediate hexatic phase characterized by six-fold orientational order [5, 6]. We note that each dislocation is composed of a pair of disclinations, or rotational defects; isolated disclinations reduce the orientational order of the system, but a pair of disclinations *bound* together to form a dislocation have no net effect on the orientational order. Raising the temperature even further will eventually induce the disclination pairs to unbind, destroying the orientational order and transforming the hexatic phase into the isotropic phase. This phase map for this two-step process is illustrated schematically in Figure 1.2. Furthermore, defects in soft matter have been used as tools to investigate a wide range of phenomena from knot theory [7, 8] to controlled self-assembly [9–12], to hierarchical materials [13–15].

Apart from both their effect on physical systems and their use as tools, defects are fascinating objects in their own right as they can both be required by the topology

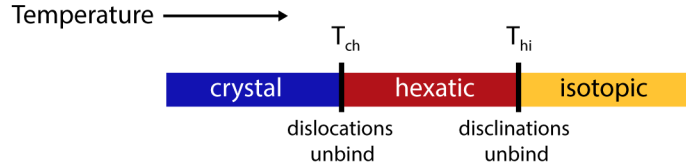


Figure 1.2: Schematic of the phase behavior for melting in 2D. T_{ch} and T_{hi} are the transition temperatures for the crystalline-hexatic transition and the hexatic-isotropic transition, respectively.

and interact with geometry of the space they inhabit. Consider, for example, a dense packing of rods in a plane at zero temperature. In order to maximize the entropy of the system, the rods need to align along the same direction, resulting in the uniaxial nematic phase [16]. We characterize this preferred local alignment with a director, \mathbf{n} , where the inversion symmetry of the system dictates that \mathbf{n} and $-\mathbf{n}$ describe the same state. Since rotating the director by π about an axis orthogonal to \mathbf{n} does not change the state, we say that the system has 2-fold order. Clearly, it is easy to fill space on the plane with a homogeneous director field, as shown schematically in Figure 1.3(A). However, if we now try to pack rods on the surface of a sphere, for example along either the latitude or longitude lines of the Earth’s globe [Figure 1.3(B)], we see that there are defects in the order that correspond to the singular points at the poles, where \mathbf{n} is undefined. Since one “cannot comb a hairy ball without a cowlick,” or singularity in the pattern of the hair, the presence of singularities is no accident — it is a consequence of confining the nematic to the surface with the topology of a sphere [17, 18].

To formally relate the topology of the sphere with the presence of singularities, we need a few topological notions. The sphere is an example of a differentiable surface that is compact, has no boundary, and is orientable. Compact surfaces must both be bounded and contain their limit points. Here, the term “bounded” means the surface has some finite size and is distinct from whether or not the surface has a boundary. The boundary of a surface is defined as the set of points that can be approached from

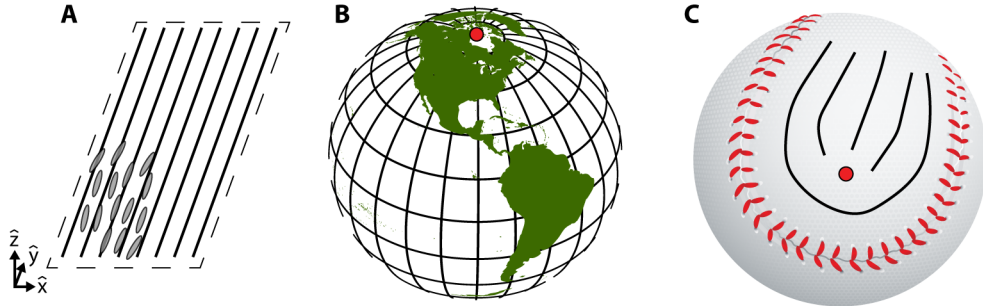


Figure 1.3: Packing rods in two dimensions. (A-C), Rod-like particles preferentially align along a common axis, given by the black lines. (A) On a plane, the alignment can be homogeneous everywhere. (B,C) On a sphere, there must be singularities (\bullet) in the alignment directions, as shown for alignment directions along (B) the latitude or longitude lines on a globe and an alignment direction along (C) the stitching on a baseball. Note that while only one singularity is visible in (B,C), there are 2 singularities in (B) and 4 in (C).

both the interior and the exterior of the surface. Finally, orientable surfaces have a consistently defined normal vector everywhere. For example, 2D Euclidean space, denoted as \mathbb{R}^2 , is a surface but it is not bounded and thus it is not compact. Given $\mathbf{r} \in \mathbb{R}^2$, the 2D open unit disc $|\mathbf{r}| < d$ is not compact since it does not contain the circle with radius d . However, the 2D unit disc $|\mathbf{r}| \leq d$ satisfies both conditions and thus is compact. In addition, we see that $|\mathbf{r}| \leq d$ has a boundary $\partial\mathbf{r}$ at $|\mathbf{r}| = d$, as $\partial\mathbf{r}$ can be approached by points in both the interior and the exterior of the disc. We call surfaces that are compact and without a boundary *closed surfaces*. Finally, all of these examples are also orientable; it is trivial to define a consistent surface normal everywhere.

One can characterize the topological properties of a surface via its Euler characteristic, χ , which one can calculate using the Gauss-Bonnet theorem. For a closed surface, the theorem states that [19]

$$\chi = 2(1 - g), \quad (1.1)$$

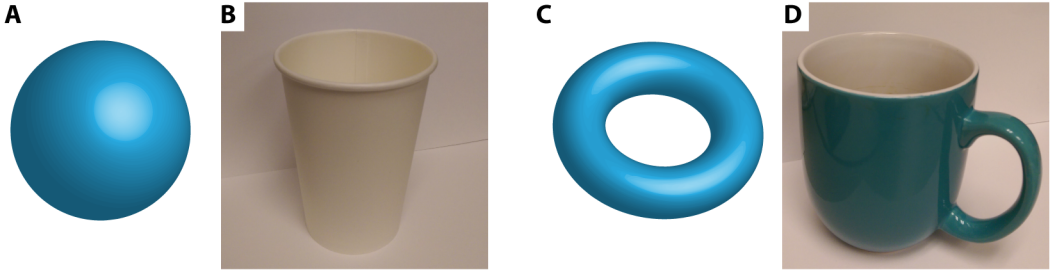


Figure 1.4: Closed surfaces with the same Euler characteristic are homeomorphic. (A,B) Closed surfaces with no handle like a (A) sphere and (B) the surface of a cup can be continuously deformed into each other. (C,D) Closed surfaces with a single handle like a (C) torus and (D) the surface of a coffee mug can be continuously deformed into each other. However, the surfaces in (A,B) cannot be continuously deformed into the surfaces in (C,D) as the process of adding a handle breaks the surface.

where g is the genus, or number of handles, of the surface. The Euler characteristic is a topological invariant — continuously deforming a surface, i.e. under a homeomorphism, does not change its Euler characteristic. A homeomorphism is a continuous function with a continuous inverse that maps between topological spaces while preserving topological properties. For example, a sphere has no handles, thus $g = 0$ and $\chi = 2$. Since a homeomorphism preserves the topological properties, any surface with $g = 0$ is topologically equivalent, or homeomorphic, to the sphere, and therefore also has $\chi = 2$. For example, a sphere [see Figure 1.4(A)] is homeomorphic to the surface of the kind of cup pictured in Figure 1.4(B), as neither has a handle. Similarly, the torus and the surface of the coffee mug pictured in Figure 1.4(C,D), respectively, are also homeomorphic to each other. However, the sphere [Figure 1.4(A)] and the torus [Figure 1.4(C)] are not homeomorphic, as one cannot add a handle to the sphere by simply bending and stretching the surface. A handle can only be added by tearing or breaking a surface.

With these definitions, we can extend the statement, one “cannot comb a hairy ball without a cowlick” to, “one cannot comb a hairy surface with $\chi = 2$ without a singularity in the hair.” In an orientation field like a director field, singularities

are called “disclinations.” It is useful to characterize a disclination by how much the director rotates as one progresses along a closed contour encircling the disclination. For a contour ∂A and the angle $\phi(\mathbf{r})$ parameterizing the director field, with \mathbf{r} being the position vector of a point on the surface, we can calculate [6, 19, 20]

$$s \equiv \frac{1}{2\pi} \oint_{\partial A} d\mathbf{r} \cdot \nabla \phi(\mathbf{r}) = \frac{1}{2\pi} \oint_{\partial A} d\phi, \quad (1.2)$$

where $d\phi$ is an exact differential. However, since ϕ is not a single-valued scalar field, ϕ is not conservative, and s is not path independent [21]. If we map ϕ on ∂A onto points on \mathbb{S}^1 , the unit circle, we see that s is the number of times the director field wraps the unit circle. Since we cannot eliminate the enclosed disclination with continuous deformations of the director, disclinations are topological and s is known as the winding number, or “topological charge.” Regardless of aligning rods along the latitudes or the longitudes on the Earth’s globe, the director along a contour encircling either pole rotates by 2π , as depicted in Figure 1.5(A). Thus, both the north and the south poles have charge $s = +1$, bringing the total charge on the surface to $+2$. The formal statement connecting a vector or director field on a closed surface with the topology of the surface is the Poincaré-Hopf theorem [19]:

$$\sum_{i=1}^N s_i = \chi, \quad (1.3)$$

where N is the number of disclinations, each of topological charge s_i .

For nematic order, $s \in n/2$, where $n \in \mathbb{Z}$, the integers; however, for polar order, $s = n$. For example, the defect structure in Figure 1.5(B) has $s = +1/2$ and can exist for nematic order, since \mathbf{n} and $-\mathbf{n}$ describe the same state. Attempting to construct such a disclination for polar order, as illustrated by following the vectors as they go from blue to cyan along the red contour in Figure 1.5(C), we see that cyan vector at the end of the path points opposite to the blue vector at the beginning of the path.

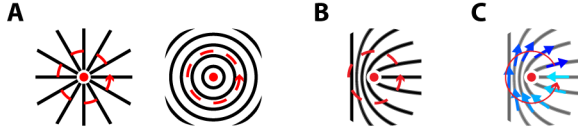


Figure 1.5: Topological charge of disclinations. (A), The director rotates by 2π along the contour enclosing the singularity (•), giving $s = +1$ for both disclinations. (B) The director rotates by π along the contour enclosing the singularity (•), giving $s = +1/2$. (C) Attempting to construct an $s = +1/2$ disclination for a vector field results in a discontinuity in the vector field along the contour. This is seen by following the red contour as the vectors go from blue to cyan.

Note also that the Poincaré-Hopf Theorem only requires the net charge on the surface to be equal to χ ; we can construct a director or a vector field on a closed surface with any combination of defects so long as the total topological charge is equal to χ .

In thermal equilibrium, physical ordered systems constrained to a closed surface must minimize their free energy while complying with the constraint imposed by the Poincaré-Hopf theorem. For an orientationally ordered phase where the particles prefer to align parallel to each other, we can write the free energy as the cost of distorting the material from the homogeneously aligned state. In the continuum limit, this distortion free energy is a functional of the orientation field,

$$F_d = \frac{1}{2}k_F \int d^2r |\nabla\phi(\mathbf{r})|^2, \quad (1.4)$$

where k_F is the elastic constant governing the cost of distortion. If we have polar order described by a vector field, then Eq. 1.4 with ϕ and $\phi + 2\pi$ identified is a continuum description of the classical 2D X-Y model governing spins on a fixed lattice [1]; for nematic order, Eq. 1.4 with ϕ and $\phi + \pi$ identified is the 2D Frank-Oseen free energy [5] in the 1-constant approximation [22].

Nematics on a sphere were predicted [9, 23, 24] to minimize the free energy not with two $s = +1$ defects [Figure 1.3(B)] but with four $s = +1/2$ defects arranged on the vertices of a tetrahedron [Figure 1.3(C)]. Prior work in the Fernández-Nieves

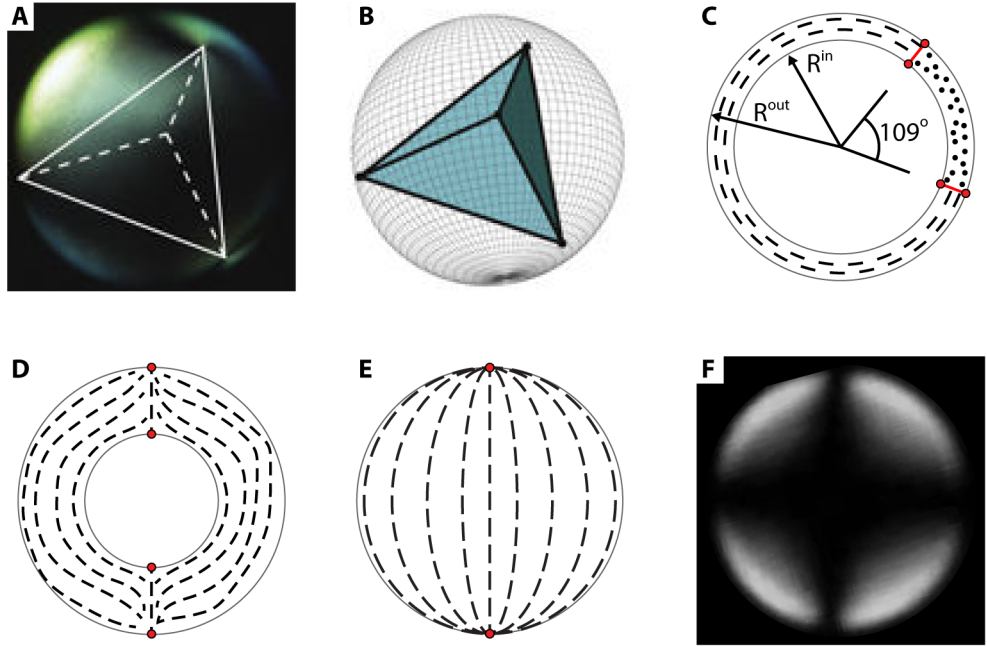


Figure 1.6: Shells of nematic liquid crystal. (A-C) Thin shells of NLC have four $s = +1/2$ defects, with an experimental crossed-polar image in (A), the tetrahedron highlighted in (B), and a cross-section schematically showing the director configuration in (C). The cross-section is of a great circle containing two $s = +1/2$ defects (●) on both the inner and outer surface of the shell, with a red singular line connecting corresponding disclinations. The disclinations occupy the vertices of a tetrahedron and thus are separated by 109° in the cross-section. (D) Cross-section of the director configuration in a thick shell. Here, the two $s = +1$ disclinations (●) on each surface are no longer connected by a singular line. (E,F) As $R^{in} \rightarrow 0$, the thick shell becomes a bipolar droplet, with a cross-section of the director field in (E) and a corresponding crossed-polar image in (F). Images/Schematics in (A,B) reproduced from Ref. [26] with permission from Macmillan Publishers Ltd: Nature Physics, copyright 2011.

group addressed this situation experimentally, using glass-based microfluidic devices to fabricate double emulsions [25], with a shell of nematic liquid crystal (NLC) between an inner water droplet and an outer water continuous phase [26, 27]. By decreasing the osmotic pressure in the outer continuous phase of the nematic shells, swelling of the inner droplet was induced. This swelling decreased the thickness of the NLC shell to create an experimental realization of a 2D nematic on the surface of a sphere [27]. In this thin-shell limit, the four $s = +1/2$ defects arranged on the vertices of a tetrahedron was observed; see Figure 1.6(A,B).

However, this tetrahedral arrangement of $s = +1/2$ defects only exists in thin enough shells, as characterized by the relative shell thickness $h' = (R^{out} - R^{in})/R^{out}$, with R^{in} and R^{out} being the inner and outer radius of the nematic shell, as defined schematically in Figure 1.6(C). As h' is increased, the shell also becomes inhomogeneous due to density differences between the inner droplet and the NLC shell. This thickness heterogeneity drives defects to the thinnest portion of the shell; this means that the $s = +1/2$ defects are no longer arranged in a tetrahedron. In addition, as h' is increased, the shell can no longer be considered 2D.

The situation is now 3D, and there are two spherical interfaces where the topological charge on the interface is constrained by the Poincaré-Hopf theorem, with a bulk region between the two surfaces filled with NLC. Each $s = +1/2$ defect on the outer surface is then connected to a corresponding $s = +1/2$ disclination on the inner surface via a singular line that threads through the bulk. This is depicted schematically in Figure 1.6(C) for a great circle containing two $s = +1/2$ disclinations on each surface. As h' is increased, so does the energetic cost of each singular line. Eventually, as $h' \gtrsim 1/2$, the energetic cost of the singular lines threading through the bulk is too great, and pairs of $s = +1/2$ disclinations each transition to a single $s = +1$ surface disclination [26], known as a boojum [28].

Unlike the $s = +1/2$ defects, the corresponding boojums on the inner and outer surface are not connected by a singular line; instead, the director in the shell region “escapes into the third dimension,” and acquires a component along the radius of the droplet, removing all the singularities in the bulk region. The increased energetic cost of a single boojum as compared to two $s = +1/2$ defects is compensated by the energetic decrease of removing the singular regions in the bulk of the shell. This is depicted schematically for the special case of a homogeneous shell, in Figure 1.6(D). For a heterogeneous thickness, the boojums migrate towards the thinnest portion of the shell. In addition, the shells are not restricted to either four $s = +1/2$ disclinations

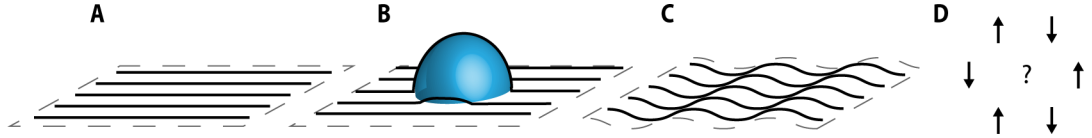


Figure 1.7: Geometrical frustration in nematics and in magnetism. (A), A flat plane can support a homogeneous director field, indicated by the black lines. (B), Adding a hemisphere to the plane disrupts the homogeneous state, the Gaussian curvature of the hemisphere makes a distortion-free state impossible. (C), Modulating the surface with a sine wave adds mean curvature but not Gaussian curvature to the surface; the homogeneous state on the surface is still possible. (D), Geometrical frustration in magnetism. Perfect antiferromagnetic order cannot exist on a triangular lattice.

or two $s = +1$ boojums; there are also hybrid shells with two $s = +1/2$ disclinations and a single boojum [26]. For $h' = 1$, there is no inner water droplet and we have a single droplet of NLC within a continuous water phase, with the boojums on opposite poles. This director arrangement is the classic bipolar configuration, with the director field and associated crossed polar image shown in Figure 1.6(E,F), respectively.

This example with the shells shows that even if Eq. 1.4 favors a homogeneous orientation field, corresponding to the zero elastic free energy configuration, sometimes distortions are unavoidable due to the topological constraints imposed by the surface. However, ordered materials are also sensitive to the local geometry. For example, consider, once more, rods packed on a plane with a homogeneous director field, as shown schematically in Figure 1.7(A). If we change the geometry and introduce a hemispherical ‘‘bump’’ in the plane, as illustrated in Figure 1.7(B), evenly spaced director lines on the plane do not maintain their spacing on the bump. Thus, we no longer have a homogeneous director everywhere on the surface. This inability to maintain the preferred local order due to the geometry of the surface is called *geometrical frustration*. Geometrical frustration is also commonly seen in magnetic systems. For example, it is impossible to have a triangular lattice with antiferromagnetic order everywhere; the topology of the lattice frustrates the local antiferromagnetic order, as illustrated schematically in Figure 1.7(D).

An important aspect of the local geometry of a surface is its curvature; consider a curve constrained to lie in \mathbb{R}^2 , $\mathbf{r}(s)$, with s being the arclength parameter. Such an example of a planar curve is drawn schematically in Figure 1.8(A). The unit tangent to the curve at s is given by $\mathbf{T}(s) = d\mathbf{r}(s)/ds = \mathbf{r}'(s)$, and the local curvature $\kappa(s)$ by $\mathbf{k}(s)\kappa(s) = \mathbf{T}'(s) = \mathbf{r}''(s)$, with $\mathbf{k}(s)$ the unit normal vector to the curve [see Figure 1.8(A)] and $\kappa(s) = 1/R(s)$, where $R(s)$ is the radius of the osculating circle, or circle that best approximates $\mathbf{r}(s)$ at s . This radius is commonly known as the “radius of curvature” at s . The sign of the curvature relates to the direction \mathbf{k} rotates as s increases: if \mathbf{k} rotates towards \mathbf{T} [blue circle, see Figure 1.8(A)], $\kappa < 0$, while if \mathbf{k} rotates away from \mathbf{T} [red circle, Figure 1.8(A)], $\kappa > 0$.

Now consider a 2D orientable surface given by $\mathbf{R}(u^1, u^2) \in \mathbb{R}^3$, with $(u^1, u^2) \in U \subset \mathbb{R}^2$ local coordinates on the surface, and with U a local coordinate patch. We define a normal section at a point $\mathbf{r} \in U$ on the surface as the planar curve resulting from the intersection between the surface and a plane containing $\mathbf{k}(\mathbf{r})$. Since the orientation of the plane is not unique, there are infinitely many planes that can contain $\mathbf{k}(\mathbf{r})$, and therefore infinitely many normal sections at a given point \mathbf{r} . The curvature of a given normal section at \mathbf{r} is called the normal curvature. A normal section, the plane containing \mathbf{k} , and the osculating circle whose R determines the normal curvature $\kappa(s)$, are drawn schematically in Figure 1.8(B) for an example surface. Among all possible normal curvatures at \mathbf{r} , there is always a maximum and minimum normal curvature, with the planes containing the associated normal sections orthogonal to each other [29]. These two curvatures are the *principal* curvatures at \mathbf{r} , $\kappa_1(\mathbf{r})$ and $\kappa_2(\mathbf{r})$, and their associated tangent vectors at \mathbf{r} are the principal directions; these directions and curvatures are drawn schematically for an example surface in Figure 1.8(C). From κ_1 and κ_2 , we define two important quantities: the Gaussian curvature $K \equiv \kappa_1\kappa_2$ and the mean curvature $H \equiv (\kappa_1 + \kappa_2)/2$.

We now see that adding the hemispherical bump to the plane, which has $K =$

$H = 0$ everywhere, changes the geometry by adding both non-zero mean and Gaussian curvatures. However, it is the Gaussian curvature and not the mean curvature that is responsible for geometrical frustration. We see this by considering the modulation of the flat plane with a sine wave in one direction, as shown in Figure 1.7(C). In this case, $K = 0$ everywhere while H changes throughout the surface. Despite the fact that $H \neq 0$ everywhere, we can still maintain a homogeneous director field, in contrast to our example surface with $K \neq 0$ at the bump [Figure 1.7(B)]. This is a reflection of the fact that Gaussian curvature is a property of the surface alone, that is, it is an *intrinsic* curvature. We can determine the Gaussian curvature of a surface without knowing anything about the space the surface is embedded in. In contrast, determining the mean, or *extrinsic*, curvature of a surface requires knowledge of the space the surface is embedded in.

Revisiting the Euler characteristic, we can rewrite the Gauss-Bonnet theorem for a differentiable closed surface as

$$\chi = \frac{1}{2\pi} \int K d^2r = 2(1 - g). \quad (1.5)$$

It is evident from Eq. 1.5 that the Gaussian curvature provides the connection between the local geometry and the topology of a closed surface. This is a very important fact. Even though K is a property of the local *geometry*, integrating K over a closed surface yields a *topological* invariant.

The connection between K and the geometrical frustration is explicitly stated through the coupling of K to the free energy of an orientationally ordered phase confined to a surface. Considering the topological charge density

$$\rho(\mathbf{r}) \equiv 2\pi \sum_i s_i \delta(\mathbf{r} - \mathbf{r}_i), \quad (1.6)$$

due to disclinations indexed by i and possessing charge s_i and position \mathbf{r}_i , where

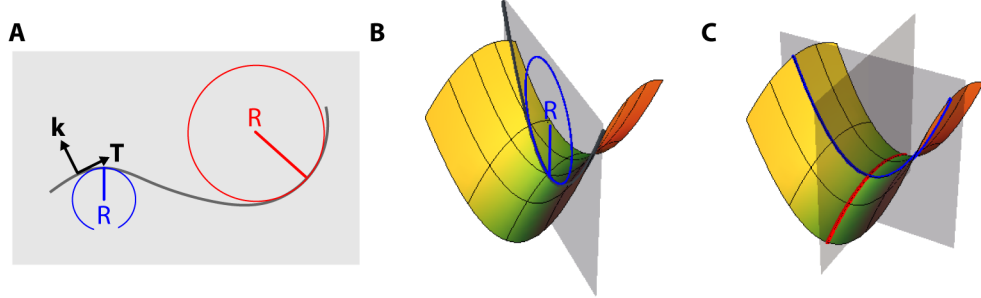


Figure 1.8: Planar and surface curvature. (A), A planar curve with unit tangent vector \mathbf{T} and unit normal vector \mathbf{k} . The osculating circles and associated radii of curvature are given for two points on the curve; the negative curvature is in blue and the positive curvature in red. (B), A normal section of a saddle-surface at a point corresponds to a planar curve, with the curve drawn in dark gray and the plane containing the curve indicated in transparent gray. The osculating circle and radius of curvature at the point of interest are drawn in blue. (C), The principal curvatures κ_1 and κ_2 at the point of interest on the surface from (B) are the maximum and minimum normal curvatures and are always in orthogonal directions. Here these directions are highlighted with the red and blue contours on the surface.

$\delta(\mathbf{r} - \mathbf{r}_i)$ is the Dirac delta function, we can express Eq 1.4 as [1, 23, 30]

$$F_d = -\frac{1}{2}k_f \int d^2r d^2r' G_L(\mathbf{r}, \mathbf{r}') [\rho(\mathbf{r}) - K(\mathbf{r})][\rho(\mathbf{r}') - K(\mathbf{r}')], \quad (1.7)$$

where G_L is the Green's function of the Laplace-Beltrami operator, the standard Laplacian operator generalized to curved space [30]. If we write $G_L(\mathbf{r}, \mathbf{r}') = (1/2\pi) \ln |\mathbf{r} - \mathbf{r}'|$, the free-space Green's function in 2D, and make the variable change $K(\mathbf{r}) = -\Omega(\mathbf{r})$, Eq. 1.7 becomes,

$$F_d = -\frac{1}{4\pi}k_f \int d^2r d^2r' \ln |\mathbf{r} - \mathbf{r}'| [\rho(\mathbf{r}) + \Omega(\mathbf{r})][\rho(\mathbf{r}') + \Omega(\mathbf{r}')], \quad (1.8)$$

the Coulomb energy in 2D for a charge distribution $\rho(\mathbf{r})$ in a background of charge density $\Omega(\mathbf{r})$. From this analogy, it is clear that topological defects couple to the Gaussian curvature of the underlying surface; in particular, defects are attracted to regions of like-signed Gaussian curvature [30].

To investigate the role of curvature on ordered materials, we need to consider a space with varying Gaussian curvature and, ideally, a space including Gaussian curvatures of differing signs. While there have been new discoveries as a result of examining defect structures on spheres [31–36], including prior work with spherical nematic shells [26, 27], the Gaussian curvature, and therefore the background topological charge density, is constant in these cases. As a result, the impact of curvature only enters through the sphere radius. This is borne out in both the size-dependent onset of grain-boundary scars in colloidal crystals on the surface of emulsion drops [32, 33], and in the fact that the positions of the four $s = +1/2$ defects in nematic shells are entirely determined by the defect-defect interactions, with the underlying geometry playing no role [27].

The simplest closed surface having regions of both $K > 0$ and $K < 0$ is the torus [Figure 1.4(C)], which has $g = 1$ and thus $\chi = 0$. In addition, we see that not only does a torus have sphere-like, positive Gaussian curvature on its outer region and saddle-like, negative Gaussian curvature on its inner region, but according to Eq 1.5, the integrated Gaussian curvature over an entire torus must vanish. Similarly, by Eq. 1.3, an orientationally ordered material on the surface of a torus must have no net topological charge, and thus can support a defect-free configuration.

Prior work investigating nematic order inside a torus used toroidal droplets made from a NLC, with the nematic director constrained to lie parallel to the interface between the toroidal droplet and the outer continuous medium [37, 38]. The varying curvature of the torus yielded a double-twisted ground state with no defects [37], as drawn for both a right-handed and a left-handed structure in Figure 1.9(A,B), respectively. Theoretically, the amount of twist in the ground state can be controlled by the aspect ratio, or slenderness of the torus $\xi = R_0/a$, with R_0 the radius of the central circle of the torus and a the tube radius of the torus, as defined in the top view schematic in Figure 1.9(C). Our results revealed that the double-twist is directly

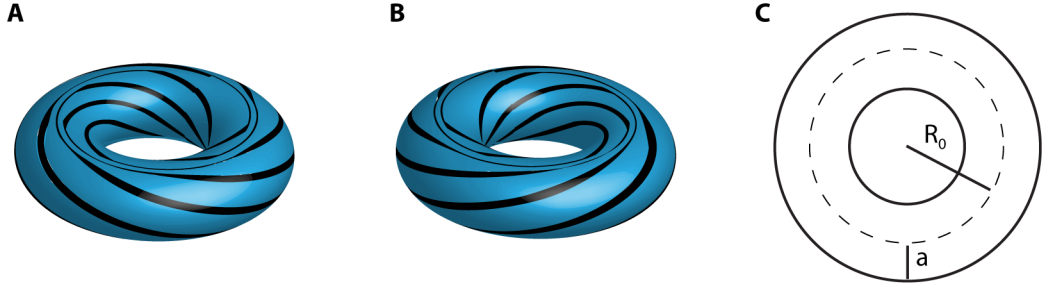


Figure 1.9: Doubly-twisted tori. (A,B), Schematics showing a (A) right-handed and (B) left-handed double-twist. (C), Schematic defining the central ring radius R_0 and tube radius a in a torus.

related to a director distortion called saddle-splay, which favors the director in the plane of the surface aligning along the smallest principal curvature [37, 39]. In addition, as seen by the possibility of having either a right-handed or a left-handed twist, this double-twisted state manifests itself through a spontaneous reflection symmetry breaking, where the form of the free energy resembles that of the Landau theory of magnetism. This analogy is exact for a linear twist in the cylindrical limit, where $\xi \rightarrow \infty$ [40]. These results clearly illustrate how confinement within surfaces of non-constant K can affect the ground state of a system, even in the absence of defects.

There are, however, 3D nematic fields with defects in their bulk. For example, consider a nematic inside a volume with the director at the surface of the volume perpendicular to the surface. We call this homeotropic anchoring. If the volume is a sphere, we then see that irrespective of how we arrange the director in the bulk, there must be an irreducible singularity. Bulk singularities that are points are known as hedgehogs and are characterized by their hedgehog charge,

$$q = \frac{1}{4\pi} \int_{S^2} d\theta d\phi \mathbf{n} \cdot [\partial_\theta \mathbf{n} \times \partial_\phi \mathbf{n}], \quad (1.9)$$

where the integral is taken over a topologically spherical surface enclosing the defect, and θ and ϕ are, respectively, the polar and azimuthal angles on that surface [20]. In

this case, instead of counting the number of times the director wraps around \mathbb{S}^1 , as we did for the topological charge, we consider the orientation of \mathbf{n} on the spherical surface enclosing the defect mapped to \mathbb{S}^2 , the unit sphere. The director serves as the map,

$$\begin{aligned}\mathbf{n} : \mathbb{S}^2 &\rightarrow \mathbb{S}^2 \\ (\theta, \phi) &\mapsto \mathbf{k}(\theta, \phi),\end{aligned}$$

where \mathbf{k} is a vector normal to the “surface” defined by the director. The integrand in Eq. 1.9 is the determinant of the Jacobian matrix of the map; it counts the area swept out on the target sphere by \mathbf{n} on the surface enclosing the defect. Thus, the hedgehog charge is then the number of times the orientations of \mathbf{n} cover \mathbb{S}^2 [20]. Therefore, confining a NLC to a volume that is topologically spherical with homeotropic boundary conditions must yield a total “hedgehog charge” $|q| = 1$.

In this Thesis, we investigate the role of geometry in the interplay between order and confinement. In Chapter 2, we begin with an introduction to the theory of nematic liquid crystals. Then, in Chapter 3, we consider nematic order on the surface of a torus. This is different from previous studies where the NLC filled the torus [37, 41, 42]. Due to the difficulty of creating a thin, stable, toroidal shell of a NLC, we use a polymeric nematic that self-assembles at the interface between two immiscible liquids. Importantly, with this system we can generate stable toroidal droplets as in our previous work, and investigate 2D nematic order on a toroidal surface. In addition, the nematic is active, meaning that the individual constituent particles have their own source of internal energy. The activity then drives the nematic out of equilibrium at the individual particle level, generally causing the generation of pairs of $s = \pm 1/2$ defects that are constantly in motion and constantly being created and annihilated. Even though we have an inherently nonequilibrium material, we find that

predictions built upon Eq. 1.7 hold and that adding activity to order qualitatively resembles bringing an equilibrium system to the high temperature limit. However, there are significant differences with equilibrium nematics, which we will highlight.

In Chapter 4, we consider a NLC confined to toroidal droplets with homeotropic anchoring. With the director constrained to lie perpendicular to the surface, the saddle-splay distortion does not affect the free energy minimization. However, we still find a twisted ground-state configuration, where the amount of twist depends on ξ , eventually disappearing as $\xi \rightarrow \infty$. Experiments with NLC confined to straight and bent cylindrical capillaries under homeotropic boundary conditions reveal that the twist is a response to the additional curvature induced when deforming a cylinder of homeotropic nematic into a torus. This is new; prior experiments in cylinders found a twisted ground state only when NLC that favor twist distortions were used. In our case, the confining geometry induces twist even in NLC that do not preferentially favor twist distortions.

In Chapter 5, we return to a spherical topology, confining NLC to a capillary bridge with homeotropic anchoring to study the influence of confinement shape on defect type. We generate waist-shaped and barrel-shaped bridges and find that waist-shaped bridges contain hyperbolic defects with negative hedgehog charge while barrel-shaped bridges contain radial defects with positive hedgehog charge. In addition, we find that the ratio of the bridge height to its width determines whether the singularity is a ring defect or a hedgehog.

In Chapter 6, we summarize, conclude, and present results that open the door to future work that builds on this Thesis.

CHAPTER 2

FUNDAMENTALS OF NEMATIC LIQUID CRYSTALS

2.1 Local order and defects

Uniaxial nematic liquid crystals are an ordered phase resulting from breaking the continuous rotational symmetry of a collection of anisotropic, typically rod-like or plate-like, particles [22]. As either the concentration of the particles is increased [16] or the temperature of the system is decreased [43], there is a point where a phase transition happens and the system breaks continuous rotational symmetry and develops order. The order is characterized by a spontaneously chosen preferred direction or axis; rod-like particles prefer to have their long axis aligned along this direction and plate-like particles prefer to have their short axis along this direction [1, 22].

Note that the system still possesses continuous rotational symmetry about the preferred alignment direction as well as continuous translational symmetry in all directions. This is illustrated with rod-like particles in Figure 2.1. In panel (A), the system is isotropic and there is no preferred alignment direction. In contrast, in panels (B) and (C), the rods now align along a preferred direction denoted by \mathbf{n} and called the director. As a result, in Figure 2.1(B) and Figure 2.1(C), the system has broken continuous rotational symmetry about the two axes orthogonal to \mathbf{n} . Note that even though in Figure 2.1(C) the rods align more strongly along \mathbf{n} than the rods in Figure 2.1(B), the system possesses the same symmetry in both situations.

Regardless of the rotational symmetry of the system, the system never breaks translational symmetry. This can be seen in Figure 2.1(D), where we show the centers of mass of the rods for all the cases in Figure 2.1(A–C), illustrating that there is no positional order and the system still possesses continuous translational symmetry.

If the concentration of the particles were further increased or the temperature were further decreased, the system would eventually break translational symmetry and the nematic phase would transition to a crystalline phase, with three broken continuous translational symmetries [22]. Hence, the liquid-crystalline nematic phase is an intermediate “mesophase” that possesses the continuous translational symmetries of the isotropic “liquid phase” as well as some of the broken rotational symmetries of the “crystalline” phase.

We briefly mention that nematics can be biaxial instead of uniaxial. Here, the constituent particles are bar-like such that there is no longer a single axis of symmetry that can characterize the particle geometry [1, 22]. Instead, we would need to define two axes, hence the name biaxial. However, in this Thesis, we will focus only on uniaxial NLC whose constituent particles are rod-like.

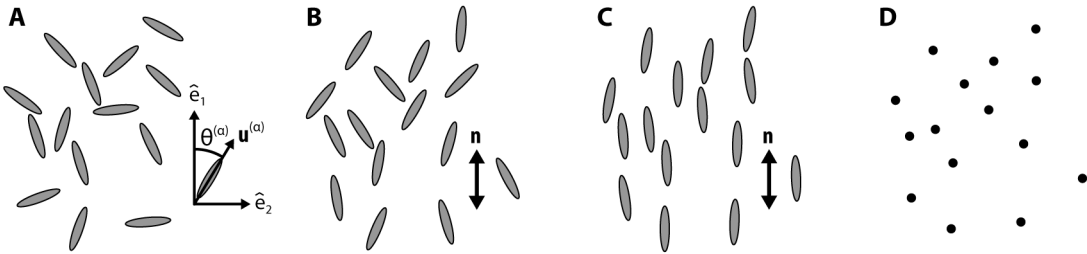


Figure 2.1: Symmetries in nematic phase. (A), A collection of rod-like particles in the isotropic phase. The orientation of the rod with index α is given by the angle \mathbf{u}^α , defined schematically in the image. (B), The rods from (A) in the nematic phase. The rods are preferentially but weakly aligned along the director \mathbf{n} , denoted in the panel. (C), The rods from (A,B) in the nematic phase. Here, the rods are strongly aligned along \mathbf{n} , denoted in the panel. (D), The positions of the center of mass of the rods in (A–C), highlighting the continuous translational symmetry of the rods.

2.1.1 The director and the order parameter

Given a group of rods, we want to determine if the system is in the isotropic or the nematic phase, in addition to finding the director, \mathbf{n} , provided that the rods are in the nematic phase. Since we have a collection of rods with no specified head nor

tail, the director possesses inversion symmetry, where \mathbf{n} and $-\mathbf{n}$ describe the same physical state. In addition, we take the director to have unit length, $\mathbf{n} \cdot \mathbf{n} = 1$. Thus, to indicate nematic order, we need an order parameter that goes to 0 in the isotropic phase, is nonzero in the nematic phase, and describes the broken symmetry [1, 22]. We will first derive this quantity for a collection of rods laying in a 2D plane and then generalize to rods in 3D. Let a 2D collection of rods laying in a plane be indexed by $\alpha = 1, 2, \dots, N$, such that the orientation of a given rod can be specified with the unit vector $\mathbf{u}^{(\alpha)} = u_i^{(\alpha)} \hat{e}_i$, as seen in Figure 2.1(A), where we use the Einstein summation convention to sum over repeated indices and $\{\hat{e}_1, \hat{e}_2\}$ is the standard basis in \mathbb{R}^2 . Note that due to the inversion symmetry of the nematic phase $\langle \mathbf{u}^{(\alpha)} \rangle_\alpha = 0$, where $\langle \cdot \rangle_\alpha$ represents an ensemble average over all α . Thus, to accommodate the inversion symmetry of $\mathbf{u}^{(\alpha)}$, we will construct a symmetric rank-2 tensor from $\mathbf{u}^{(\alpha)}$.

Let:

$$\mathbf{Q} = \left\langle \mathbf{u}^{(\alpha)} \otimes \mathbf{u}^{(\alpha)} - \frac{1}{2} \mathbb{1} \right\rangle_\alpha, \quad (2.1)$$

with \otimes the outer product. Now, $\text{tr}\{\mathbf{Q}\} = \langle \mathbf{u}^{(\alpha)} \cdot \mathbf{u}^{(\alpha)} - 1 \rangle_\alpha = 0$, making \mathbf{Q} traceless [1, 22]. We need \mathbf{Q} to be traceless if we wish to use \mathbf{Q} as an order parameter with $Q_{ij} = 0$ in the isotropic phase.

To determine the director, we need to diagonalize \mathbf{Q} . Without loss of generality, we choose a new orthonormal basis in the plane, $\{\hat{e}'_1, \hat{e}'_2\}$. The transformation from the unprimed to the primed basis is given by the matrix $V_{ij} = \hat{e}'_i \cdot \hat{e}_j$. Note that $\mathbf{V}^T \mathbf{V} = V_{ij} V_{jk} = \mathbb{1}$, implying that $\mathbf{V}^T = \mathbf{V}^{-1}$, and \mathbf{V} is orthogonal. We then have:

$$\begin{aligned} \mathbf{Q}' &= \mathbf{V} \mathbf{Q} \mathbf{V}^T = \left\langle (\mathbf{V} \mathbf{u}^{(\alpha)}) \otimes (\mathbf{V} \mathbf{u}^{(\alpha)}) \right\rangle_\alpha - \frac{1}{2} \mathbb{1} \\ &= \begin{pmatrix} \langle \cos^2 \theta'^{(\alpha)} \rangle_\alpha - 1/2 & \langle \sin \theta'^{(\alpha)} \cos \theta'^{(\alpha)} \rangle_\alpha \\ \langle \sin \theta'^{(\alpha)} \cos \theta'^{(\alpha)} \rangle_\alpha & \langle \sin^2 \theta'^{(\alpha)} \rangle_\alpha - 1/2 \end{pmatrix}, \end{aligned} \quad (2.2)$$

where $\cos \theta'^{(\alpha)} = \mathbf{u}^{(\alpha)} \cdot \hat{e}'_1$ and $\sin \theta'^{(\alpha)} = \mathbf{u}^{(\alpha)} \cdot \hat{e}'_2$.

Since \mathbf{Q} is symmetric, we can always find a basis of eigenvectors where \mathbf{Q}' is diagonal. Choose the \hat{e}'_i to be the eigenvectors of \mathbf{Q} . This implies $\mathbf{V}\mathbf{Q}\mathbf{V}^T$ must be diagonal such that $\langle \sin \theta'^{(\alpha)} \cos \theta'^{(\alpha)} \rangle_\alpha = \langle \sin(2\theta'^{(\alpha)}) \rangle_\alpha = 0$. This can occur in two instances. First, if we choose the collection of rods to be randomly oriented as in the isotropic phase, $\langle \sin(2\theta'^{(\alpha)}) \rangle_\alpha = 0$ as sine is an odd function. However, in this case we also have $\langle \cos^2 \theta'^{(\alpha)} \rangle_\alpha - 1/2 = \langle \sin^2 \theta'^{(\alpha)} \rangle_\alpha - 1/2 = 0$, and thus $\mathbf{Q} = 0$. This first situation simply shows the correct behavior in the isotropic phase. The second situation is the one we are seeking. For $\langle \sin(2\theta'^{(\alpha)}) \rangle_\alpha$ to be 0, the collection of rods must on average point along \hat{e}'_i , implying that $\theta'^{(\alpha)} \approx 0$ or $\pi/2$. This further indicates that \mathbf{n} is either along \hat{e}'_1 or along \hat{e}'_2 , the eigenvectors of \mathbf{Q} .

We now take Eq. 2.2 and write it assuming the collection of rods on average points along \hat{e}'_1 , hence $\mathbf{n} = \hat{e}'_1$. This yields:

$$\mathbf{V}\mathbf{Q}\mathbf{V}^T = \begin{pmatrix} \langle \cos^2 \theta'^{(\alpha)} \rangle_\alpha - 1/2 & 0 \\ 0 & \langle \sin^2 \theta'^{(\alpha)} \rangle_\alpha - 1/2 \end{pmatrix} = \begin{pmatrix} S/2 & 0 \\ 0 & -S/2 \end{pmatrix}, \quad (2.3)$$

where $S = 2\langle \cos^2 \theta'^{(\alpha)} \rangle_\alpha - 1$. From Eq. 2.3, we find that the eigenvalue associated to the eigenvector \hat{e}'_1 is $S/2$, while for the eigenvector \hat{e}'_2 the eigenvalue is $-S/2$. Since we specified that the rods prefer to align along \hat{e}'_1 , we see that \mathbf{n} is the eigenvector that corresponds to the largest eigenvalue of \mathbf{Q} . S is often called the scalar order parameter and denotes how well-aligned the system is [22]. For example, if every rod was aligned along \hat{e}'_1 such that $\mathbf{u}^{(\alpha)} = \hat{e}'_1$, $S = 1$. Similarly, if we again check the isotropic limit of a random collection of rods, we see that $S = 0$, as desired. Returning to Figure 2.1, we see that $S = 0$ in Figure 2.1(A), and that $0 < S[\text{Figure 2.1(B)}] < S[\text{Figure 2.1(C)}] < 1$. Thus, \mathbf{Q} serves as the tensor order parameter for a collection of rods, where the director corresponds to the eigenvector associated with the largest eigenvalue of \mathbf{Q} , and that eigenvalue gives S , the scalar order parameter [1, 22].

In terms of the director, we can now write \mathbf{Q} in 2D as:

$$\mathbf{Q} = S \left(\mathbf{n} \otimes \mathbf{n} - \frac{1}{2} \mathbb{1} \right). \quad (2.4)$$

Generalizing to 3D, we have a similar expression for a collection of rods [22]:

$$\mathbf{Q} = \left\langle \mathbf{u}^{(\alpha)} \otimes \mathbf{u}^{(\alpha)} - \frac{1}{3} \mathbb{1} \right\rangle_{\alpha}, \quad (2.5)$$

that can be written in terms of the director as:

$$\mathbf{Q} = S \left(\mathbf{n} \otimes \mathbf{n} - \frac{1}{3} \mathbb{1} \right), \quad (2.6)$$

with $S = \frac{1}{2} \langle 3 \cos^2 \theta'^{(\alpha)} - 1 \rangle_{\alpha} = \langle P_2(\cos \theta'^{(\alpha)}) \rangle_{\alpha}$, where again $\theta'^{\alpha} = \arccos(\mathbf{u}^{\alpha} \cdot \mathbf{n})$, and $P_2(\cdot)$ is the Legendre Polynomial of order 2 [1, 22]. As in two dimensions, we take the eigenvector associated with the largest eigenvalue to be \mathbf{n} . Thus, for a collection of rods, we can determine if the collection is nematic or isotropic and, if applicable, \mathbf{n} by calculating \mathbf{Q} according to Eqs. 2.1 or 2.5 and diagonalizing.

2.1.2 Defects in a nematic

While we briefly mentioned the dimensionality of defects and their associated classification schemes in Section 1, here we take a deeper look and use homotopy theory as laid out in references [20, 44, 45] to introduce a more complete theory of defects in nematic materials. Homotopy theory deals with classifying elements of topological spaces using a group structure; in this case, we will classify defects as members of the first and second homotopy groups. As mentioned in Chapter 1, defects in ordered media are defined generally as regions where the characteristic order of the phase is not satisfied. In a nematic phase, defects are locations where \mathbf{n} is undefined. For a nematic in 3D, these locations can be 0-dimensional (0D) (point defects), 1-dimensional

(1D) (line defects), or 2D (wall defects). General examples of defects with different dimensionality in 3D and 2D are drawn schematically in Figure 2.2. Note that when a 3D defect structure depends only on 2 coordinates, as seen in the invariance along \hat{z} in the wall and line defects in Figure 2.2, the director in the xy plane appears as if we were in 2D. For example, a wall in 3D is similar to a line in 2D and a line in 3D is similar to a point in 2D, as highlighted by the arrows in Figure 2.2.

However, while it is appealing to equate similar-looking structures in 2D and 3D, the additional possible director orientations in a 3D nematic mean that a 3D nematic is fundamentally different than a 2D nematic. To characterize these differences as well as classify the defects themselves we turn to the homotopy theory of defects. For clarity, we refer to Table 2.2 for definitions of some useful concepts from group theory.

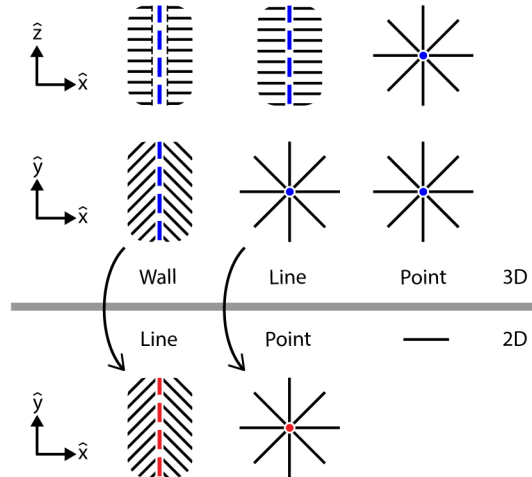


Figure 2.2: Different types of defects in 3D and 2D. In 3D, there is the 2D wall defect, the 1D line defect, and the 0D point defect. Cross-sections of these three structures are shown schematically in the xy plane and the xz plane. The defects are marked with either a dot or a dashed line. The heads of the “nails” in the xz cross-section of the wall, point into the page. In 2D, a nematic can have 1D line defects and 0D point defects, where the singular region is highlighted with either a dashed line or a point. Note that the wall and line structures in 3D are invariant along the \hat{z} -direction. This invariance means that the xy cross-section of the wall and line structure in 3D map to the line and point structure in 2D, as shown by the arrows in the schematic.

Consider a set of vectors in 2D such that their orientations can be described by a single angle. We can map these vector orientations onto an *order parameter space* given by the 1-sphere, \mathbb{S}^1 , the unit circle in the plane, such that \mathbb{S}^1 describes all the possible orientations of the vectors. If instead we consider a nematic, \mathbb{S}^1 is no longer an appropriate order parameter space as the orientations of \mathbf{n} are periodic on the interval $[0, \pi)$ and not on the interval $[0, 2\pi)$. Instead, for 2D nematics the order parameter space is \mathbb{RP}^1 , the real projective plane in 1D, which corresponds to \mathbb{S}^1 with antipodal points identified [20, 44, 45]. This means that specifying the director along a contour in real space will determine a mapping to the order parameter space.

For example, consider both the purple contour and the red contour in the real space director schematic in Figure 2.3(A) and their associated mappings to \mathbb{RP}^1 in the schematic in Figure 2.3(B,C). Both contours are closed. However, we see in Figure 2.3(A) that the red contour encloses a singularity while the purple contour does not. Similarly, we see that in the order parameter space in Figure 2.3(B), the purple contour does not span \mathbb{RP}^1 and thus can be continuously deformed to a point in \mathbb{RP}^1 . In contrast, the red contour in Figure 2.3(C) spans \mathbb{RP}^1 and cannot be shrunken continuously to a point. Thus, the presence of a singularity in the area bounded by the red contour in real space results in a nonzero winding number in the associated contour in the order parameter space.

In fact, it is easy to see that a mapping of the director along the blue contour in Figure 2.3(D) will result in a contour in \mathbb{RP}^1 that spans \mathbb{RP}^1 and goes in opposite direction to the red contour in Figure 2.3(C). A mapping of the director to \mathbb{RP}^1 along the green contour in Figure 2.3(E) will result in a contour that wraps \mathbb{RP}^1 twice in the same direction as the red contour. Explicitly, we see that the defect structures in Figure 2.3(A,D,E) all have different winding numbers in \mathbb{RP}^1 , and thus cannot be mapped onto each other with continuous deformations. In the language of homotopy theory, we say that any two contours that can be continuously deformed into each

other (i.e., via a homeomorphism) are homotopic [44]. More generally, any contour in \mathbb{RP}^1 with winding number k is homotopic to any other contour in \mathbb{RP}^1 with winding number k , and only to contours with winding number k [20, 44, 45]. For example, note that as a single point in \mathbb{RP}^1 corresponds to a homogeneous \mathbf{n} -field in real space, we see that the singularity-free director field with $k = 0$ bounded by the purple contour in Figure 2.3(A) is homotopic to the homogeneous state of any orientation, but is not homotopic to the director field with $k = 1$ bounded by the red contour in Figure 2.3(A). Thus, contours with the same winding number form a homotopy class, where we can now start to think about categorizing the different homotopy classes of defects using a group structure.

While we could form the group using the winding numbers in \mathbb{RP}^1 themselves, we will instead use the winding number about \mathbb{S}^1 , such that the winding number is equivalent to measuring the amount of director rotation around a contour in real space [6, 19, 20]. Reproducing Eq. 1.2 from Chapter 1 for a director field parametrized by the angle $\phi(\mathbf{r})$, we characterize the defects with their winding number, s [20, 45]:

$$s = \frac{1}{2\pi} \oint_{\partial A} d\mathbf{r} \cdot \nabla \phi(\mathbf{r}), \quad (2.7)$$

where ∂A is the boundary of some area A containing the defect and the integral is performed along the boundary keeping A to the left. Since we have already established that the defects in a 2D nematic have integer winding numbers in \mathbb{RP}^1 , we see that $s = n/2$, with $n \in \mathbb{Z}$, giving us a discrete set of elements. In addition, we know that winding numbers are additive [44], such that combining the effect of multiple defects is commutative and associative. The additivity can be seen in Figure 2.3(F), where a contour surrounding two $s = +1/2$ defects has the same winding number in \mathbb{RP}^1 as the contour encircling the single $s = +1$ defect in Figure 2.3(E). Similarly, the additivity of defects also means that the (additive) inverse of a defect with winding number $+k$

is a defect with winding number $-k$. For example, combining an $s = +1/2$ defect and an $s = -1/2$ defect will result in the homogeneous state. Finally, we note that the homogeneous state acts as the identity element for the set of defects as $k + 0 = k$. Since we have satisfied the axioms for a group laid out in Table 2.2, we see that these defects belong to the group $(\mathbb{Z}/2, +)$, the Abelian group formed from the set of half-integers with addition. In addition, because we calculate our winding numbers in \mathbb{S}^1 , the group $(\mathbb{Z}/2, +) = \pi_1(\mathbb{RP}^1)$, where $\pi_1(\mathbb{RP}^1)$ is the first *homotopy group*, also known as the *fundamental group*, of \mathbb{RP}^1 [20, 44, 45]. As $s \in \pi_1(\mathbb{RP}^1)$, s is a topological quantity that is consequently often referred to as “topological charge.”

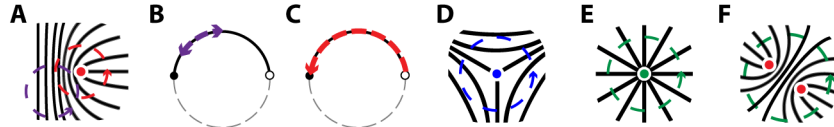


Figure 2.3: Examples of defect structures and the order parameter space in 2D. (A), An $s = +1/2$ defect with the singularity denoted with a red dot. The director along the red and purple contours is mapped to \mathbb{RP}^1 in (B). (B), A schematic showing \mathbb{RP}^1 (black line) as \mathbb{S}^1 (full circle) with antipodal points identified. The purple contour in \mathbb{RP}^1 corresponds to the purple contour in real space drawn schematically in (A). The purple contour can be continuously deformed to a point in \mathbb{RP}^1 . (C), A schematic showing \mathbb{RP}^1 (black line) as \mathbb{S}^1 (full circle) with antipodal points identified. The red contour in \mathbb{RP}^1 corresponds to the purple contour in real space drawn schematically in (A). The red contour spans \mathbb{RP}^1 , and thus has a winding number of $+1$ in \mathbb{RP}^1 and $+1/2$ in \mathbb{S}^1 . (D), An $S = -1/2$ defect with the singularity at the blue point. In \mathbb{RP}^1 , the blue contour would have the same winding as the red contour in (C), but would go the opposite direction. (E), An $s = +1$ defect (green dot) encircled by the green contour. In \mathbb{RP}^1 , the contour would have the same direction as the red contour in (C), but would cover \mathbb{RP}^1 twice and \mathbb{S}^1 once. (F), Two $s = +1/2$ defects (red dots) placed near to each other such that the green contour encircling both defects sees the same winding in order parameter space as the green contour in (E). Thus, far from the defects, we cannot distinguish between structures resulting from a single $s = +1$ defect and two $s = +1/2$ defects, reflecting the additivity of topological charge in 2D.

This approach is not limited to 2D. In fact, for a general order parameter space \mathbb{P} with dimension t' and a defect with dimension t , the codimension $d = t' - t$ defines the order of the homotopy group needed to characterize the defects in \mathbb{P} , $\pi_d(\mathbb{P})$ [45].

We note that for $d = 0$, there are no topological defects in nematic materials as any defect structure with $d = 0$ is homotopic to a nonsingular distortion [44]. For example, consider the singular line defect in 2D depicted in Figure 2.4(A). Here, the order parameter space is \mathbb{RP}^1 , giving $t' = 1$, and the defect is a line with $t = 1$, such that $d = 0$. This structure can be continuously deformed to remove the singularity, yielding the nonsingular structure in Figure 2.4(B). Thus, since a singular line in 2D is homotopic to the undistorted state, it is not topologically stable. This does not mean that lines in 2D or walls in 3D cannot exist, merely that their existence is determined by energetics such that these structures are usually found only in situations with very strong spatial confinement or in the presence of an external field [1, 22].



Figure 2.4: Singular line defects are topologically unstable in 2D. (A) a singular line defect in 2D, with the singular region denoted in red. (B) A nonsingular structure resulting from a continuous deformation of (A).

Now, we consider a nematic in 3D. Immediately, we see that the order parameter space is no longer \mathbb{RP}^1 , but instead is \mathbb{RP}^2 , the unit 2-sphere \mathbb{S}^2 with antipodal points identified, as we now need 2 angles to characterize all the possible orientations of \mathbf{n} [20, 44, 45]. Another way to visualize \mathbb{RP}^2 is as a hemisphere where only the base has antipodal points identified. We first consider line defects with $d = 1$ such that we characterize them with $\pi_1(\mathbb{RP}^2)$, the fundamental group of \mathbb{RP}^2 .

Again, we consider \mathbf{n} along a closed 1D contour in real space and the associated 1D contour in \mathbb{RP}^2 , with the topological charge given by the winding number in \mathbb{S}^1 . However, we note that in \mathbb{RP}^2 , we can only have defects with $s = 0, 1/2$, as any contour on \mathbb{RP}^2 with an integer value of s can be continuously deformed into a point

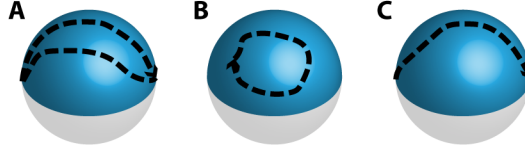


Figure 2.5: Contours in \mathbb{RP}^2 . (A–C), Schematics showing \mathbb{RP}^2 (blue hemisphere) as S^2 (full sphere) with antipodal points identified. A (A) contour that wraps \mathbb{RP}^2 twice can be (B) slid off and is homotopic to a point. A (C) contour that starts and ends at antipodal points is not homotopic to a point and is the only nontrivial contour in \mathbb{RP}^2 .

on \mathbb{RP}^2 since “you cannot lasso a sphere” [20]. More explicitly, any contour on \mathbb{RP}^2 with integer s must start and end at the same point. Thus it can be “slid” to one side of the sphere and deformed to a point on \mathbb{RP}^2 , as illustrated schematically in Figure 2.5(A,B). This means that the only stable contours in \mathbb{RP}^2 are those that start and end at antipodal points [see Figure 2.5(C)], wrapping \mathbb{RP}^2 exactly once. This also means that contours starting and ending at the same point on \mathbb{RP}^2 can be freely added and subtracted from a contour starting and ending at antipodal points on \mathbb{RP}^2 ; thus, all contours starting and ending at antipodal points on \mathbb{RP}^2 are homotopic. Explicitly, this means that contours with $s = -1/2$ are homotopic to contours with $s = 1/2$ such that $\pi_1(\mathbb{RP}^2)$ has only one nontrivial element, resulting in $s \in \{0, 1/2\}$ [20]. As with walls in 3D and lines in 2D, this does not mean that $s = +1$ lines in 3D are impossible to create, it only means that they are not topologically stable structures and thus can only be stabilized by energetics. Similarly, since an $s = -1/2$ line and an $s = +1/2$ line are homotopic, preferentially generating one structure over the other is a matter of tuning the free energy of each structure.

We lastly consider point defects in 3D characterized by the second homotopy group of \mathbb{RP}^2 , $\pi_2(\mathbb{RP}^2)$. Now, instead of mapping 1D closed contours in real space to \mathbb{RP}^1 and \mathbb{RP}^2 as we did with the fundamental group, we map a topologically spherical surface enclosing the defect to \mathbb{RP}^2 [20, 44, 45]. In real space, we restate Eq. 1.9 and

calculate the topological “hedgehog charge” of a defect as [20]:

$$q = \frac{1}{4\pi} \oint_{\partial V} d\theta d\phi \mathbf{n} \cdot [\partial_\theta \mathbf{n} \times \partial_\phi \mathbf{n}], \quad (2.8)$$

where θ and ϕ are the polar and azimuthal spherical angles, respectively, and ∂V is the bounding surface of the closed volume V containing the defect. The volume V must be homotopic to a sphere and thus can have no holes or handles. From Chapter 1, we know that this means that the Euler characteristic of ∂V is $\chi = 2$. Physically, q relates the orientations of \mathbf{n} taken on a topologically spherical surface enclosing the defect to the number of times the orientations cover \mathbb{S}^2 [20]. Similar to how the winding numbers for the fundamental group are characterized with \mathbb{S}^1 , here we are calculating a “covering number” using \mathbb{S}^2 . Hedgehog charge is additive such that calculating q for a volume containing only a $+q$ point defect and $-q$ point defect charge will yield $q_{net} = 0$. Thus, $\pi_2(\mathbb{RP}^2) = (\mathbb{Z}, +)$, the Abelian group consisting of the integers under addition.

It is important to note that there are 2 possible ways to turn a given director field into a vector field; either we take the vectors as \mathbf{n} or as $-\mathbf{n}$. Since we measure the hedgehog charge by considering how \mathbf{n} on a surface homeomorphic to \mathbb{S}^2 covers \mathbb{RP}^2 , this ambiguity means that any defect in isolation can only be determined up to $|q|$ [20]. Thus, while topological character is determined by homotopy theory, the sign of charge can only be determined relative to a *basepoint* defining the projection from \mathbb{RP}^2 to \mathbb{S}^2 [20]. For example, the defect structures drawn schematically in Figure 2.6(A,B) cannot be distinguished *a priori* in order parameter space. However, if we choose a basepoint such that the structure in Figure 2.6(A) has $q = +1$, evaluating the structure in Figure 2.6(B) under the same basepoint will yield $q = -1$. We will keep this basepoint for the remainder of the Thesis.

Similar to how additivity means that a volume enclosing a $+q$ point defect and $-q$

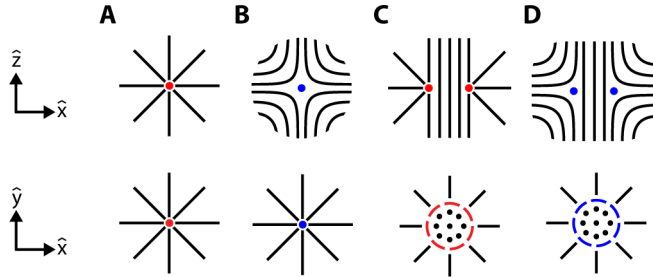


Figure 2.6: Examples of defect structures in 3D. (A-D), Cross sections in the xz and xy planes of defect structures with $|q| = 1$. Once we choose a reference point that defines the projection of \mathbf{n} onto the unit sphere, we can distinguish the structures in A,C from the structures in B,D. Without loss of generality, we take the convention that the structures in A,C have $q = +1$ such that the structures in B,D have $q = -1$. (A,B), schematics of a (A) radial and a (B) hyperbolic hedgehog defect. (C,D), schematics of a (C) radial ring and a (D) hyperbolic ring defect. Note that the ring defects in (C,D) are formed by an $s = +1/2$ and an $s = -1/2$ line defect that has closed in on itself.

point defect charge will yield $q_{\text{net}} = 0$, the point defect structures in Figure 2.6(A,B) are not the only structures with $|q| = 1$. In fact, ring defects, as depicted schematically in Figure 2.6(C,D) are homotopic to their respective point defect counterparts in Figure 2.6(A,B). Shrinking the ring radius of the radial ring in Figure 2.6(C) yields the radial hedgehog shown in Figure 2.6(A) and shrinking the ring radius in the hyperbolic ring in Figure 2.6(D) yields a hyperbolic hedgehog like the one shown in Figure 2.6(B). A ring defect can be thought of as a line defect in 3D [see Figure 2.2] that is bent into a circle. Hence, if we were to draw a closed 1D contour that passed through the ring and “linked” with the ring defect, we would find that radial rings with $q = +1$ are formed with $s = +1/2$ lines and hyperbolic rings with $q = -1$ are formed with $s = -1/2$ lines.

Finally, we briefly want to touch on the use of the term “charge” to characterize defects in NLC. The choice of this term is no accident and reflects an analogy with electric charges. This analogy is born out not only in the additivity of both defect charges and electric charges, but also in their pairwise interactions [1, 22, 46]. Defects in 2D and 3D with like-signed charge repel and defects with opposite-signed charge

attract and even annihilate.

2.2 Frank-Oseen free energy

Since the constituent particles, or mesogens, in a nematic material prefer to align along the \mathbf{n} , the ideal state for a nematic phase is a homogeneously-aligned state with \mathbf{n} a constant everywhere. Distortions from this uniform state cost energy. Since in most experiments the director distortions occur over much larger length scales than the length of the mesogens — $|\nabla \mathbf{n}|a \ll 1$, where a is the mesogen length — we can bypass the behavior of individual mesogens and instead use a continuum model for the free energy density that depends on \mathbf{n} only. Here, we follow the work of F.C. Frank [5] and expand about the undistorted director state in powers of $|\nabla \mathbf{n}|$. This is a phenomenological approach similar to Hooke’s elasticity theory of a solid [1, 47]; however, instead of focusing on restoring stresses that oppose strains, we look for restoring torques that oppose curvature-strains in the director field. This is again a reflection that there is no restriction to the center-of-mass positions of the mesogens; the nematic elasticity only opposes deformations in the orientations of the mesogens.

2.2.1 A brief derivation

Let a local coordinate system at a point be defined by $\{x_1, x_2, x_3\}$ such that we can define $\mathbf{n} = (\mathbf{n} \cdot \hat{e}_i)\hat{e}_i = n_i\hat{e}_i$, where we again sum over repeated indices, and \hat{e}_i is the unit vector associated with x_i and $\{\hat{e}_1, \hat{e}_2, \hat{e}_3\}$ forms an orthonormal basis. If we let \hat{e}_3 be parallel to \mathbf{n} at the point and consider situations where $x_i \ll 1$, we can locally

expand n_i as:

$$\begin{aligned} n_1 &= \frac{\partial n_1}{\partial x_1}x_1 + \frac{\partial n_1}{\partial x_2}x_2 + \frac{\partial n_1}{\partial x_3}x_3 + \mathcal{O}(x^2) \\ &= a_1x_1 + a_2x_2 + a_3x_3 + \mathcal{O}(x^2) \end{aligned} \quad (2.9)$$

$$\begin{aligned} n_2 &= \frac{\partial n_2}{\partial x_1}x_1 + \frac{\partial n_2}{\partial x_2}x_2 + \frac{\partial n_2}{\partial x_3}x_3 + \mathcal{O}(x^2) \\ &= a_4x_1 + a_5x_2 + a_6x_3 + \mathcal{O}(x^2) \end{aligned} \quad (2.10)$$

$$n_3 = 1 + \mathcal{O}(x^2).$$

Now expanding about the undistorted state, we can write the free energy density to quadratic order in the first derivatives as:

$$f(\mathbf{n}) = K_i a_i + K_{ij} a_i a_j, \quad (2.11)$$

where $i, j = \{1, 2, \dots, 6\}$, giving us 42 possible terms. However, any free energy must respect the symmetry of the nematic phase and be invariant under exchange of i and j , invariant under inversion of $\mathbf{n} \rightarrow -\mathbf{n}$, invariant under arbitrary rotations about \mathbf{n} , and invariant with respect to the handedness of the coordinate system [5]. Under these conditions, all of the 6 K_i terms vanish and of the 36 terms in K_{ij} , 26 vanish and only 4 are independent, giving the coefficient matrix:

$$K_{ij} = \begin{pmatrix} K_{11} & 0 & 0 & 0 & (K_{11} - K_{22} - K_{24}) & 0 \\ 0 & K_{22} & 0 & K_{24} & 0 & 0 \\ 0 & 0 & K_{33} & 0 & 0 & 0 \\ 0 & K_{24} & 0 & K_{22} & 0 & 0 \\ (K_{11} - K_{22} - K_{24}) & 0 & 0 & 0 & K_{11} & 0 \\ 0 & 0 & 0 & 0 & 0 & K_{33} \end{pmatrix}. \quad (2.12)$$

Substituting Eq. 2.12 into Eq. 2.11 and collecting terms, we are left with the expression:

$$f(\mathbf{n}) = \frac{1}{2}K_{11}(a_1 + a_5)^2 + \frac{1}{2}K_{22}(a_2 - a_4)^2 + \frac{1}{2}K_{33}(a_3^2 + a_6^2) - (K_{22} + K_{24})(a_1a_5 - a_2a_4). \quad (2.13)$$

If we return to the source of the a_i coefficients in Eqs. 2.9, 2.10, we can uncover the physical significance of the distortions:

$$s_1 = a_1 = \frac{\partial n_1}{\partial x_1} \quad s_2 = a_5 = \frac{\partial n_2}{\partial x_2} \quad (2.14)$$

$$t_1 = -a_4 = -\frac{\partial n_2}{\partial x_1} \quad t_2 = a_2 = \frac{\partial n_1}{\partial x_2} \quad (2.15)$$

$$b_1 = a_3 = \frac{\partial n_1}{\partial x_3} \quad b_2 = a_6 = \frac{\partial n_2}{\partial x_3}, \quad (2.16)$$

where we have renamed the coefficients to reflect their associated distortion, with s_1 and s_2 signifying a “splay” distortion, t_1 and t_2 signifying a “twist” distortion, and b_1 and b_2 signifying a “bend” distortion. These distortions in the local frame are easily visualized, as seen in Figure 2.7(A–C), respectively. Now if we use Eqs. 2.14–2.16 to re-write Eq. 2.13, we have:

$$f(\mathbf{n}) = \frac{1}{2}K_{11}(s_1 + s_2)^2 + \frac{1}{2}K_{22}(t_1 + t_2)^2 + \frac{1}{2}K_{33}(b_1^2 + b_2^2) - (K_{22} + K_{24})(s_1s_2 + t_1t_2). \quad (2.17)$$

Hence, we see that each term in the free energy density comes from a different distortion, such that the elastic constants K_{ij} hold the relative importance of each distortion for a given material. For example, consider a NLC with $K_{11} \gg K_{33} = K_{22} = K_{24}$; under confinement or strain, this material will prefer to bend and twist instead of splay. The elastic constants are named after their associated distortion,

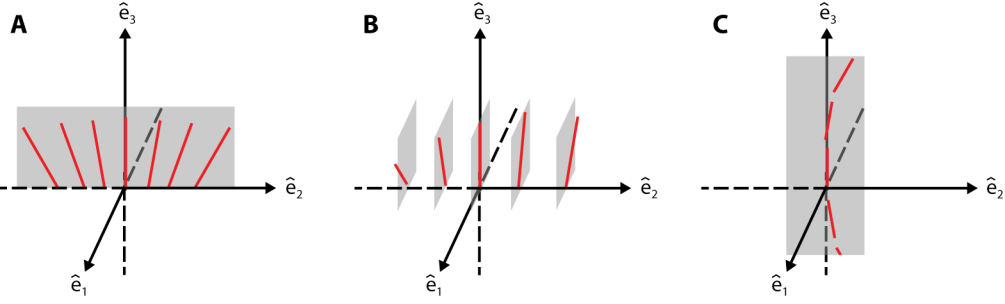


Figure 2.7: Nematic distortions in the local frame. (A), A schematic showing a splay distortion corresponding to a nonzero s_2 . (B), A schematic showing a twist distortion corresponding to a nonzero t_2 . (C), A schematic showing a bend distortion corresponding to a nonzero b_2 .

with K_{11} known as the splay elastic constant, K_{22} the twist elastic constant, K_{33} the bend elastic constant, and K_{24} the saddle-splay elastic constant. Note that the saddle-splay distortion is unique as it is associated with both the twist elastic constant and the saddle-splay elastic constant.

The ability to associate individual distortions with their elastic constant gives the Frank-Oseen free energy incredible intuitive power; it is easy to visualize each distortion's contribution to the director field. Finally, we can recast the distortions in Eq. 2.13 in terms of standard vector calculus operations, arriving at the well-known expression for the Frank-Oseen Free Energy [5]:

$$f(\mathbf{n}) = \frac{1}{2}K_{11}(\nabla \cdot \mathbf{n})^2 + \frac{1}{2}K_{22}(\mathbf{n} \cdot \nabla \times \mathbf{n})^2 + \frac{1}{2}K_{33}(\mathbf{n} \times \nabla \times \mathbf{n})^2 - \frac{1}{2}(K_{22} + K_{24})\nabla \cdot (\mathbf{n}\nabla \cdot \mathbf{n} + \mathbf{n} \times \nabla \times \mathbf{n}). \quad (2.18)$$

Note that while Frank pioneered the phenomenological approach for a liquid crystalline free energy, his was not the first attempt to construct a free energy for liquid crystals. Oseen arrived at a similar expression to Eq. 2.18 before Frank, but he approached the problem from a microscopic approach under the assumption that the free energy could be calculated considering interactions between all possible pairs of

molecules [48]. While Oseen's final expression for a nematic misses some of the terms in Eq. 2.18, it is close enough that Eq. 2.18 carries the names of both Frank and Oseen.

2.2.2 Nehring, Saupe, and second derivatives

We arrived at Eq. 2.18 by expanding about the undistorted state to quadratic order in powers of the 1st derivatives of \mathbf{n} . Due to the symmetry of the nematic, all of the terms linear in $|\nabla \mathbf{n}|$ vanished, making the quadratic terms the lowest order surviving terms in the expansion. However, as Nehring and Saupe pointed out, a full expansion to the lowest order should also include 2nd derivatives of \mathbf{n} as they can contribute to the Frank-Oseen free energy at order $\mathcal{O}(x^2)$ as well [49]. In fact, Oseen's original free energy expression also included terms depending on 2nd derivatives of \mathbf{n} that Frank neglected [48]. Thus, Eq. 2.11 becomes:

$$f(\mathbf{n}) = K_i a_i + K_{ij} a_i a_j + K'_{ij} a_{i,j}, \quad (2.19)$$

where $a_{i,j}$ represents $\frac{\partial a_i}{\partial x_j}$, giving us 18 terms in the K'_{ij} coefficient matrix. Again using the symmetries of a nematic, collecting terms, and rewriting the expression in terms of vector calculus manipulations, we arrive at a new expression for the free energy:

$$\begin{aligned} f(\mathbf{n}) = & \frac{1}{2}(K_{11} - 2K'_{13})(\nabla \cdot \mathbf{n})^2 + \frac{1}{2}K_{22}(\mathbf{n} \cdot \nabla \times \mathbf{n})^2 + \frac{1}{2}(K_{33} + 2K'_{13})(\mathbf{n} \times \nabla \times \mathbf{n})^2 \\ & - \frac{1}{2}(K_{22} + K_{24})\nabla \cdot (\mathbf{n}\nabla \cdot \mathbf{n} + \mathbf{n} \times \nabla \times \mathbf{n}) + K'_{13}\nabla \cdot (\mathbf{n}\nabla \cdot \mathbf{n}), \end{aligned} \quad (2.20)$$

where we see that the elastic constants associated with splay and bend are renormalized by K'_{13} , and that a new term called “splay-bend” associated with the distortion $\nabla \cdot (\mathbf{n}\nabla \cdot \mathbf{n})$ has appeared [49].

Since Eqs 2.18 and 2.20 are phenomenological expressions, renormalizing the splay and bend elastic constants doesn't affect underlying physics. This leaves the addition of the splay-bend term as the most significant effect of considering 2nd order derivatives of \mathbf{n} . The splay-bend term itself is subject to controversy as its inclusion to the free energy makes the free energy unbounded from below [50–52]. We follow Ref. [53] and illustrate this with a simple example of a NLC confined between two parallel plates. Let one plate be at $z = 0$ and the other at $z = d$, and let the director vary only in the xz -plane. We can then write our director in terms of the angle ϕ in the xz -plane measured off of the x -axis. Let the director field have the form $\phi_n(z) = \phi_d + \beta((z/d)^n - 1)$, such that $\phi(0) = \phi_d - \beta$ and $\phi(d) = \phi_d$, with ϕ_d and β fixed angles that give the boundary conditions. In this case, n is a positive integer that governs how the director varies between the two plates. This geometry is known as the splay-bend geometry. For simplicity, we take $K_{11} = K_{33} = K$, and assume n is large, allowing us to approximate the free-energy as,

$$F \approx \frac{1}{4} \frac{K\beta^2}{d^2} \left(1 + \frac{2K_{13} \sin(2\phi_d)}{K\beta} \right) n. \quad (2.21)$$

If we require $|\beta|K < 2|K_{13} \sin(2\phi_d)|$ and $K_{13} \sin(2\phi_d)/\beta < 0$, then the $1 + 2K_{13} \sin(2\phi_d)/(K\beta)$ term in Eq. 2.21 is negative, and

$$\lim_{n \rightarrow \infty} F = -\infty, \quad (2.22)$$

$$\lim_{n \rightarrow \infty} \phi_n(z) = \begin{cases} \phi_d - \beta & \text{if } 0 \leq z < d \\ \phi_d & \text{if } z = d. \end{cases} \quad (2.23)$$

Here, we see that our director field has a free energy that diverges to $-\infty$, leading to a discontinuity in our director field. The discontinuity is called the Oldano-Barbero discontinuity. Recall that we initially derived the Frank-Oseen free energy assuming

small deformations — however, we have just shown a situation where the Frank-Oseen free energy diverges and leads to a discontinuity in the director field. This situation is called the Oldano-Barbero paradox [52–55].

The easiest way to solve the paradox is to set $K'_{13} = 0$. It is worth noting that there has been a concerted effort to solve the paradox without setting $K'_{13} = 0$ [54–57]. However, careful experiments in the splay-bend geometry have found $K'_{13} = 0$ within experimental error, and the experimenters never observe a discontinuity in the director field [58]. Consequently, the most common approach is to neglect the splay-bend term altogether [56, 57].

2.2.3 Insights from microscopic calculations

There has been significant theoretical effort, starting with the pioneering work of Oseen, to relate the microscopic interactions between the nematic mesogens to the macroscopic, measurable K_{ij} of the nematic phase [48, 56, 57, 59–63]. While an in-depth discussion of the various methods and results is beyond the scope of this document, it is worthwhile to examine the general process and consider the implications for the K_{ij} in the phenomenological expressions derived earlier. At the most basic level, the total interaction energy for a system is the sum over the pairwise interaction energy for all pairs of mesogens in the system.

However, an energy constructed upon the physical mesogens themselves requires us to know the position and orientation of each individual mesogen. Instead, it is typical to consider instead the particle density as a function of orientation and position and integrate over all possible pairs of points in the volume [57]. This is a density functional theoretic approach [64] and thus yields an energy similar to the general expression [56, 59]:

$$F = \int d\mathbf{R} d\mathbf{R}' G(\mathbf{R}, \mathbf{R}'), \quad (2.24)$$

where \mathbf{R} and \mathbf{R}' are positions, and $G(\mathbf{R}, \mathbf{R}')$ is an interaction energy density satis-

fying $G(\mathbf{R}, \mathbf{R}') = 0$ for $|\mathbf{R} - \mathbf{R}'| \gg 0$, reflecting the finite interaction range between the mesogens. However, we are looking for a free energy and not just the interaction energy of the system. Thus, it is common to calculate the energy for a homogeneous state and then expand about the homogeneous state to get an expression for a distortion free energy, δF ; this is similar to how we derived the Frank-Oseen free energy earlier. Since we are looking to derive an expression for the free energy as a functional of director field, we must satisfy

$$\delta F = \int d\mathbf{R} d\mathbf{R}' G(\mathbf{R}, \mathbf{R}') = \int d\mathbf{r} f(\mathbf{r}), \quad (2.25)$$

where $f(\mathbf{r})$ is a function of position, \mathbf{r} , and here $G(\mathbf{R}, \mathbf{R}')$ represents the energy of the distorted state relative to the homogeneous state. Note that there is not a unique relation between $f(\mathbf{r})$ and $G(\mathbf{R}, \mathbf{R}')$; more specifically, f will be determined by how we choose \mathbf{r} . For example, if $\mathbf{r} = \mathbf{R}$, then $f(\mathbf{r}) = \int d\mathbf{R}' G(\mathbf{r}, \mathbf{R}')$. However, if $\mathbf{r} = (\mathbf{R} + \mathbf{R}')/2$, then $f(\mathbf{r}) = \int d\mathbf{R}' G(2\mathbf{r} - \mathbf{R}', \mathbf{R}')$. This provides a condition on the elastic constants we use to calculate $f(\mathbf{r})$: the elastic constants in $f(\mathbf{r})$ cannot depend on how we choose \mathbf{r} [56].

Given this condition, microscopic calculations show that K_{11} , K_{22} , K_{33} , and K_{24} are real physical material properties [56, 57, 59–62]. However, K'_{13} depends on the choice of \mathbf{r} , and therefore cannot be a real material parameter. Physically, we can think about this result in terms of how the free energy scales in terms of the amplitude, ϵ , and wavelength, ζ , of an arbitrary distortion in a NLC. Since K_{11} , K_{22} , K_{33} , and K_{24} are all composed of only 1st derivatives, their contribution to the free energy $\sim (\epsilon/\zeta)^2$. However, K'_{13} is a 2nd derivative with a contribution to the free energy $\sim \epsilon/(\zeta^2)$. If we consider a distortion with $|\epsilon| < 1$ and $\zeta \gg 1$, the linear dependence on the amplitude in the K'_{13} term means that it will dominate the other K_{ij} that are $\sim \epsilon^2$ [56]. Thus, K'_{13} makes a homogeneous director field unstable to long wavelength

distortions. Consequently, $K'_{13} = 0$ and the common approach of neglecting splay-bend is valid. [56, 61]. With $K'_{13} = 0$, we see that Eq. 2.20 reduces to the expression for the Frank-Oseen free energy in Eq. 2.18.

Microscopic calculations also show that close to a boundary, K_{ij} in general deviate from their bulk values and become position-dependent. This is because the mesogens are now interacting with the material outside of the nematic volume [56, 59, 65]. However, this interaction is limited by the range of the intermolecular potential, such that the position dependence of the K_{ij} vanishes over a small boundary layer — beyond this layer the K_{ij} return to their bulk values, which depend only on the specific nematic material.

In summary, microscopic calculations show that the free energy of a NLC is composed of terms quadratic in $|\nabla \mathbf{n}|$. Even though terms linear in $|\nabla^2 \mathbf{n}|$ could in principle contribute to the free energy to the same order as terms quadratic in the 1st derivatives, microscopic calculations show that the coefficients associated with 2nd-derivative distortions vanish, thus removing the problems that the 2nd-derivative distortions bring.

2.2.4 Saddle-splay and curvature-coupling

If we take a look at the terms in the Frank-Oseen free energy in Eq. 2.18, we can see a difference between the saddle-splay term and the splay, twist, and bend terms. Notice that since all the $K_{ij} \geq 0$, the energetic cost of splay, bend, and twist distortions are positive semi-definite. In contrast, the saddle-splay distortion can be either positive or negative. In addition, the saddle-splay distortion is the divergence of a vector, giving us the option of re-writing the distortion in terms of a surface integral using

the divergence theorem [66]:

$$F_{24}[\mathbf{n}] = -\frac{1}{2} \int_V d^3\mathbf{r} \left\{ (K_{22} + K_{24}) \nabla \cdot (\mathbf{n} \nabla \cdot \mathbf{n} + \mathbf{n} \times \nabla \times \mathbf{n}) \right\} \quad (2.26)$$

$$= -\frac{1}{2}(K_{22} + K_{24}) \oint_{\partial V} d^2\mathbf{r} \left\{ \mathbf{k} \cdot (\mathbf{n} \nabla \cdot \mathbf{n} + \mathbf{n} \times \nabla \times \mathbf{n}) \right\}, \quad (2.27)$$

where V is a volume, ∂V is a piecewise smooth manifold bounding V , and \mathbf{k} is the unit surface normal.

Note that \mathbf{n} needs to be continuous and differentiable everywhere on V . However, since ∂V only needs to be piecewise smooth, we can always draw the manifold to exclude any regions where \mathbf{n} is not continuous and differentiable. Therefore, the divergence theorem can always be applied, implying that any saddle-splay distortion in V must affect \mathbf{n} or its derivatives on ∂V . In contrast, splay, bend, and twist distortions can exist purely in the bulk, such that \mathbf{n} is affected in V but not on ∂V . In fact, the ability to generate pure bulk distortions for splay, twist, and bend allow for easy measurements of K_{ij} via the Freederickz transition, for example [22, 67–71]. In these measurements, the bulk volume is always large enough such that any contribution from the position-dependence of K_{ij} near the boundaries is negligible.

Due to the connection between the bulk saddle-splay distortion and the director orientation on a bounding manifold, the saddle-splay distortion term is often referred to as a surface-like term and sometimes even referred to as an effective anchoring term [22, 65, 72–75]. Since any measurement of K_{24} requires \mathbf{n} or its derivatives to change at an interface, there is concern that the position-dependence of K_{ij} near an interface leads to the inability to measure the bulk value of K_{24} without contamination from the interface. However, we emphasize that while it is tempting to treat F_{24} as a surface term where the energy cost is calculated using the value of K_{ij} at the interface

like,

$$F_{24}[\mathbf{n}] = -\frac{1}{2}(K_{22}(\mathbf{r}) + K_{24}(\mathbf{r}))_{\mathbf{r} \rightarrow \partial V} \oint_{\partial V} d^2\mathbf{r} \left\{ \mathbf{k} \cdot (\mathbf{n} \nabla \cdot \mathbf{n} + \mathbf{n} \times \nabla \times \mathbf{n}) \right\}, \quad (2.28)$$

this is incorrect. The divergence theorem cannot be used if K_{ij} is position-dependent since the integrand in Eq. 2.26 is no longer the divergence of a vector. In fact, measuring K_{24} is in principle no different than measuring any of the K_{ii} — provided the volume of the bulk is much larger than the boundary layer, the influence of the position-dependence of K_{ij} is negligible.

To demonstrate this, we return to Eq. 2.26 and insert the position-dependence:

$$F_{24} = -\frac{1}{2} \int_V d^3\mathbf{r} \left\{ (K_{22}(\mathbf{r}) + K_{24}(\mathbf{r})) \nabla \cdot (\mathbf{n} \nabla \cdot \mathbf{n} + \mathbf{n} \times \nabla \times \mathbf{n}) \right\}. \quad (2.29)$$

Integrating Eq. 2.29 by parts with $\mathbf{A}(\mathbf{r}) = \mathbf{n} \nabla \cdot \mathbf{n} + \mathbf{n} \times \nabla \times \mathbf{n}$,

$K_*(\mathbf{r}) = -(K_{22}(\mathbf{r}) + K_{24}(\mathbf{r})/2)$, and $\boldsymbol{\alpha}$ describing the boundary yields:

$$\int_V d^3\mathbf{r} \left\{ K_*(\mathbf{r}) \nabla \cdot \mathbf{A} \right\} = \oint_{\partial V} d^2\mathbf{r} \left\{ \mathbf{k} \cdot (K_*(\boldsymbol{\alpha}) \mathbf{A}(\boldsymbol{\alpha})) \right\} - \int_V d^3\mathbf{r} \left\{ \mathbf{A} \cdot \nabla K_*(\mathbf{r}) \right\} \quad (2.30)$$

$$= K_*(\boldsymbol{\alpha}) \oint_{\partial V} d^2\mathbf{r} \left\{ \mathbf{k} \cdot \mathbf{A}(\boldsymbol{\alpha}) \right\} - \int_V d^3\mathbf{r} \left\{ \mathbf{A} \cdot \nabla K_*(\mathbf{r}) \right\}, \quad (2.31)$$

where we have chosen \mathbf{k} as the outward-pointing unit normal and we have pulled $K_*(\boldsymbol{\alpha})$ out of the integral as K_* only depends on the distance from the boundary [56]. Now, we separate $K_*(\mathbf{r}) = K_* + K_*^s(\mathbf{r})$ into the bulk material constant K_* and the position-dependent contribution $K_*^s(\mathbf{r})$, where $K_*^s(\mathbf{r})$ decays across a boundary layer of thickness d_l . Substituting this into Eq. 2.31, we are left with:

$$\begin{aligned} \int_V d^3\mathbf{r} \left\{ K_*(\mathbf{r}) \nabla \cdot \mathbf{A} \right\} &= (K_* + K_*^s(\boldsymbol{\alpha})) \oint_{\partial V} d^2\mathbf{r} \left\{ \mathbf{k} \cdot \mathbf{A}(\boldsymbol{\alpha}) \right\} \\ &\quad - \int_V d^3\mathbf{r} \left\{ \mathbf{A} \cdot \nabla K_*^s(\mathbf{r}) \right\}. \end{aligned} \quad (2.32)$$

If we now expand $\mathbf{A}(\mathbf{r})$ and $\nabla K_*^s(\mathbf{r})$ over the boundary layer with $\mathbf{r} = \boldsymbol{\alpha} - \zeta \mathbf{k}$, where ζ is the distance from the boundary, we have:

$$\mathbf{A}(\boldsymbol{\alpha} - \zeta \mathbf{k}) \approx \mathbf{A}(\boldsymbol{\alpha}) - \zeta (\mathbf{k} \cdot \nabla \mathbf{A}(\boldsymbol{\alpha})) \quad (2.33)$$

$$\nabla K_*^s(\boldsymbol{\alpha} - \zeta \mathbf{k}) \approx \mathbf{k}(\mathbf{k} \cdot \nabla K_*^s(\boldsymbol{\alpha} - \zeta \mathbf{k}))_{\zeta=0} - \zeta \mathbf{k}(\mathbf{k} \cdot \nabla(\mathbf{k} \cdot \nabla K_*^s(\boldsymbol{\alpha} - \zeta \mathbf{k})))_{\zeta=0} \quad (2.34)$$

As $K_*^s(\mathbf{r})$ decays across a boundary layer of thickness d_l , we can approximate the leading order term in $\nabla K_*^s(\boldsymbol{\alpha} - \zeta \mathbf{k})$ as:

$$\mathbf{k}(\mathbf{k} \cdot \nabla K_*^s(\boldsymbol{\alpha})) = \begin{cases} \mathbf{k} \frac{K_*^s(\boldsymbol{\alpha})}{d_l} & 0 \leq \zeta \leq d_l \\ 0 & \text{otherwise} \end{cases} \quad (2.35)$$

Thus, to leading order we can write the 2nd term in Eq. 2.32 as

$$\int_V d^3 \mathbf{r} \{ \mathbf{A} \cdot \nabla K_*^s(\mathbf{r}) \} \approx \int_V d^3 \mathbf{r} \{ \mathbf{A}(\boldsymbol{\alpha}) \cdot \mathbf{k}(\mathbf{k} \cdot \nabla K_*^s(\boldsymbol{\alpha})) + \mathcal{O}(\zeta) \} \quad (2.36)$$

$$\approx \mathbf{k} \cdot \nabla K_*^s(\boldsymbol{\alpha}) \int_V d^3 \mathbf{r} \{ \mathbf{A}(\boldsymbol{\alpha}) \cdot \mathbf{k} + \mathcal{O}(\zeta) \} \quad (2.37)$$

$$\approx \frac{K_*^s(\boldsymbol{\alpha})}{d_l} \oint_{\partial V} d^2 \mathbf{r} d_l \{ \mathbf{A}(\boldsymbol{\alpha}) \cdot \mathbf{k} \} \quad (2.38)$$

$$\approx K_*^s(\boldsymbol{\alpha}) \oint_{\partial V} d^2 \mathbf{r} \{ \mathbf{k} \cdot \mathbf{A}(\boldsymbol{\alpha}) \} + \mathcal{O}(d_l^2). \quad (2.39)$$

Substituting back into Eq. 2.32, we have:

$$\int_V d^3 \mathbf{r} \{ K_*(\mathbf{r}) \nabla \cdot \mathbf{A} \} \approx K_* \oint_{\partial V} d^2 \mathbf{r} \{ \mathbf{k} \cdot \mathbf{A}(\boldsymbol{\alpha}) \}, \quad (2.40)$$

giving us the saddle-splay contribution to the free energy,

$$F_{24} \approx -\frac{1}{2}(K_{22} + K_{24}) \oint_{\partial V} d^2 \mathbf{r} \{ \mathbf{k} \cdot (\mathbf{n} \nabla \cdot \mathbf{n} + \mathbf{n} \times \nabla \times \mathbf{n}) \} + \mathcal{O}(d_l^2). \quad (2.41)$$

Thus, even though the saddle-splay distortion must be measured in the presence of

an interface, where K_{ij} are position-dependent, the free energy of the saddle-splay distortion is primarily driven by the bulk value of K_{24} and K_{22} with corrections on the order of the square of the boundary layer thickness.

The saddle-splay distortion can also serve to couple the director to the curvature of the interface. Consider a nematic constrained to lie in the plane of the interface. Then, ignoring the corrections in Eq. 2.41 for simplicity, we can write the free energy of the saddle-splay distortion as:

$$F_{24} = -\frac{1}{2}(K_{22} + K_{24}) \oint_{\partial V} d^2\mathbf{r} \{\mathbf{k} \cdot (\mathbf{n} \times \nabla \times \mathbf{n})\}, \quad (2.42)$$

since $\mathbf{n} \cdot \mathbf{k} = 0$. Now rearranging the integrand, we can take advantage of the fact that $\mathbf{n} \cdot \mathbf{n} = 1$ and write:

$$\mathbf{k} \cdot (\mathbf{n} \times \nabla \times \mathbf{n}) = \mathbf{k} \cdot \mathbf{n} \cdot (\nabla \mathbf{n}) - \mathbf{k} \cdot (\mathbf{n} \cdot \nabla) \mathbf{n} \quad (2.43)$$

$$= -\mathbf{k} \cdot (\mathbf{n} \cdot \nabla) \mathbf{n}. \quad (2.44)$$

Again taking advantage of the fact that $\mathbf{k} \cdot \mathbf{n} = 0$, we can re-write \mathbf{n} in terms of an orthonormal basis defined on the surface like $\mathbf{n} = (\hat{e}_i \cdot \mathbf{n})\hat{e}_i$, where now $i = 1, 2$. Note that our director is now in 2D as we have restricted \mathbf{n} to be on the surface. Re-writing the right-hand side (RHS) of Eq. 2.44, we have:

$$-\mathbf{k} \cdot (\mathbf{n} \cdot \nabla) \mathbf{n} = \mathbf{n} \cdot (\mathbf{n} \cdot \nabla) \mathbf{k} - (\mathbf{n} \cdot \nabla)(\mathbf{k} \cdot \mathbf{n}) \quad (2.45)$$

$$= \mathbf{n} \cdot (\mathbf{n} \cdot \nabla) \mathbf{k} \quad (2.46)$$

$$= n_i \hat{e}_i \cdot (n_j \hat{e}_j \cdot \nabla) \mathbf{k} \quad (2.47)$$

$$= -n_i n_j (-\hat{e}_i \cdot (\hat{e}_j \cdot \nabla) \mathbf{k}) \quad (2.48)$$

$$= -n_i L_{ij} n_j \quad (2.49)$$

$$= -\mathbf{n} \cdot \mathbf{L} \cdot \mathbf{n}, \quad (2.50)$$

where \mathbf{L} is the Weingarten Matrix whose components are [19, 29]:

$$L_{ij} = -\hat{\mathbf{e}}_i \cdot (\hat{\mathbf{e}}_j \cdot \nabla) \mathbf{k} \quad (2.51)$$

The Weingarten Matrix describes how a curved surface changes in space, and its invariants give the mean and Gaussian curvature of the surface: $H = \text{tr}\{\mathbf{L}\}/2$ and $K = \det\{\mathbf{L}\}$, respectively. As $K = \kappa_1 \kappa_2$, we see that finding κ_1 and κ_2 , the principal curvatures, becomes an eigenvalue problem; the eigenvectors of \mathbf{L} give the principal curvature directions, and the associated eigenvalues are the principal curvatures themselves. Now, choosing $\hat{\mathbf{e}}_1$ and $\hat{\mathbf{e}}_2$ as the principal curvature directions, then we can write the saddle-splay free energy in terms of κ_1 and κ_2 as [39]:

$$F_{24} = \frac{1}{2}(K_{22} + K_{24}) \oint_{\partial V} d^2 \mathbf{r} \left\{ \kappa_1 n_1^2 + \kappa_2 n_2^2 \right\}, \quad (2.52)$$

where n_1 and n_2 are the components of the director along the 1st and 2nd principal curvature directions, respectively. Thus, for \mathbf{n} at an interface constrained to lie in the plane of the interface, the free energy of the saddle-splay distortion is minimized when \mathbf{n} at the interface is aligned along the smallest curvature. We emphasize that this curvature-coupling does not result from interactions between the NLC mesogens at the interface and the material outside of the nematic volume — it comes from the interactions in the nematic volume itself.

2.3 Landau-de Gennes free energy

The Frank-Oseen free energy in Eq. 2.18 is not the only phenomenological free energy expression. In fact, to understand the nematic-isotropic phase transition, we need to write a phenomenological free energy that depends on an order parameter such as \mathbf{Q} . This tensor-based approach to a free energy was developed by de Gennes in the spirit of a Landau-type theory [22]. However, this \mathbf{Q} -based phenomenological free energy

can also be used to calculate a distortion free energy by expanding in invariants of $\nabla \mathbf{Q}$, as we did to obtain the Frank-Oseen free energy [22, 76, 77].

2.3.1 The isotropic-nematic phase transition

We consider a free energy density built on an expansion in powers of $\mathbf{Q}(\mathbf{r})$. Crucially, the symmetry of a Landau-type free energy describing a phase transition needs to be the same as the higher-symmetry phase [1, 22]. In addition, the value of the free energy cannot depend on the choice of coordinate system, such that we expand not just in powers of \mathbf{Q} , but in terms of scalar invariants of powers of \mathbf{Q} . For this example, we neglect the positional dependence of $\mathbf{Q}(\mathbf{r})$ and instead consider a mean approximation $\langle \mathbf{Q}(\mathbf{r}) \rangle = \mathbf{Q}$. We now write \mathbf{Q} in 3D without loss of generality as:

$$\mathbf{Q} = \begin{pmatrix} -\frac{S}{3} & 0 & 0 \\ 0 & -\frac{S}{3} & 0 \\ 0 & 0 & \frac{2S}{3} \end{pmatrix}. \quad (2.53)$$

If we consider the trace and determinant of \mathbf{Q}^p , where $p \in \mathbb{N}$, we see from Table 2.1 that invariants of powers of \mathbf{Q} can be written in terms of powers of S . Note that because \mathbf{Q} is traceless, \mathbf{Q} is also traceless. Therefore, we can write the Landau-de Gennes free energy for the phase transition in 3D in the form [1, 22]:

$$f_{phase}(\mathbf{Q}) = f(S) = f_0 + \frac{1}{2}AS^2 + \frac{1}{3}BS^3 + \frac{1}{4}CS^4 + \mathcal{O}(S^5), \quad (2.54)$$

where f_0 is a constant that we can take to be 0. Then, $f_{phase}(S) > 0$ implies the isotropic phase is the equilibrium phase while $f_{phase}(S) < 0$ corresponds to the nematic phase as the equilibrium phase, with the phase transition occurring at $f_{phase}(S) = 0$. Since \mathbf{Q} is traceless, there is no linear dependence on S in Eq. 2.54. In principle, the coefficients A , B , and C are temperature dependent. However, in practice, of-

Table 2.1: Scalar invariants of powers of \mathcal{Q} in 3D

$\text{tr}\{\mathcal{Q}\} = 0$
$\text{tr}\{\mathcal{Q}^p\} \propto S^p, \quad p = 2, 3, \dots$
$\det\{\mathcal{Q}^p\} \propto S^{3p}, \quad p = 1, 2, 3, \dots$

ten only the coefficient associated with the lowest order term contains temperature dependence [1, 22]. Specifically, limiting the temperature dependence to only A is also consistent with molecular theories of the nematic-isotropic phase transition [22]. Thus, with T the temperature and T_{NI} the nematic-isotropic phase transition temperature, let $A = A_0(T - T_{NI})$, $B = B_0$, and $C = C_0$, allowing us to rewrite Eq. 2.54 as:

$$f_{phase}(S) = f_0 + \frac{1}{2}A_0(T - T_{NI})S^2 + \frac{1}{3}B_0S^3 + \frac{1}{4}C_0S^4. \quad (2.55)$$

We see that Eq. 2.55 predicts a first-order phase transition provided $B_0 \neq 0$, as a nonvanishing B_0 means that at $T = T_{NI}$, the minima in $f_{phase}(S)$ occur at $S = 0$ and $S = -B_0/C_0$, giving a discontinuity in S across the transition. Indeed, observations that state functions such as the density and S are discontinuous through the nematic-isotropic transition confirm that the nematic-isotropic phase transition in 3D is first-order [22].

If we follow the same procedure for the nematic-isotropic phase transition in 2D, we can write \mathcal{Q} as:

$$\mathcal{Q} = \begin{pmatrix} S/2 & 0 \\ 0 & -S/2 \end{pmatrix}, \quad (2.56)$$

such that $\text{Tr}\{\mathcal{Q}^p\} = 0$ for $p = 1, 3, 5, \dots$. This implies that a Landau-type free energy in 2D will look like:

$$f_{phase}(S) = f_0 + \frac{1}{2}A_0(T - T_{NI})S^2 + \frac{1}{4}C_0S^4. \quad (2.57)$$

Now with the absence of a term proportional to S^3 , the phase transition is predicted to be continuous, as S can vary continuously from $S = 0$ in the isotropic phase to $S \neq 0$ in the nematic phase as T passes through T_{NI} [22]. This can be seen by setting $T = T_{NI}$ and noticing that there is only one minimum in $f_{phase}(S)$, and it occurs at $S = 0$. Note that experiments of thin films of NLC have yet to show a continuous nematic-isotropic transition; however, the films always have a macroscopic thickness such that no experiment has yet probed the nematic-isotropic phase transition in strictly 2D [78]. However, the nematic-isotropic phase transition in 2D has been explored heavily in simulations, and while the literature agree that the transition should be continuous, there is no clear consensus on the specific order of the transition [79].

2.3.2 The distortion free energy

If we consider $\mathbf{Q}(\mathbf{r})$ instead of the mean approximation \mathcal{Q} , we can write a distortion free energy similar to the Frank-Oseen free energy. Since a Landau-type free energy is an expansion in the scalar order parameter near the phase transition, in general is only valid near the phase transition. However, in NLC, $S(T_{NI}) \approx 0.3$ to 0.4, and $S(T \ll T_{NI}) \approx 0.6$ to 0.8. Hence, we see that S near T_{NI} is not so different than S well below T_{NI} , indicating that we may still use a Landau-de Gennes free energy inside the nematic phase [77].

There are 3 independent scalar invariants quadratic in $\nabla \mathbf{Q}$, allowing us to write the distortion free energy density as [76, 77]:

$$f_d(\mathbf{Q}) = \frac{1}{2} L_1 \frac{\partial Q_{ij}}{\partial x_k} \frac{\partial Q_{ij}}{\partial x_k} + \frac{1}{2} L_2 \frac{\partial Q_{ij}}{\partial x_j} \frac{\partial Q_{ik}}{\partial x_k} + \frac{1}{2} L_3 \frac{\partial Q_{ij}}{\partial x_k} \frac{\partial Q_{kj}}{\partial x_i} \quad (2.58)$$

Note that the L_i are constants that only depend on the interactions between the molecules and are temperature independent [77]. The temperature-dependence of the Landau-de Gennes distortion free energy is included in \mathbf{Q} through S . Since the

Frank-Oseen free energy does not include S , the K_{ij} themselves must change with temperature such that the magnitude of the free energy is temperature dependent. Thus, reconciling the Frank-Oseen free energy and the Landau-de Gennes distortion free energy can yield insights into the temperature dependence of the K_{ij} [76, 77]. To do this, we start by substituting the definition of \mathbf{Q} from Eq. 2.6 into the terms of Eq. 2.58 and simplifying. Using the notation that $A_1 = (\nabla \cdot \mathbf{n})^2$, $A_2 = (\mathbf{n} \cdot \nabla \times \mathbf{n})^2$, $A_3 = (\mathbf{n} \times \nabla \times \mathbf{n})^2$, and $A_{24} = \nabla \cdot (\mathbf{n} \nabla \cdot \mathbf{n} + \mathbf{n} \times \nabla \times \mathbf{n})$, we have the relations [76, 77]:

$$\frac{\partial Q_{ij}}{\partial x_k} \frac{\partial Q_{ij}}{\partial x_k} = 2S^2(A_1 + A_2 + A_3 - A_{24}), \quad (2.59)$$

$$\frac{\partial Q_{ij}}{\partial x_j} \frac{\partial Q_{ik}}{\partial x_k} = S^2(A_1 + A_3), \quad (2.60)$$

$$\frac{\partial Q_{ij}}{\partial x_k} \frac{\partial Q_{kj}}{\partial x_i} = S^2(A_1 + A_3 - A_{24}). \quad (2.61)$$

Now we can re-write Eqs. 2.58 using Eqs. 2.59–2.61 and collect common terms in the A_i 's:

$$f_d = L_1 S^2(A_1 + A_2 + A_3 - A_{24}) + \frac{1}{2} L_2 S^2(A_1 + A_3) + \frac{1}{2} L_3 S^2(A_1 + A_3 - A_{24}) \quad (2.62)$$

$$\begin{aligned} &= \frac{1}{2} A_1(2L_1 S^2 + L_2 S^2 + L_3 S^2) + \frac{1}{2} A_2(2L_1 S^2) \\ &\quad + \frac{1}{2} A_3(2L_1 S^2 + L_2 S^2 + L_3 S^2) \\ &\quad - \frac{1}{2} A_{24}(2L_1 S^2 + L_3 S^2). \end{aligned} \quad (2.63)$$

Comparing Eq. 2.63 to Eq. 2.18, we find:

$$K_{11} = K_{33} = 2L_1S^2 + L_2S^2 + L_3S^2, \quad (2.64)$$

$$K_{22} = 2L_1S^2, \quad (2.65)$$

$$K_{24} = 2L_1S^2 + L_3S^2. \quad (2.66)$$

Unfortunately, note that the Landau-de Gennes distortion free energy to quadratic order requires K_{11} and K_{33} to be equal. As $K_{11} \neq K_{33}$ generally, one way to capture this behavior is to add a single higher-order invariant that contains both \mathbf{Q} and $\nabla\mathbf{Q}$ [76, 77, 80]. While there are 6 possible invariants that could be added, the invariant

$$Q_{ij} \frac{\partial Q_{kl}}{\partial x_i} \frac{\partial Q_{kl}}{\partial x_j} = S^3 \left[\frac{2}{3}A_3 - \frac{1}{3}(A_1 + A_2 + A_3 - A_{24}) \right], \quad (2.67)$$

yields the best agreement with experimental data and is thus the most commonly chosen invariant [76, 77, 80]. By adding this invariant to Eq. 2.58, we get:

$$f_d(\mathbf{Q}) = \frac{1}{2}L_1 \frac{\partial Q_{ij}}{\partial x_k} \frac{\partial Q_{ij}}{\partial x_k} + \frac{1}{2}L_2 \frac{\partial Q_{ij}}{\partial x_j} \frac{\partial Q_{ik}}{\partial x_k} + \frac{1}{2}L_3 \frac{\partial Q_{ij}}{\partial x_k} \frac{\partial Q_{kj}}{\partial x_i} + \frac{1}{2}L_4 Q_{ij} \frac{\partial Q_{kl}}{\partial x_i} \frac{\partial Q_{kl}}{\partial x_j}, \quad (2.68)$$

such that we obtain the modified relations between the K_{ij} and the L_i :

$$K_{11} = 2L_1S^2 + L_2S^2 + L_3S^2 - \frac{2}{3}L_4S^3, \quad (2.69)$$

$$K_{22} = 2L_1S^2 - \frac{2}{3}L_4S^3, \quad (2.70)$$

$$K_{33} = 2L_1S^2 + L_2S^2 + L_3S^2 + \frac{4}{3}L_4S^3, \quad (2.71)$$

$$K_{24} = 2L_1S^2 + L_3S^2 - \frac{2}{3}L_4S^3. \quad (2.72)$$

Similar to the approach of Nehring and Saupe with the Frank-Oseen free energy, we can also consider the role of terms linear in 2nd derivatives of \mathbf{Q} . The 2nd derivative terms predict that both K_{13} and K_{24} could depend linearly on S [74]. However, once

K_{13} is required to be zero, all the contributions from the 2nd derivative terms vanish.

We briefly note that the fact the elastic constants in the Landau-de Gennes distortion free energy do not depend on S has practical applications beyond making predictions about the temperature dependence of the Frank-Oseen elastic constants. Since \mathbf{n} is undefined at a defect, simulating a director field that contains defects requires one to exclude every defect using a cutoff length in order to keep the free energy from diverging. In addition, it is not trivial to represent a director field using vectors as differences in orientation are degenerate on π for a director field and degenerate on 2π for vectors. In contrast, \mathbf{Q} does not depend on whether it is constructed with \mathbf{n} or $-\mathbf{n}$; there is no ambiguity in representing the state of the nematic orientation at any given point. In addition, since \mathbf{Q} contains S , \mathbf{Q} can go to 0 at a defect such that no part of the simulation volume needs to be excluded. This makes the Landau-de Gennes distortion free energy the preferred method for numerical simulations of nematic materials [80]. It is worth noting that the majority of the simulation works ignore the role of K_{24} when making a mapping of L_i to the Frank-Oseen elastic constants. Thus, since L_2 and L_3 differ only by the saddle-splay distortion [see Eq. 2.62], L_3 is typically folded into L_2 and the Landau-de Gennes free energy is written only in terms of L_1 , L_2 , and L_4 [77, 80]. However, due to its simplicity and the fact that the K_{ij} are associated with distinct distortions that are easily visualized, the Frank-Oseen free energy is typically used in analytic theory.

2.3.3 The scaling of the Frank elastic constants

From the relations in Eqs. 2.69–2.72, we see that to leading order the Frank-Oseen elastic constants scale with S^2 ; the S^3 scaling comes entirely from the single higher-order term [see Eq. 2.67]. Since S is a monotonic function of T [22], the S -dependence

of K_{ij} also reflects the temperature dependence near the phase transition. However, as $S(T_{NI})$ is not infinitely small at the phase transition and $S(T < T_{NI}) \approx S(T_{NI})$, the temperature scaling predicted by the Landau-de Gennes free energy can still be used throughout the nematic phase [77].

In fact, there is work that finds that fitting L_1 , L_2 , and L_4 from Eqs. 2.69–2.71 to the measured K_{ii} captures qualitatively the behavior of the K_{ii} throughout the nematic range [77]. Since all the K_{ii} generally have, to leading order, the same scaling with S , their ratio is temperature-independent. This implies that the equilibrium director configuration is also temperature-independent, even if both the actual magnitude of the Frank-Oseen free energy and the director fluctuations about the mean vary with temperature.

2.4 Experimental characterization of nematic liquid crystals

2.4.1 Confinement and boundary conditions

Successfully confining nematic materials is more than simply forcing the nematic into an arbitrary volume, we also have to specify the boundary conditions. For example, confining a NLC to a spherical volume where the material is free to take any orientation on the boundary is uninteresting as the director field can remain homogeneous, as if the sphere did not exist. However, if we enforce homeotropic boundary conditions such that the director must be everywhere perpendicular to the surface, then we see that there must be a defect in the volume, as seen schematically by the red dot in the radial configuration [81] depicted in Figure 2.8(A). Since in this situation the director at the boundary of the sphere will cover \mathbb{S}^2 exactly once, from Eq. 2.8, we see that the sum of all the defects in such a spherical volume must have $|q_{net}| = 1$. Similarly, if we instead enforce degenerate planar boundary conditions such that the director must everywhere lie parallel to the surface, the Poincaré-Hopf Theorem requires a total topological charge of $s = +2$ on the surface. One way to

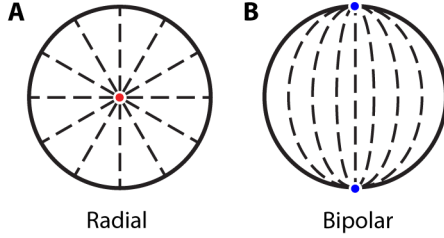


Figure 2.8: Nematic liquid crystal confined to a spherical volume. (A), The classic radial director configuration found under homeotropic boundary conditions. The defect is indicated by \bullet . (B), The classic bipolar director configuration found under degenerate planar boundary conditions. The 2 defects are indicated by \bullet .

satisfy this condition is with a bipolar configuration where two $s = +1$ defects place themselves at opposite poles of the sphere [81], as seen schematically by the blue dots in Figure 2.8(B).

Formally, if \mathbf{k} is the boundary normal, homeotropic anchoring has $|\mathbf{k} \cdot \mathbf{n}| = 1$ and degenerate planar anchoring has $|\mathbf{k} \cdot \mathbf{n}| = 0$, where \mathbf{n} is the director at the boundary. These are not the only two options; we can also have degenerate tilt boundary conditions, where $0 < |\mathbf{k} \cdot \mathbf{n}| < 1$, with a tilt angle given by $\theta = \arccos |\mathbf{k} \cdot \mathbf{n}|$. Note that planar anchoring does not have to be degenerate. The direction in the plane of the boundary can be specified as well, breaking the degeneracy such that $\mathbf{n} \parallel \boldsymbol{\sigma}$, where $\boldsymbol{\sigma}$ is a unit vector and $\mathbf{k} \cdot \boldsymbol{\sigma} = 0$. Homeotropic anchoring, degenerate planar anchoring, and planar anchoring are illustrated schematically for a flat substrate in Figure 2.9(A-C), respectively.

In an experiment, confinement takes place with either solid boundaries, such as glass cells and capillaries, or fluid boundaries such as in emulsions of a nematic material dispersed in an outer immiscible liquid phase. It is also possible to confine a nematic using both solid boundaries and fluid boundaries, as with a droplet of NLC sitting on a solid base. In such a sessile drop, the solid boundary provides a flat base for the NLC; however, the remainder of the confinement is provided by the free surface, where the NLC is in contact with air. In general, a NLC in contact with

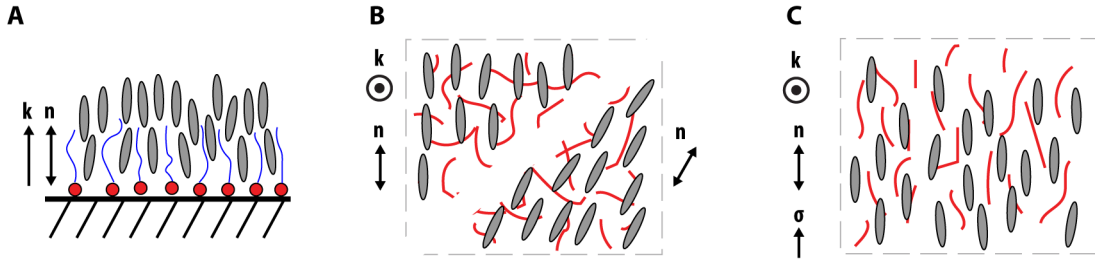


Figure 2.9: Common anchoring schemes for nematic liquid crystals. (A), Homeotropic anchoring enforced by surfactant molecules. The polar heads of the molecules adsorb to the substrate, with the nonpolar tails extending into the NLC. The tails serve to align the nematic mesogens along the surface normal, making $\mathbf{k} \parallel \mathbf{n}$, as seen in the schematic. (B), Degenerate planar anchoring enforced by randomly oriented polymers on the substrate. The polymers only require that the mesogens lie in the plane of the interface such that $\mathbf{k} \perp \mathbf{n}$. Since there is no preferred direction in the plane of the substrate, the mesogens are free to choose any director in the plane, as depicted in the schematic. (C), Planar anchoring enforced via aligned polymers on the substrate. Here, the polymers have an alignment direction, setting the direction that the NLC mesogens also prefer to align along, such that $\mathbf{n} \parallel \boldsymbol{\sigma}$, where $\boldsymbol{\sigma}$ is a vector describing the polymer alignment direction, as defined in the schematic.

an arbitrary boundary will be subject to degenerate tilt boundary conditions. Thus, for experiments that require a specific boundary condition we must treat the interface.

In order to discuss specific strategies for enforcing anchoring, we must first narrow down the compounds that might be used. NLC can be divided into two broad categories, thermotropics and lyotropics [22]. In thermotropic LC's, temperature is an important control parameter. If the temperature is too high, the nematic phase will melt to the isotropic phase and if the temperature is too low, the nematic phase will phase transition to a less symmetric LC phase or to a crystalline phase. Lyotropic LC's are suspensions of particles in a solvent and therefore are sensitive to both concentration as well as temperature.

In this Thesis, we will primarily use 4-cyano-4'-pentylbiphenyl (5CB), a thermotropic liquid crystal whose mesogens are ~ 2 nm long [22]. 5CB belongs to the cyanobiphenyl family of NLC, which are characterized by a cyano (CN) group bonded

to a biphenyl (C_6H_4)(C_6H_4) group bonded to an alkyl group of given length, C_pH_{2p+1} , where p is the number of carbon atoms in the group [22]. In the case of 5CB, the chemical formula is: $(CN)(C_6H_4)(C_6H_4)(C_5H_{11})$. Thus, we see that the “5” in 5CB refers to the number of carbon atoms in the alkyl group. Since the different cyanobiphenyls generally only differ in the number of carbon atoms in the alkyl group, the anchoring techniques we cover below for 5CB are general and should apply to any p CB.

To enforce homeotropic anchoring for 5CB against a smooth, isotropic solid boundary such as a glass capillary or glass slide, it is common to either deposit surfactant molecules or bond silanes to the surface. In both cases, the smooth surface becomes decorated with long chains that stick up normal to the surface. The nematic mesogens at the surface are aligned by the chains, enforcing homeotropic anchoring at the surface [22], as seen schematically in Figure 2.9(A). For example, to enforce homeotropic anchoring for 5CB on glass, we dip coat glass slides in a 0.1% w/w lecithin in hexane solution and then let the slides dry. When the hexane evaporates, the polar head of the lecithin molecule is attached to the glass surface, leaving the long tails sticking up from the glass [82].

Similarly, it is common to enforce homeotropic anchoring in solution also using surfactants. Here, for an organic NLC dispersed in an aqueous phase, the polar head of the surfactant sits in the aqueous phase while the hydrophobic tail inserts itself into the NLC volume, aligning the NLC at the interface [11, 83]. For example, we use sodium dodecyl sulfate (SDS) in water to enforce homeotropic anchoring in 5CB emulsions and liquid bridges. While homeotropic anchoring can be enforced with as little as 1 mM SDS in H_2O , we use a solution of 8 mM SDS in H_2O for the strongest possible anchoring [83]. At concentrations above 8 mM, SDS forms micelles in H_2O such that working with higher concentrations does not yield any more free SDS in solution that could potentially adsorb to the interface and contribute to a larger anchoring strength [84]. This concentration is known as the critical micelle

concentration (CMC) and is a common feature in solutions of surfactants or other amphiphilic molecules [84, 85].

While smooth, isotropic solid boundaries can exhibit degenerate planar anchoring, in general the anchoring will be degenerate and tilted. Thus, a surface is often coated with a polymer such that the polymer orientations on the surface are random. For example, spin coating poly(methyl methacrylate) onto glass produces planar degenerate anchoring for 5CB [86]. Since the polymers have no preferred alignment in the plane of the surface, the mesogens are free to choose their own director in the plane [87], as seen schematically in Figure 2.9(B).

If a preferred anchoring direction in the plane, σ , is desired, the polymer coating can be rubbed along σ , aligning the polymers and creating “grooves” in the polymer coating along the rubbing direction, as seen schematically in Figure 2.9(C). The NLC will align along the rubbing direction, breaking the degeneracy in the anchoring [22]. Note that rubbed polymer surfaces do not have perfect planar anchoring but rather exhibit a small tilt angle [88]. Thus, when designing planar-aligned liquid crystalline cells, where the NLC is confined between two parallel plates with planar anchoring, the rubbing direction on the plates will be anti-parallel. The anti-parallel rubbing aligns the tilt angles at the plates such that the NLC can still form a homogeneously-aligned domain between the plates [88].

For dispersions of organic NLC droplets such as 5CB in a continuous aqueous phase, we add a polymer like PEO or PVA to the aqueous phase [26, 89]. The polymer adsorbs to the interface between the NLC and the continuous phase, giving degenerate planar anchoring. We know of no easy way to break the planar degeneracy in the anchoring when dealing with a liquid-liquid interface. In addition, we note that even though 5CB exhibits degenerate planar anchoring at the interface with

pure water, the addition of a polymer strengthens the anchoring as well as acting to stabilize the emulsion when 5CB droplets are dispersed in H₂O [26, 89].

2.4.2 Birefringence and optically polarized microscopy

Once the nematic is confined in the desired volume with the desired boundary conditions, the most common way to study the sample is with optical polarized microscopy. This technique takes advantage of the birefringence of the NLC to determine the director in the sample. For a uniaxial nematic, the index of refraction along \mathbf{n} is known as the “extraordinary index of refraction”, denoted n_E , and the index of refraction perpendicular to \mathbf{n} is called the “ordinary index of refraction”, denoted as n_o . Since the index of refraction along \mathbf{n} is n_E , the director also serves as the optic axis of uniaxial nematics [88]. The birefringence is defined as $\Delta n = n_E - n_o$ [88]. If $n_E > n_o$, $\Delta n > 0$ and the material has positive birefringence. Conversely, if $\Delta n < 0$, the material has negative birefringence. Thus, the index of refraction affecting the incident light on a birefringent material will depend on the polarization of the light relative to \mathbf{n} [88].

While unpolarized light will be unaffected by the birefringent material, in general polarized light will have its polarization state affected. Consider linearly polarized light incident upon a birefringent material with n_E along \hat{x} and n_o along \hat{y} . If the incident light is polarized along \hat{x} or \hat{y} , it will encounter only either the extraordinary index of refraction or the ordinary index of refraction and will leave the birefringent volume with no change in its polarization state. However, now let the incident light be linearly polarized at 45°. In this case, the incident light can be decomposed into one component along \hat{x} and another component along \hat{y} . Since each component will see a different index of refraction, they will propagate at different speeds, creating a phase difference between the two components of the incident light.

This phase difference is known as the retardation and is given in multiples of 2π by $\Gamma = 2\pi\Delta n d/\lambda$, where d is the thickness of the birefringent material, and λ is the wavelength of the incident light in vacuum [88]. For our example of incident light linearly polarized at 45° , let $\Delta n d = \lambda/2$ such that $\Gamma = \pi$. The light after leaving the sample will now be polarized at -45° , and the birefringent material has the properties of a half-waveplate [88]. Similarly, if $\Delta n d = \lambda$, $\Gamma = 2\pi$, the birefringent material is a full-waveplate and the output light will be unchanged [88].

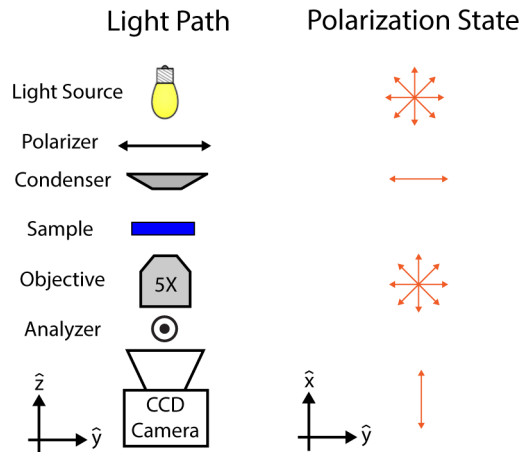


Figure 2.10: Schematic of the light path and polarization state for optically polarized microscopy (OPM). OPM places a linear polarizer called the “polarizer” before the condenser and another linear polarizer called the “analyzer” after the objective. The polarization states depicted in the figure assume the sample is birefringent and the pass axes of the polarizer and the analyzer are orthogonal.

Optical polarized microscopy (OPM) takes advantage of birefringence and turns the change in polarization into changes in transmitted intensity. The typical setup uses a pair of linear polarizers into the light path of a standard wide-field optical microscope. A linear polarizer is an optical element that only passes light polarized along a specific axis known as the “pass axis” [88]. Thus, unpolarized light incident upon a linear polarizer will have its intensity reduced by half and the output light

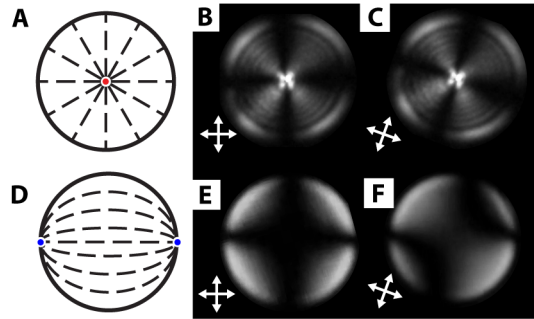


Figure 2.11: Example OPM textures for a bipolar drop and a radial drop. (A–C), schematic and textures for a radial drop. The textures in (B,C) have the polarizer and analyzer directions specified on the images, with the drops oriented as depicted in (A). Note how the texture only changes orientation with the polarizer and analyzer orientation, but does not change character. (D–F), schematic and texture for a bipolar drop. The textures in (E,F) have the polarizer and analyzer directions specified on the images, with the drops oriented as depicted in (D). Note how the texture changes as the polarizer and analyzer rotate.

will be linearly polarized along the pass axis of the polarizer. Illustrating the light path for optical polarized microscopy, the incident light passes through the first linear polarizer, known as the “polarizer”, through the sample, through the objective, and through the second linear polarizer, known as the “analyzer”, before it is incident on the eyepiece or the camera used to capture the microscope image [88]. The light path is illustrated schematically in Figure 2.10. If the polarizer and analyzer are “crossed,” or oriented with their pass axes orthogonal to each other, any isotropic sample will be entirely dark. This is because the sample does not affect the polarization state of the incident light such that the linearly polarized light from the polarizer is blocked by the analyzer. However, if the sample is birefringent, the polarization state of the incident light will change and some of the light will pass through the analyzer and be transmitted onto the eyepiece or camera. This is illustrated in the schematic in Figure 2.10.

The intensity pattern in the image output from an OPM setup can then be used to deduce information about the sample. While for our purposes we typically care

about the spatial variation of the optic axis, and thus the spatial variation in \mathbf{n} , OPM can also be used to determine the birefringence of the sample [88]. For example, we consider 5CB confined to spherical nematic droplets. Under homeotropic anchoring the droplet will have the classic “radial” director field [see Figure 2.11(A)] while under degenerate planar anchoring the droplet will have the classic “bipolar” configuration [see Figure 2.11(D)] [81]. These configurations can be distinguished by their OPM textures, as seen in Figure 2.11(B,C) for a radial drop and Figure 2.11(E,F) for a bipolar drop. Note how the light and dark portions of the bipolar texture change from Figure 2.11(E) to Figure 2.11(F) as the polarizer and analyzer change orientation, while still crossed. The radial texture only rotates with the polarizer and analyzer but does not change in the frame of the polarizer and analyzer; see Figure 2.11(B,C).

Table 2.2: Basic group theory definitions [90, 91].

set: A collection of objects
group: A set, Σ , and a binary operation, or group multiplication, \cdot , that combines two elements in the set to form a third element in the set, satisfying: <ul style="list-style-type: none"> associativity: $\forall a, b, c \in \Sigma, (a \cdot b) \cdot c = a \cdot (b \cdot c)$. identity: $\exists! e \in \Sigma$ s.t. $\forall a \in G, a \cdot e = e \cdot a = a$. invertability: $\forall a \in \Sigma, \exists! a^{-1} \in \Sigma$ s.t. $aa^{-1} = a^{-1}a = e$, with e the identity. If $\forall a, b \in \Sigma, a \cdot b = b \cdot a$, the group is said to be Abelian. Note that the requirement $\forall a, b \in \Sigma, a \cdot b \in \Sigma$ is known as closure .
Lie group: A group that is also a differentiable manifold, whose group operation is also differentiable. Lie groups are associated with continuous symmetries, for example, $SO(3)$, the set of all rotations in 3D Euclidean space under multiplication. Other common Lie groups include n -dimensional Euclidean space \mathbb{R}^n under vector addition, and $GL(2)$, the group of 2×2 invertible matrices, also under multiplication.
discrete group: A group whose elements must be countable. This is instantly satisfied if there are a finite number of elements in the group. In this case the order of the group is given by the number of elements in the group. If there are an infinite number of elements, there must be a one-to-one mapping from the elements to the integers.
homomorphism: A structure-preserving map, φ , between the groups G and H , $\varphi : G \rightarrow H$. A homomorphism must satisfy, $\forall a, b \in G, \varphi(a \cdot b) = \varphi(a) \cdot \varphi(b)$. Since $\forall a \in G, \varphi(a) \in H$, we see that a homomorphism preserves the group multiplication. A homomorphism is not necessarily a one-to-one mapping. If the homomorphism is one-to-one, then the homeomorphism is an isomorphism .

CHAPTER 3

ACTIVE NEMATICS ON THE SURFACE OF A TORUS

3.1 Introduction

Active materials are composed of constituent particles that each can convert stored internal energy, or ambient energy, into work. As a result, they are intrinsically out of equilibrium [92–94]. Due to being out of equilibrium, the system is athermal and cannot be understood within the framework of equilibrium statistical mechanics. However, the constituent particles in active materials are still in motion, similar to the particles in thermal systems. This is in contrast to passive athermal materials like jammed or granular systems, where individual particles are static. As a consequence, active materials can exhibit a wide range of emergent phenomena. Examples include flocking transitions, observed in groups of starlings [95, 96]; elastic behavior, observed in colonies of fire-ants [97]; and “superfluid-like” behavior, observed in bacterial suspensions [98, 99]. Within the current theoretical framework of “active matter,” the emergent phenomenology is typically governed by a single control parameter called the “activity” [92–94]. For example, in the starlings and bacterial suspensions, the activity is associated to the speed of the individual particles; the flocking and superfluid-like behavior only exists for nonzero average velocity. When the particle speed is zero, both the starlings and the bacteria become passive athermal materials. Activity is in general defined differently for different systems, with the only requirement being that the passive state corresponds to zero activity.

Note that active materials can be composed of individual units of any size, provided the activity is strong enough. In fact, the previous examples span 4 orders of magnitude in size, from the starlings at $\mathcal{O}(10^{-1})$ m to the bacteria at $\mathcal{O}(10^{-5})$ m, with

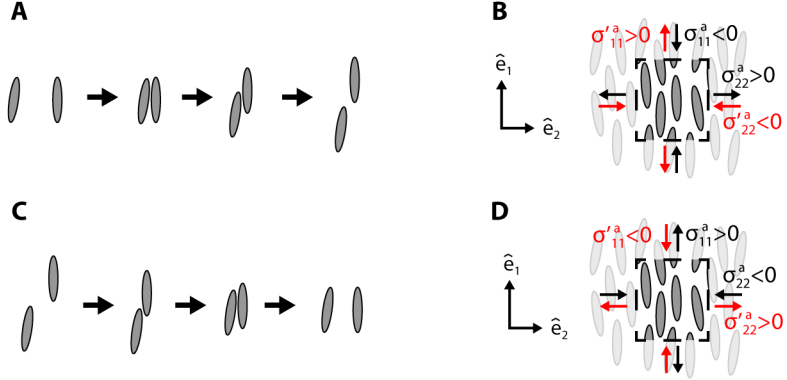


Figure 3.1: Interactions in extensile and contractile nematics. (A,C), Two-particle interaction for extensile (A) and contractile (C) mesogens. The arrows represent time. (B,D), Active stress exerted on a small area by the surroundings (σ) and on the surroundings by the small area (σ') for (B) extensile and (D) contractile interactions.

their respective behavior all understood within the same framework of “active matter.” However, despite the fact that the strength of the activity typically governs the system-wide behavior, there is still no general *a priori* understanding of how adding activity to a passive system will affect its properties and behavior. Here, we consider how activity affects the interplay between nematic order, geometry, and topology.

Much like equilibrium nematics, the individual mesogens of active nematic materials are anisotropic and thus form a nematic phase; however, the addition of activity to nematic order modifies the interaction between the mesogens. With the exception of bacteria introduced into lyotropic liquid crystals [100], to date the majority of experimental and theoretical work on active nematics has taken place in 2D. Thus, we will highlight the effect of activity on a nematic in 2D. Consider a pair of active rod-like particles in 2D. If the active nematic is “extensile,” when the two rods touch they will slide past each other and then separate, as illustrated in Figure 3.1(A); however, if the active nematic is “contractile,” when two rods touch they will slide towards each other and then separate, as illustrated in Figure 3.1(C).

We can also think about the effect of these interactions at the continuum level; considering the forces from the surrounding material acting on a small area of the ne-

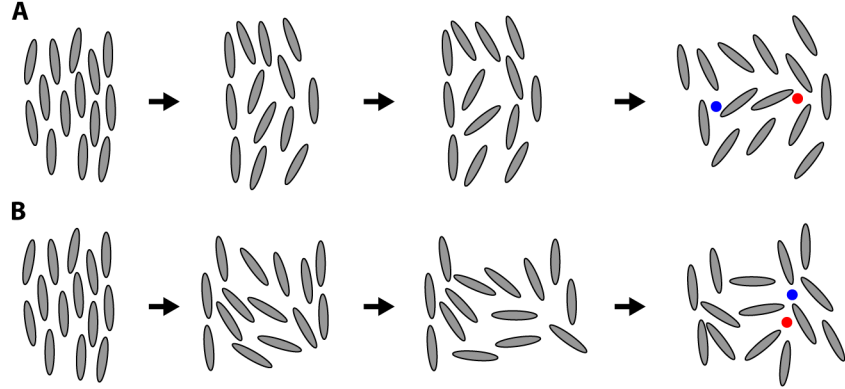


Figure 3.2: Activity generates defect pairs. An (A) extensile and (B) contractile active nematic evolving over time. In both cases a $s = \pm 1/2$ defect pair is generated, with the defects indicated by (●), and (•), respectively.

matic and enforcing conservation of momentum, we arrive at the Cauchy momentum equation:

$$\rho \frac{D\mathbf{v}}{Dt} = \nabla \cdot \boldsymbol{\tau}, \quad (3.1)$$

where $D/Dt = \partial/\partial t + \mathbf{v} \cdot \nabla$ is the material derivative, \mathbf{v} is the fluid velocity, and $\boldsymbol{\tau}$ is the stress tensor. We can rewrite $\nabla \cdot \boldsymbol{\tau}$ in Eq. 3.1 for an incompressible active nematic fluid in terms of the viscosity, η , the pressure, p , the stress from the nematic elasticity $\boldsymbol{\sigma}^{elastic}$, and the stress from the activity $\boldsymbol{\sigma}^{active}$, yielding:

$$\rho \frac{D\mathbf{v}}{Dt} = \eta \nabla^2 \mathbf{v} - \nabla p + \nabla \cdot \boldsymbol{\sigma}^{elastic} + \nabla \cdot \boldsymbol{\sigma}^{active}. \quad (3.2)$$

Since the active forces act along the director, we can write $\boldsymbol{\sigma}^{active} = \alpha \mathbf{Q}$, where \mathbf{Q} is the 2D nematic tensor order parameter defined in Eq. 2.4. If $\mathbf{n} \parallel \hat{e}_1$, with $\{\hat{e}_1, \hat{e}_2\}$ the standard orthonormal basis, then the active stress becomes

$$\boldsymbol{\sigma}^{active} = \alpha S \begin{pmatrix} 1/2 & 0 \\ 0 & -1/2 \end{pmatrix}. \quad (3.3)$$

Then, if $\alpha < 0$, $\sigma_{11}^{active} = -|\alpha|S/2 < |\alpha|S/2 = \sigma_{22}^{active}$, as illustrated by the black

arrows in Figure 3.1(B). Similarly, if $\alpha > 0$, $\sigma_{22}^{active} = -|\alpha|S/2 < |\alpha|S/2 = \sigma_{11}^{active}$ [black arrows, Figure 3.1(D)]. However, these stresses represent the active stresses of the surrounding material on the area of interest; the active stress due to the area of interest, $\boldsymbol{\sigma}'^{active}$, will have the opposite sign. This is illustrated by the red arrows in Figure 3.1(B,D). When $\alpha < 0$, [Figure 3.1(B)] the activity works to extend the nematic along the director, while when $\alpha > 0$ [Figure 3.1(C)], the activity works to contract the nematic along the director. Hence, extensile interactions have $\alpha < 0$ while contractile interactions have $\alpha > 0$ [101].

To further see the ramifications of the activity, we evaluate $\nabla \cdot \boldsymbol{\sigma}^{active}$,

$$\partial_j \sigma_{ij}^{active} = \alpha \partial_j (S(n_i n_j - \delta_{ij}/2)) \quad (3.4)$$

$$= \alpha(\partial_j S)(n_i n_j - \delta_{ij}/2) + \alpha S((\partial_j n_i)n_j + n_i(\partial_j n_j)) \quad (3.5)$$

$$\nabla \cdot \boldsymbol{\sigma}^{active} = \alpha(\nabla S)^T(\mathbf{n} \otimes \mathbf{n} - \mathbb{1}/2) + \alpha S((\mathbf{n} \cdot \nabla)\mathbf{n} + \mathbf{n}(\nabla \cdot \mathbf{n})) \quad (3.6)$$

$$= \alpha(\nabla S)^T(\mathbf{n} \otimes \mathbf{n} - \mathbb{1}/2) + \alpha S(\mathbf{n}(\nabla \cdot \mathbf{n}) - \mathbf{n} \times \nabla \times \mathbf{n}). \quad (3.7)$$

The second term in Eq. 3.7 relates the force density due to the activity to splay and bend distortions in the nematic. First, consider $\alpha S \mathbf{n}(\nabla \cdot \mathbf{n})$. The force is always along the director, with the magnitude of the force proportional to the divergence. Note that the term is symmetric, so regardless of computing the term with \mathbf{n} or $-\mathbf{n}$, the direction of the force is the same; for $\alpha > 0$, the diverging structure will act like a “source” and the force will amplify the splay, while for $\alpha < 0$ the diverging structure will act like a “sink” and the active force will reduce the splay. Second, consider $-\alpha S \mathbf{n} \times \nabla \times \mathbf{n}$. Here, the force will be perpendicular to \mathbf{n} and thus work to either amplify ($\alpha < 0$) or suppress ($\alpha > 0$) bend distortions. In addition, the magnitude of the force is proportional to the magnitude of the bend distortion. Since the term is symmetric, $\alpha < 0$ will always cause the force to amplify a bend distortion, while $\alpha > 0$ will cause the active force to suppress a bend distortion.

Thus, contractile activity with $\alpha > 0$ amplifies splay distortions and suppresses bend distortions, while extensile activity with $\alpha < 0$ amplifies bend distortions and suppresses splay distortions. Consequently, if the active stress is greater than the elastic stress, extensile active nematics are unstable to bend distortions while contractile active nematics are unstable to splay distortions [101–103]. This instability is illustrated for an extensile and contractile active nematic in Figure 3.2(A,B), respectively, where the instability in both cases eventually results in the creation of an $s = \pm 1/2$ defect pair.

While active nematics can exist in a defect-free state for low activity [104, 105], the activity is generally large enough such that the steady-state is often full of pairs of $s = \pm 1/2$ defects that are continuously created and annihilated [15, 100, 101, 106–108]. Since the active stress acts along the director, the polar structure of the $s = +1/2$ defects will cause these $s = +1/2$ defects to act like self-propelled particles, with the propulsion direction depending on the type of activity [101, 106]. For example, consider the director structure of an $s = +1/2$ defect shown by the white lines in Figure 3.3(A); an extensile stress along the director will cause the bend distortion to grow and the splay distortion to decrease, causing the defect to propagate along the red arrow. In contrast, the interactions in a contractile nematic will cause the defect to propagate opposite to the red arrow. However, due to the three-fold symmetry of $s = -1/2$ defects, as shown by the white lines in Figure 3.3(B), any stress along the director will have no effect on the defect position. Thus, $s = -1/2$ defects are not driven by the activity and instead are only advected by interactions between the defects. As a consequence, the dynamics in an active nematic are driven only by the motion of $s = +1/2$ defects [105].

Recent experimental studies with active nematics yielding self-regulated behaviors such as self-sustained oscillations [109], spontaneous formation of morphological features such as kinks and protrusions [107, 109], and undirected motility [107, 109]

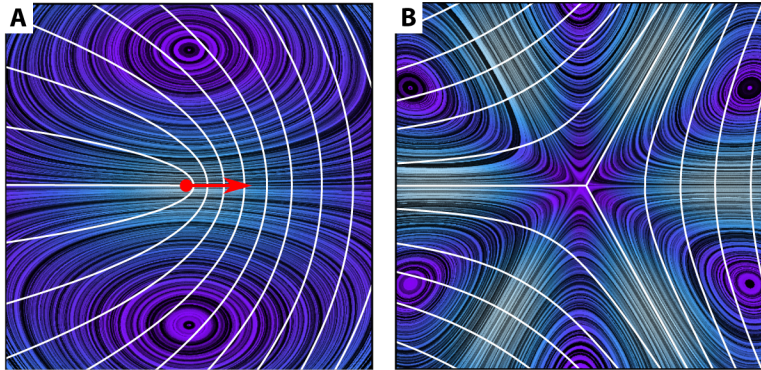


Figure 3.3: Flow fields for active disclinations. (A,B) Flows generated by active (A) and $s = +1/2$ and (B) $s = -1/2$ disclinations, with the director lines drawn in white. Due to the polar structure of the active flow, $s = +1/2$ disclinations propel along their symmetry axis. The red arrow represents the propulsion direction for an extensile nematic; $s = +1/2$ disclinations will propel in the opposite direction for a contractile nematic.

have acted as stimulus to investigate how biological functionality emerges from the interplay between activity, the geometry of the system, and the structure of the internal phase [110–112]. In this context, defects in active nematics could be harnessed to achieve life-like functionality, as defects are extremely sensitive to the intrinsic curvature of the space they inhabit. This is illustrated in Eq. 1.7, where topological defects on a surface are treated like point charges interacting among themselves and with a background charge density provided by the Gaussian curvature of the surface.

However, despite theoretical interest in the interplay between varying Gaussian curvature and topological defects, with few exceptions [113–116], there has been little experimental work with defects on surfaces where the Gaussian curvature is non-constant. More notably, there has been no experimental work where the defects have the option to explore regions with both positive and negative Gaussian curvature.

In this latter scenario with nematic order, the topological charge is expected to unbind; starting with an $s = \pm 1/2$ defect pair, the $s = +1/2$ defect will migrate to a region of positive Gaussian curvature, while the $s = -1/2$ defect will instead migrate to a region of negative Gaussian curvature [30, 117, 118]. For example, consider the

schematic of a torus in Figure 3.4(A) with the $K > 0$ region in red and the $K < 0$ region in blue. For a torus specified by a central ring radius, R_0 , and a tube radius, a , we use the toroidal coordinates $\{r, \theta, \varphi\}$, with $\{r, \theta\}$ the usual polar coordinates in the circular cross section and φ the azimuthal angle [see Figure 3.4(B)]. We define the aspect ratio of the torus as $\xi = R_0/a$. For low ξ , the ground state of a nematic on a torus is predicted to have defects due the ability of the defects to “screen” the Gaussian curvature of the surface. Specifically, introducing 4 pairs of $s = \pm 1/2$ defects onto the surface, as depicted in Figure 3.4(A), completely screens the Gaussian curvature of the surface. We see that the $s = +1/2$ defects are predicted to minimize their energy when they are located on the outside of the “hole,” thereby screening the positive Gaussian curvature, and the $s = -1/2$ defects are predicted to sit on the inside of the “hole” to screen the negative Gaussian curvature. The repulsion between the like-signed defects cause the defects to be spaced in intervals of $\varphi = \pi/2$; increasing the repulsion can lead to fewer than 4 pairs of defects as the ground state. In addition, the ground state is only predicted to be defective when the curvature is large enough to overcome the attraction between opposite-signed defects.

For the schematic in Figure 3.4(A), if we integrate over the red $K > 0$ region where $\theta \in [\pi/2, 3\pi/2]$, and consider $\varphi \in [0, \varphi']$, we can compare the integral as a function of φ' with the net topological charge in the region. Since both of these quantities depend on φ' , we get the parametric curve depicted in red in Figure 3.4(C). Similarly, integrating over the blue $K < 0$ region defined by $\theta \in [-\pi/2, \pi/2]$ as a function of φ' and comparing with the net topological charge in the region yields the parametric curve depicted in blue in Figure 3.4(C). We see that the curves in Figure 3.4(C) have positive slopes, indicating the curvature-induced defect unbinding, and the curves are stepped, reflecting the discrete nature of the topological charge. Recall for nematics in 2D, the topological charge occurs in quanta of $1/2$. In addition, note that the total integrated Gaussian curvature in the $K > 0$ region and the $K < 0$ region is $+4\pi$ and

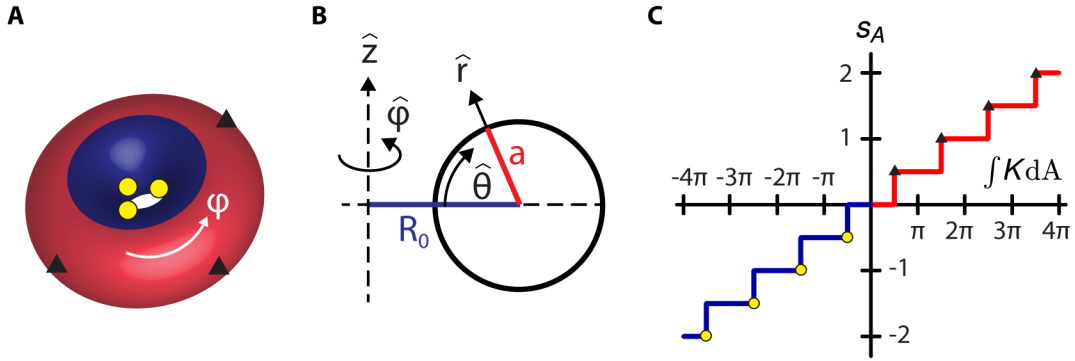


Figure 3.4: Curvature-induced defect unbinding for a nematic on a torus. (A) A schematic of a torus with 4 pairs of unbound pairs of $s = \pm 1/2$ defects. The 3 visible $s = +1/2$ defects are indicated by \blacktriangle and the 3 visible $s = -1/2$ defects are indicated by \bullet . The red region on the torus has $K > 0$ and the blue region has $K < 0$. (B) A schematic of a cross-section of a torus defining the toroidal coordinate system $\{r, \theta, \varphi\}$. A given torus is specified by its central circle radius, R_0 and its tube radius, a , which combine to form the aspect ratio, $\xi = R_0/a$. (C) Plot of topological charge vs integrated Gaussian curvature as φ increases for the torus in (A). The red curve corresponds to integrating over the red region defined by $\theta \in [\pi/2, 3\pi/2]$ and the blue curve corresponds to integrating over the blue region defined by $\theta \in [-\pi/2, \pi/2]$. The positive slope indicates defect unbinding.

-4π , respectively. Since each $s = \pm 1/2$ defect corresponds to a π rotation of \mathbf{n} , the four pairs of defects on the torus exactly screens the total integrated K of the $K > 0$ and $K < 0$ regions.

In this chapter, we address this situation experimentally using a 2D extensile active nematic on the surface of a toroidal droplet. The active nematic is composed of microtubules driven by kinesin motors and fueled by adenosine triphosphate (ATP); the strength of the activity in this material is tuned by the ATP concentration, with higher ATP concentrations causing the kinesin motors to introduce more kinetic energy into the system. Since the torus has a handle, it has a genus of one and thus according to the Poincaré-Hopf Theorem written in Eq. 1.3, the nematic field must have zero net topological charge. In our experiments, the activity is large enough such that the torus is always populated with a sea of constantly moving $s = \pm 1/2$ defects that are dynamically created and annihilated. The topological constraints,

nevertheless, force the number of $s = +1/2$ defects to be equal to the number of $s = -1/2$ defects.

Interestingly, despite the nonequilibrium dynamics of the defects, we find that on average, pairs of $s = \pm 1/2$ topological defects unbind, with the individual defects migrating to regions with like-signed Gaussian curvature. However, as a result of the averaging process in our analysis, the average topological charge in a region on the surface ceases to take on discrete values and instead becomes a continuous variable. In addition, contrary to expectations from equilibrium predictions [117–121], we find that this active unbinding depends only on the local geometry and that it is independent of the system size and aspect ratio.

Our studies are performed with two different ATP concentrations and thus two different levels of activity. We find that the unbinding depends on activity. In addition, we characterize the defect number fluctuations in a region on the surface and find that the relative root-mean-squared (RMS) defect number fluctuations is inversely proportional to the square root of the average number of defects in the region. Interestingly this is the expected result for an equilibrium system of particles subject to number fluctuations. A numerical integration of the equation of motion of active nematic defects [101, 106, 109] performed by Luca Giomi and Dan Pearce at the University of Leiden confirms our experimental results and indicates that the defect unbinding depends on the defect number density and that the unbinding can be suppressed in the limit of high activity. Furthermore, by using topological defects as micro-rheological tracers and quantitatively comparing our experimental and theoretical results, we are able to estimate the Frank elastic constant, the active stress α , and the defect mobility of a microtubule-kinesin active nematic liquid crystal for the first time. Overall, our results not only confirm the theory of topological defects on curved surfaces, but also demonstrate the interesting phenomenology that arises from adding activity to the interplay between geometry, topology, and order. Our

work thus provides insights into the physics of partially ordered active matter and introduces a new avenue for the quantitative mechanical characterization of active fluids.

3.2 Making active nematic toroids

3.2.1 Active nematic formulation

We use the microtubule-kinesin active nematic system pioneered by the Dogic Group at Brandeis University as published in references [15, 107–109, 122]. Microtubules are long, hollow rods that self-assemble from dimers of the α - and β -tubulin proteins [123]. The α/β -tubulin dimers polymerize end-to-end to form long chains that then assemble laterally to create cylindrical structures with a helical wrapping of α - and β -tubulin chains [123, 124], as depicted schematically in Figure 3.5. This structure gives microtubules a polarity with the (+) end associated with the unpolymerized β -tubulin subunits and the (-) end associated with the unpolymerized α -tubulin subunits [123, 124].

While the microtubules serve as the mesogens of the active nematic, the activity comes from kinesin motor proteins bound in clusters to a streptavidin protein. When in contact with a microtubule, kinesin “walks” along the microtubule in discrete steps from the (-) end towards the (+) end, hydrolyzing one ATP molecule into an adenosinediphosphate (ADP) molecule for every 8-nm step [125]. Thus, a kinesin cluster in contact with two antiparallel microtubules will induce a sliding motion due to the motion of the kinesin motors that will displace the two microtubules in opposite directions [107, 126]. Conversely, a kinesin cluster in contact with two parallel microtubules will simply walk along both microtubules in the same direction and thus induce no relative motion between the microtubules [107, 126]. These two scenarios are illustrated schematically in Figure 3.5(B).

Apart from the activity provided by the kinesin motors, the microtubules in solu-

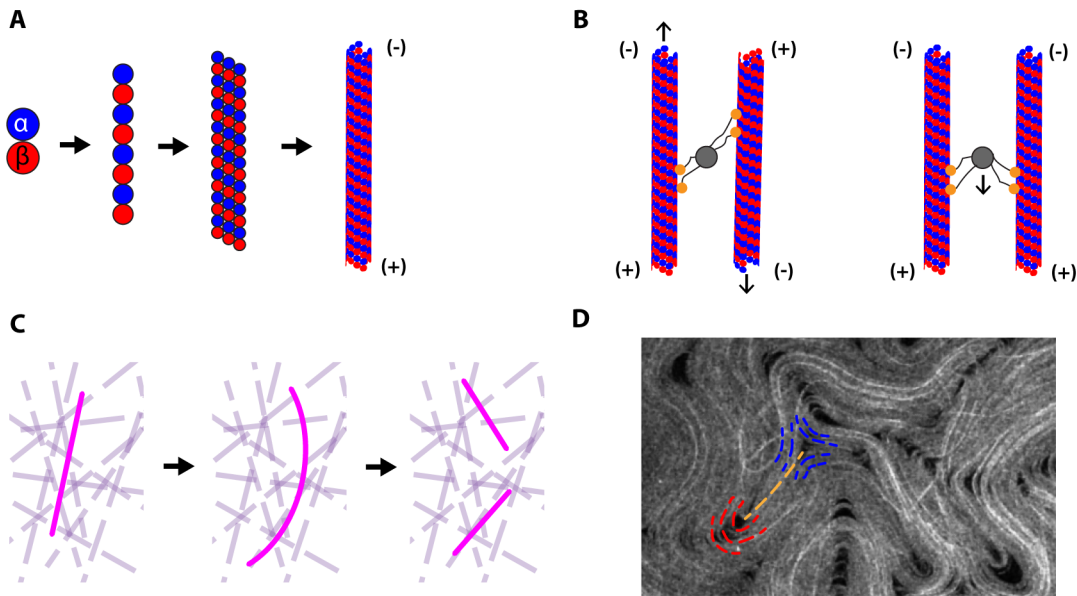


Figure 3.5: Microtubule-kinesin active nematic liquid crystal. (A) Schematic of tubulin polymerizing into a microtubule. The α/β -tubulin dimers polymerize end-to-end to form chains which then polymerize laterally to form microtubules. The microtubule polarity is indicated on the schematic, with (-) associated to free α -tubulin and (+) associated to free β -tubulin. (B) Kinesin (\bullet) walks along microtubules from the (-) end to the (+) end. When kinesin are bound to streptavidin (\circ) to form clusters, these clusters can generate relative motion between two antiparallel microtubules. In contrast, parallel microtubules exhibit no relative motion, with the kinesin-streptavidin cluster simply translating itself in the shared (+) direction. (C) Microtubules and kinesin-streptavidin clusters bundle together by depletion form fibers that slide past each other. When the concentration of fibers is high enough to form a viscoelastic network, individual fibers cannot slide freely and instead will buckle and fracture. (D) In the presence of a liquid-liquid interface, the fibers will deplete to the interface and undergo an isotropic-nematic transition, with the fiber direction giving the nematic director. Pictured is a fluorescence microscopy snapshot of an active nematic, where the microtubules are fluorescently labeled such that the fiber direction is apparent. The director surrounding an $s = +1/2$ and $s = -1/2$ defect pair is highlighted by the dashed red and blue lines, respectively, with the fracture line connecting the pair highlighted with a yellow dashed line.

tion interact via the depletion interaction [127], which is introduced by the presence of poly(ethylene glycol) (PEG, 20 kDa) as a depletant. The depletion interaction “bundles” the microtubules together to form filaments that continuously slide past each other due to the extensile interaction exerted by the kinesin motors [107, 126, 128]. In 3D, when the concentration of filaments in the solution is large enough, the filaments form a viscoelastic network [107, 129]. This network inhibits the sliding motion of the filaments such that they eventually buckle at a critical length scale [107, 129] and fracture into smaller fragments that subsequently recombine with other filaments, starting the sliding-and-buckling process anew, as illustrated in Figure 3.5(C).

In the presence of a liquid-liquid interface, the depletion interaction drives the filaments to the interface between the microtubule solution and the outer phase. As the concentration at the interface increases, the filaments locally align and undergo a transition to the nematic phase [107, 108, 122], as seen in the example fluorescence microscopy image in Figure 3.5(D), where the microtubules are fluorescently labeled such that the fiber direction is readily apparent. Thus, the filament direction provides the director for the 2D active nematic at the interface.

We note that the sliding-and-buckling phenomenology of the active filaments is the physical mechanism behind the extensile active stress in the nematic phase; it is directly responsible for the bend instability and associated defect formation in the microtubule-kinesin active nematics. In the nematic phase, when the filaments buckle and fracture, an $s = \pm 1/2$ defect pair is produced, with the defects nucleating at opposite ends of the fracture line [101, 107], as highlighted by the yellow dashed line in the example image in Figure 3.5(D).

Microtubules, kinesin-streptavidin complexes (K/SA), ATP, a depletant, and an outer liquid phase constitute the essential ingredients for an active nematic. However, there are many more compounds in this active nematic solution that serve to enable measurements [107, 108], prolong activity [107, 108], and allow for the silicone-based

outer phase that we use to make our toroidal droplets [108]. As mentioned earlier and shown in Figure 3.5(D), the microtubules are fluorescently labeled such that the active nematic can be imaged with fluorescence or fluorescence confocal microscopy. To prevent the excitation source from damaging the fluorophores (photobleaching) or killing the kinesin motors (phototoxicity), the active solution contains trolox (Sigma, 238813) and two anti-oxidant solutions. Anti-oxidant solution 1 (AO1) is composed of glucose and dithiothreitol (DTT) and Anti-oxidant solution 2 (AO2) is composed of glucose oxidase (Sigma, 238813) and catalase (Sigma, C40). The active solution also includes an ATP regeneration system to keep the ATP concentration in an active nematic solution constant. This system is driven by the enzyme mixture pyruvate kinase/lactate dehydrogenase (PK/LDH, Sigma, P-0294) which consumes phosphoenol pyruvate (PEP) to convert ADP to ATP at a rate faster than the K/SA hydrolyzes ATP to ADP [130].

We note that when driven to the liquid-liquid interface, the active filaments do not ever contact the outer phase. Instead, the interface is packed with a suitable surfactant such that the active nematic filaments deplete to the polar portion of the surfactant molecule. The surfactant is then moved along the interface by the motion of the active filaments such that the viscosity of the outer oil phase significantly affects the dynamics of the active nematic [108]. For a silicone-based outer fluid, we include the triblock copolymer Pluronic F127 (F127) composed of 2 hydrophilic PEG blocks attached to a central hydrophobic poly(propylene oxide) (PPO) block like PEG-PPO-PEG [131]. Finally, the solution is buffered using a specially designed microtubule buffer (M2B) to keep the enzymes and the motors in their preferred environments [107].

For an experiment, we build the active nematic solution from stock solutions per the recipe in Table 3.1. The stock solutions in their given compositions are **bolded** such that PEP refers to the general compound while **PEP** refers to the

Table 3.1: Stock solutions used to form an active nematic solution. The stock solutions in their given compositions are **bolded**.

M2B	— 80 mM 1,4-piperazinediethanesulphonic (PIPES) buffer [132] + 2 mM MgCl ₂ + 1mM egtazic acid (EGTA), pH 6.8
PEP	— 200 mM in M2B , pH 6.8.
PK/LDH	— Used as purchased.
ATP	— 50 mM in M2B , pH 6.8
DTT	— 0.5 mM in M2B , pH 6.8
trolox	— Used as purchased.
MIX	— 67 mM MgCl ₂ in M2B
PEG	— (20 kDa) 6% w/w in M2B
F127	— 12% w/w in M2B
glucose	— 300 mg/mL in 20 mM K ₂ HPO ₄ + 70 mM KCl (pH 7.2)
glucose oxidase	— 20 mg/mL in 20 mM K ₂ HPO ₄ (pH 7.5)
catalase	— 3.5 mg/mL in 20 mM K ₂ HPO ₄ (pH 7.4)
K/SA	— 0.175 mg/mL K401 + 0.1 mg/mL streptavidin (Invitrogen, S-888) + 12.5 mM imidazole (pH 6.8) + 1 mM MgCl ₂ + 0.75 mM DTT + 12.5 mM ATP in M2B . K401 consists of 401 amino acids of the N-terminal motor domain of <i>D. melanogaster</i> kinesin purified as previously published [107].
MT	— 8 mg/mL tubulin labeled with AlexaFluor 647 at 28% labeling efficiency in M2B . Tubulin was purified as previously published [132].

stock concentration/formulation as defined in Table 3.1 and originally prepared by the Dogic Group at Brandeis. The stock solutions were shipped to Georgia Tech, and we pipetted the stock solutions as received into aliquots suitable to make 100 μL of active nematic solution. The aliquots are stored in a freezer at -80°C to prevent degradation of the active compounds. Prior to each experiment, we remove a set of aliquots from the freezer, quickly thaw the aliquots to room temperature by holding them in our closed hands, and then place all the aliquots on ice except for the **MT** aliquot. We leave the **MT** aliquot out at room temperature so that the tubulin can self-assemble into microtubules. The polymerization of microtubules is temperature-dependent, with tubulin polymerizing to form microtubules at room temperature and microtubules depolymerizing into tubulin at low temperature [107].

We then make the initial mixtures and the pre-solution according to the recipe in Table 3.2, leaving the pre-solution on ice. We wait at least 90 minutes after bringing the **MT** aliquot to room temperature before mixing it with the pre-solution to form the final active nematic solution as specified in Table 3.2. Note that we bring the pre-solution to room temperature before adding in the microtubules such that the microtubules do not depolymerize when they are added to the pre-solution. Once we mix the final solution together, we perform our experiments and observe the active nematic until activity ceases.

3.2.2 Flat sample confirmation

Upon receiving the stock solutions, we first made a bulk active gel according to the procedures published in Ref. [107] to confirm the integrity of the solutions through the shipping process. To make an active gel, we have to construct a sample chamber where the depletion interaction cannot drive the bundles to aggregate on the walls of the chamber. We build the sample chamber from a glass coverslip attached via two-sided tape to a microscope slide to form a rectangular channel, as previously

Table 3.2: Recipe for 100 μL active nematic solution

Initial mixtures	
A01	1.5 μL DTT + 1.5 μL glucose
A02	1.5 μL glucose oxidase + 1.5 μL catalase
ATP2	2 μL ATP in: 18 μL M2B for a 144 μM final ATP concentration. 38 μL M2B for a 36 μM final ATP concentration.
Pre-solution	
2.21 μL	A01
2.21 μL	A02
2.83 μL	ATP2
2.83 μL	PK/LDH
4.83 μL	MIX
10.00 μL	trolox
13.33 μL	PEP
13.33 μL	PEG
16.67 μL	F127
6.67 μL	K/SA
8.40 μL	M2B
Active nematic solution	
83.33 μL	Pre-solution (full volume is 83.33 μL)
16.67 μL	MT

published [107]. Prior to construction, we coat the coverslip and microscope slide with polyacrylamide brushes according to the published protocol [107], reproduced in Appendix A, such that the PEG can penetrate between the brushes, keeping the depletion interaction from driving the active filaments to the glass surface, where they would adsorb [107].

To make the rectangular sample chambers from the polyacrylamide-coated glass, we cut strips of 2-sided tape such that they are ≈ 1 mm wide and longer than the coverslip. We then affix the tape strips to the microscope slide in parallel with ≈ 2 mm between the edges of adjacent strips, and then stick the coverslip onto the tape to create a parallel series of rectangular channels. Finally, we fill the channels with the active solution using capillary action and seal the ends of the channel with epoxy (DEVCON, 5-minute). A schematic of the sample chamber and assembly process is shown in Figure 3.6. The samples are now ready to be imaged using fluorescence or

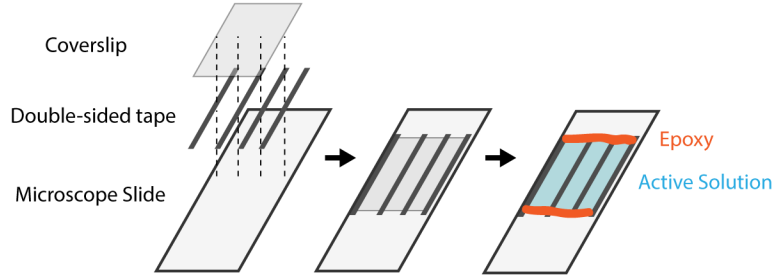


Figure 3.6: Schematic and assembly of a sample chamber for an active gel.

fluorescence confocal microscopy.

We confirmed that the stock solutions received produced an active gel with fluorescent active filaments that underwent the sliding/buckling/fracture/recombination cycles. The activity in the gel sample appeared constant for the entirety of its ≈ 24 hr lifespan. The observed behavior qualitatively agreed with previously published behavior by the Dogic group [107].

3.2.3 Making toroidal droplets

With the integrity of the active solution confirmed, we turn to making stable toroidal droplets with our active solution. We generate our toroidal droplets following the procedure detailed in Refs. [38, 133, 134]. The setup consists of a rotating stage holding a cuvette containing the continuous, or outer phase, and a syringe holding the dispersed, or inner phase connected to a needle inserted into the cuvette. We control the angular velocity of the rotation, ω , by driving the rotating stage with a motor powered by a constant voltage source. We control the position of the needle in the cuvette with a micromanipulator, and the flow rate and volume of the inner phase with a syringe pump. In addition, we place a camera below the rotation stage such that we can image the droplet generation process.

This setup is depicted schematically in Figure 3.7(A). We insert the needle into the cuvette offset from the center of rotation such that pumping the inner phase into the cuvette while the cuvette is rotating will generate a curved jet, as shown in the

example image in Figure 3.7(B). Provided that we rotate fast enough such that the curved jet closes upon itself before it undergoes breakup, we form a toroidal droplet, as shown in the example image in Figure 3.7(C). This condition is a balance of two timescales: (i) the timescale required to undergo breakup, $t_b \approx \mu_o a_{jet} f(\mu_i/\mu_o)/\gamma$, where μ_o is the viscosity of the outer phase, μ_i is the viscosity of the inner phase, a_{jet} is the radius of the jet, $f(\mu_i/\mu_o)$ a function that depends on the viscosity contrast, and γ is the interfacial tension between the inner and outer phases; and (ii), the timescale required to close the curved jet onto itself, $T = 2\pi/\omega = 2\pi R_{tip}/U$, where R_{tip} is distance from the center of rotation to the needle, as depicted in Figure 3.7(C), and U is the linear velocity of the continuous phase at the needle.

Equating the two timescales and rearranging terms allows us to express this condition as: $\text{Ca}_o > (2\pi/f(\mu_i/\mu_o))R_{tip}/a_{jet}$, where $\text{Ca}_o = \mu_o U / \gamma$ is a dimensionless group called the Capillary number quantifying the relative importance of the viscous stresses and the stresses due to surface tension. We note that $a_{jet} \approx a_{tip}$, the radius of the needle. A jet will thus form at sufficiently high U for given inner and outer materials. To control the size and aspect ratio of the toroidal droplet, we tune R_0 by changing R_{tip} while tuning a through the total injected volume.

Toroidal droplets generated in this way are unstable due to surface tension, which acts to minimize the interfacial area between two immiscible fluid phases; since the sphere minimizes the surface area for a given volume, spherical droplets are stable [47]. The surface tension causes a pressure jump, ΔP , across a fluid-fluid interface. This pressure jump is known as the Laplace pressure [47]:

$$\Delta P = P_i - P_o = 2\gamma(-H), \quad (3.8)$$

where P_i is the pressure in the inner fluid phase, P_o is the pressure in the outer fluid phase, and H is the mean curvature of the interface. Recall that $H = \text{tr}\{\mathbf{L}\}/2$, where

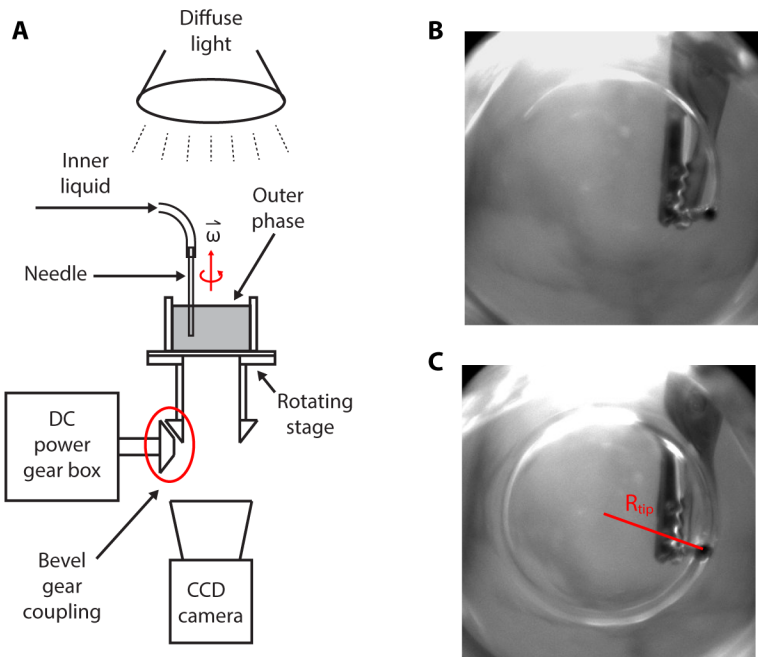


Figure 3.7: Making toroidal droplets. (A) Schematic of the apparatus used to make toroidal droplets. The inner fluid is injected into a cuvette on a rotating stage. The stage is driven by a DC motor and the entire process is imaged from below with a CCD camera. (B) A curved jet pulled from the needle by the viscous drag of the rotating bath. (C) A toroidal droplet formed when the curved jet in (B) closed upon itself. R_{tip} is the distance from the needle to the center of rotation.

\mathbf{L} is the Weingarten Matrix from Eq. 2.51 defined such that the mean curvature of a sphere with radius r choosing an outward-facing normal is $H = -1/r$ everywhere on the surface of the sphere.

The Laplace pressure tells us that not only does a spherical droplet have greater pressure on the inside than on the outside, but also that due to its constant mean curvature, the pressure inside the droplet is constant. Thus, there is no flow inside a spherical droplet. This is similar to a cylindrical thread with radius r , where $H = -1/(2r)$ everywhere on the surface such that there is no flow inside a cylindrical structure. However, the interface is always fluctuating, creating pressure fluctuations that induce flow. A spherical surface is stable with respect to the fluctuations; in contrast, a cylindrical thread is unstable, and the induced flow drives the cylindrical thread to break up into spherical droplets. This instability is known as the Rayleigh-Plateau instability. Toroidal droplets also break up via a similar instability, with the tube of the toroidal droplet breaking into spherical droplets [133, 135].

However, toroidal droplets can also transform to a spherical droplet via another instability. For a torus, H varies along the surface, causing the pressure inside the torus to also vary. This inhomogeneous pressure induces flow that causes the “hole” to shrink continuously until it closes onto itself, resulting in the formation of a single spherical droplet [133, 136]. This instability is thus known as the shrinking instability, and is unique to toroidal droplets. While the study of the fluid modes in nontrivial topologies is interesting in its own right and has led to insights into fluid phenomena such as charged jets [135] and viscous fingering [137], here we are interested in preventing the growth of these instabilities and generating stable toroidal droplets.

To achieve this, we need to counter the stress due to surface tension responsible for destabilizing a toroidal droplet. We do this by using a yield stress material as the outer phase instead of a pure viscous liquid [38, 138]. Yield stress materials have a threshold stress, τ_c , such that they respond like elastic solids to imposed stresses

$\tau < \tau_c$, and flow like viscous liquids for $\tau > \tau_c$. Provided that τ_c is greater than the stress due to surface tension, the toroidal droplet will be unable to transform into one or more spherical droplets and will be indefinitely stable.

Since the stress due to surface tension is given by the Laplace pressure, we see that balancing the Laplace pressure and τ_c will give us a critical radius of curvature, R_c , determining the stability of a toroidal drop, $\gamma/\tau_c \sim R_c$. If the smallest radius of curvature on a toroidal drop is larger than R_c , the toroidal droplet will be stable — usually, the smallest radius of curvature on a torus is the tube radius. However, for toroids with $\xi \lesssim 2$, the radius of the “hole” becomes the smallest radius of curvature in the droplet and thus will determine the stability of the toroidal droplet. As the active nematic solution is aqueous, we use an oil-based yield stress material, DC-9041 (Dow Corning), a silicone elastomer. To tune the yield stress, we dilute pure DC-9041 with 10 cSt PDMS oil (Clearco). We dilute to 74% – 77% w/w DC-9041 to form stable active nematic toroids with tube radii between 150 μm and 300 μm , and “hole” radii between 150 μm and 1 mm.

Making a toroidal droplet in a yield stress material has some key differences to making a toroidal droplet in a viscous fluid. Notably, the yield stress material is only fluid-like in regions where the stress is greater than τ_c . Thus, for best results, we need to pre-shear the yield stress medium such that the greatest possible volume of yield stress material is fluidized. We do this by letting the cuvette rotate with the needle inserted for up to 30 s before we begin pumping the inner liquid into the cuvette. While a pre-shear is not strictly necessary to form a toroidal droplet, the cross-section of the tube of a toroidal droplet made with a pre-shear is generally more circular than that of a toroidal droplet made with minimal pre-shear. This is because the wider the volume of fluidized yield stress material, the less the pumped volume “climbs” up the needle. We also find that making toroidal droplets close to the free-surface of the yield stress material helps to mitigate climbing, as the free

surface provides a natural limit to the height of the droplet.

For most experiments with toroidal droplet, there is a large amount of the inner phase available and we simply fill a syringe with the inner phase. However, for the active experiments, we have only 100 μL of active solution per experiment, which is not enough to even fill the Luer-lock syringe tips we use to connect a syringe to the tubing. Instead, we fill the system primarily with paraffin oil (Lamplight) as a dummy fluid and load the active solution only into the tubing connecting the syringe tip and the needle. Thus, we use a length of tubing such that the volume of the fluid in the tubing is greater than 100 μL .

We start by pumping the dummy fluid to fill the entire tubing; this removes all the air from the system. We then submerge the free end of the tubing into the vial containing the active solution and withdraw the dummy fluid. As we withdraw the dummy fluid, the active solution is pulled into the tubing. We ensure that the interface between the dummy liquid and the active solution has no air bubbles. Air bubbles in the tubing will inhibit forming high-quality toroidal droplets as the air bubble acts as a “spring” in the fluid system. This introduces a significant time lag between the start and stop of the syringe pump and the beginning and end of the fluid flow from the needle, hampering our ability to control the flow precisely. In addition, it is important to withdraw the dummy fluid slowly ($\approx 1 \text{ mL/s}$) when loading the active nematic solution to prevent forming an emulsion between the active fluid and the dummy fluid in the tube.

3.3 Imaging active nematic toroids

Once the active nematic toroidal droplet is made, we let the droplet rest for 2 – 4 hours to ensure the depletion interaction has driven most of the filaments to the surface of the toroidal droplet. We now consider the nematic to be fully formed, as the concentration of the filaments on the surface of the droplet is at its maximum.

We then image the droplet via fluorescence confocal microscopy (Nikon A1R or Zeiss LSM 700) until the activity ceases. This typically occurs between 6 – 10 hours after making the toroidal droplet.

3.3.1 Confocal fluorescence microscopy

Fluorescence is an inelastic process where a material absorbs and then re-emits light; the initial absorption excites a singlet state in the material which then decays via photon emission. The absorption and emission are characterized by their respective spectra, with the peak in the emission spectrum occurring at a longer wavelength than the peak in the absorption spectrum.

Unlike traditional wide-field microscopy, confocal microscopy allows us to image individual planes in the image such that we can construct a 3D representation of the sample [139]. In confocal microscopy, a screen with an aperture is placed in front of the detector at an optically conjugate plane to the focal plane in the sample. Since light from the focal plane is in focus at optically conjugate planes, we say that the plane is confocal; this is depicted in Figure 3.8(A) [140]. However, since the majority of the confocal plane is blocked by a screen, only light from the confocal point to the aperture will pass through the aperture. This is depicted in Figure 3.8(A), where only the red light from the confocal point passes completely through the aperture; the majority of the light from the nonconjugate blue and green points is blocked by the screen. The location of the focal plane in the sample is changed by translating the microscope stage up and down. The location of the confocal point in the sample is changed by either translating the sample (scanning confocal microscopy) or by using mirrors to raster the confocal point across the confocal plane (scanning laser confocal microscopy) [139, 141, 142]. Either of these methods allows the experimenter to build up a full 3D representation of the sample.

Both of the microscopes we use are scanning laser confocal microscopes. In scan-

ning laser confocal microscopy, the illumination source is a laser and the illumination is epifluorescent. This means that the laser beam illuminates the sample through the objective, with the objective then focusing the laser onto the confocal point in the sample. The illuminated confocal point in the sample then fluoresces and the output intensity is recorded. This process is enabled with a dichroic mirror that reflects light with a wavelength $\lambda < \lambda_c$ and transmits light with $\lambda > \lambda_c$. The mirror allows the excitation and emission light to share the same path to and from the confocal point. As depicted in Figure 3.8(B), the excitation light passes through a confocal aperture, is reflected by the mirror, passes through the objective, and is focused onto the confocal point in the sample. The emitted light then travels the same path back through the objective, passes through the mirror, passes through a confocal aperture, and is incident on the detector. In addition, there is often a second filter placed between the dichroic mirror and the detector to further prevent the excitation light from reaching the detector. Since the excitation and emitted light share the same path, a single set of mirrors placed between the mirror and the objective scans the confocal point for both the emitted and excited light across the sample [139].

Like any form of optical microscopy, the limiting resolution in the focal plane is set by the diffraction limit; the light from the objective is not focused to a point but instead forms a circular diffraction pattern. The first minimum of this pattern has a diameter [143]:

$$d \approx 1.22\lambda/\text{NA}, \quad (3.9)$$

where $\text{NA} = n \sin \theta$ is the numerical aperture of the objective, with n the index of refraction of the ambient medium and θ the half-angle of the cone of light focused by the objective. d is known as the diameter of the Airy disc. Generally, two point sources can be distinguished if the maximum of the diffraction pattern from one point falls on the first minimum of the pattern from the second point. This is known as the Rayleigh criterion; Eq. 3.9 thus also gives the resolution as $d/2$ for an objective

with a given NA [143]. This criterion also then imposes a lower limit on the size of the confocal aperture, as an aperture smaller than d doesn't increase the resolution, it just decreases the amount of light incident on the detector.

In practice, the resolution in an experiment is instead generally set by the pixel size on the detector. The distance between the detector and the confocal aperture can be varied to “zoom” in and out without changing the objective magnification; zooming in corresponds to a smaller area in the sample illuminating the full detector, whole zooming out does the opposite. The system reaches the fundamental resolution limit when the pixel length is $d/4$, corresponding to the Nyquist criterion; however, this means that the total sample area imaged is small. Typically, we choose a pixel length around d , sacrificing resolution but increasing the area of the sample we image. For example, on the Nikon microscope, we use a 10x objective with NA = 0.3 and thus $d \approx 2.8 \text{ } \mu\text{m}$ for the emission light with wavelength $\lambda = 700 \text{ } \mu\text{m}$. The majority of our data are taken with a pixel length $2.5 \text{ } \mu\text{m}/\text{px}$; for our typical image size of $512 \text{ px} \times 512 \text{ px}$, this corresponds to a scan area of $1.28 \text{ mm} \times 1.28 \text{ mm} = 1.64 \text{ mm}^2$. In this case, the resolution is set by the pixel length and not the diffraction limit of the imaging system.

In a confocal microscope, we also have to consider the axial resolution, or the ability to distinguish between points on the focal plane and points above and below the focal planes. Alternately, this can be thought of as the thickness of an optical section. In our experiments, we never set the diameter of the confocal aperture smaller than the Airy disc. In this regime, the resolution is determined by the full-width half-maximum (FWHM) of the intensity distribution in the axial direction [144]:

$$\text{FWHM}_{\text{axial}} \approx \frac{\sqrt{2}nb}{\text{NA}}, \quad (3.10)$$

where b is the diameter of the aperture. If we take the diameter of the aperture to be

the diameter of the Airy disc, we see that $\text{FWHM}_{\text{axial}} \sim \text{NA}^{-2}$; the axial resolution is more sensitive to the numerical aperture than the resolution in the focal plane. For example, in our experiments with $\text{NA} = 0.3$ and a typical pinhole diameter of $2.5 \mu\text{m}$, $\text{FWHM}_{\text{axial}} \approx 11.8 \mu\text{m}$. To fully realize this resolution, we take data at heights separated by $\text{FWHM}_{\text{axial}}/2$, satisfying the Nyquist criterion.

In fluorescence microscopy, we have to worry about the excitation light damaging fluorophores and rendering them unable to fluoresce, also known as photobleaching. Photobleaching of a single fluorophore can be modeled by a statistical process, with a constant probability of photobleaching for absorption-emission cycle. Thus, since the laser only illuminates the portion of the sample that is being imaged, photobleaching is less of a concern in scanning laser fluorescence microscopy than it is in widefield fluorescence microscopy, where the entire sample is always illuminated. However, even in scanning laser confocal microscopy, a high enough laser intensity or a long enough imaging time will always result in significant photobleaching in the sample.

In our experiments, only the microtubules are labeled with fluorophores, such that we only image the active filaments. Thus, as shown in the example image in Figure 3.8(C), where the height is denoted by false color, we can acquire a 3D image stack showing only the active nematic depleted to the toroidal surface.

3.3.2 Confocal setup and parameters

We used two different confocal microscopes to collect the data; we started with a Zeiss LSM 700 and then switched to a newer Nikon A1R when the latter was purchased by Professor Peter Yunker in the School of Physics. Both instruments are scanning laser confocal microscopes. Procedurally, both microscopes scan the image plane with a focused laser beam while recording the output intensity, adjust the height of the stage to change the focal plane, and then repeat the process until the image stack is acquired. While the image stack can be thought of in terms of 3D voxels, the

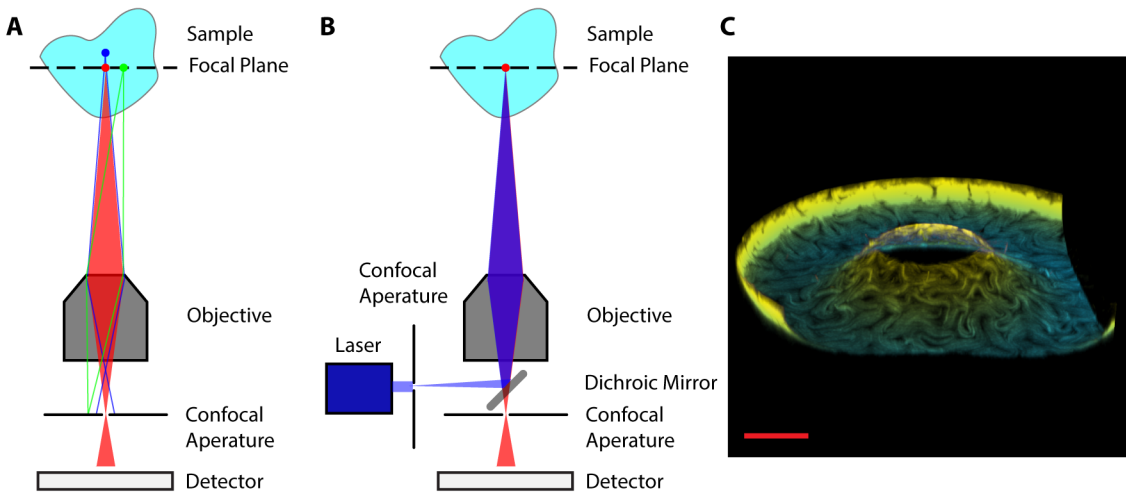


Figure 3.8: Confocal microscopy. (A) Schematic showing the effect of the confocal aperture in front of the detector. Light from the red point is in focus at the aperture in the confocal plane, and thus can pass entirely through the aperture. In contrast, the blue light is emitted above the focal plane; the light is out of focus at the confocal plane and does not pass through the aperture. Similarly, the green light is in focus at the confocal plane, but it is not emitted from a conjugate point to the aperture and thus does not pass through the aperture. (B), Schematic of laser confocal fluorescence microscopy. There is a confocal aperture in front of the laser such that the laser is focused by the objective onto the focal plane in the sample. Thus, the maximum excitation will be at the conjugate point in the focal plane. As in (A), only the emitted light from the conjugate point in the focal plane is incident on the detector. A dichroic mirror allows the excited and emitted light to share the same path to and from the sample, but passes only the emitted light to the detector. Scanning mirrors (not drawn) between the dichroic mirror and the objective raster the conjugate point over the focal plane to construct a full image of the focal plane. (C) An example image stack of an active nematic torus, where the image stack has been reoriented to provide perspective and the data have been false-colored by height. This image stack was taken with a typical set of parameters: total size, $1.28 \text{ mm} \times 1.28 \text{ mm} \times 0.21 \text{ mm}$, pixel size, $2.5 \mu\text{m}/\text{px} \times 2.5 \mu\text{m}/\text{px} \times 7 \mu\text{m}/\text{px}$. The scale bar is $250 \mu\text{m}$.

z -resolution between focal planes is less than the xy -resolution in the focal plane such that it is more convenient to think of the image acquisition as a stack of 2D images.

We note that we are inherently restricted to only imaging the lower half of the toroidal droplet due to refraction effects. The light emitted from the upper half of the toroidal droplet travels through the aqueous active solution and then is refracted by the curved interface between the active solution and the yield stress material. In contrast, the light from the lower portion of the toroid is emitted directly into the yield stress material such that its light path is unaffected by refraction. However, even though we can in principle image up to the midpoint of the torus, in practice we typically stop our image stack below the midpoint. This is because the time required to adjust the stage height is the slowest portion of the imaging process for both of the confocal microscopes we use. Since we wish to acquire as many frames as possible for each toroid, we must balance the time required to take an image stack versus the size of the image stack.

The microtubules are dyed with AlexaFluor 647, which has an excitation peak at 651 nm and an emission peak at 667 nm [145], as displayed in Figure 3.9(A). Thus, we use a 633 nm laser as our illumination source and a Cy5 filter set such that only the emitted light reaches the detector. The Cy5 filter set includes a 590 – 650 nm bandpass excitation filter, a 660 nm longpass dichroic mirror, and a 663 – 738 nm emission filter [146]. The filters and mirror are designed with steep passband transitions such that the quoted ranges are good representations of the passband. Note that for illumination with a laser, the excitation filter is unnecessary, but is standard when purchasing the filterset. The excitation filter is necessary in wide-field fluorescence microscopy when illuminating with a white-light source.

While the two confocal microscopes we used operate in the same manner, there are key differences that affect the quality of the data and thus affect the measurement protocol. The Zeiss microscope uses standard photomultiplier tubes (PMT) as the

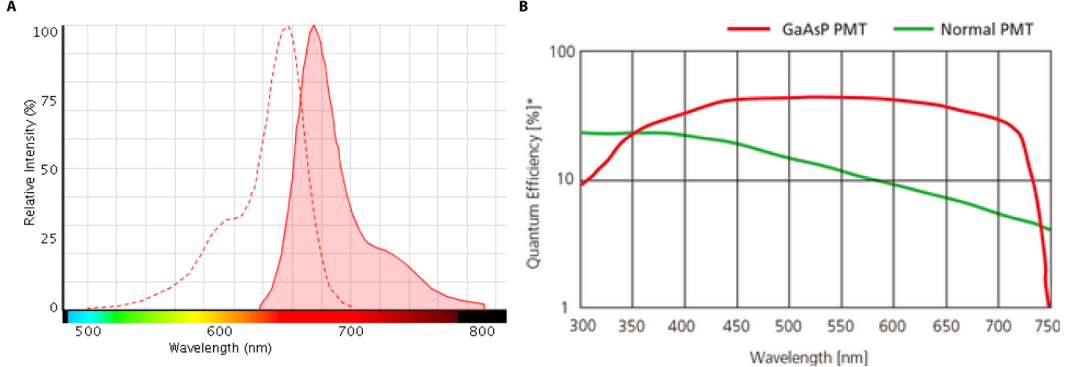


Figure 3.9: Fluorophore spectra and detector quantum efficiencies for our experimental system. (A), AlexaFluor 647 (red dashed line) excitation and (shaded red area) emission spectra. Spectra from Ref. [145]. (B), Quantum efficiency as a function of wavelength for a (green line) standard PMT and a (red line) GaAsP PMT as a function of wavelength. Plot from Ref. [146].

detector. Unfortunately, standard PMTs do not detect wavelengths above 600 nm well, as the quantum efficiency of the detector decreases with increasing wavelength and is typically below 10% above that wavelength [green line, Figure 3.9(B)] [146]. This means that we have to increase the intensity of the laser, increase the gain on the detector, and even average two scans of each image plane in order to increase the signal-to-noise ratio to an acceptable level. As a result, data from the Zeiss microscope take longer to collect and the active nematic exhibits mild photobleaching for long acquisitions. However, we note that the photobleaching is mild and does not decrease the signal-to-noise ratio enough to affect our data analysis.

In contrast, the Nikon microscope uses a Gallium Arsenide Phosphide (GaAsP) PMT in conjunction with standard PMTs to increase the quantum efficiency of the detector suite for larger wavelengths. GaAsP PMTs maintain a roughly constant quantum efficiency of $\approx 50\%$ up to 700 nm [red line, Figure 3.9(B)] [146]. Thus, we can keep both the laser power and detector gain low while still only needing a single scan of the image plane to acquire a higher quality image stack than we get from the Zeiss microscope. We therefore can acquire image stacks with a higher time

resolution, a higher image quality, and with no noticeable photobleaching when using the Nikon microscope.

We set up a measurement as follows. First, we place the sample on the microscope stage and find the toroidal droplet using standard brightfield microscopy. We then select the 633 nm laser and Cy5 filter set from the available options on the microscope. Next, we set the microscopes to scan the focal plane and display the output in real time. We lower the stage to find the bottom of the sample, set this height to be the bottom of the image stack, and then raise the stage to determine the highest plane that we will measure. As a rule of thumb we aim for 15 – 30 image planes, depending on the microscope used to acquire the data. If we image too few planes, we don't image the highly curved areas of the droplet. If we image too many planes, we don't acquire enough frames over the life of the active nematic. Each 512 px \times 512 px image plane typically takes 0.8 s to acquire, and it takes about 1 s to move between planes. Overall, this means that a full image stack takes between 30 s and 1 min to acquire.

Now that we have set up the size of the image stack, we turn to adjusting the laser intensity and gain to produce the highest quality images. The laser intensity incident on the sample is tuned by an acousto-optical tunable filter (AOTF) placed at the output of the laser, and before the laser enters the confocal microscope. An AOTF is a tunable diffraction grating, where the grating is formed by standing acoustic waves that create a periodic index of refraction. By changing the frequency of the acoustic waves, the AOTF will diffract more or less light into the confocal microscope [147]. The gain in the detector corresponds to the voltage applied across the dynodes in the photomultiplier tubes [148]. This is controlled in the imaging software by a slider from 1 to 255, with 1 corresponding to the minimum operating voltage and 255 the maximum operating voltage. We first find the image plane with the brightest intensity, and manipulate the intensity and gain such that at most $\approx 5\%$ of the pixels

are saturated. While a higher laser power and lower gain will produce better quality images, setting the laser power too high can lead to excessive photobleaching for long time measurements. We typically set the laser power to approximately 3% of the maximum 15 mW output. With this laser power, we need a gain roughly halfway between the minimum and maximum values. If we are on the Zeiss microscope, we set the microscope to scan each image plane twice and average the measurements such that we can reduce the overall laser power and minimize photobleaching.

For both microscopes, we then go to the bottom plane where the emitted intensity is weakest and set an offset corresponding to an intensity floor for the measurement. Pixels with an intensity below the offset are set to 0. This helps to remove some of the thermal noise in the image; in practice, we have enough signal that this parameter does not really matter.

Once these parameters have been set, we turn on a focusing system to eliminate the effect of thermal and mechanical drift in the measuring system. Ambient temperature changes and mechanical slop in the measuring system cause the measured distance between the objective and a given reference plane in the sample to change over time. This will result in the physical sample volume imaged by the confocal changing over time. The focusing system uses a lens and an LED to form an image of the interface between the coverslip or microscope slide and the sample. Turning on the focusing system corresponds to the software adjusting the lens to form the image of this interface without changing the current height of the microscope stage. The software then maintains this image of the interface by adjusting the height of the microscope stage, naturally compensating for thermal drift and mechanical slop. By maintaining this image of the interface, the focusing system naturally maintains the focal plane of the confocal microscope in the sample.

Finally, we set the microscope to image continuously for 12 hours, starting the next image stack as soon as it finishes the previous stack until the 12 hours have

expired. We note that files imaged for longer than 12 hours can be difficult to work with due to their large size. Once the image acquisition is finished, we crop the raw confocal time series to only include the portion where the toroidal droplet is active. We save this cropped version in single multi-page `.tiff` file including the metadata containing acquisition parameters. This standardizes the data format between the different microscopes to make it easier to read in to the computer.

3.3.3 Inputting confocal data into MATLAB

The core routine to load the image stack into MATLAB comes from the `bioformats` toolbox put out by the Open Microscopy Environment [149]. The Open Microscopy Environment maintains the open-source `OME-TIFF` image format for microscopy data. The `bioformats` toolbox allows us to call the imaging parameters such as pixel-to-length conversions, framerate, etc., as well as access the total times series of image stacks as a 3D array in MATLAB. The data are stored as a stack of 2D arrays, where each array holds data from a measurement of a confocal plane at a moment in time. The 2D arrays are stored in the order that they were taken; this corresponds to concatenating the full 3D image stacks along the z direction in the order the individual stacks were taken. Thus, to locate a specific 3D image stack you have to know which stack in the time series you want as well as the number of planes in each image stack. Since the entire image series from the confocal can be up to 8 Gb, we first extract the relevant data and then remove the image series from memory so that we have the free memory needed to analyze the data.

We first determine the surface of the toroidal droplet by averaging the image planes at a given height over time and then applying an intensity threshold. Since we have fluorescence confocal data where the fluorescent media has depleted to the surface of the torus, averaging over time creates a clear intensity image of the toroidal surface as both transient structures in the bulk as well as the filamentary structures of the

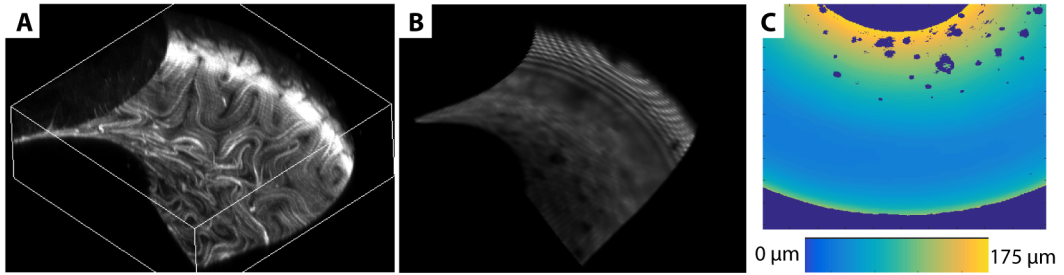


Figure 3.10: Determining the surface of a toroid from confocal microscopy data. (A) Example confocal image stack at a moment in time. (B) The average over time of all the image stacks. Here, the averaging washes out stray filaments in the bulk as well as the nematic structure of the filaments, as seen in (A), giving us an intensity image of the surface itself. (C) The height of the surface $h(x, y)$, where h is determined by thresholding (B) and then averaging the height of the bright pixels in the thresholded image stack for every (x, y) position.

active nematic are washed out in the averaging process, as seen in the example images in Figure 3.10(A,B). We next threshold the data to binarize the image stack; this lets us make the distinction between the surface of the toroidal droplet and everything else. There are a large range of threshold values that do not change the shape of the surface or affect the final curvature values; we choose the smallest threshold value that produces a smooth surface with no extraneous bright pixels that are not on the surface.

From the binarized 3D array, we look at every xy position and determine the lowest z value that contains a nonzero value. We take this z value to be the height h of the toroidal surface and record it in an array, giving us $h = f(x, y)$, as shown in Figure 3.10(C) for the example image in Figure 3.10(B). This is commonly known as a Monge parameterization of the surface [19].

We next consider the intensity stack for each time point and perform a maximum intensity projection into the xy -plane with the caveat that we only consider pixels that are within ± 5 z-stack planes of the height at each individual point. This process largely prevents transient bright filaments in the bulk of the toroidal droplet from affecting our measurements. Thus, we now have recorded our surface and reduced

our data from a time-series of 3D image stacks to a time-series of 2D images such that we have the intensity $I = f(x, y, t)$. An example projection at an instant in time for the image stack in Figure 3.10(A) is shown in Figure 3.11(A). Once we have extracted the time-series of data on the surface, we work to: (i) determine the director and defects from the intensity projections, and (ii) calculate the surface curvature and surface normals using $h(x, y)$.

3.4 Determining director and defects

In the intensity projection of a confocal stack at a time t_0 , \mathbf{n} is given by the direction of the microtubule bundles. This direction is obtained from the grayscale image by finding the direction along which the intensity fluctuates the least for each pixel using a technique called coherence-enhanced diffusion filtering (CEDF) [150]. CEDF is used extensively in computer vision and in cell segmentation in biology, but it has not yet been used in the Physics literature [151]. We illustrate this technique with an example analysis of the intensity projection shown in Figure 3.11(A).

3.4.1 Coherence-enhanced diffusion filtering

To begin with, the original intensity image $I = I(x, y, t_0)$ is denoised using a Gaussian blur of standard deviation σ and side length $6\sigma - 1$ to lessen contributions to the intensity fluctuations from random noise, giving us the blurred image I_σ . The result of blurring the example image as well as the inset isolated defect pair in Figure 3.11(A) is seen in the main image and inset of Figure 3.11(B), respectively. This blur was performed using a $5 \text{ px} \times 5 \text{ px}$ Gaussian filter with $\sigma = 1 \text{ px}$.

Next, the gradient tensor for I_σ is calculated for each pixel:

$$(\nabla I_\sigma)(\nabla I_\sigma)^T = \begin{bmatrix} (\nabla_x I_\sigma)(\nabla_x I_\sigma) & (\nabla_x I_\sigma)(\nabla_y I_\sigma) \\ (\nabla_y I_\sigma)(\nabla_x I_\sigma) & (\nabla_y I_\sigma)(\nabla_y I_\sigma) \end{bmatrix}. \quad (3.11)$$

Since the microtubule bundles have head-tail symmetry, we cannot use the gradient vector alone to define the bundle orientation as the vector has a defined head and tail. The rank-2 gradient tensor is symmetric and is the same whether it is constructed with the gradient vector or the negative gradient vector. Thus, we use the gradient tensor to “remove the head” from the gradient vector.

We now define the coherence direction of a symmetric rank-2 tensor as the direction of the eigenvector associated with the smallest eigenvalue. Recall that according to the Spectral theorem, any symmetric real matrix is diagonalizable, with the diagonal elements the eigenvalues of the matrix and the associated orthonormal basis formed by the eigenvectors. The coherence direction represents the direction along which the spatial intensity fluctuations are the weakest and is defined on the interval $[0^\circ, 180^\circ]$. The coherence direction calculated for the gradient tensor of each pixel for I_σ shown in the main image and inset of Figure 3.11(B) is seen in the main image and inset of Figure 3.11(C), where the orientation of the coherence direction on the interval $[0^\circ, 180^\circ)$ measured clockwise (CW) off of the horizontal axis has been mapped to the grayscale intensity values $[0, 255]$, with 0 corresponding to black and 255 to white. We see that there are still too many fluctuations in the coherence directions shown in Figure 3.11(C) to determine \mathbf{n} .

We remove the remaining small-scale fluctuations in this image by performing another average, this time a component-wise average of the gradient tensor for each pixel. This operation gives us the structure tensor for each pixel and can be written as:

$$K_\rho * (\nabla I_\sigma)(\nabla I_\sigma)^T = \begin{bmatrix} K_\rho * (\nabla_x I_\sigma)(\nabla_x I_\sigma) & K_\rho * (\nabla_x I_\sigma)(\nabla_y I_\sigma) \\ K_\rho * (\nabla_y I_\sigma)(\nabla_x I_\sigma) & K_\rho * (\nabla_y I_\sigma)(\nabla_y I_\sigma) \end{bmatrix}, \quad (3.12)$$

where K_ρ is a Gaussian filter with standard deviation ρ , where ρ should be about the size of the relevant coherence feature in the image, and $*$ is a convolution. If ρ is too

small, the coherence directions of the structure tensor will resemble those from the gradient tensor, while if ρ is too large the desired coherence features will be washed out by the averaging.

The coherence direction of the structure tensor calculated with $\rho = 5$ px and filter size 29 px \times 29 px for each pixel of I_σ seen in the main image and inset of Figure 3.11(B), is shown in the main image and inset in Figure 3.11(D), respectively. As before, the orientation on the interval $[0^\circ, 180^\circ)$ measured CW off of the horizontal axis has been mapped to the grayscale intensity values $[0, 255]$. We note that the coherence direction of the structure tensor for each pixel represents the local director and corresponds to the “molecular director,” \mathbf{u} .

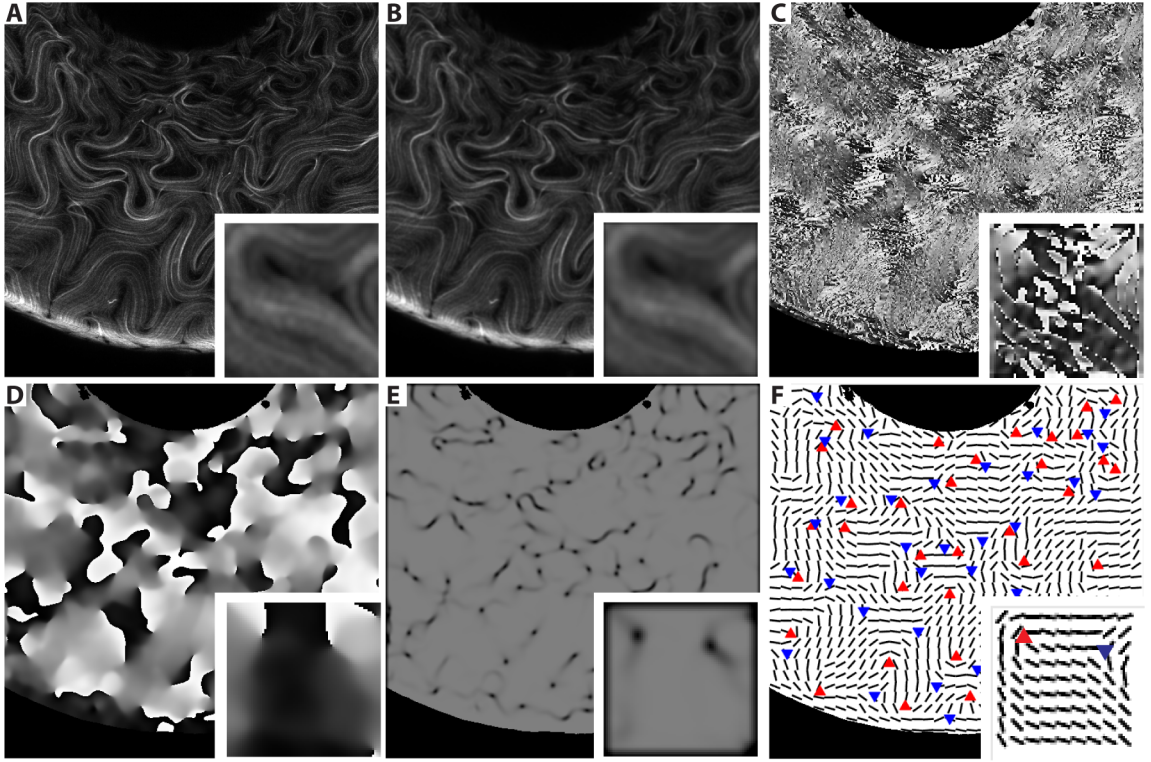


Figure 3.11: Step-by-step output to find the director and defects from an active nematic image. (A), Maximum-intensity projection of a confocal stack onto the xy plane for a single frame. Inset: Close up of a defect pair. (B), Image from (A) after applying a $5 \text{ px} \times 5 \text{ px}$ Gaussian blur with standard deviation 1 px. Inset: The same operation applied to the image in the inset of (A). (C), Coherence directions of the tensors formed from the gradient of the image in (B). Black represents 0° and white represents 180° measured CW from the horizontal. Inset: The same operation applied to the image in the inset of (B). (D), Coherence directions of the structure tensors formed by component-wise averaging the gradient tensors formed from image (B). Black represents 0° and white represents 180° measured CW from the horizontal. The averaging is done with a $29 \text{ px} \times 29 \text{ px}$ Gaussian filter with standard deviation 5 px. Inset: The same operation applied to the image in the inset of (B). (E), The scalar order parameter S obtained by diagonalizing the \mathbf{Q} formed from the directions in image (D). \mathbf{Q} is formed for each point by considering the directions of all points in a 5 pixel radius. Inset: The same operation applied to the image in the inset of (D). (F), The director obtained by diagonalizing the \mathbf{Q} formed from the directions in image (D). \mathbf{Q} is formed for each point by considering the directions of all points in a 5 pixel radius. The defects are calculated by considering points of low S and calculating the \mathbf{n} -rotation along a path encircling the point. $s = +1/2$ defects are represented by \blacktriangle and $s = -1/2$ defects are represented by \blacktriangledown . Inset: The same operation applied to the image in the inset of (D).

3.4.2 Calculating the director

From \mathbf{u} , we compute the 2D tensor nematic order parameter defined in Eq. 2.1, taking the average over the \mathbf{u} of all points within a specified radius β of the point of interest. We perform this averaging using a mean filter of radius β . We then diagonalize \mathbf{Q} as shown in Eq. 2.4, providing \mathbf{n} and S for each pixel. For the orientations of \mathbf{u} that are displayed in Figure 3.11(D), we choose $\beta = 5$ px to produce S and n as shown in Figure 3.11(E,F), respectively. We map the values $S = [0, 1]$ in Figure 3.11(E) to the grayscale intensity values $[0, 127]$ such that black represents $S = 0$ and the lightest gray represents $S = 1$. Thus, the dominant gray shade in Figure 3.11(E) indicates uniform alignment within the 5 px radius. We chose this map so that we can display S on top of either a white background or a black background. In addition, note that only every 7th value of \mathbf{n} is plotted in Figure 3.11(F) to ensure the \mathbf{n} -field is clear to the eye. In reality there is a value for \mathbf{n} at every pixel.

The process of determining the director relies on the choice of three parameters: σ , the standard deviation of the filter for the initial blur, ρ , the standard deviation of the filter to produce the structure tensor, and β , the radius of the disc filter used to determine \mathbf{Q} . We choose the parameters such that the director field calculated on a random sampling of 3 – 5 intensity images in a given time series best agrees by eye with the actual intensity images. We find best results keeping $\sigma = 0.5$ px and varying ρ between 5 px and 8 px and varying β between 5 px and 6 px. The variations in ρ and β are a result of different scales between pixels and μm depending on the microscope used, the microscope zoom, and the output image size. However, since the initial blur is responsible for removing random noise at the pixel level, we find best results keeping $\sigma = 0.5$ px always. Once we determine \mathbf{n} and S , we are ready to find the defects.

3.4.3 Finding defect location and topological charge

We mentioned in Chapter 1 that defects are singularities in the director field; in addition, $S \ll 1$ at a defect. Therefore, we start by selecting pixels with $S < 0.1$ as potential defect candidates. For every candidate, we first consider all pixels in a $5 \text{ px} \times 5 \text{ px}$ plaquette centered on the point of interest and ensure that there are no other candidates in the plaquette with a lower value of S . We then calculate the **n**-rotation about the point of interest according to Eq. 2.7. Explicitly, we numerically evaluate $s = (1/2\pi) \oint \frac{\partial\phi}{\partial u} du$ counterclockwise (CCW) along the edge of the plaquette, where u is the arclength along the square contour and ϕ is the orientation of **n**. We take the point of interest to be a $s = \pm 1/2$ defect if $s \in \pm[0.49, 0.51]$. The $s = \pm 1/2$ defects calculated for our example analysis are plotted on top of the **n**-field in Figure 3.11(F), with $s = +1/2$ defects indicated by \blacktriangle and $s = -1/2$ defects indicated by \blacktriangledown .

We store the defect locations in a list recording the frame and position of each defect. The $s = +1/2$ and $s = -1/2$ defects are stored separately. For toroids made with 36 μM ATP, our time resolution is high enough to track the defects. We track $s = +1/2$ and $s = -1/2$ defects independently using a combinatorics-based particle tracking algorithm [152, 153]. For tracked defects, we store the defect identity in addition to the frame and position so that we can reconstruct individual defect trajectories.

3.4.4 Measuring defect charge in a specified region

Once we have identified all the defects in every frame, we want to be able to look at a specific region on the torus and determine the topological charge in that region over time. We do this by placing the defect locations at each time frame into a binary array, or mask, where a “1” indicates a defect and the rest of the array is set to “0”. We create separate arrays for the $s = +1/2$ and $s = -1/2$ defects. We then

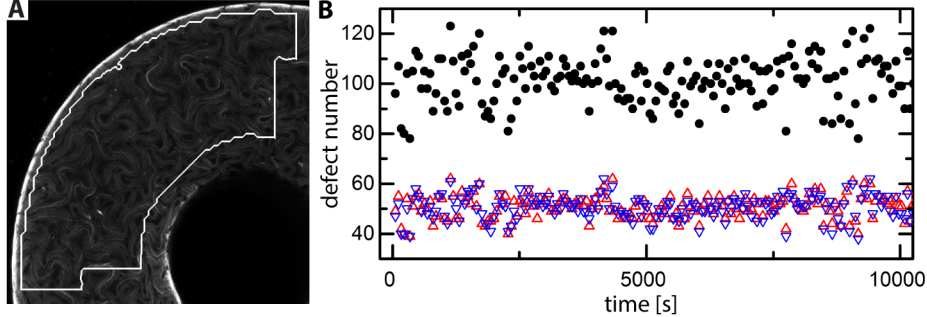


Figure 3.12: Defect number fluctuations in a region. (A) The region outlined in white has $(1/2\pi) \int K dA = 0$ and Area $A = 0.795 \text{ mm}^{-2}$. (B) Plot of the number of (Δ) $s = +1/2$ defects, (∇) $s = -1/2$ defects, and (\bullet) total number of defects over time in the region highlighted in (A).

concatenate the masks such that the final binary arrays $J^{(+)}(x, y, t)$ and $J^{(-)}(x, y, t)$ hold the $s = +1/2$ and $s = -1/2$ defects over time, respectively. Now, if we have a binary mask defining a region $\Theta(x, y)$, where pixels in the region have a value of 1 and pixels outside of the region have a value of 0, determining the number of $s = +1/2$ and $s = -1/2$ defects in a region over time, $N_{\Theta}^{(\pm)}(t)$, is a matter of calculating the sum $N_{\Theta}^{(\pm)}(t) = \sum_{x,y} J^{(\pm)}(x, y, t)\Theta(x, y)$. We plot $N_{\Theta}^{(\pm)}(t)$ and $N_{\Theta}(t) = N_{\Theta}^{(+)}(t) + N_{\Theta}^{(-)}(t)$ in the example region in Figure 3.12(A) over time in Figure 3.12(B), showing that both $N_{\Theta}^{(\pm)}(t)$ and $N_{\Theta}(t)$ fluctuate, with the fluctuations in each quantity centered around a mean. Thus, given $\bar{N}_{\Theta}^{(\pm)} = (1/T) \sum_{t=0}^T N_{\Theta}^{(\pm)}(t)$, the time-averaged number of $s = \pm 1/2$ defects over a time period T , we can calculate the time-averaged topological charge in a region as $\bar{s}_{\Theta} = (\bar{N}_{\Theta}^{(+)} - \bar{N}_{\Theta}^{(-)})/2$.

Due to the discrete nature of our data, it is possible to “miss” defects, especially when a pair of defects are close together. Typically, since one defect in the pair will have a lower value of S , the defect with the larger value of S will be ignored. Since topological charge is a discrete quantity, every missed defect in a region causes the total topological charge in that region to have an error of $\pm 1/2$. This gives us a way to characterize the error in our defect-finding routine. If the error is completely random, the measured time-averaged topological charge, \bar{s}_{Θ} , will converge to the actual value

of the time-averaged topological charge, \bar{s}_Θ^{actual} . However, if there is a systematic error, \bar{s}_Θ will converge to $\bar{s}_\Theta^{actual} \pm n/2$, where $n \in \mathbb{N}$. For example, if our routine were to always miss a single $s = +1/2$ defect, $\bar{s}_\Theta - \bar{s}_\Theta^{actual} = -1/2$. We first monitor \bar{s}_Θ as a function of averaging time to check for convergence, as shown for three regions in Figure 3.13. We find that the time-averaged topological charge in a region converges if we average over enough time frames. Next, we use topology to quantify the error in every measurement and rule out a systematic error in our analysis.

We test for a systematic error in the measured topological charge by considering a region of interrogation as its own entity, i.e. a compact surface with a boundary. Note that a compact surface with a boundary is topologically like a disc. For a compact surface with a boundary, we can write the Gauss-Bonnet theorem as:

$$\chi = 2(1 - g) - h, \quad (3.13)$$

where χ is the Euler characteristic, g is the genus, and h is the number of boundaries. Thus according to Eq. 3.13, our regions of interrogation have $\chi = 1$. Importantly, the Poincaré-Hopf theorem as written in Eq. 1.3 only applies for surfaces with a boundary if the director at the boundary is either everywhere tangential or everywhere normal to the boundary. In our case, the director is free to take any value on the boundary and thus can act as a source or sink of topological charge such that we can't write a relation between only the topological charge on the surface and the Euler characteristic of the surface.

Instead, we must use an extended version of the Poincaré-Hopf theorem [154] that accounts for variations of the director on the boundary:

$$\chi = s_{bulk} + s_{boundary} = \sum_i s_i + s_{boundary}, \quad (3.14)$$

where s_i is the charge of a defect in the bulk of the region calculated via Eq. 2.7, and

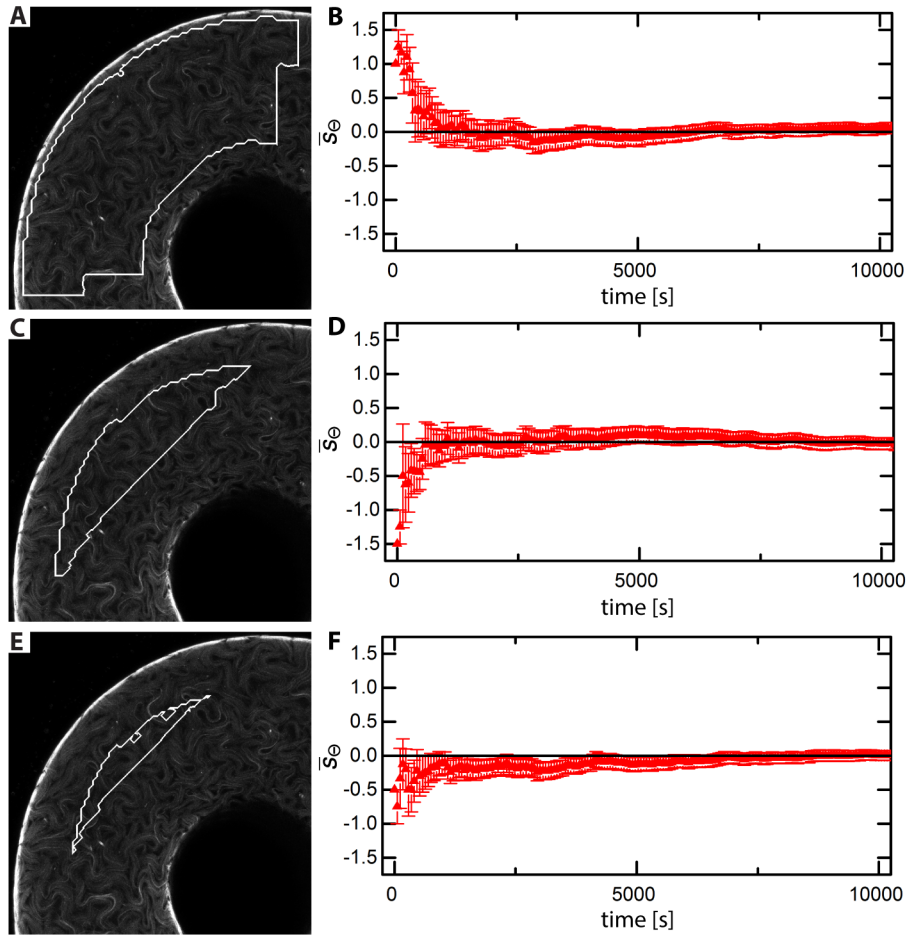


Figure 3.13: Time-averaged topological charge measured for different areas on a toroid with $\xi = 2.0$ and $a = 372 \mu\text{m}$. (A,C,E) The region outlined in white has (A) $(1/2\pi) \int K dA = 0$ and area $A = 0.795 \text{ mm}^{-2}$, (C) $(1/2\pi) \int K dA = 0$ and area $A = 0.211 \text{ mm}^{-2}$, (E) $(1/2\pi) \int K dA = 0$ and area $A = 0.064 \text{ mm}^{-2}$. (B,D,F) Plot of time-averaged topological charge vs averaging time for the region highlighted in (A,C,E), respectively. The error for each point is the standard error of the mean.

s_{boundary} is called the edge or boundary charge.

3.4.5 Edge charge

Recall that the topological charge is the winding number of the director along a closed contour in real space, where the director is specified with respect to a fixed frame. To find the edge charge we consider \mathbf{n} along the edge and calculate the associated winding number in \mathbb{RP}_1 , but here we measure the director orientation with respect to a moving frame on the boundary. This moving frame is called the Frenet-Serret frame and is defined by the unit tangent vector, \mathbf{T} , and unit normal vector, \mathbf{k} , along the boundary. If we let ϕ describe the director orientation with respect to the fixed coordinate system and ψ describe the orientation of \mathbf{T} with respect to the fixed coordinate system, then $\phi' = \psi - \phi$ gives the director orientation with respect to the Frenet-Serret frame [19, 29]. These two frames and the associated angles are illustrated in Figure 3.14(A). Thus, we calculate the edge charge like:

$$s_{\text{boundary}} = \frac{1}{2\pi} \oint d\phi'. \quad (3.15)$$

As a check, we can substitute the definition of ϕ' into Eq. 3.15 and re-write the edge charge as:

$$s_{\text{boundary}} = \frac{1}{2\pi} \oint \left\{ d\psi - d\phi \right\} = \frac{1}{2\pi} \oint d\psi - s_{\text{bulk}}. \quad (3.16)$$

If we perform the integral in Eq. 3.16 in the direction of the unit tangent vector, the Turning of Tangents theorem says that $\oint d\psi = 2\pi$ [29]. Thus, $s_{\text{boundary}} = 1 - s_{\text{bulk}}$ such that we recover $\chi = s_{\text{bulk}} + s_{\text{boundary}} = 1$, as required for our surface with a single boundary.

For example, consider a uniform director filed in a circular region, as drawn in the upper part of Figure 3.14(B). There is no defect in the bulk, so $s_{\text{bulk}} = 0$. Now considering the director variation along the boundary in the Frenet-Serret frame, as

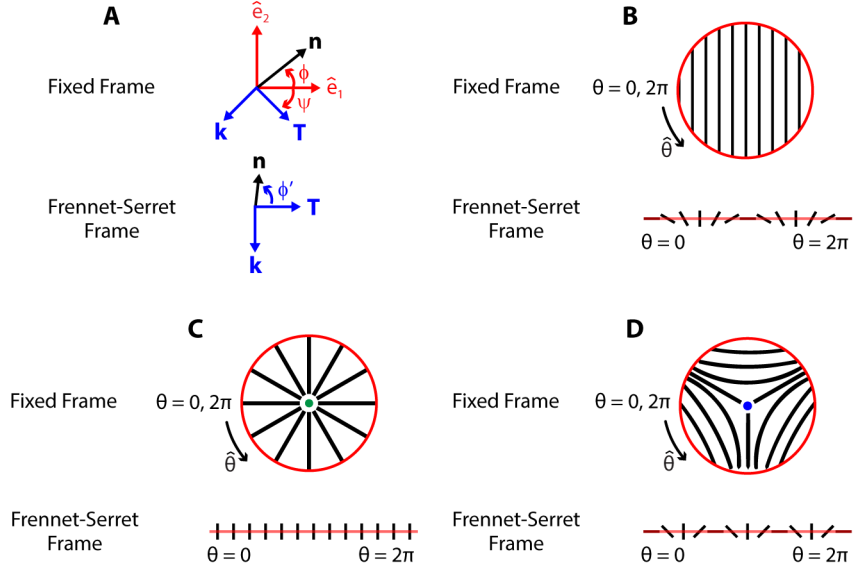


Figure 3.14: Schematic illustration of boundary and bulk charge. (A), The fixed frame is defined by the orthonormal basis $\{\hat{e}_1, \hat{e}_2\}$. The Frenet-Serret frame is a moving orthonormal frame defined by the unit tangent vector and unit normal vector, $\{T, k\}$. In the fixed frame, the director orientation and tangent vector orientation are given by ϕ and ψ , respectively. In the Frenet-Serret frame, the director orientation is ϕ' . (B-D) An example director field in a circular region drawn in a fixed frame and the director field at the boundary drawn in the Frenet-Serret frame. For the defect-free director field in (B), integrating $d\phi$ from $\Theta = 0$ to $\Theta = 2\pi$ yields a $s_{bulk} = 0$, while integrating $d\phi'$ from $\Theta = 0$ to $\Theta = 2\pi$ yields a $s_{boundary} = 1$, such that $s_{bulk} + s_{boundary} = 1$. Performing the same calculations for the director field containing the (C) $s = +1$ defect and (D) $s = -1/2$ defect yields $s_{bulk} + s_{boundary} = 1 + 0 = 1$, and $s_{bulk} + s_{boundary} = -1/2 + 3/2 = 1$, respectively.

drawn in the lower part of Figure 3.14(B), we see that the director rotates by 2π , corresponding to $s_{boundary} = 1$ and thus $s_{bulk} + s_{boundary} = 1$. This is illustrated in Figure 3.14(C,D) with further examples where the circular region contains a director field with a single $s = +1$ defect, and where the director field has a single $s = -1/2$ defect, respectively.

We can determine if we have systematic error in our defect detection routine with Eq. 3.14, as the sum of the edge charge and the topological charge from all the defects in the bulk should be equal to 1. We do this by independently determining $s_{boundary}$ using Eq. 3.15 and s_{bulk} using our defect-finding algorithm.

For some binary mask $\Theta(x, y)$ defining a region, we take the boundary, $\partial\Theta$, of the binary mask to be the pixels with value 1 connected to at least one 0-valued pixel. We consider two pixels connected if they share an edge; pixels that share a corner are not connected. An example mask and its boundary are shown in Figure 3.15(A,B), respectively. Along the boundary, the normalized displacement vector between the i^{th} and the j^{th} pixel is defined as:

$$\Delta \mathbf{R}_{[i,j]} = \frac{\mathbf{R}_{[j]} - \mathbf{R}_{[i]}}{|\mathbf{R}_{[j]} - \mathbf{R}_{[i]}|}. \quad (3.17)$$

We estimate the unit tangent vector for a pixel of interest by averaging the local normalized displacement vectors:

$$\mathbf{T} \approx \frac{\Delta \mathbf{R}_{[i,i+1]} + \Delta \mathbf{R}_{[i,i+2]} + \Delta \mathbf{R}_{[i-1,i]} + \Delta \mathbf{R}_{[i-2,i]}}{|\Delta \mathbf{R}_{[i,i+1]} + \Delta \mathbf{R}_{[i,i+2]} + \Delta \mathbf{R}_{[i-1,i]} + \Delta \mathbf{R}_{[i-2,i]}|}, \quad (3.18)$$

where the pixel of interest is indexed by i and an increasing index corresponds to a CCW displacement along the boundary. To complete the Frenet-Serret frame, we estimate the outward pointing unit normal \mathbf{k} by applying a $-\pi/2$ CCW rotation to \mathbf{T} at every pixel. The normal vectors for the example boundary in Figure 3.15(B) are plotted on the boundary in Figure 3.15(C). Finally, we calculate $\phi' = \psi - \phi$ and numerically evaluate Eq. 3.15.

We test our routine by first integrating the normal vectors along $\partial\Theta$, as shown in Figure 3.15(D), finding $\oint_{\partial\Theta} d(\psi - \pi/2) = \oint_{\partial\Theta} d\psi = 2\pi$, as desired. We now consider a small circular region and validate the algorithm using director fields from our active nematic toroids, as shown in the example in Figure 3.15(E). From the defects found by our algorithm, with $s = +1/2$ defects indicated by (\times) and $s = -1/2$ defects indicated by (\circ) in the example image in Figure 3.15(E), we calculate $s_{\text{bulk}} = \sum_i s_i = -1/2$. Plotting $\oint_{\partial\Theta} d\phi'$ for the example in Figure 3.15(E) in Figure 3.15(F), we see that $s_{\text{boundary}} = 3/2$, resulting in $s_{\text{bulk}} + s_{\text{boundary}} = 1$, as required.

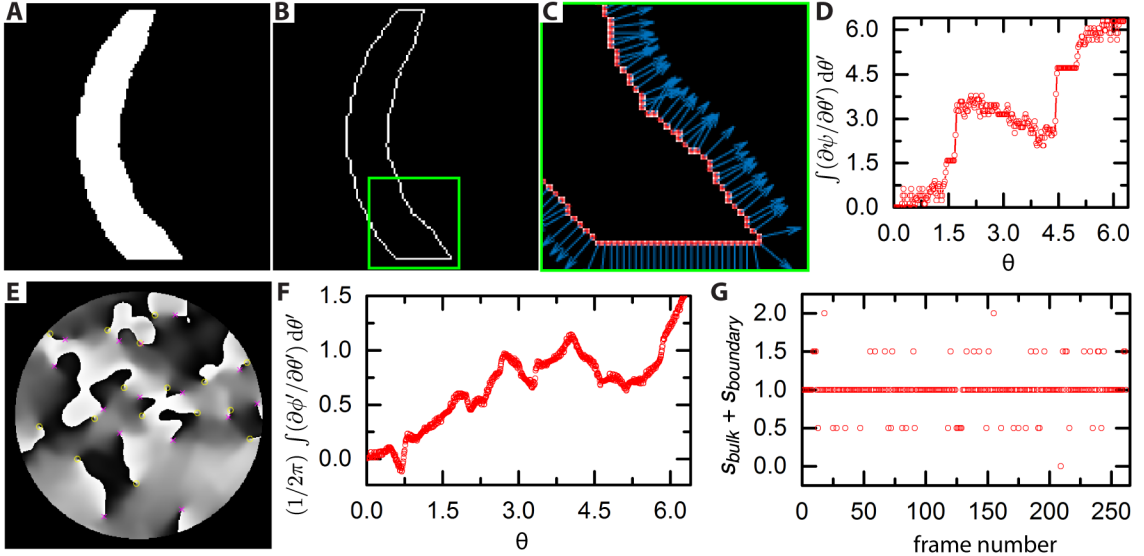


Figure 3.15: Boundary charge and defect detection error on active nematic toroids. (A-D), Validation of the Frenet-Serret frame. For the example mask in (A), we find the (B) boundary, estimate the unit tangent vectors, and then rotate the tangent vectors by $-\pi/2$ to get the (C) unit normal vectors and complete the Frenet-Serret frame. The image in (C) is zoomed in on the highlighted portion of (B) to better show the arrows. (D), We check the Frenet-Serret frame in (C) by integrating the change in the unit normal vector along the boundary, $\int_0^\theta d(\psi - \pi/2) = \int_0^\theta d\psi = \int_0^\theta (\partial\psi/\partial\theta') d\theta'$, and see that the integral goes to 2π , as desired. (E), Circular region containing a director field from an active nematic toroid with $s = \pm 1/2$ defects found with our algorithm and labeled by (\times), (\circ), respectively, giving $s_{bulk} = \sum_i s_i = -1/2$. (F), $\int_{\theta=0}^{2\pi} d\phi'$ along the boundary yields $s_{boundary} = 3/2$ as $\theta \rightarrow 2\pi$. (G), $s_{bulk} + s_{boundary}$ for 262 frames evaluated using the region in (A) applied to a torus with $\xi = 2.4$ and $a = 268 \mu\text{m}$. There are 55 frames with $s_{bulk} + s_{boundary} \neq 1$ and 207 frames with $s_{bulk} + s_{boundary} = 1$, leading to $P(error) = 0.21$ and $\text{mean}(error) = 0.004$.

We now consider a region in the intensity projection for a torus and monitor s_{bulk} and $s_{boundary}$ over time. For the example region in Figure 3.15(A), we plot $s_{bulk} + s_{boundary}$ for every time frame in Figure 3.15(G). We see in this example that 55 frames out of 262 frames have an error; however, the error is typically only $\pm 1/2$, with only three frames having an error of ± 1 . Calculating $\text{mean}(error) = \text{mean}(s_{bulk}(t) + s_{boundary}(t) - 1)$, for Figure 3.15(G), we have $\text{mean}(error) = [26(1/2) + 26(-1/2) + 2(1) + 1(-1)]/262 = 0.004$. Importantly, since $|\text{mean}(error)| \ll 1/2$, we see that the error in our analysis is random and we can trust the time-averaged topological charge.

3.5 Measuring surface curvature

From $h(x, y)$, we wish to calculate the Gaussian curvature of the surface. Recall from Chapter 2 that $K = \det\{\mathbf{L}\}$. Thus, we need to calculate the Weingarten matrix.

3.5.1 The Weingarten matrix

For a smooth surface $\mathbf{R} = \{x, y, h(x, y)\}$, it is straightforward to use differential geometry and directly calculate the Weingarten matrix. Note, however, that our surfaces are discrete and noisy and thus taking first and second derivatives is not obvious. To avoid this, we rearrange Eq. 2.51 and notice that the Weingarten matrix relates a displacement in the tangent plane of a surface with the corresponding change in the unit normal vector along the displacement via,

$$\begin{pmatrix} [(\hat{e}_1 \cdot \nabla) \mathbf{k}] \cdot \Delta \mathbf{r} \\ [(\hat{e}_2 \cdot \nabla) \mathbf{k}] \cdot \Delta \mathbf{r} \end{pmatrix} = -\mathbf{L} \begin{pmatrix} \Delta \mathbf{r} \cdot \hat{e}_1 \\ \Delta \mathbf{r} \cdot \hat{e}_2 \end{pmatrix} \quad (3.19)$$

where \hat{e}_i with $i = 1, 2$ is an orthonormal basis in the tangent plane, \mathbf{k} is the unit normal vector, and $\Delta \mathbf{r} = \Delta r_j \hat{e}_j$ is an arbitrary displacement in the tangent plane. Note that the relation, $(\hat{e}_j \cdot \nabla) \mathbf{k} = -L_{ij} \hat{e}_i$, Weingarten's formula, comes from the fact that the change in the surface normal due to infinitesimal displacements in the

tangent plane is also in the tangent plane [29].

Thus, for a point of interest on the surface, we can consider local displacement vectors and the corresponding change in the unit surface normal and then fit L_{ij} according to Eq. 3.19 using an iteratively-reweighted least squares (IRLS) routine [155, 156]. This technique allows us to characterize a noisy surface without taking a discrete derivative and without any prior knowledge about the surface features. In addition, an IRLS routine is a robust fit able to reject outliers and accommodate the noise in our data.

3.5.2 Iteratively-reweighted least squares

Consider a set of observations of a random variable where each observation is denoted by $y_{(i)}$ and is associated with a random variable $x_{(i)}$. Given a model $y'_{(i)} = g(x_{(i)}, \boldsymbol{\alpha})$, where $\boldsymbol{\alpha}$ is the parameter vector for the model, we can define the error of the model for each observation by the residual, $\gamma_{(i)} = y_{(i)} - y'_{(i)} = y_{(i)} - g(x_{(i)}, \boldsymbol{\alpha})$. A least-squares fit works to find the $\boldsymbol{\alpha}$ that minimizes the sum of the squared residuals:

$$\arg \min_{\boldsymbol{\alpha}} \sum_i \gamma_{(i)}^2. \quad (3.20)$$

If the model is linear, the fit has an analytic solution [157]. In addition, for normally-distributed data, the result of least-squares fit gives the maximum-likelihood values of $\boldsymbol{\alpha}$ [157].

However, since the cost of an error in a least squares fit scales quadratically with the size of the error, outliers can have a disproportionate effect on the final fit. In fact, extreme outliers are often referred to as lever points for this exact reason.

One way to treat noisy or uncertain data is to assign a weight to each data point

such that data points with larger error are weighted less. The fit then becomes:

$$\arg \min_{\alpha} \sum_{(i)} (w_i \gamma_{(i)})^2, \quad (3.21)$$

where $w_{(i)}$ is the weight associated to the observation $y_{(i)}$. A weighted linear least-squares fit of this type is still analytically solvable [157]. Unfortunately, weighted least-squares is still very sensitive to outliers if it is not obvious *a priori* which data are the outliers.

Instead, we can construct a fit that is inherently less sensitive to outliers by replacing the square of the residual with a general cost function:

$$\arg \min_{\alpha} \sum_{(i)} \text{cost}(\gamma_{(i)}), \quad (3.22)$$

such that the fit can deprioritize or even reject entirely large sources of error. These cost functions are known as maximum-likelihood-type estimators, or M-estimators [157]. Note that choosing the cost function $\text{cost}(\gamma_{(i)}) = \gamma_{(i)}^2$ gives a regular least-squares fit. Unfortunately, a general cost function is not often analytically solvable or easy to minimize. However, provided the cost function is differentiable, we can solve Eq. 3.22 with an iteratively-reweighted least-squares (IRLS) process.

To do this, we need to recast Eq. 3.22 in terms of a weighted least-squares fit. We start by taking the derivative of Eq. 3.22 with respect to α_j :

$$\sum_i \frac{\partial \text{cost}(\gamma_{(i)})}{\partial \gamma_{(i)}} \frac{\partial \gamma_{(i)}}{\partial \alpha_j} = 0. \quad (3.23)$$

Notice that if we define a weight function like $w(\gamma_{(i)}) = \frac{1}{\gamma_{(i)}} \frac{\partial \text{cost}(\gamma_{(i)})}{\partial \gamma_{(i)}}$, we can rewrite Eq. 3.23 as:

$$\sum_{(i)} w(\gamma_{(i)}) \gamma_{(i)} \frac{\partial \gamma_{(i)}}{\partial \alpha_j} = 0. \quad (3.24)$$

Solving Eq. 3.24 for $\boldsymbol{\alpha}$ is equivalent to minimizing:

$$\arg \min_{\boldsymbol{\alpha}} \sum_i \left\{ (w_{(i)}(\gamma_{(i)}) \gamma_{(i)}(\boldsymbol{\alpha}))^2 \right\}, \quad (3.25)$$

a weighted least-squares fit, as desired. Hence, solving Eq. 3.22 is equivalent to solving a weighted least-squares fit, where we have expressed $\gamma_{(i)}$ inside the minimization as an explicit function of $\boldsymbol{\alpha}$ for clarity. Since our weights are dependent on the residuals, we solve Eq. 3.25 iteratively, where the weights for an iteration (p) are determined by the residuals from the previous iteration, giving:

$$\boldsymbol{\alpha}^{(p+1)} = \arg \min_{\boldsymbol{\alpha}} \sum_i \left\{ \left[w_{(i)}(\gamma_{(i)}^{(p)}) \gamma_{(i)}^{(p+1)}(\boldsymbol{\alpha}) \right]^2 \right\}, \quad (3.26)$$

where $w_{(i)}(\gamma_{(i)}^{(p)})$ are the weights calculated using the residuals for iteration p . The weights for a given iteration are constants and do not change during the minimization. With enough iterations, the $\gamma_{(i)}$ converge and we have the $\boldsymbol{\alpha}$ values that solve Eq. 3.25. The entire process can be described by the recursion relation:

$$\begin{aligned} \gamma_{(i)}^{(p+1)} &= y_{(i)} - g(x_{(i)}, \boldsymbol{\alpha}^{(p+1)}) \\ &= y_{(i)} - g\left(x_{(i)}, \arg \min_{\boldsymbol{\alpha}} \sum_i \left\{ \left[w_{(i)}(\gamma_{(i)}^{(p)}) \gamma_{(i)}^{(p+1)}(\boldsymbol{\alpha}) \right]^2 \right\}\right). \end{aligned} \quad (3.27)$$

Since these cost functions do not need to be everywhere convex, they may not necessarily have a global minimum, or even a guaranteed convergence. However, those that are not globally convex often deal with large error more severely than convex functions. Thus, to get the best of both worlds, we will first fit our surface using a convex M-estimator until the fit converges and then fit the output of the convex M-estimator with a globally non-convex M-estimator. Following Ref. [156], we use the convex “Fair” M-estimator and the non-convex “Geman-McClure” (GMC) M-estimator [158], where the functional forms of the cost function and weight functions

are provided in Table 3.3 and plotted in Figure 3.16. Both the GMC and the Fair M-estimator have a tuning constant, c , that adjusts the influence of errors on the fitting weights for the next iteration; decreasing c reduces the influence of large residuals. This can be seen by considering the blue and red curves in Figure 3.16(B–D), where $c_{blue} = 2c_{red}$. Notice how increasing c causes the weights for large residuals to increase; data with a large residual have more influence in the blue curves than in the red curves.

This raises the question of how to compare different M-estimators and how to choose a value for the tuning parameters. One way to do this is to test an M-estimator with some tuning parameter using data drawn from a Gaussian with zero mean and unit variance, the standard normal distribution. For example, let the model $g(x_{(i)}, \boldsymbol{\alpha})$ estimate the mean of the distribution given the input x . The residuals are $\gamma_{(i)} = 0 - g(x_{(i)}, \boldsymbol{\alpha})$, such that the sample variance is $(1/N) \sum_i^N \gamma_{(i)}^2$ and the variance of the mean is $(1/N^2) \sum_i^N \gamma_{(i)}^2 = (1/N) \sum_i^N \gamma_{(i)}^2 / N$. Notice that if our model just returns the value of the observation, $g(x_{(i)}, \boldsymbol{\alpha}) = x_{(i)}$, then we recover the well-known formulas for both the sample variance $(1/N) \sum_i^N x_{(i)}^2$, and sample variance of the mean $(1/N) \sum_i^N x_{(i)}^2 / N$. We compare the sample variance of the mean from the model $g(x_{(i)}, \boldsymbol{\alpha})$ versus that from the observation itself $x_{(i)}$ in the limit that $N \rightarrow \infty$ via the asymptotic relative efficiency (ARE):

$$ARE = \lim_{N \rightarrow \infty} \frac{(1/N) \sum_i^N x_{(i)}^2 / N}{(1/N) \sum_i^N \gamma_{(i)}^2 / N} \quad (3.28)$$

$$= \frac{\lim_{N \rightarrow \infty} \sum_i^N x_{(i)}^2}{\lim_{N \rightarrow \infty} \sum_i^N \gamma_{(i)}^2} \quad (3.29)$$

$$= \frac{N}{\lim_{N \rightarrow \infty} \sum_i^N \gamma_{(i)}^2}, \quad (3.30)$$

where we have taken advantage of the fact that $\lim_{N \rightarrow \infty} (1/N) \sum_i^N x_{(i)}^2 = 1$, the true variance for the standard normal distribution.

We see that if $g(x_{(i)}, \boldsymbol{\alpha})$ produces a variance of the mean of $1/N$, the ARE will be unity, or 100%. Similarly, if $g(x_{(i)}, \boldsymbol{\alpha})$ produces a smaller variance of the mean, the efficiency will be greater than 100%. The ARE thus can be used to give context to an estimator with a set of input parameters. We note that the literature generally quotes parameters for their M-estimators that have 95% ARE; the red curves in Figure 3.16(B–D) were computed with these values [155, 158, 159].

Table 3.3: Cost and weight functions of common M-estimators. x are the residuals and c is a tuning parameter.

	$cost(x)$	$w(x)$
least-squares:	$\frac{x^2}{2}$	1
L_p :	$\frac{ x ^p}{p}$	$ x ^{p-2}$
Fair:	$c^2 \left[\frac{ x }{c} - \log \left(1 + \frac{ x }{c} \right) \right]$	$\frac{1}{1 + x /c}$
Geman-McClure:	$\frac{(x/c)^2}{1 + (x/c)^2}$	$\frac{2}{(1 + (x/c)^2)^2}$
Cauchy:	$\frac{c^2}{2} \log (1 + (x/c)^2)$	$\frac{1}{1 + (x/c)^2}$

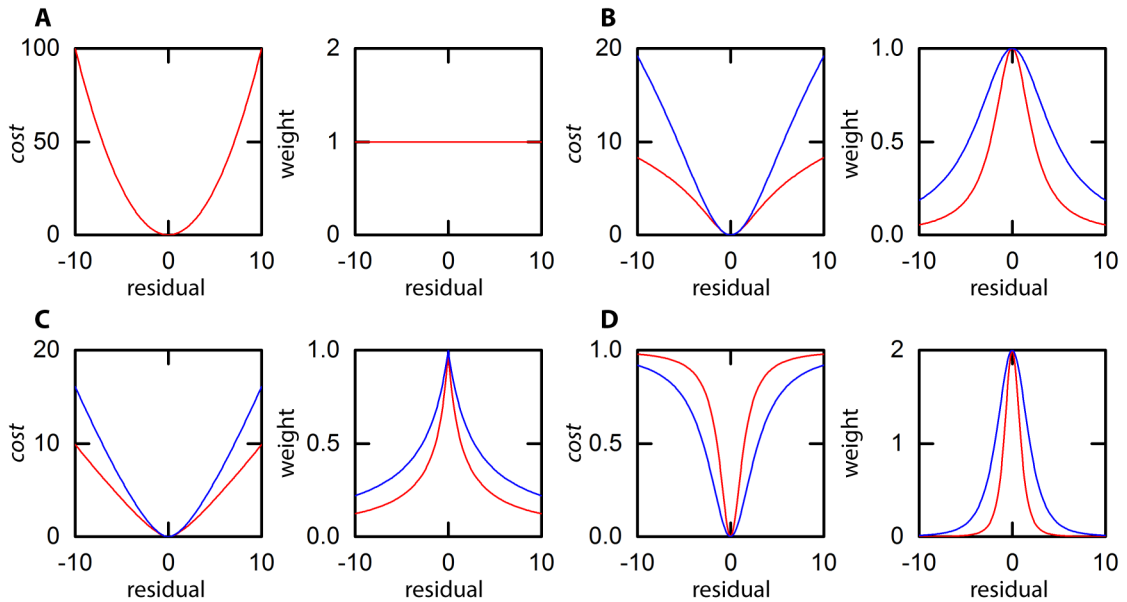


Figure 3.16: Plots of the cost functions and weight functions for common M-estimators. (A) The cost and weight function for a least-squares fit. (B-D) The cost and weight functions for a (B) Cauchy M-estimator, a (C) Fair M-estimator, and a (D) GMC M-Estimator, with the tuning parameter for the red curves set to yield 95% efficiency on a standard normal, and the tuning parameter for the blue curve set to twice the value in the red curve. The least-squares estimator in (A) and the Fair estimator in (C) have everywhere convex cost functions, in contrast to the Cauchy and the GMC M-estimators in (B,D), respectively.

3.5.3 Fitting the Weingarten matrix on a surface

From a Monge parameterization $h(x, y)$ of a surface [19, 29], we start by computing the Delaunay triangulation [160] such that every point or pixel in $h(x, y)$ is a vertex in the triangulation. From the triangulation, we estimate \mathbf{k} at every vertex as the average of the unit normals of the adjacent faces. Once we have a triangulation and the \mathbf{k} estimates, we proceed to fit the curvature.

Let $\mathbf{R}_{[0]}$ be an example point of interest with normal $\mathbf{k}_{[0]}$. We first make an initial fit using regular least-squares to serve as an input into the IRLS routine. We consider all points within a distance d_1 of $\mathbf{R}_{[0]}$ to be within the region of interest and then use $\mathbf{k}_{[0]}$ to transform the region of interest into the tangent plane at $\mathbf{R}_{[0]}$. This step allows us to characterize the surface locally in terms of an orthonormal basis $\{\hat{e}_1, \hat{e}_2, \mathbf{k}\}$, where \hat{e}_1 and \hat{e}_2 are in the tangent plane. We then calculate the displacement vectors in the tangent plane $\Delta\mathbf{R}_{[i,j]} = \mathbf{R}_{[j]} - \mathbf{R}_{[i]}$ and the change in the unit normal $\Delta\mathbf{k}_{[i,j]} = \mathbf{k}_{[j]} - \mathbf{k}_{[i]}$ for every possible pair of points in the region of interest, with individual points indexed with i and j . Importantly, as depicted in Figure 3.17, the pairs of points do not need to include $\mathbf{R}_{[0]}$; this reduces the influence of error in $\mathbf{R}_{[0]}$ and $\mathbf{k}_{[0]}$. Since we are considering how \mathbf{k} changes along $\Delta\mathbf{R}$, a finite displacement vector, $\Delta\mathbf{k}$ is not generally in the tangent plane. Thus, we need to extend the Weingarten Matrix to consider the component of $\Delta\mathbf{k}$ along \mathbf{k} [155, 156]:

$$\begin{pmatrix} \Delta\mathbf{k} \cdot \hat{e}_1 \\ \Delta\mathbf{k} \cdot \hat{e}_2 \\ \Delta\mathbf{k} \cdot \mathbf{k}_0 \end{pmatrix} = \Lambda \begin{pmatrix} \Delta\mathbf{R} \cdot \hat{e}_1 \\ \Delta\mathbf{R} \cdot \hat{e}_2 \end{pmatrix} = \begin{pmatrix} L_{11} & L_{12} \\ L_{21} & L_{22} \\ M_1 & M_2 \end{pmatrix} \begin{pmatrix} \Delta\mathbf{R} \cdot \hat{e}_1 \\ \Delta\mathbf{R} \cdot \hat{e}_2 \end{pmatrix}, \quad (3.31)$$

where we have added M_1 and M_2 to \mathbf{L} to form Λ , the extended Weingarten Matrix. This additional information will eventually allow us to re-estimate \mathbf{k} [156].

We now have a system of three equations to fit with 5 parameters, as $L_{12} = L_{21}$.

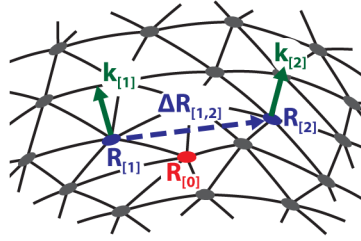


Figure 3.17: Schematic of the quantities used to calculate the Gaussian curvature of a triangulated surface. $\mathbf{R}_{[0]}$ is the point of interest. $\mathbf{R}_{[1]}$ and $\mathbf{R}_{[2]}$ are an example pair of points close to the point of interest with $\Delta\mathbf{R}_{[1,2]} = \mathbf{R}_{[2]} - \mathbf{R}_{[1]}$ the displacement vector in the tangent plane of $\mathbf{R}_{[0]}$. $\mathbf{k}_{[1]}$ and $\mathbf{k}_{[2]}$ are the unit surface normal vectors associated to $\mathbf{R}_{[1]}$ and $\mathbf{R}_{[2]}$.

If we naively expand Eq. 3.31 directly into three equations,

$$\Delta k_1 = L_{11}\Delta R_1 + L_{12}\Delta R_2 \quad (3.32)$$

$$\Delta k_2 = L_{21}\Delta R_1 + L_{22}\Delta R_2 \quad (3.33)$$

$$\Delta k_k = M_1\Delta R_1 + M_2\Delta R_2, \quad (3.34)$$

where we have expanded the vectors like $\mathbf{v} \cdot \hat{e}_i = v_i$ and Δk_k refers to the component of $\Delta\mathbf{k}$ along the surface normal, we see that L_{12} will be determined entirely by the variation along \hat{e}_2 , and L_{11} by the variation along \hat{e}_1 . The result of L_{12} from fitting Eq. 3.32 will then set the value of L_{21} in the fit of Eq. 3.33 so that only L_{22} is free to vary during the fit. This means that in principle, the choice of \hat{e}_i could affect the output curvature. To account for this, we manipulate Eqs. 3.32–3.34 to be:

$$\Delta k_2\Delta R_2 - \Delta k_1\Delta R_1 = (\Delta R_2)^2 L_{22} - (\Delta R_1)^2 L_{11} \quad (3.35)$$

$$\Delta k_1 + \Delta k_2 - L_{11}\Delta R_1 - L_{22}\Delta R_2 = (\Delta R_1 + \Delta R_2)L_{12} \quad (3.36)$$

$$\Delta k_k = M_1\Delta R_1 + M_2\Delta R_2. \quad (3.37)$$

If we do the fits in Eqs. 3.35–3.37 in order, the values of L_{11} and L_{22} from fitting Eq. 3.35 are inserted as fixed parameters into the fit of Eq. 3.36. However, now the

values of L_{ij} are determined by the variation in both directions in the tangent plane. Once we have estimates of the elements of Λ from the initial least-squares fit, we move on to fitting the curvature with the IRLS routine.

We now choose all points within a distance d_2 of $\mathbf{R}_{[0]}$, where $d_2 > d_1$, and as before, transform into the tangent plane and calculate the associated $\Delta\mathbf{k}_{[i,j]}$ and $\Delta\mathbf{R}_{[i,j]}$ between all pairs of points. In addition, we calculate a geometric weight for each $\Delta\mathbf{R}_{[i,j]}$:

$$m_{(ij)} = \frac{C}{\Delta\mathbf{R}_{[0,i]}^2 + \Delta\mathbf{R}_{[0,j]}^2}, \quad (3.38)$$

where C is a normalization constant such that $\sum_{i,j} m_{(ij)} = 1$. The geometric weight ensures that data far from $\mathbf{R}_{[0]}$ contribute less to the curvature at $\mathbf{R}_{[0]}$ [155, 156]. We then pass the $\Delta\mathbf{k}_{[i,j]}$, the $\Delta\mathbf{R}_{[i,j]}$, the $m_{[i,j]}$, the initial values in Λ , the appropriate tuning parameters, and a convergence tolerance to our IRLS routine. Our routine starts by calculating the residuals using Λ from the previous fit like:

$$\gamma_{(ij)}^{(p)} = \sqrt{|\Delta\mathbf{k}_{[i,j]} - \Lambda^{(p)} \Delta\mathbf{R}_{[i,j]}|^2}, \quad (3.39)$$

where p is the iteration number and the 0th iteration refers to the initial least-squares fit. The routine then calculates the weights for the Fair M-estimator seen in Table 3.3, multiplies the Fair weights for each pair of points with the associated $m_{(ij)}$ to get the final fitting weight, performs a weighted least-squares fit of Eqs. 3.35–3.37, and then repeats the process from the beginning until the fit converges. For the Fair fit we take the tuning constant $c_F^{(p+1)} = c_F^{initial} \text{median}\{\gamma^{(p)}\}$, where p is the iteration number, $\gamma^{(p)}$ is a vector of the residuals, and $c_F^{initial}$ is an input parameter. We include the median of the residuals in our tuning constant so that the tuning parameter in the fit doesn't need to be adjusted as much between datasets with different levels of noise. In this case, we use the median of the residuals, as the mean can be distorted by large errors. The Fair fit converges when the cost function changes by less than the specified

convergence tolerance between subsequent iterations. While we set an upper limit of 50 iterations for the Fair fit, the fit typically converges in fewer than 20 iterations taking the convergence tolerance to be 0.001.

The final values of Λ from the Fair fit are then used as the initial values for an IRLS fit using a GMC M-estimator. The overall flow of the algorithm is the same for the GMC M-estimator as it was for the Fair M-estimator. However, there are some key differences in how the fitting weights are handled. Here, it is possible to reject outliers by calculating the fitting weights as,

$$w_{(ij)}^{(p+1)} = \begin{cases} 0 & \text{if } \gamma_{(ij)}^{(p)} > b c_{GMC}^{(p)} \\ \frac{2}{(1 + (\gamma_{(ij)}^{(p)} / c_{GMC}^{(p)})^2)^2} & \text{otherwise} \end{cases}, \quad (3.40)$$

where $c_{GMC}^{(p)} = c_{GMC}^{initial} \text{median}\{\gamma^{(p)}\}$ is the tuning constant for the GMC fit, and $c_{GMC}^{initial}$ and b are input parameters. We have modified the standard GMC weight function to exclude data with a residual that is too large. The outlier rejection works by comparing each residual against the median of the residuals. The parameter b then determines how much variance with respect to the median residual is allowed. In addition, since the GMC fit is not guaranteed to converge, we ensure that the $c_{GMC}^{(p)} \leq c_{GMC}^{(0)}$ by setting iterations with $c_{GMC}^{(p)} > c_{GMC}^{(0)}$ to have $c_{GMC}^{(p)} = c_{GMC}^{(0)}$.

The GMC fit converges when the cost function changes by less than the specified convergence tolerance between subsequent iterations. We set an upper limit of 20 iterations for the GMC fit, but the fit typically converges in fewer than 10 iterations when taking the convergence tolerance to be 0.001. We display this entire IRLS fitting process for an example point, with the residuals, the weights, Λ , and K displayed for the Fair fit and the GMC fit in Figure 3.18(A,B), respectively. The initial output of the least squares fit is passed to the Fair function and displayed as the 0th iteration [Figure 3.18(A)]. Note how the *cost* changes largely between the 0th and 2nd, but

changes very little between the 2nd and 4th iterations [Figure 3.18(A)]. The Fair fit converges on the 4th iteration; the values are then passed the GMC fit [Figure 3.18(B)].

In the subsequent GMC fit displayed in Figure 3.18(B), the dashed line indicates the outlier rejection criterion; residuals above the dashed line have their weight set to 0. Note how the ability to reject outliers lets the GMC fit in Figure 3.18(B) find a solution where a majority of the residuals are small. Similar to the Fair fit, the cost in the GMC fit drops rapidly; by the 8th iteration both the cost and the Gaussian curvature are very close to their final values [Figure 3.18(B)]. The GMC fit converges on the 10th iteration. The routine outputs the GMC weights from the final fitting iteration and the final values of \mathbf{A} . Finally, we calculate the Gaussian curvature of at $\mathbf{R}_{[0]}$ taking $K = \det\{\mathbf{L}\}$ and move on to correcting $\mathbf{k}_{[0]}$.

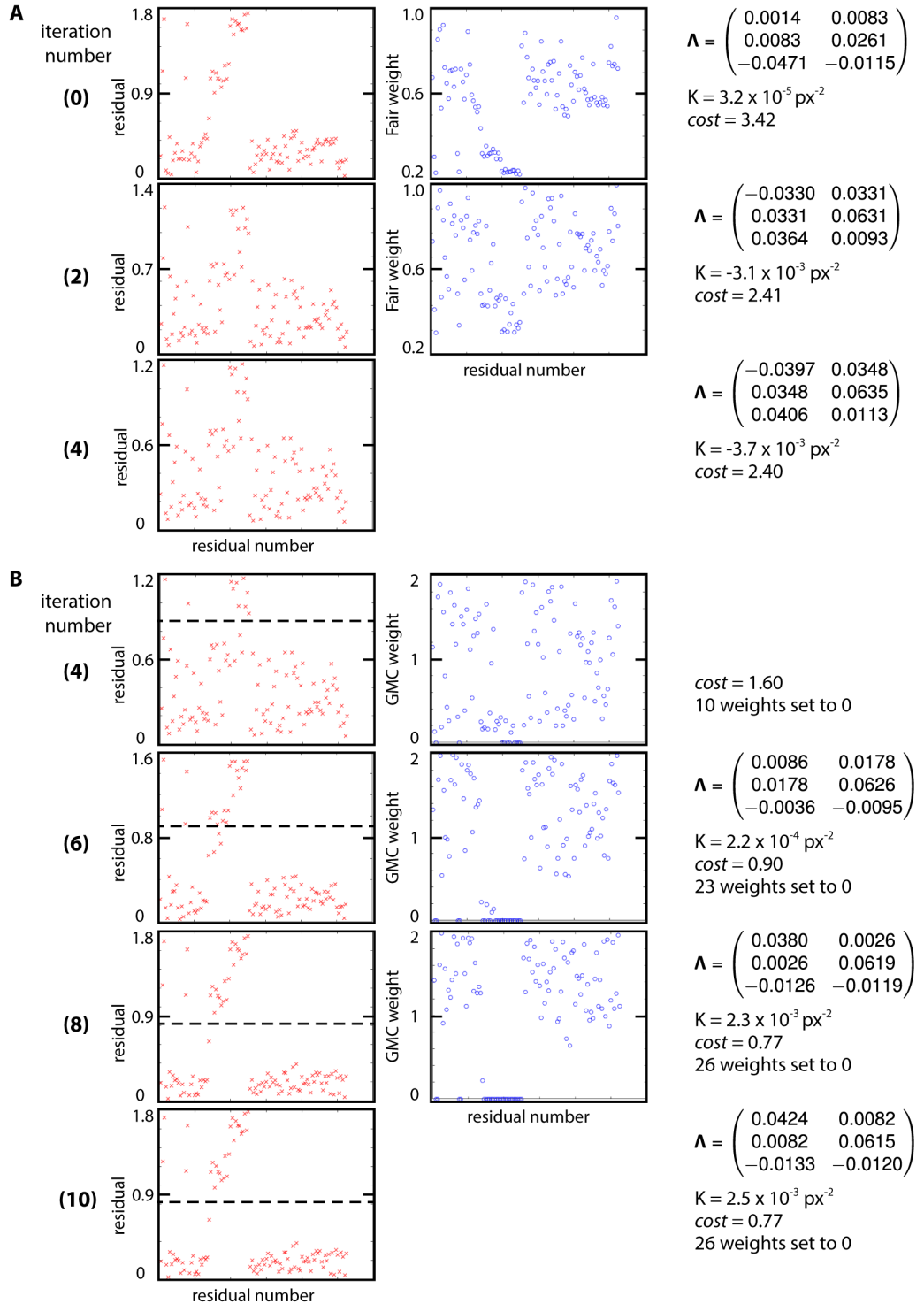


Figure 3.18: Example IRLS fit of the curvature at a point on a surface. (A,B) Residuals, weights, Λ , K , and cost for the (A) Fair M-estimator and (B) GMC M-estimator over multiple iterations, with the iteration number to the left of the residuals. The 0th iteration corresponds to the output from the initial least-squares fit. The dashed line in (A) is the outlier rejection criterion; residuals above the line have their weight set to 0.

3.5.4 Correcting the surface normal vectors

We use the fitting weights from the final iteration (p) and the final values in Λ to correct our initial estimate of $\mathbf{k}_{[0]}$ using a weighted average [156]:

$$\mathbf{k}_{[0]}^{(p)} = \frac{\sum_i m_{(0i)} w_{(0i)}^{(p)} (\mathbf{k}_{[i]}^{(0)} - \Lambda^{(p)} \Delta \mathbf{R}_{[0,i]})}{\sum_j m_{(0j)} w_{(0j)}^{(p)}}, \quad (3.41)$$

where $\mathbf{k}_{[0]}^{(p)}$ corresponds to the re-estimated unit normal. Note that here we have only used pairs of points that include $\mathbf{R}_{[0]}$. This re-estimation uses the fitted curvature to determine what the surface normal should be.

3.5.5 Finding the area element

Once we have the re-estimated normal vectors everywhere on the surface, we can calculate the determinant of the metric [29],

$$g = \frac{1}{(\mathbf{k}^{(p)} \cdot \hat{\mathbf{z}})^2}. \quad (3.42)$$

The determinant of the metric lets us connect areas in our flat intensity projection with areas on our curved toroidal surface via the local area element [29], $dA = \sqrt{g} dx dy$. Physically, we see that in the Monge parameterization, \sqrt{g} reflects the tilt angle of the surface when compared to the flat plane that parameterizes the height of the surface.

3.5.6 Validation on test surfaces

We validate our routine on hemispheres and saddle-like surfaces with varying levels of random noise inserted into the height of the surface in order to mimic the noise in our confocal data. We specify the noise as a percentage of the radii of curvature

used to generate the test surface. A surface without noise is insensitive to d_1 , d_2 , and the tuning constants in the fit. This is shown for the noiseless hemisphere in Figure 3.19(A) with $K = 1.1 \times 10^{-3} \text{ px}^{-2}$, where the initial least-squares fit and the output of the IRLS fit are shown in Figure 3.19(B,C), respectively, and the color scale is displayed in Figure 3.19(I). We test surfaces with up to 3% noise; this is greater than the noise in our toroidal droplets. We find that setting $b = 2$ and $c_F^{initial} = 1.3998$ and $c_{GMC}^{initial} = 1.4826$, their respective 95% efficiency values [158, 159], works well. In addition, we see that d_2 matters far more than d_1 ; increasing d_2 improves the noise tolerance of the fit.

For a given amount of noise, we fit a test surface multiple times while increasing d_2 until the change in the curvature with increasing d_2 is small enough. This process is illustrated for the example hemisphere with 1% noise and an initial $K = 1.1 \times 10^{-3} \text{ px}^{-2}$ displayed in Figure 3.19(D). The output from the initial least-squares fit is shown in Figure 3.19(E) and the outputs from increasing values of d_2 are shown in Figure 3.19(F-H), where the color scale is displayed in Figure 3.19(I). Note that K does not change appreciably between $d_2 = 8$ in Figure 3.19(G) and $d_2 = 10$ in 3.19(H). For the final fitting parameters $d_1 = 4$ and $d_2 = 10$, we take the mean and standard deviation of K everywhere on the surface, $\bar{K} = 1.0 \times 10^{-3} \text{ px}^2$ and $\sqrt{\Delta K^2} = 0.1 \times 10^{-3} \text{ px}^2$. This shows that the fit deals well with noise on the surface provided d_2 is large enough. While we could in principle set d_2 to the size of the surface to eliminate this step, our fit runtime scales factorially with increasing d_2 such that we must balance runtime against improvements in the output curvature.

We also test a saddle surface with negative Gaussian curvature everywhere on the surface and $K = -0.4 \times 10^{-3} \text{ px}^{-2}$ in the middle of the surface. Similar to the hemisphere, the surface without noise [see Figure 3.20(A)] is insensitive to d_1 and d_2 [Figure 3.20(B,C), respectively]. In addition, when we fit to a noisy surface [see Figure 3.20(D)], we again see that increasing d_2 allows the fit to deal with noise and

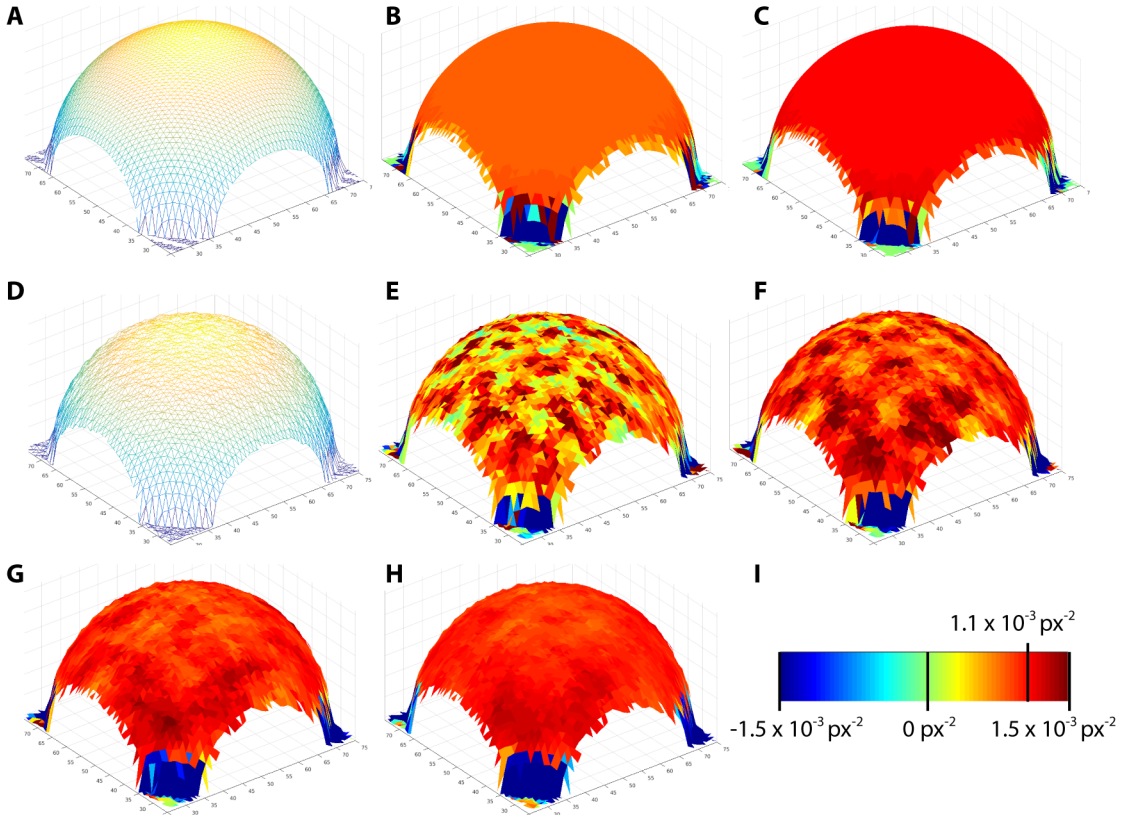


Figure 3.19: Fitting the curvature of hemispheres with varying noise. (A-C) A hemisphere with $r = 30$ px and $K = 1.1 \times 10^{-3}$ px $^{-2}$ everywhere. The original triangulation is displayed in (A), the output of the initial least-squared fit with $d_1 = 2$ in (B), and the output of the IRLS fit with $d_2 = 4$ in (C), with the color scale for the curvature in (I). (D-H) The hemisphere in (A) with random noise from a distribution with mean 0 px and width 0.3 px added to the height at every point in the triangulation. The triangulation is displayed in (D), the output of the initial least-squared fit with $d_1 = 4$ in (E), and the output of the IRLS fit with $d_2 = 6, 8, 10$ in (F-H), respectively, with the color scale for the curvature in (I).

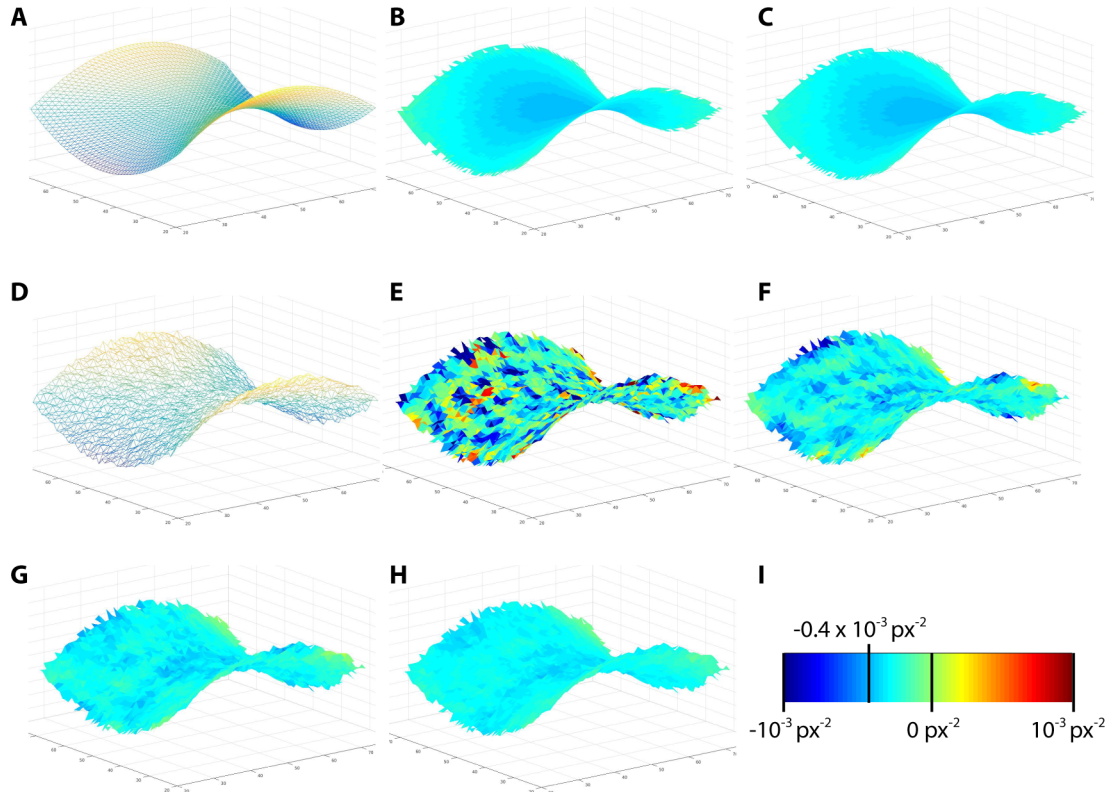


Figure 3.20: Fitting the curvature on a saddle surface with varying noise. (A-C) A saddle surface with $K = -0.4 \times 10^{-3} \text{ px}^{-2}$ in the center of the surface. The original triangulation is displayed in (A), the output of the initial least-squared fit with $d_1 = 2$ in (B), and the output of the IRLS fit with $d_2 = 4$ in (C), with the color scale for the curvature in (I). (D-H) The surface in (A) with random noise from a distribution with mean 0 px and width 0.3 px added to the height at every point in the triangulation. The triangulation is displayed in (D), the output of the initial least-squared fit with $d_1 = 4$ in (E), and the output of the IRLS fit with $d_2 = 6, 8, 10$ in (F-H), respectively, with the color scale for the curvature in (I).

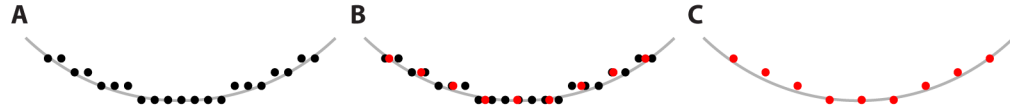


Figure 3.21: Downsampling a surface. (A), Imaging the curved contour in gray leads to “step” artifacts in the black points. (B), We downsample the black points to get the red points. (C), The red points still represent the gray contour without so many step artifacts.

return Gaussian curvature similar to that of the noiseless surface [Figure 3.20(F–H)].

Overall, our curvature fitting routine works well far from the boundaries. Near the boundaries, the curvature fit does not always work very well, as seen in the curvature near the corners in Figure 3.19(C,F–H), as there is less long-range information available when a point is within d_2 of a boundary. As a consequence, we typically neglect curvature values within $d_2/2$ of the boundary.

3.5.7 Measuring the curvature of toroidal droplets

Before we measure the curvature of the $h(x, y)$ output from time-averaging the intensity of a confocal image stack, we first have to remove measurement artifacts. Since $h(x, y)$ is a discrete quantity set by the height resolution of the confocal, the triangulated surface appears to have “steps” where the measured surface jumps from the height of one image plane to another. This is illustrated in the schematic in Figure 3.21(A), where imaging the gray contour leads to steps in the (\bullet) data points. The steps on the surface are artifacts and affect the curvature measurement; the steps create flat areas with no curvature, while the jumps in height have large curvature. We remove these steps by downsampling the initial $h(x, y)$ until the output triangulation show no steps. For our example with the gray contour [Figure 3.21(A)], we downsample the (\bullet) points, yielding the (\circ) points [Figure 3.21(B)]; the (\circ) points still represent the gray contour well [Figure 3.21(C)]. If we downsample too much, we risk eliminating real curvature features in our data. In practice, we typically downsample

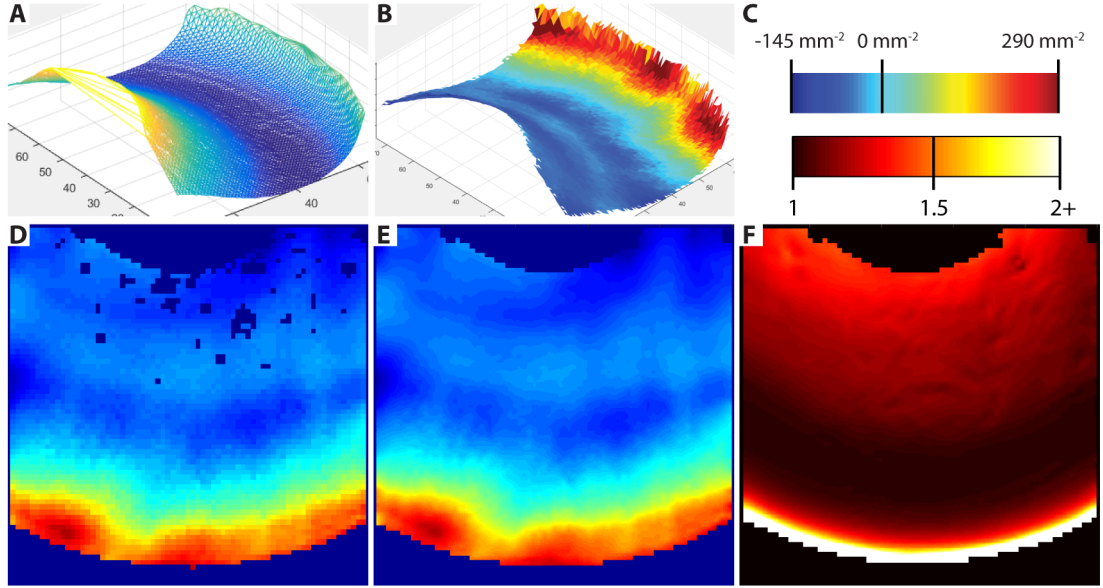


Figure 3.22: Measuring the Gaussian curvature and \sqrt{g} on a torus. (A) Triangulation colored by height formed from a downsampled $h(x, y)$. (B-D) The Gaussian curvature of the triangulation in (A) displayed as a (B,D) triangulation and an image, respectively, with the values given by the upper colorbar in (C). (E) The Gaussian curvature in (D), upsampled and with missing data filled in using linear interpolation to return the data to its original size. (F) The upsampled and filled in \sqrt{g} obtained from the corrected normal vectors with the values given by the lower colorbar in (C).

$h(x, y)$ with an initial size $512 \text{ px} \times 512 \text{ px}$ to a final size $75 \text{ px} \times 75 \text{ px}$. We triangulate the downsampled surface, as shown in Figure 3.22(A). We fit the curvature on the triangulation with $d_1 = 4$ and $d_2 = 12$, as shown in Figure 3.22(B,D), and then use linear interpolation to upsample the final $K(x, y)$ and $\sqrt{g}(x, y)$ back to the original size, as seen in Figure 3.22(E,F), respectively.

3.6 Defect charge and curvature

From the fitted curvatures and the defect locations over time, we look to compare the time-averaged topological charge in a region with the integrated Gaussian curvature of the region.

3.6.1 Finding regions of specific integrated Gaussian curvature

We start by considering a binary mask $\Theta_0(x, y)$ representing the full area in the intensity projection where we have data for the director field. We then remove the outer 10 px to 30 px of $\Theta_0(x, y)$ by successively finding the boundary $\partial\Theta_0$ of the region and setting the pixels to 0 until $\Theta_0(x, y)$ only contains places where we trust the curvature. This mask serves as our base from which we will determine any subregion $\Theta(x, y)$ we wish to look at. From some $\Theta(x, y)$, we calculate the integrated Gaussian curvature in that region numerically,

$$\oint_{\Theta} K dA \approx \sum_{x,y} \Theta(x, y) K(x, y) \sqrt{g}(x, y). \quad (3.43)$$

Since the area is positive-definite, the maximum integrated Gaussian curvature and the minimum integrated Gaussian curvature masks are easy to generate simply by starting with the base $\Theta_0(x, y)$ and setting the pixels with $K < 0$ or $K > 0$ to 0. These two masks define the range of integrated Gaussian curvature that we can probe for the imaged section of a single toroid. We can also easily divide the base $\Theta_0(x, y)$ into halves or thirds to consider regions of different integrated Gaussian curvature.

We can also find regions with specific values of integrated Gaussian curvature. From some starting $\Theta(x, y)$ we calculate the starting integrated Gaussian curvature and determine whether it is greater or less than the desired value. The routine then finds the boundary, $\partial\Theta$, and sets all the pixels on $\partial\Theta$ with the appropriately signed K to 0. For example, if the current integrated Gaussian curvature is greater than the target integrated Gaussian curvature, all the boundary pixels with $K > 0$ are set to 0. This process is repeated until the difference between the current integrated Gaussian curvature and the target integrated Gaussian curvature changes sign. The routine then takes the most recently removed boundary pixels and adds them back to the modified $\Theta(x, y)$ one-by-one until the difference between the current integrated

Gaussian curvature and the target integrated Gaussian curvature has the same sign as the difference between the initial integrated Gaussian curvature and the target integrated Gaussian curvature.

3.6.2 Time-averaged defect charge as a function of integrated Gaussian curvature: curvature-induced defect unbinding

We correlate the time-averaged topological charge in a region with the integrated Gaussian curvature of that region for both 36 mM ATP and 144 mM ATP. We find that for both ATP concentrations, \bar{s}_Θ is linear with $\int_\Theta K dA$, as shown in Figure 3.23, where we plot data from toroids with a range of ξ and a . The slope of each curve, C' , is positive, consistent with the curvature-induced defect unbinding predicted theoretically. Recall that for an equilibrium nematic, we expect the charge to be a discrete multiple of 1/2 and increases as a step function as we integrate K along the azimuthal direction [see Figure 3.4(A)]. However, due to the large number of defects and their constant motion, the time-averaged topological charge becomes a real number. Furthermore, \bar{s}_Θ only depends on the integrated Gaussian curvature and is independent of ξ and a . This implies that the unbinding only depends on the local geometry and is insensitive to the global size and shape of the system.

This is direct contrast to equilibrium simulations and theory, where defect unbinding only appears in toroids with curvatures large enough to overcome the attraction between opposite signed defects [118, 119]. In addition, in equilibrium systems, the repulsions between like-signed defects and the defect core energies affect the number of defects in a defective ground state [119]. This implies that in equilibrium, ξ and a are predicted to not only affect whether or not defects exist in the ground state, but also the number of defects in the ground state [117–121].

We also note that the lines in Figure 3.23(A,B) both go through $(0, 0)$, indicating that regions with $\oint_\Theta K dA = 0$ have $\bar{s}_\Theta = 0$, a topological requirement for the

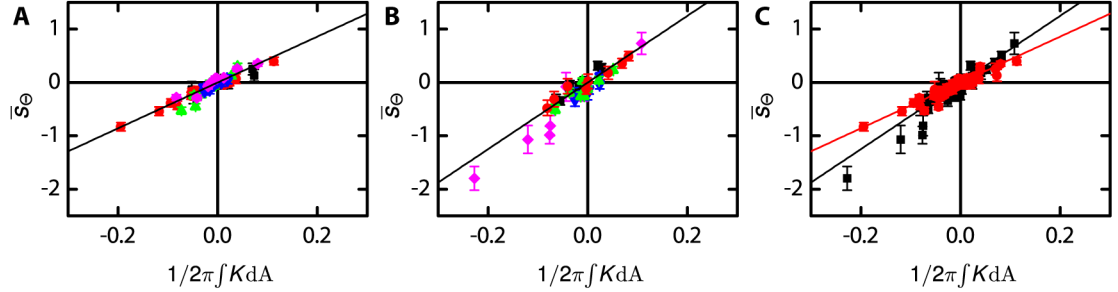


Figure 3.23: Defect unbinding in active nematic toroids. (A,B) Time-averaged topological charge in an area vs the integrated Gaussian curvature of the area for toroids with (A) 144 μM ATP, (B) 36 μM ATP, and (C) both ATP concentrations with the data from (A) in red and the data from (B) in black. The lines in (A) and (B) are weighted averages of a linear fit to the data for each individual toroid in the plot and have slopes 4.3 ± 0.7 and 6.3 ± 0.5 , respectively with intercepts 0.01 ± 0.02 and 0.02 ± 0.03 , respectively. The toroids in (A) have: (●) $\xi = 1.6$ and $a = 275 \mu\text{m}$, (▲) $\xi = 2.0$ and $a = 372 \mu\text{m}$, (◆) $\xi = 2.4$ and $a = 268 \mu\text{m}$, (■) $\xi = 5.9$ and $a = 200 \mu\text{m}$, and (▼) $\xi = 6.6$ and $a = 167 \mu\text{m}$. The toroids in (B) have: (●) $\xi = 1.8$ and $a = 334 \mu\text{m}$, (▲) $\xi = 2.7$ and $a = 365 \mu\text{m}$, (◆) $\xi = 3.6$ and $a = 151 \mu\text{m}$, (■) $\xi = 4.7$ and $a = 200 \mu\text{m}$, and (▼) $\xi = 6.0$ and $a = 547 \mu\text{m}$.

entire toroid. In our case, however, we see that this is true irrespective of the region we consider, provided the region has vanishing integrated Gaussian curvature. This is shown explicitly in Figure 3.13, where all the regions under consideration, Figure 3.13(A,C,E), have $\int_{\Theta} K dA = 0$ and vanishing time-averaged topological charge [Figure 3.13(B,D,F)]. This implies that a region with $\oint_{\Theta} K dA = 0$ is representative of an entire toroid. Again, this is in contrast to equilibrium nematics, where the small defect number and lack of significant defect motion result in different regions with the same net integrated Gaussian curvature generally enclosing a different topological charge. Finally, we see that changing the ATP concentration yields a different amount of unbinding, with $C' = 4.3 \pm 0.7$ for the 144 μM ATP concentration and $C' = 6.3 \pm 0.5$ for the 36 μM ATP concentration, indicating that increasing activity leads to less curvature-induced unbinding. This is seen explicitly in Figure 3.23(C), where we plot the data for both ATP concentrations to emphasize that ATP and thus activity is the dominant factor in the amount of unbinding.

Thus, our results suggest that activity is playing a role that reminds us of temperature in equilibrium systems. In 2D, the nematic-isotropic phase transition is predicted to be continuous [79], such that the nematic elasticity should vanish smoothly on the approach to the phase transition. As an equilibrium nematic gets sufficiently close to the nematic-isotropic phase transition, thermal fluctuations will begin to play an increasingly dominant role. The fluctuations will eventually mobilize the defects and produce results that could resemble in some ways what we see in our active nematic.

3.7 Defect number distributions

Because of the continuous creation, annihilation, and motion of the defects, the defect number in a region fluctuates over time, as shown in Figure 3.12(B). For the 144 μM ATP toroids, we have enough timeframes to obtain the defect number distribution for regions containing different \bar{N}_Θ . The defect number distributions are Gaussian, as shown in Figure 3.24(B,D,F) for three distributions obtained on the same toroid with $\xi = 1.6$ and $a = 275 \mu\text{m}$; each distribution is obtained from the region bounded with the white border in the associated image in Figure 3.24(A,C,E), respectively. In each image, the region is not necessarily contiguous and has vanishing integrated Gaussian curvature; however, each region has a different total area [see Figure 3.24(A,C,E)].

Since the data are described by a Gaussian, we obtain both the fluctuations in the defect number, $\sqrt{\Delta N_\Theta^2}$, and the mean number of defects, \bar{N}_Θ , by fitting each distribution to $A \exp(-\bar{N}_\Theta^2/(2\Delta N_\Theta^2))$, with A a free parameter [see Figure 3.24(B,D,F)]. We then plot the relative root-mean-squared (RMS) fluctuations, $\sqrt{\Delta N_\Theta^2} / \bar{N}_\Theta$, vs \bar{N}_Θ for every region on all of our toroids on a log-log plot, as shown in Figure 3.24(G).

We see that like the time-averaged topological charge, all the data collapse onto a line, regardless of the ξ and a variation between the toroids. We take the weighted average of a linear fit on a log-log scale to the data from each individual toroid, where the error in the fit determines the weight, and find a final slope -0.53 ± 0.04 and

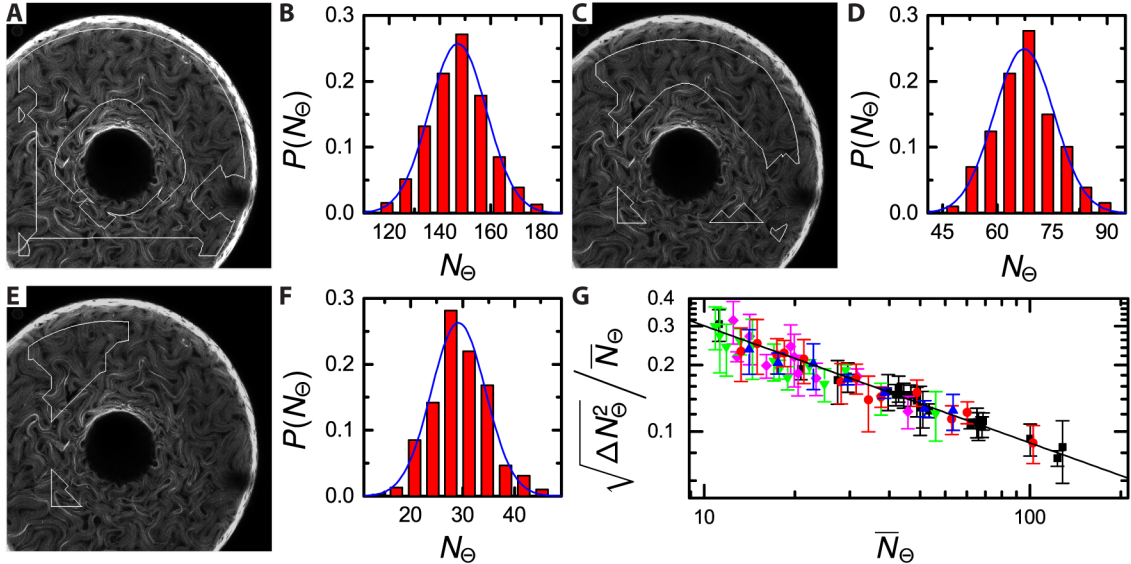


Figure 3.24: Defect number distributions. (A,C,E) For an experiment with $\xi = 1.6$ and $a = 275 \mu\text{m}$, the regions outlined in white have vanishing integrated Gaussian curvature and total area (A) $A_\Theta = 0.75 \text{ mm}^{-2}$, (B) $A_\Theta = 0.34 \text{ mm}^{-2}$, and (C) $A_\Theta = 0.15 \text{ mm}^{-2}$. (B,D,F) The probability of finding a number of defects in the regions in (A,C,E), respectively. (G) The relative RMS defect number fluctuations in a region vs the time-averaged defect number in the region for experiments with (■) $\xi = 1.6$ and $a = 275 \mu\text{m}$, (●) $\xi = 2.0$ and $a = 372 \mu\text{m}$, (▲) $\xi = 2.4$ and $a = 268 \mu\text{m}$, (▼) $\xi = 5.9$ and $a = 200 \mu\text{m}$, and (◆) $\xi = 6.6$ and $a = 167 \mu\text{m}$. The line is the weighted average of a linear fit on a log-log scale to the data for each individual toroid and has slope -0.53 ± 0.04 and intercept 0.02 ± 0.04 .

final intercept 0.02 ± 0.04 . This means that $\sqrt{\Delta N_\Theta^2} / \bar{N}_\Theta \sim \bar{N}_\Theta^{-1/2}$, which is the expected result for an equilibrium system subject to number fluctuations [161, 162]. Again, this suggests that the role of activity is somewhat reminiscent to the role of temperature in equilibrium systems.

3.8 Comparison with numerical simulations

To gain further insight about our experimental findings, we compare with numerical simulations performed by Luca Giomi and Dan Pearce at the University of Leiden. The simulations treat the defects as point particles with the system energy given by Eq. 1.7. For a torus with N defects, the simulation has $N/2$ $s = +1/2$ defects and

$N/2$ $s = -1/2$ defects in order to satisfy the Poincaré-Hopf Theorem.

3.8.1 Simulation details

Defects are modeled as massless particles on the torus [see Figure 3.25(A)], with the i^{th} defect having charge $s_{(i)}$, position $\mathbf{r}_{(i)}$, and orientation $\mathbf{p}_{(i)} = -\cos \psi \hat{\theta} + \sin \psi \hat{\varphi}$, with $\hat{\theta}$ and $\hat{\varphi}$ unit vectors on the surface of the torus [Figure 3.4], and ψ an angle in the tangent plane measured off of $\hat{\theta}$. The defects are governed by the following equations of motion,

$$\frac{d\mathbf{r}_{(i)}}{dt} = v_0 \mathbf{p}_{(i)} + \mu \left[\sum_{j \neq i=1}^N \mathbf{F}_{(ij)} - \nabla_{(i)} V \right] + \zeta_{(i)}^{\text{trans}} \quad (3.44)$$

$$\frac{d\psi_{(i)}}{dt} = \zeta_{(i)}^{\text{rot}}, \quad (3.45)$$

where v_0 is the speed associated to the self-propulsion of the $s = +1/2$ defects, μ is a mobility coefficient, and $\zeta_{(i)}^{\text{trans}}$ and $\zeta_{(i)}^{\text{rot}}$ are uncorrelated translational and rotational noises, reproducing the fluctuations of the defects[163]. Both $\mathbf{F}_{(ij)}$ and $V_{(i)}$ are calculated from Eq. 1.7,

$$\mathbf{F}_{(ij)} = 4\pi^2 k_F s_{(i)} s_{(j)} \nabla_{(j)} G(\mathbf{r}_{(i)}, \mathbf{r}_{(j)}) \quad (3.46)$$

$$V = -2\pi s_{(i)} k_F \int dA G(\mathbf{r}, \mathbf{r}_{(i)}) K(\mathbf{r}), \quad (3.47)$$

where $G(\mathbf{r}_{(i)}, \mathbf{r}_{(j)})$ is the Laplacian Green function on the torus and k_F is the Frank constant in 2D. $\mathbf{F}_{(ij)}$ and $V_{(i)}$ are, respectively, the force resulting from defect-defect interactions and the potential energy associated to the interaction between the defect and the local Gaussian curvature.

There are three main material parameters in an active nematic that affect its dynamics, α , k_F , and the shear viscosity, η . Since the simulations are in 2D, these quantities are all 2D and have units $[\alpha] = \text{Force}/\text{Length}$, $[k_F] = \text{Force} \times \text{Length}$, and

$[\eta] = \text{Force} \times \text{Time}/\text{Length}$. From Eq. 3.2 we know that α measures the strength of the activity that causes the nematic to deform. Since these deformations are resisted by the passive nematic elasticity, we can combine α and k_F to form the active length scale $\ell_a = \sqrt{k_F/|\alpha|}$, that represents the length at which the active stresses and passive elastic stresses balance. The active stress can deform the material when the wavelength of the distortion is longer than ℓ_a , but the passive elasticity prevents deformations with a shorter wavelength. In this sense, ℓ_a can be thought of as the buckling length of the active nematic, giving the size of the distortion surrounding a $s = \pm 1/2$ defect. Thus, when $\ell_a \lesssim L$, with L the system size, the passive elasticity and the active stresses roughly balance and few defects are created [105]. In this regime, the flow is laminar [105]. However, when $\ell_a \ll L$, the active stresses dominate and pairs of $s = \pm 1/2$ spontaneously create and annihilate. The passive elasticity prevents like-signed defects from having a separation distance smaller than ℓ_a ; similarly, the active stresses create a $s = \pm 1/2$ defect pair whenever there is a region of undistorted nematic larger than ℓ_a [105]. As a consequence, the active length scale is proportional to and of the same order of magnitude as the distance between defects, $\lambda = \sqrt{A_{torus}/N} = 2\pi a \sqrt{\xi/N}$, with $A_{torus} = 4\pi^2 R_0 a = 4\pi^2 \xi a^2$, the surface area of a torus.

Due to the large number of defects and their constant motion, the nematic dynamics become turbulent, with the characteristic velocity of the $s = +1/2$ defects as $v_0 \approx \alpha \ell_a / \eta = \text{sign}(\alpha) \sqrt{|\alpha| k_F} / \eta$. [105, 164]. Thus, the dimensionless distance between defects $\lambda' = \lambda/a$ and the dimensionless speed $v'_0 = v_0 a / (\mu k_F)$ specify all the relevant material properties of the active nematic in the numerical simulations.

For fixed λ' , we find that \bar{s}_Θ is a linear function of the integrated Gaussian curvature, and the line passes through $(0, 0)$. This implies that, as in the experiments, regions with vanishing integrated Gaussian curvature are representative of the full torus. However, in the simulation, we can easily tune v'_0 . For increasing v'_0 , we find

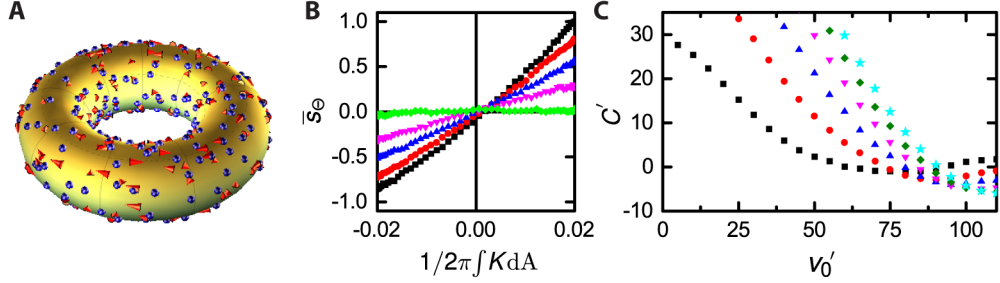


Figure 3.25: Defect unbinding in simulations depends on defect velocity and defect density. (A) Schematic of a torus with $\xi = 3$ and 250 defect pairs on the surface ($\lambda' = 0.49$) at a single moment in time. (B), Plot of time-averaged topological charge in a region vs the integrated Gaussian curvature in that region for a simulation with $\lambda' = 0.49$ and (■) $v'_0 = 10$, (●) $v'_0 = 20$, (▲) $v'_0 = 30$, (▼) $v'_0 = 40$, and (◆) $v'_0 = 60$. (C) The slope of the curves in (B), C' , vs defect velocity for simulations with (■) $\lambda' = 0.69$, (●) $\lambda' = 0.49$, (▲) $\lambda' = 0.40$, (▼) $\lambda' = 0.34$, (◆) $\lambda' = 0.31$, and (★) $\lambda' = 0.28$.

that C' decreases [see Figure 3.25(B)], eventually approaching zero. At this point, activity dominates over the elastic forces associated to defect-curvature interactions, confirming that, from this perspective, the role of activity is reminiscent of the expected role of thermal fluctuations close to the nematic-isotropic phase transition in passive nematics. However, we emphasize that in equilibrium, both the $s = +1/2$ and the $s = -1/2$ defects would randomly explore the toroid as a result of thermal motion. This is in contrast to our active system, where only the $s = +1/2$ defects are driven by activity. In addition, the direction of the velocity of an $s = +1/2$ defect is determined by the defect's structure, while in passive nematics thermal fluctuations will cause the defect to diffuse isotropically. The motion of the $s = +1/2$ defects can thus be thought of as a persistent, or correlated, random walk, where the defect's current trajectory influences its future trajectory. Finally, we see that the observed behavior of C' with v'_0 is maintained irrespective of λ' , as shown in Figure 3.25(C).

3.8.2 Matching simulation parameters to experiment

To quantitatively compare the experimental and simulated results, we need λ' and thus the total defect density on our experimental toroids. Since both our simulations

and our experiments indicate that regions with vanishing integrated Gaussian curvature are representative of the full torus, that is, that $\bar{N}/A_{torus} = \bar{N}_\Theta/A_\Theta$, where $\int_\Theta K dA = 0$, we use these regions to compare between the experiment and the simulation. We note that \bar{N}_Θ/A_Θ varies linearly with $\langle K \rangle_\Theta = (\int_\Theta K dA)/A_\Theta$ such that we can fit a line to this relation and take the value of \bar{N}_Θ/A_Θ at $\langle K \rangle_\Theta = 0$ to be \bar{N}/A_{torus} [see Figure 3.26]. We calculate λ' for each toroid and find that the λ' values for each ATP concentration are similar to each other. Thus, we take a weighted average to obtain $\lambda' = 0.31 \pm 0.04$ and $\lambda' = 0.3 \pm 0.1$ for the 144 μM and 36 μM ATP concentrations, respectively. In addition, we perform a weighted average on the value of \bar{N}_Θ/A_Θ for $\langle K \rangle_\Theta = 0$ to get the defect density for each ATP concentration, with $\bar{N}/A_{torus} = (157 \pm 19)$ defects/mm² for the 144 μM ATP concentration and $\bar{N}/A_{torus} = (90 \pm 14)$ defects/mm² for the 36 μM ATP concentration. We see that in our experiments, increasing $|\alpha|$ leads to increasing values of \bar{N}/A_{torus} , consistent with the idea that $\ell_a = \sqrt{k_F/|\alpha|} \sim \lambda = \sqrt{A_{torus}/\bar{N}}$. However, λ' doesn't change between the ATP concentrations in our experiments because the toroids we used for the 36 μM ATP concentration had a larger tube radius than the toroids used for the experiments with 144 μM ATP.

We now return to the plot of C' vs v'_0 and indicate our experimentally measured C' values with a horizontal line, as seen in Figure 3.26(B,C) for 144 μM and 36 μM ATP, respectively. We then consider our experimental values of λ' and highlight the crossing point between the experimentally measured C' values and the relevant simulation curve with a vertical dashed line. This crossing point gives the values $v'_0 = 81 \pm 2$ and $v'_0 = 80 \pm 10$, for the 144 μM and 36 μM ATP concentration. Rewriting the expression for v'_0 in terms of λ' , we have $v'_0 = (|\alpha|a^2\lambda')/(\mu k_F \eta)$, showing that the large uncertainty in v'_0 for the 36 μM ATP toroids comes from the large uncertainty in the associated λ' . However, since we see that v'_0 doesn't change appreciably when we change α in our experiments, this implies that one or more of μ , k_F , and η must

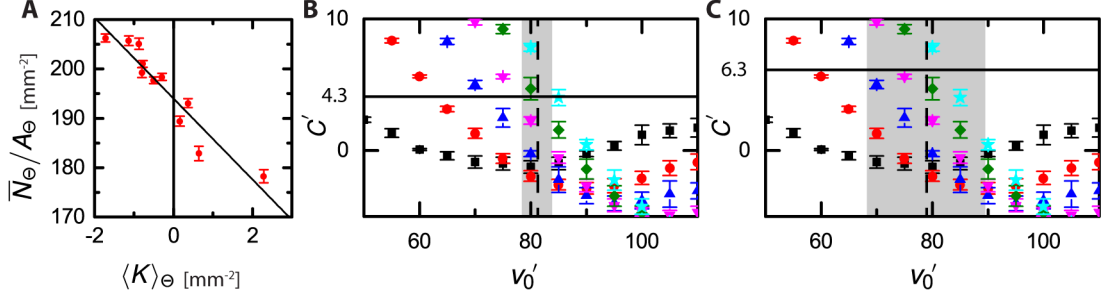


Figure 3.26: Quantitatively comparing experiment and simulation. (A) Time-averaged defect density in a region vs the mean Gaussian curvature of that region for an experiment with $\xi = 1.6$, $a = 275$ μm . (B,C) C' vs defect velocity for simulations with (■) $\lambda' = 0.69$, (●) $\lambda' = 0.49$, (▲) $\lambda' = 0.40$, (▼) $\lambda' = 0.34$, (◆) $\lambda' = 0.31$, and (★) $\lambda' = 0.28$, with the horizontal line corresponding to the experimental value of (B) $C' = 4.3$ for the 144 μM ATP toroids and (C) $C' = 6.3$ for the 36 μM ATP toroids. In both plots, the vertical dashed line marks the crossing of the horizontal line and the $\lambda' = 0.31$ simulation curve, with the gray background giving the error due to the uncertainty in the λ' for the respective experimental measurements.

also depend on α .

We confirm our estimate of v'_0 for the 144 μM ATP concentration by calculating the defect number distributions in the simulations. Similar to the experiment, we see that the probability of finding a number of defects in a region is Gaussian [see Figure 3.27(A)]. In the simulation, however, we have the ability to easily vary v'_0 . We plot $\sqrt{\Delta N_\Theta^2} / \bar{N}_\Theta$ vs $\bar{N}_\Theta^{-1/2}$ and see they are linearly related, as shown for 3 values of v'_0 in Figure 3.27(B). We then correlate $\sqrt{\Delta N_\Theta^2 / \bar{N}_\Theta}$ with v'_0 and plot the relationship in Figure 3.27(C), where the vertical line corresponds to the experimental result of $v'_0 = 81 \pm 2$. Comparing with the simulation, we find $\sqrt{\Delta N_\Theta^2 / \bar{N}_\Theta} \approx 0.99$, shown with a dashed line in Figure 3.27(C). From the intercept of the line plotted in Figure 3.24(G), we obtain $\sqrt{\Delta N_\Theta^2 / \bar{N}_\Theta} = 1.02 \pm 0.04$, consistent with the numerical results.

The agreement between the experiments and the theory reveals that the interaction between curvature and topological charge depends only on two parameters: (i) the dimensionless mean distance between defects, λ' , and (ii) the dimensionless speed

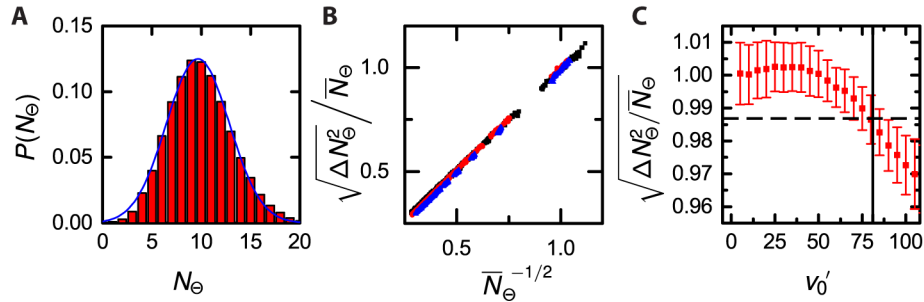


Figure 3.27: Defect number fluctuations depend on defect velocity. (A) Probability of finding a number of defects in a given region for a simulation with $\lambda' = 0.49$, $v'_0 = 50$. The blue curve is a fit of the data to a Gaussian. (B) Relative RMS defect number fluctuations in a region vs $\bar{N}_\Theta^{-1/2}$, with \bar{N}_Θ the time-averaged number of defects in the region for simulations with (■) $v'_0 = 4$, (●) $v'_0 = 50$, and (▲) $v'_0 = 80$. (C) Slope of the relative RMS fluctuations vs $\bar{N}_\Theta^{-1/2}$ plotted against the dimensionless defect velocity. The vertical solid line corresponds to $v'_0 = 81$.

of the defects, v'_0 , which relates to the intrinsic activity of the system. We emphasize that both of these parameters reflect local interactions that do not depend on the global size or geometry of the system. We find that because of the large number of defects and their constant motion, the average topological charge becomes a continuous variable. In addition, our results confirm that in the turbulent regime and free of any influence by a boundary, the mean distance between defects acts as a proxy for ℓ_a . Finally, in our experiments, we managed to change α while keeping λ' constant. Since v'_0 also doesn't change when we change α , we see that one or more of μ , k_F , and η must also depend on α .

3.8.3 Estimates of material parameters

The agreement between the experiment and the theory prompts us to use the topological defects as micro-rheological tracers and perform topological micro-rheology to estimate the material parameters of our active material. From our confocal data, we measure the typical value of the defect speed for both ATP concentrations, $v_0 \approx 1.5$ $\mu\text{m/s}$ and $v_0 \approx 0.25$ $\mu\text{m/s}$ for toroids with 144 μM ATP and 36 μM ATP, respec-

tively. Since v_0 clearly depends on the active stress, α , but v'_0 does not, we see that the defect mobility, μ , and/or the Frank constant in 2D, k_F , must depend on α . We use an estimate of the viscosity in 3D, $\eta_{3D} \approx 13$ Pa s from Ref. [108, 165], and take the average distance between defect, λ , to be equal to the active length scale, $\lambda = \ell_a$, in the expressions for v_0 and ℓ_a :

$$v_0 = \frac{\alpha\lambda}{\eta} = \frac{\alpha_{3D}\lambda}{\eta_{3D}} \quad (3.48)$$

$$\lambda = \sqrt{\frac{k_F}{|\alpha|}} = \sqrt{\frac{k_{F,3D}}{|\alpha_{3D}|}} \quad (3.49)$$

to estimate $|\alpha_{3D}| \approx 250$ mPa and $k_{F,3D} \approx 1.6 \times 10^{-9}$ N for 144 μM ATP and $|\alpha| \approx 30$ mPa and $k_{F,3D} \approx 3.4 \times 10^{-10}$ N for 36 μM ATP. We emphasize that these values are the first estimates of their kind.

In addition, since $k_F \approx k_{F,3D}l_{layer}$, we estimate the nematic layer thickness, $l_{layer} \approx 15$ μm from our confocal data for both ATP concentrations and calculate $k_F \approx 2.4 \times 10^{-14}$ N m for the 144 μM ATP concentration and $k_F \approx 5.1 \times 10^{-15}$ N m for the 36 μM ATP concentration. Combining this with the average tube radius $a = 260 \pm 40$ μm and $a = 320 \pm 70$ μm , for the 144 μM and 36 μM ATP concentrations, respectively, and the dimensionless defect velocity $v'_0 \approx 80$ for both ATP concentrations, we find $\mu \approx 200$ m/(N s) for both ATP concentrations. These values are summarized in Table 3.4. From these measurements, we see that k_F depends somewhat on α ; it is this dependence that is responsible for v'_0 not changing in our experiments with different α but constant λ' . The estimated values of k_F are also much larger than typical elastic constants for thermotropic liquid crystals ($\mathcal{O}(10^{-11}$ N)). One consequence of these large k_F values is that thermal fluctuations are not strong enough to cause the defects to move in the absence of activity. We can illustrate this by estimating a stress due to thermal fluctuations in the active nematic, $k_b T / (\text{microtubule length})^3 \approx (4 \times 10^{-21}) \text{J}/((1.5 \times 10^{-6}) \text{m})^3 \approx 1 \text{mPa}$. Comparing with Table 3.4, we see that the

Table 3.4: Estimates of material parameters for an active nematic on a toroid for 144 μM and 36 μM ATP.

	144 μM ATP	36 μM ATP
$ \alpha_{3D} $	250 mPa	30 mPa
$k_{F,3D}$	1.6×10^{-9} N	3.4×10^{-10} N
k_F	2.4×10^{-14} N m	5.1×10^{-15} N m
μ	200 m/(N s)	200 m/(N s)

stress due to thermal fluctuations is significantly weaker than $|\alpha|$.

Notably, topological defect micro-rheology is in principle geometry independent, and solely dependent on the fact that the nematic is in the turbulent regime and away from boundaries. To illustrate this, we consider experiments using an active nematic formulation identical to ours depleted onto a flat surface [122]. We consider the region highlighted in Figure 4D of Ref. [122] far from the boundary for an active nematic with 140 μM ATP. We take the average defect speed and defect density for that region when the system is in the turbulent regime, finding $v_0 = 1 \mu\text{m/s}$ and $\lambda = 50 \mu\text{m}$. We obtain $\alpha = 260 \text{ mPa}$ and $k_{F,3D} = 7 \times 10^{-9} \text{ N}$, consistent with the estimates from our data. Topological defect micro-rheology should also be valid for other types of two-dimensional active nematics, such as confined bacterial suspensions in a lyotropic liquid crystal [100].

3.9 Conclusions

We have performed the first experimental and theoretical study of an active liquid crystal confined on a surface having non-trivial geometry and topology: a toroid. Activity drives the system in a turbulent state characterized by a large concentration of defects of topological charge $s = \pm 1/2$. Like swimming microorganisms, these active defects are able to explore their surroundings. Most notably, we confirm that they are sensitive to the intrinsic geometry of the space they inhabit. This yields the spontaneous segregation of defects in regions of like-sign Gaussian curvature. Sur-

prisingly, this curvature-induced defect unbinding is driven only by local interactions. Furthermore, we determine that the defects can be used as micro-rheological tracers, and we provide the first estimates of the active stress, the Frank elastic constant, and the defect mobility of active nematic liquid crystals.

In the process of this work, we have leveraged techniques from the computer vision literature to determine the director from intensity images of the active nematic and to measure the curvature of a noisy surface. Prior to this work there were no standard method in the physics literature to accomplish either task. We anticipate that the analysis techniques used here will become the standard to measure the director in polymeric nematics and to measure the curvature of noisy surfaces. Overall, our results highlight the fundamental role of defects in living matter and introduce a new framework to explore the mechanical properties of active fluids.

CHAPTER 4

HOMEOTROPIC NEMATICS CONFINED IN TOROIDS AND BENT CAPILLARIES

4.1 Introduction

A system with broken reflection symmetry cannot be superimposed onto its reflection using only translations and rotations; it has a handedness and thus is chiral [1]. Chirality can have important consequences for a system. For example, as first shown by Pasteur [166], a material’s ability to rotate the polarization state of linearly polarized light results from broken reflection symmetry. This phenomenon is called optical activity and the handedness of the system determines the rotation sense of the light polarization [166]. Chiral systems can also exhibit “structural color,” where light interacting with a microscopic pattern produces color; for example, jeweled beetles appear iridescent due to light interacting with the chiral patterns on a beetle’s exoskeleton [167, 168].

Chiral systems can be formed from chiral building blocks, as in some photonic metamaterials [169, 170], or chirality can emerge via spontaneous symmetry breaking in an achiral system [171]. This latter scenario is often studied in nematic liquid crystals, where the mesogens are achiral [37, 40, 172–180]. Here, the symmetry-breaking is driven by the material elasticity; if the minimum energy state is chiral, then there must be a nontrivial twist distortion in the system.

This simplest way to break the reflection symmetry in a NLC is to prescribe twist with boundary conditions, as in the twisted nematic cell shown in Figure 4.1(A). In this scenario, the NLC is confined between two parallel plates with strong planar anchoring on each plate, specified by σ_1 and σ_2 , respectively. If the plates are in the

xy -plane and the distance between them is H , then $\mathbf{n}(z = 0) = \boldsymbol{\sigma}_1$ and $\mathbf{n}(z = H) = \boldsymbol{\sigma}_2$. When $\boldsymbol{\sigma}_1 \cdot \boldsymbol{\sigma}_2 = 0$, the boundary conditions require \mathbf{n} to twist by $\pm\pi/2$ along a vertical path. Computing the free energy density for such a cell using a linear twist ansatz $\mathbf{n} = \hat{x} \cos(\tau z/H) + \hat{y} \sin(\tau z/H)$, with τ the twist angle of the director between the plates, we have:

$$f = K_{22}(\mathbf{n} \cdot \nabla \times \mathbf{n})^2 = K_{22}\tau^2/H^2, \quad (4.1)$$

In the cell shown in Figure 4.1(A), $|\tau| = \pi/2$. Following the director along \hat{z} , we see that the twist is counterclockwise and thus is called a left-handed (LH) twist. However, the system could just as easily have a right-handed (RH) twist, as the spontaneous reflection symmetry breaking has no preference for either handedness in this case. We also see that the amount of twist is set by the anchoring conditions, and is the same for any NLC provided the material obeys the boundary conditions. However, if we were to change $\boldsymbol{\sigma}_1$ and $\boldsymbol{\sigma}_2$ such that $|\tau| \neq \pi/2$, the choice of handedness becomes biased; for example, if $\boldsymbol{\sigma}_1 \cdot \boldsymbol{\sigma}_2 = 1/\sqrt{2}$, then $\tau = \pi/4$ or $-3\pi/4$, leading to a difference in the free energy between the two twist directions. Consequently, the system will have a greater probability to have $\tau = \pi/4$, since this twist corresponds to the minimum energy state.

If we want to explore scenarios where the NLC has equal probability to adopt either handedness with $|\tau| \neq \pi/2$, we need scenarios where more than one distortion is at play. For example, consider a standard bipolar drop with degenerate planar anchoring, as shown schematically in Figure 2.11(A). Here, there are both splay and bend distortions, and the structure is achiral. If K_{22} and K_{33} are small enough compared to K_{11} , the bipolar drop will twist [see Figure 4.1(B)], relieving some of the splay distortions with the less costly twist and bend distortions [172, 173, 175]. The criterion governing this instability is called the Williams criterion, $K_{11} > K_{22} +$

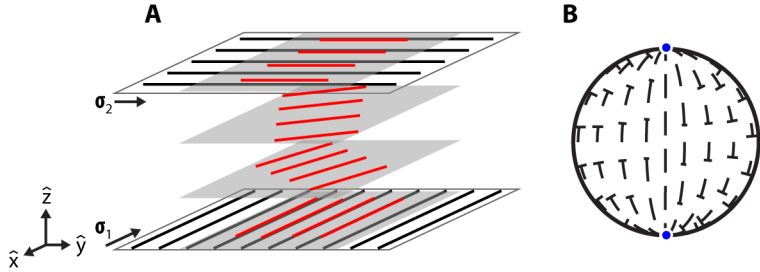


Figure 4.1: Spontaneous reflection symmetry breaking in twisted nematic cells and twisted bipolar droplets. (A), Schematic of a twisted nematic cell with a twist angle of $\pi/2$. The system could also satisfy the boundary conditions by twisting with the opposite handedness. (B), Schematic of a cross-section of the director in a twisted bipolar droplet. The nails represent the director going into the page. As with (A), the system could twist with the opposite handedness.

$0.431K_{33}$ [172, 181]. As with the twisted NLC cell with $|\tau| = \pi/2$, the handedness of the twist is randomly chosen. Provided K_{11} , K_{22} , and K_{33} satisfy the Williams criterion, the magnitude of the twist is determined by the elastic constants; in this scenario there is no way to tune the twist apart from changing the material properties of the NLC.

Prior work in our group with NLC confined to toroids with degenerate planar boundary conditions demonstrated that the amount of twist resulting from spontaneous symmetry breaking is not always only determined by the elastic constants [37]. We found a doubly-twisted director configuration in toroidal droplets, where the magnitude of the twist grew with decreasing ξ . Schematics of an achiral and of a doubly-twisted director field are shown in Figure 4.2(A,B) and Figure 4.2(C,D), respectively. Under degenerate planar anchoring, the saddle-splay distortion drives the director at the interface to align along the smallest principal curvature of the interface according to Eq 2.52 [39]. For example, consider a cylinder with radius a in the standard cylindrical coordinates $\{r, \theta, z\}$. The principal curvatures are $\kappa_1 = -1/a$ along $\hat{\theta}$ and $\kappa_2 = 0$ along \hat{z} . Thus, saddle-splay distortion will try to align the director along $\hat{\theta}$.

Increasing the difference between the principal curvatures of the interface will

cause the system to twist more. In our cylindrical example, this corresponds to decreasing a . For a torus, we have another option. In the $\{r, \theta, \varphi\}$ toroidal coordinates defined schematically in Figure 3.4(B), we can write the two principal curvatures:

$$\kappa_1 = -\frac{1}{a} \quad (4.2)$$

$$\kappa_2(\theta) = \frac{\cos(\theta)}{a(\xi - \cos(\theta))}, \quad (4.3)$$

Thus, decreasing ξ in our toroidal droplets causes $|\kappa_1 - \kappa_2(0)| = \xi/(a(\xi - 1))$ to increase, leading to our observations of increasing twist with decreasing ξ , as shown by the (●) symbols in Figure 4.2(E).

However, the twist still depends on the elastic constants. This is easiest to see by considering the Frank-Oseen free energy of a linear double-twist in the $\xi \rightarrow \infty$ “cylindrical limit” of a torus. Here, we use the ansatz in toroidal coordinates:

$$\mathbf{n} = \hat{\theta} \frac{\omega r}{a - g \frac{r}{\xi} \cos \theta} + \hat{\varphi} \sqrt{1 - \left(\frac{\omega r}{a - g \frac{r}{\xi} \cos \theta} \right)^2}, \quad (4.4)$$

where ω and g are parameters that determine the amount of twist and splay in the director field, respectively; $g = 1$ corresponds to a splay-free configuration. The free energy per unit length in this limit is given by:

$$\frac{F}{2\pi K_{33}} = \frac{K_{22} - K_{24}}{K_{33}} \omega^2 + \frac{\omega^4}{4} + \frac{K_{22}}{K_{33}} \sum_{n=3}^{\infty} \frac{\omega^{2n}}{2n}. \quad (4.5)$$

For $\omega \ll 1$, we can ignore the higher-order terms in the summation and minimize F to obtain:

$$\omega = 0; \quad \omega = \pm \sqrt{2 \frac{K_{24} - K_{22}}{K_{33}}}. \quad (4.6)$$

In this case $\omega = 0$ corresponds to a maximum in F . The twist angle is obtained by

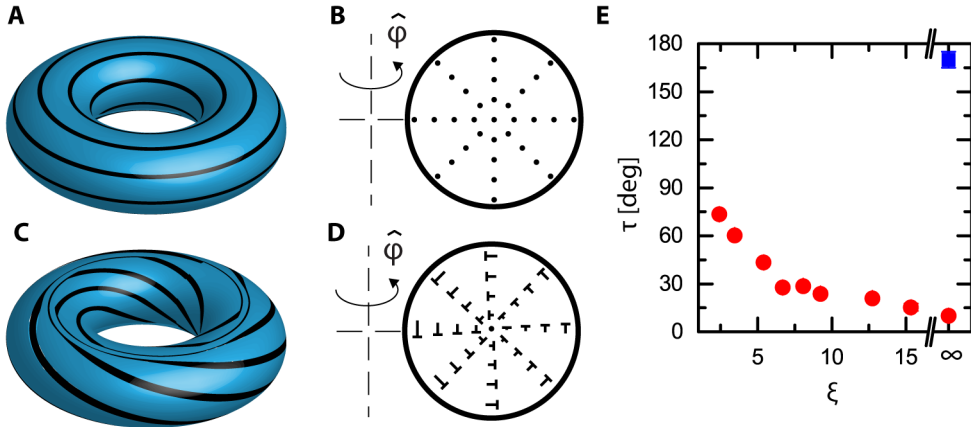


Figure 4.2: NLC in toroids with degenerate planar anchoring has a doubly-twisted ground state. (A-D), Director schematics for nematic toroids with degenerate planar anchoring. (A,B) Schematics for the twist-free state with (A) showing the director at the surface and (B) showing the director in a cross-section of the tube. (C,D) Schematics for doubly-twisted state with (C) showing the director at the surface and (D) showing the director in a cross-section of the tube. The nails represent the director going into the page. (E) Twist angle measured through the tube τ vs aspect ratio ξ for (●) 5CB and (■) SSY confined to toroidal droplets and cylindrical geometries. $\xi = \infty$ corresponds to measurements in a cylindrical geometry, and $\xi < \infty$ are previously published data in toroidal droplets from Ref. [37].

considering the angular difference between $\mathbf{n}(r = a, \theta = \pi/2)$ and $\mathbf{n}(r = a, \theta = 3\pi/2)$:

$$\begin{aligned}
 \tau &= \arccos(\mathbf{n}(r = a, \theta = \pi/2) \cdot \mathbf{n}(r = a, \theta = 3\pi/2)) \\
 &= \arccos(1 - 2\omega^2) \\
 &= \arcsin(2\omega\sqrt{1 + \omega^2}) \\
 &= 2\arcsin(\omega).
 \end{aligned} \tag{4.7}$$

Clearly then, the system will break reflection symmetry when $K_{24} > K_{22}$, and $|\tau|$ increases with increasing K_{24} and decreasing K_{22} .

We [40] and others [179] explored this directly by confining a Lyotropic Chromonic Liquid Crystal (LCLC) to a cylindrical capillary under degenerate planar anchoring conditions. LCLC are an aqueous dispersion of plank-like molecules that self-assemble into columnar aggregates; these aggregates then form a nematic at appro-

priate temperature and concentration [182]. In the nematic phase, LCLC typically have $K_{11} \sim K_{33} \sim 10K_{22}$; in the capillary, the small K_{22} yielded measured values of $|\tau| \approx 170^\circ$ for the LCLC Sunset Yellow (SSY). For comparison, using the value of $K_{22}/K_{33} = 0.4$ for 5CB and the value of $K_{24} = (1.04 \pm 0.04)K_{22}$ measured from our experiments with 5CB confined to toroidal droplets under degenerate planar anchoring, $\tau_{\xi \rightarrow \infty} = 19^\circ [+8^\circ, -19^\circ]$. We verify the twist in this limit directly using 5CB confined to a cylindrical geometry and find $|\tau_{\xi \rightarrow \infty}| = 9^\circ \pm 1^\circ$. In fact, in our experiments, even when $\xi \sim 1$, we never measured $|\tau| > 80^\circ$. We place these measurements of (■) SSY and (●) 5CB in cylindrical geometries on the twist-angle plot in Figure 4.2(E). Thus, even though saddle-splay lets us tune chirality via geometry, there is still a large influence from the material constants.

Inspired by these results in planar-anchored nematic toroids and capillaries, in this Chapter we consider 5CB confined to a toroidal droplet under homeotropic anchoring. For homeotropic anchoring, the saddle-splay contribution to the free energy is always a constant for a given geometry. Despite the fact that the saddle-splay distortion does not enter into the energy minimization problem for homeotropic nematics, we find spontaneous reflection symmetry breaking and geometrically-controlled chirality. Prior results for NLC with $K_{11} \sim K_{22} \sim K_{33}$ confined under homeotropic anchoring to capillaries [183] and to toroids with $a \sim \mathcal{O}(1)$ μm [41] found an escaped-radial (ER) configuration as the ground state. In contrast, when $K_{11} \sim K_{33} \gg K_{22}$, the system breaks reflection symmetry, and adopts a twisted-escaped-radial (TER) configuration [178]. This was again observed using LCLC; as in the degenerate-planar case, the low K_{22} results in a very large total twist.

What we find here is that confining a NLC with $K_{11} \sim K_{22} \sim K_{33}$ under homeotropic anchoring to toroidal droplets with $a \sim \mathcal{O}(100)$ μm yields a TER configuration, where the total twist decreases with increasing ξ , similar to our previous findings in planar anchored toroids. We attribute the twist to the additional bend

distortion introduced as ξ decreases. This additional bend distortion is relieved by a twist distortion with a spontaneously-chosen handedness. Our work demonstrates that geometry can tune chirality, even in the absence of an explicit curvature-coupling term in the free energy.

The rest of this Chapter is organized as follows. We begin with an overview of the ER and highly-twisted TER configurations in cylindrical capillaries, discussing qualitative differences between the structures and establishing an intensity ratio as a qualitative way to distinguish between the two configurations. We then consider NLC confined with homeotropic anchoring to toroidal droplets with $a \sim \mathcal{O}(100)$ μm . At low ξ we see an intensity ratio similar to the intensity ratio from the high-twist TER capillaries, while at high ξ we see an intensity ratio comparable to that from the achiral ER capillaries. Next, we use Jones Calculus to simulate OPM textures for a given director field, and validate our implementation on well-studied director configurations in spheres. We use a linear double-twist ansatz in a torus to demonstrate technical details of our implementation. Furthermore, we establish that we can successfully simulate OPM textures from twisted director fields by comparing the measured twist angle in our simulations with the twist angle imposed by the given director field. We also simulate TER textures in toroids and capillaries, finding that the intensity ratio decreases as the twist increases. Since this relationship is monotonic, the simulations indicate that comparing the intensity ratio in different toroids serves as a proxy for comparing the amount of twist in the toroids. Finally, we confirm that the twist is driven by the local geometry by confining NLC to bent capillaries under homeotropic anchoring. We measure a local aspect ratio and find that the intensity ratio in the bent capillaries has the same behavior as the intensity ratio in our homeotropic toroids. This implies that we can tune chirality with confining geometry, even in the absence of the saddle-splay distortion that directly couples the director at the surface with the curvature of the surface.

4.2 Escaped radial and twisted escaped radial configurations in capillaries

Consider NLC confined to a cylindrical capillary under homeotropic boundary conditions; in cylindrical coordinates $\{r, \theta, z\}$, we specify the boundary conditions with $\mathbf{n} = \hat{r}$ at the boundary. Restricting ourselves to a radial director field, $\mathbf{n} = \hat{r}$ everywhere, there is an $s = +1$ line defect running along \hat{z} at the center of the capillary, as shown in Figure 4.3(A). However, recall from Chapter 2.1.2 that integer-strength disclination lines are not topologically stable in a 3D NLC. Similar to line defects in 2D nematics or wall defects in 3D nematics, the singular $s = +1$ distortion can be continuously deformed to form a nonsingular distortion, as shown in Figure 2.4 [183–185]. As illustrated in Figure 4.3(B), the radial director field “escapes into the third dimension”, such that $n_z \neq 0$, hence the name escaped-radial. In the one-constant approximation, the ER director field is analytically solvable, with $\mathbf{n} = \{\sin(\Omega), 0, \cos(\Omega)\}$, where $\Omega(r) = 2 \arctan(r/a)$ gives the director angle measured off of \hat{z} , with a the cylinder radius, as shown by the blue curve in Figure 4.3(D) [183, 184]. Provided $a \gtrsim 0.1 \mu\text{m}$, the ER configuration is the ground state solution [73]; the costly splay distortion in the vicinity of the singular line is relieved by a less-costly bend distortion, with the cost of the bend distortion increasing as a decreases. When $a \lesssim 0.1 \mu\text{m}$, the cost of the bend distortion in the escape is too great and the $s = +1$ line defect is energetically stable. For NLC where $K_{11} \neq K_{33}$, $\Omega(r)$ changes [186]. When $K_{11} \ll K_{33}$, the n_z component of the director only becomes appreciable when $r \approx 0$. Hence, when $K_{11} < K_{33}$ we say that the director escapes more gradually, or slower. In contrast, when $K_{11} \gg K_{33}$, the n_z component becomes appreciable for $r \approx a$; when $K_{11} > K_{33}$ we say that the director escapes more abruptly, or faster. These behaviors can be visualized by taking $\Omega(r) = (\pi/2)(r/a)^\phi$, where $\phi < 1$ produces a slower escape and $\phi > 1$ produces a faster escape [red contours, Figure 4.3(D)]. The $\phi = 1$ behavior is similar to the escape in the 1-constant approximation [blue line,

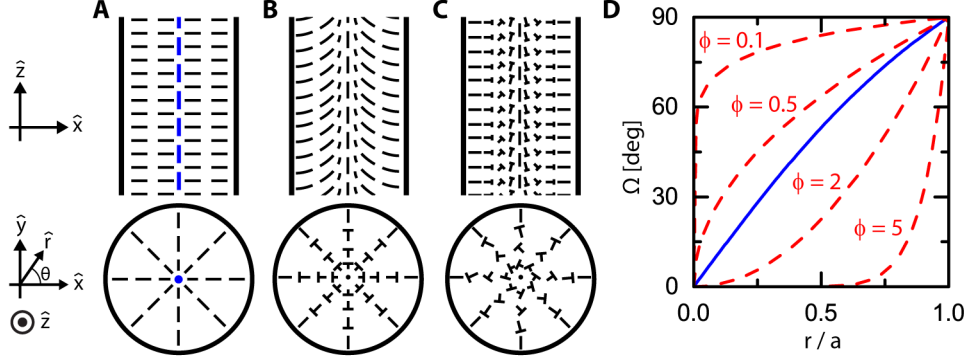


Figure 4.3: Singular and escaped-radial distortions in cylindrical geometries. (A-C), Cross-sections showing the director fields for a (A) singular $s = +1$ distortion, a (B) escaped-radial distortion, and a (C) twisted escaped-radial distortion. The nails represent the director going into the page. (D), Director angle Ω measured off of the cylinder axis as a function of normalized radius, r/a , with a the cylinder radius. The blue curve corresponds the equilibrium solution for the 1-constant approximation, while the red curves correspond to $\Omega = (\pi/2)(r/a)^\phi$, with $\phi = 0.1, 0.5, 2, 5$. The curves with $\phi = 0.1, 0.5$ escape slower than the equilibrium solution, while the curves with $\phi = 2, 5$ escape faster than the equilibrium solution.

Figure 4.3(D)].

Now with an ER configuration in the 1-constant approximation, let K_{22} vary while keeping $K_{11} = K_{33} = K$. When $K_{22} \lesssim 0.27K$ [178], the system can relieve some of the bend and splay distortions in the ER configuration by twisting, yielding the twisted escaped-radial configuration shown in Figure 4.3(C), where now \mathbf{n} has components along \hat{r} , $\hat{\theta}$, and \hat{z} . This configuration was first observed using LCLC [178]. Since $K_{22} \sim 10^{-1}K$ for LCLCs, they frequently exhibit spontaneous reflection symmetry breaking [40, 177–180].

4.2.1 Intensity profile and intensity ratio

We fill cylindrical capillaries with either 5CB or with a 31.5% w/w aqueous solution of SSY; at this concentration, SSY is in the nematic phase [182]. We use capillaries that are at least 4 cm long with diameters from 50 μm to 400 μm . To enforce homeotropic anchoring for the 5CB-filled capillaries, we first fill the capillary with

0.1% w/w lecithin in hexane and then let the hexane dry, depositing the lecithin on the inner surface of the capillary. We check each capillary with a microscope to make sure that the hexane has fully evaporated; this process can take anywhere from 10 minutes for the largest diameter capillaries to several hours for the smallest capillaries. For the SSY-filled capillaries, the capillaries were coated with parylene using chemical vapor deposition. The work was done by Karthick Nayani and Rui Chang using a commercial parylene coater (PDS2010; Specialty Coating Systems) according to a previously published protocol [178]. The precursor, [2,2]paracyclophe, was vaporized at 160° C, pyrolyzed into monomer at 650° C, and deposited at 20° C; the entire process was performed under vacuum (55 mtorr).

Bright-field images, shown in Figure 4.4(A,C), depict a 5CB and a SSY capillary, respectively. The corresponding OPM images are shown in Figure 4.4(B,D); from previous results, we expect the configurations to be ER and TER, respectively [178, 183]. By eye, it is easy to see that the OPM textures shown in Figure 4.4(B,D) are different; this makes sense when we consider the director field in each configuration and its impact on the intensity profile across the capillary. When the polarizer and analyzer (PA) are aligned along \hat{z} and \hat{x} , an OPM texture of an ER capillary [Figure 4.4(B)] should have three regions of extinction corresponding to the regions near the boundary and to the center of the capillary. In these regions, \mathbf{n} is along the P or A direction. Between these three dark regions there are two bright regions, corresponding to locations where \mathbf{n} has components along both \hat{x} and \hat{z} . This dark-bright-dark-bright-dark pattern is the signature of an ER capillary; now plotting the intensity profile across the capillary in Figure 4.4(E), we see that there are two clear intensity peaks corresponding to the bright regions, and an intensity minimum in the middle of the profile corresponding to the dark central region. Note that the intensity minimum is greater than zero; we believe this is due to scattering from thermal fluctuations in the director [22].

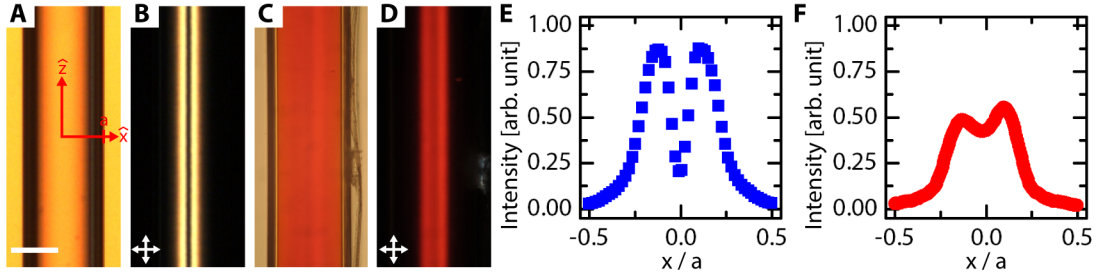


Figure 4.4: ER and TER capillaries and intensity profiles. (A,C), Bright field images of a capillary filled with (A) 5CB and (C) SSY with homeotropic anchoring. (B,D), corresponding OPM images showing that (A,B) 5CB has an ER configuration and (C,D) SSY has a TER configuration. (E,F), Intensity profiles measured across the capillary for (E) the 5CB texture in (B), and (F), the SSY texture in (D). The intensity scale is the grayscale intensity, with 1 corresponding to the white and 0 to black.

Conversely, when we look at the OPM texture for a TER configuration [Figure 4.4(D)], we see that the central region is no longer dark, but that it has an intensity comparable to the intensity of the two “bright” regions flanking the central region. We can rationalize this by following the director schematic in Figure 4.3(C) along \hat{y} through the center of the capillary. We see that the nonzero n_θ component results in \mathbf{n} having components along both \hat{x} and \hat{z} , the P and A directions, causing the transmitted intensity in this central region to grow [Figure 4.4(D)]. Plotting the intensity profile across the capillary in Figure 4.4(F), we see that there is still a central minimum surrounded by two peaks; however, the central minimum in the TER configuration is much higher than the central minimum in an ER configuration. In addition, we see that the peaks in the intensity profile do not have the same intensity value. This is a common feature of the TER profiles, and there is no trend in which side has a higher value. We quantify each intensity profile with an intensity ratio I_{max}/I_{min} , with I_{max} the average intensity of the two peaks flanking the central minimum and I_{min} the intensity of the central minimum. Our ER capillaries have $I_{max}/I_{min} \approx 4$ while our TER capillaries have $I_{max}/I_{min} \gtrsim 1$. We check that this phenomenon is not dependent on the LC chosen by comparing with the intensity pro-

file of an ER SSY capillary; while the ground state in a homeotropic SSY capillary is a TER configuration, just after being filled the SSY capillary has a transient ER configuration that spontaneously breaks reflection symmetry after a few minutes. As with the ER textures from the 5CB capillaries, $I_{max}/I_{min} \approx 4$ in the transient ER SSY capillary.

4.3 Nematic liquid crystals in toroids

We make stable toroidal droplets as detailed in Chapter 3, with 5CB as our inner liquid and an aqueous yield-stress material. Our yield-stress material for homeotropic nematic toroids is similar to that used in our prior work with planar-anchored nematic toroids [37], except here, we have replaced the polyvinyl alcohol used to enforce degenerate planar anchoring with sodium dodecyl sulfate (SDS) to enforce homeotropic anchoring. The yield-stress material consists of (i) 1.5% w/w polyacrylamide microgels (Carbopol ETD 2020), (ii) 30% w/w Ethanol, (iii) 3% w/w Glycerol, (iv) 25% w/w 32 mM SDS in ultrapure water, and (v) 40.5% w/w ultrapure water. Thus, the final mixture has approximately 8 mM SDS, a concentration that yields strong homeotropic anchoring [83]. To make the yield-stress material, we mix all the ingredients together, wait for ~ 24 hrs to allow the Carbopol to hydrate, and then neutralize the mixture by adding a volume of 2M NaOH solution until the pH ≈ 7 . Neutralizing the dispersion causes the polyacrylamide microgels to swell, increasing both the yield-stress and the transparency [37, 38].

We view our toroidal droplets from the top under both bright-field and with crossed polarizers, as shown in Figure 4.5(A,D) and Figure 4.5(B,E), respectively. In the OPM texture in Figure 4.5(B) for a toroid with $\xi = 5$, the regions where the tube of the torus is along the orientation of the polarizer and analyzer (P and A), the intensity pattern has the characteristic dark-light-dark-light-dark profile associated with an ER texture where the cylinder axis is oriented along the P and A directions.

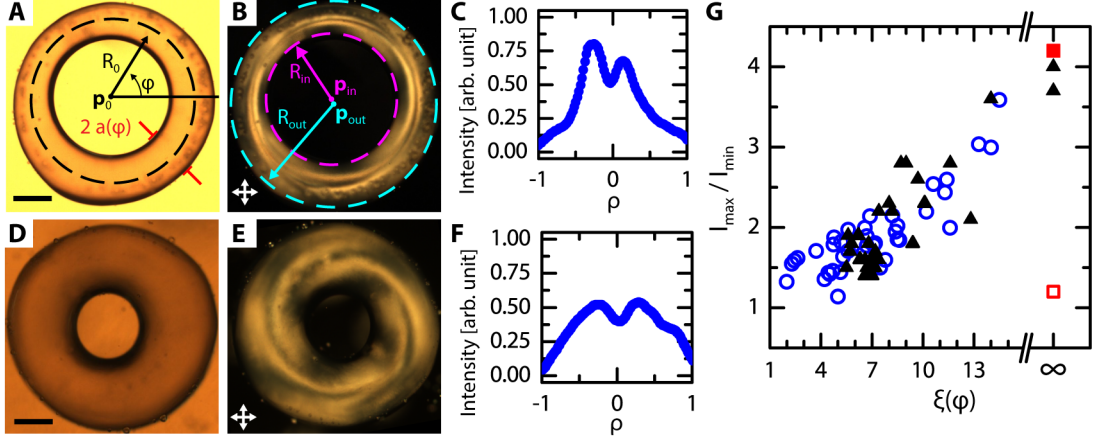


Figure 4.5: Images and intensity ratios for homeotropic nematic toroids. (A,B,D,E), (A,D) Bright-field and (B,E) associated OPM textures for toroids with (A,B) $\xi = 5$ and (D,E) $\xi = 1.8$. The central circle, defined by the radius R_0 , center \mathbf{p}_0 , and polar angle φ , as well as the local tube radius $a(\varphi)$ are defined on the image in (A). The inner and outer circles, given by the radii R_{in} and R_{out} and centers \mathbf{p}_{in} and \mathbf{p}_{out} , respectively, are drawn on the OPM texture in (B). (C,F), OPM Intensity profiles across the tube of the toroid in (B,E), respectively. These profiles are taken at $\varphi = 0$, with $\phi \in [-1, 1]$ parameterizing the contour from the inner circle to the outer circle for the given φ . Both profiles show two maxima surrounding a central minimum. We take I_{\max} to be the average of the intensity values of the maxima and I_{\min} to be the intensity at the central minimum. (G), I_{\max}/I_{\min} vs $\xi(\varphi) = R_0/a(\varphi)$ for a series of (○) homeotropic 5CB toroidal droplets, (▲) homeotropic 5CB bent and straight capillaries, and (■, □) homeotropic SSY straight capillaries. (■) corresponds to the transient ER state, while (□) corresponds to the equilibrium TER state. Scale bars in (A,D) are 250 μm .

However, for the toroid with $\xi = 1.8$, the OPM texture in Figure 4.5(E) has more of a spiral-like texture. To quantify these patterns, we measure the intensity profile across the tube of the torus.

4.3.1 Measuring the intensity profile and aspect ratio

From the top view, the azimuthal angle φ in toroidal coordinates, $\{r, \theta, \varphi\}$ [see Figure 3.4(B)], corresponds to the polar angle in a set of polar coordinates, $\{p, \varphi\}$, in the image itself. As φ is measured along the central ring of the torus, $\mathbf{p}_0 = (0, \varphi)$ corresponds to the center of the central ring of the torus in the image, as displayed on the bright-field image in Figure 4.5(A). We take our intensity profiles in the OPM textures

across the tube of the torus for a constant φ from $p = R_0 - a(\varphi)$ to $p = R_0 + a(\varphi)$, where R_0 is the radius of the central ring of the torus and a is the tube radius. We parameterize each intensity profile with a variable $\rho = (p - R_0)/a(\varphi)$, such that $\rho \in [-1, 1]$ corresponds to $p \in [R_0 - a(\varphi), R_0 + a(\varphi)]$. We note that while for a perfect torus a is constant, our toroidal droplets are not perfectly axisymmetric and thus a has some φ -dependence.

We find the central ring, find $a(\varphi)$, and determine the intensity profiles with a custom MATLAB script. We start by converting each image to grayscale using MATLAB's `rgb2gray` algorithm: $gray = 0.299R + 0.587G + 0.114B$, where R, G, B are the intensities in the red, green, and blue channels, respectively. In the grayscale images, 1 corresponds to white and 0 to black. From our top-view image, we start by selecting points along the inner and outer contours of the toroid in the image. We then fit the points on each contour to a circle, giving us the radii R_{in}, R_{out} and centers $\mathbf{p}_{in}, \mathbf{p}_{out}$ of the inner and outer contours, respectively. Examples of these contours are drawn on the OPM texture in Figure 4.5(B). Note how \mathbf{p}_{in} and \mathbf{p}_{out} in Figure 4.5(B) are close to each other but are not the same; this reflects the fact that we do not have a perfect torus.

For a given torus, we then take the average aspect ratio $\xi = R_0/a_{av} = (R_{out} + R_{in})/(R_{out} - R_{in})$, with the central ring radius $R_0 = (R_{out} + R_{in})/2$ and the average tube radius $a_{av} = (R_{out} - R_{in})/2$. We also calculate the origin of our polar coordinate system in the image, $\mathbf{p}_0 = (\mathbf{p}_{in} + \mathbf{p}_{out})/2$. For a given φ , we take the intensity profile starting at the inner contour $|\mathbf{p} - \mathbf{p}_{in}| = R_{in}$ and increasing p until we reach the outer contour $|\mathbf{p} - \mathbf{p}_{out}| = R_{out}$. The length of this profile is $2a(\varphi)$, allowing us to calculate a local aspect ratio $\xi(\varphi) = R_0/a(\varphi)$. We then parameterize each intensity profile in terms of ρ ; example profiles for $\varphi = 0$ for the OPM textures in Figure 4.5(B,E) are shown in Figure 4.5(C,F), respectively. These [Figure 4.5(C,F)] are typical intensity profiles for our homeotropic toroids, where we always take our intensity profiles with

$\hat{\varphi}$ along either the P or A direction. Like the intensity profiles of the TER capillaries [see Figure 4.4(F)], the maxima in the intensity profiles of our toroids do not always have the same value. Similarly, there is no general trend in which maximum is larger.

4.3.2 Large aspect ratio toroids

We first look at our larger ξ toroids [see Figure 4.5(A,B)]; the OPM texture resembles an ER texture and the intensity profiles [Figure 4.5(C)] show a central minimum flanked by two maxima. However, we find that $I_{max}/I_{min} < 4$, with 4 the value we observed in our ER capillaries. In the example profile in Figure 4.5(C), $I_{max}/I_{min} = 1.45$ for $\xi(\varphi = 0) = 2.8$. Thus, we hypothesize that our larger aspect ratio toroids have a TER configuration. We emphasize that this twist occurs despite the fact that we have homeotropic anchoring. With homeotropic anchoring, the saddle-splay distortion does not drive the formation of a twisted state, as it did in our previous work with NLC toroids with degenerate planar anchoring [37].

4.3.3 Small aspect ratio toroids

When we look at toroids with smaller ξ , we initially see that the intensity pattern has changed to a spiral texture of alternating dark and light regions [Figure 4.5(E)], no longer so clearly resembling the dark-bright-dark-bright-dark texture of an ER or TER texture. However, when we examine the intensity profile of the spiral textures, we still find qualitative similarities with the intensity profile of a TER configuration, with a central minimum surrounded by two maxima and $I_{max}/I_{min} < 4$. For the example profile in Figure 4.5(F), $I_{max}/I_{min} = 1.38$ and $\xi(\varphi = 0) = 2$.

For a series of toroids with different ξ and a , we plot I_{max}/I_{min} vs $\xi(\varphi)$ [(o), Figure 4.5(G)] and find that I_{max}/I_{min} increases with increasing $\xi(\varphi)$, approaching $I_{max}/I_{min} = 4$ as $\xi(\varphi) \gg 1$. From this trend, we hypothesize that the twist in our TER toroids decreases as ξ increases. In order to both qualitatively investigate the

role of twist in the intensity ratio as well as to test director configurations that could yield this spiral-like texture, we perform computer simulations of the OPM textures using Jones Calculus.

4.4 Simulating polarized optical microscopy textures for twisted escaped radial director configurations

4.4.1 Jones Calculus and simulation details

Jones Calculus is a method to describe and propagate polarized light through a birefringent material [88]. The state of the polarized light is characterized by decomposing the electric field in the plane of polarization using a 2-dimensional Jones vector while neglecting the time dependence of the electric field. We can neglect the time-dependence because while the electric field oscillates with time, the polarization state does not. For example, allowing \hat{x} to be horizontal, \hat{y} to be vertical, and $\mathbf{k}_0 = \hat{z}$ the direction of the wavevector of the polarized incident light, we can write the normalized electric field as:

$$\mathbf{E} = \hat{x}E_x e^{i\phi_x} + \hat{y}E_y e^{i\phi_y} \quad (4.8)$$

$$= e^{i\phi_x} \begin{pmatrix} E_x \\ E_y e^{i(\phi_y - \phi_x)} \end{pmatrix}. \quad (4.9)$$

Thus, the Jones vector for a horizontal polarization state, a $+45^\circ$ polarization state, and a right-handed circular polarization state can be written as $(1, 0)$, $(1, 1)/\sqrt{2}$, and $(1, i)/\sqrt{2}$, respectively. We have normalized the Jones vectors, removing the absolute phase prefactor $e^{i\phi_x}$ from Eq. 4.9 as the polarization state is dependent on neither the absolute phase nor the magnitude of the vector. Note, in particular, that the Jones vector for the right-handed circularly polarized light gives the normalized field $\mathbf{E} = \hat{x}E_x e^{i\phi_x} + \hat{y}E_y e^{i(\phi_x + \pi/2)}$, as we would expect.

Table 4.1: Jones calculus operators for common optical elements

Optical Element	Jones matrix
Linear polarizer with axis of transmission horizontal	$\begin{pmatrix} 1 & 0 \\ 0 & 0 \end{pmatrix}$
Linear polarizer with axis of transmission vertical	$\begin{pmatrix} 0 & 0 \\ 0 & 1 \end{pmatrix}$
Linear polarizer with axis of transmission at $\pm 45^\circ$ with the horizontal	$\frac{1}{2} \begin{pmatrix} 1 & \pm 1 \\ \pm 1 & 1 \end{pmatrix}$
Right/left circular polarizer	$\frac{1}{2} \begin{pmatrix} 1 & \pm i \\ \mp i & 1 \end{pmatrix}$

In order to propagate a polarization state through an optical element, such as a half-wave plate or a phase retarder, we write each component of the Jones vector representing the transformed state \mathbf{E}^{trans} as a linear combination of the components of the Jones vector representing the initial state $\mathbf{E}^{init} = E_x^{init}\hat{x} + E_y^{init}\hat{y}$:

$$\begin{aligned} \mathbf{E}^{trans} &= \begin{pmatrix} E_x^{trans} \\ E_y^{trans} \end{pmatrix} = \begin{pmatrix} AE_x^{init} + BE_y^{init} \\ CE_x^{init} + DE_y^{init} \end{pmatrix} \\ &= \begin{pmatrix} A & B \\ C & D \end{pmatrix} \begin{pmatrix} E_x^{init} \\ E_y^{init} \end{pmatrix} = \boldsymbol{\Theta} \mathbf{E}^{init}, \end{aligned} \quad (4.10)$$

where $\boldsymbol{\Theta}$ is our transformation operator, which can be written as a 2×2 Jones matrix. To propagate a Jones vector through multiple optical elements, the Jones matrix for each element is applied to the initial Jones vector sequentially. For a series of N elements:

$$\mathbf{E}^{trans} = \boldsymbol{\Theta}_N \boldsymbol{\Theta}_{N-1} \cdots \boldsymbol{\Theta}_2 \boldsymbol{\Theta}_1 \mathbf{E}^{init} = \prod_{\nu=1}^N \boldsymbol{\Theta}_\nu \mathbf{E}^{init} = \boldsymbol{\vartheta} \mathbf{E}^{init}, \quad (4.11)$$

where $\boldsymbol{\vartheta}$ is the operator representing the Jones matrix for the entire system. A list of some common optical elements represented as Jones matrices in the xy basis are found in Table 4.1.

For a general phase retarder with the optic axis along \hat{y} , the transformation operator is written as [88]:

$$\Theta = \begin{pmatrix} e^{i\phi_x} & 0 \\ 0 & e^{i\phi_y} \end{pmatrix}. \quad (4.12)$$

When the orientation of the optic axis is not along \hat{y} , we use a rotation matrix to rotate \mathbf{E}^{init} and make it coincide with \hat{y} so we can use Eq. 4.12; we undo our initial rotation with a second rotation matrix afterwards [187]:

$$\mathbf{E}^{trans} = \mathbf{R}(-\alpha)\Theta\mathbf{R}(\alpha)\mathbf{E}^{init}, \quad (4.13)$$

where $\mathbf{R}(\alpha) = \begin{pmatrix} \cos \alpha & -\sin \alpha \\ \sin \alpha & \cos \alpha \end{pmatrix}$ is the rotation matrix for an angle α measured counterclockwise with respect to the x-axis. This approach simplifies calculations for a series of optical elements.

Since we wish to simulate the OPM texture of a continuous volume with a given nematic director field, we first need to discretize the continuous nematic volume into N cubic volume elements, or voxels, of side Δ . If Δ is small enough such that the local director \mathbf{n}_ν for each voxel $\nu \in [1, N]$ can be treated as constant throughout the voxel, then each voxel can be treated as a phase retarder with the associated Jones matrix and orientation given by its \mathbf{n}_ν . In this way, we are able to treat a continuous nematic volume as a collection of independent optical elements.

The extraordinary index of refraction experienced by light incident on a birefringent uniaxial material depends on the angle γ between \mathbf{n} and \mathbf{k}_0 according to $n_e(\gamma) = n_o n_E / \sqrt{n_o^2 \sin^2 \gamma + n_E^2 \cos^2 \gamma}$ with n_o and n_E the ordinary and extraordinary index of refraction of the material, respectively. Thus, we can write the Jones matrix

for the ν^{th} voxel with the optic axis along \hat{y} as:

$$\Theta_\nu = \begin{pmatrix} e^{i(n_o 2\pi \frac{\Delta}{\lambda})} & 0 \\ 0 & e^{i(n_e(\gamma_\nu) 2\pi \frac{\Delta}{\lambda})} \end{pmatrix}, \quad (4.14)$$

where λ is the wavelength of the light in vacuum, γ_ν is the angle γ associated to the ν^{th} voxel, and where we have set $\mathbf{k}_0 = \hat{z}$ such that the plane of polarization is in the xy plane. To use the formalism underlying Eq. 4.13, we need γ_ν , \mathbf{n}_ν , and α_ν , with α_ν the angle between the projection of \mathbf{n}_ν onto the xy plane and the x-axis. Note that the angle between the average director of the overall nematic configuration, \mathbf{n}_d , and \mathbf{k}_0 is θ_0 , and the angle between the projection of \mathbf{n}_d onto the xy plane and the x-axis is α_0 . We use these two angles to control the orientation of the nematic configuration with respect to \mathbf{k}_0 such that we can simulate OPM textures for different views of the nematic configuration. In addition, we change the polarizer orientation by changing the orientation of the incident polarization, given by \mathbf{E}_P . The angles used to describe the local director as well as the angles used to describe the orientation of the entire nematic configuration are shown in Figure 4.6(A).

To find the intensity at a given point $I(\boldsymbol{\rho})$ in the simulated texture, with $\boldsymbol{\rho}$ the position vector in the texture, \mathbf{E}_P is propagated along the ray \mathbf{k}_0 passing through $\boldsymbol{\rho}$. To accomplish this, the Jones matrix and rotation matrices for every voxel encountered by \mathbf{k}_0 are applied to the initial polarization state to produce the final polarization state of the light leaving the nematic volume. A schematic of this process for a spherical nematic volume can be seen in Figure 4.6(B). Once we have propagated the polarization state through the nematic volume, we calculate $I(\boldsymbol{\rho})$ by passing the final polarization state through the analyzer and taking the magnitude squared of the result. Writing $I(\boldsymbol{\rho})$ in terms of Θ and $\mathbf{R}(\alpha)$:

$$I(\boldsymbol{\rho}) = |\Theta_A \mathbf{R}(\alpha_A) \boldsymbol{\vartheta}(\boldsymbol{\rho}) \mathbf{E}_P|^2, \quad (4.15)$$

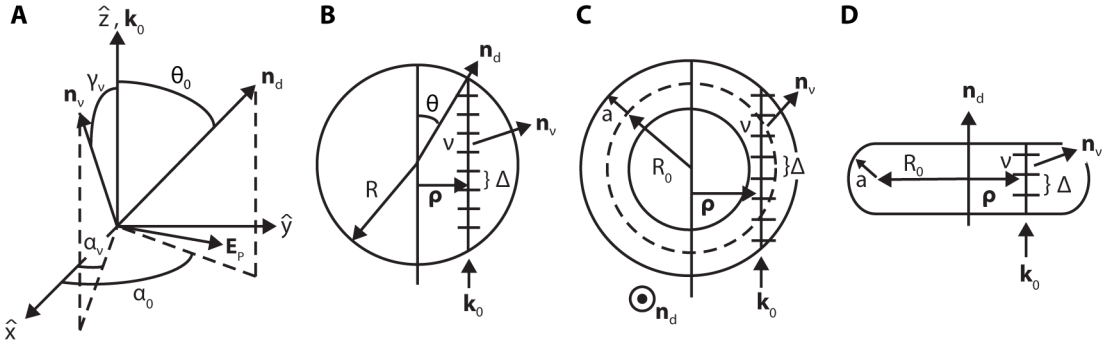


Figure 4.6: Symbols and coordinates used in simulating OPM droplet textures. (A), Relevant angles used in all simulations, where \mathbf{n}_d is the droplet director, \mathbf{n}_v is the local director, \mathbf{k}_0 is the incident wave vector, \mathbf{E}_P gives the orientation of the polarizer. \mathbf{n}_d is specified by θ_0 and α_0 , while \mathbf{n}_v is specified by γ_v and α_v , where θ_0 and γ_v are measured from \hat{z} and \mathbf{k}_0 , respectively, and α is measured off of \hat{x} . (B), Breakdown of OPM simulation parameters in a spherical geometry, where ρ is the position vector in the final image and Δ is the thickness of the voxels used in the simulation. (C,D), Breakdown of OPM simulation parameters in a torus viewed from the (C) side and from the (D) top.

where

$$\vartheta(\rho) = \prod_{\nu=1}^{N(\rho)} \mathbf{R}(-\alpha_\nu(\rho)) \Theta_\nu(\rho) \mathbf{R}(\alpha_\nu(\rho)), \quad (4.16)$$

and $\Theta_A \mathbf{R}(\alpha_A)$ is the operator and associated rotation accounting for the analyzer angle, α_A . Taking advantage of the associative property of matrix multiplication and the fact that the product of two rotation matrices is the rotation matrix of the sum of the angles, we can re-write Eq. 4.16 as:

$$\vartheta(\rho) = \mathbf{R}(-\alpha_N(\rho)) \prod_{\nu=2}^{N(\rho)} \left\{ \Theta_\nu(\rho) \mathbf{R}(\alpha_\nu(\rho) - \alpha_{\nu-1}(\rho)) \right\} \Theta_1(\rho) \mathbf{R}(\alpha_1(\rho)) \quad (4.17)$$

Therefore, the overall process to simulate an OPM texture from a given director field is: (i) discretize the volume into voxels such that the local director for each voxel can be considered constant, (ii) use the local director to calculate the angles γ and α for each voxel, (iii) use γ and α to determine the Jones matrix and rotation

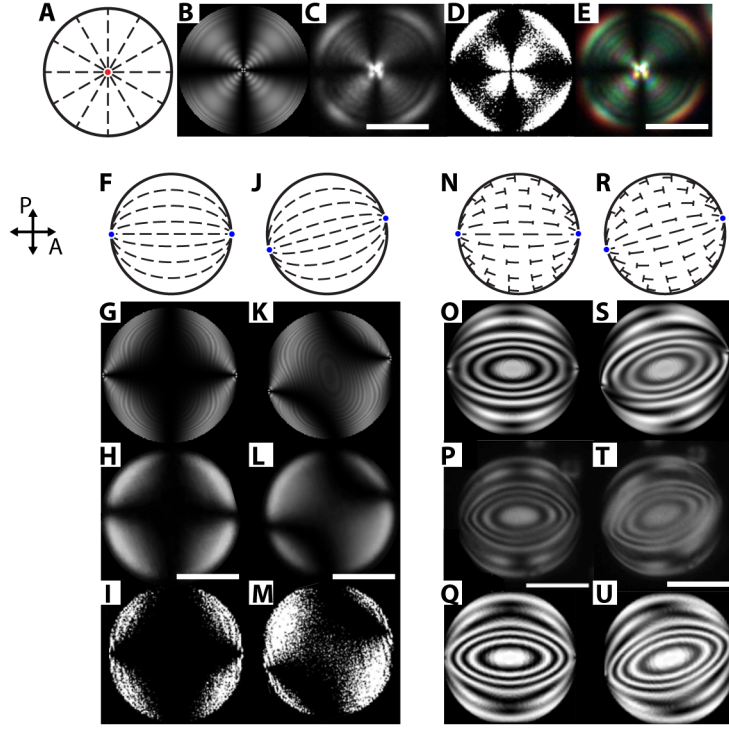


Figure 4.7: Director schematics and simulated and experimental OPM textures for (A–E) radial droplets, (F–M) bipolar droplets, and (N–U) twisted bipolar droplets. For the radial droplets, (A) is a director schematic, (B) is a simulation, (C,E) are grayscale and color experimental image, respectively, and (D) is a simulation image from Ref. [187]. For the bipolar and twisted bipolar droplets, (F–I) and (N–Q) are oriented with the bipolar axis aligned parallel to the analyzer direction while (J–M) and (R–U) have the bipolar axis rotated 15 degrees CCW from the analyzer direction. (F,J,N,R) are the schematics, (G,K,O,S) are our simulated images, (H,L,P,T) are experimental images, and (I,M,Q,U) are simulated textures from the literature. (I,M) are from Ref. [187], (P,T,Q,U) are from Ref. [177]. Scale bar is 20 μm in all images. Images from Ref. [187] reprinted with the permission of AIP Publishing.

matrix associated with each voxel, (iv) propagate the initial polarization state through the series of rotation matrices and Jones matrices, and (v) run the final polarization state through the analyzer and square the magnitude of the output to obtain the final intensity at every point. This results in the OPM texture for a single wavelength. To simulate a texture using multiple wavelengths, we average the different single-wavelength textures together.

4.4.2 Validation using spherical droplets

To test this method, we simulated OPM textures for the well-studied radial, bipolar, and twisted-bipolar director fields in spherical geometries. For a radial director field we used $\mathbf{n}^{rad} = (x, y, z)/\sqrt{x^2 + y^2 + z^2}$ [88]. A simulated texture of a 40 μm diameter sphere calculated using 20 evenly-spaced wavelengths between 400 nm and 700 nm is shown in Figure 4.7(B). We compare our simulated image both with a grayscale experimental image of a 40 μm diameter 5CB droplet in water with 8 mM SDS and with another simulated texture of a 10 μm diameter sphere from Ref. [187]. These are shown in Figure 4.7(C,D), respectively. The image in Figure 4.7(C) was converted to grayscale from the RGB image in Figure 4.7(E) using MATLAB's `rgb2gray` algorithm: $gray = 0.299R + 0.587G + 0.114B$, where R, G, B are the intensities in the red, green, and blue channels, respectively. The conversion was done to better compare the simulated and experimental textures.

Note the agreement between our simulated image and the grayscale experimental texture; both show four dark, wedge-shaped brushes that begin in the center of the droplet and extend to the edges. The bright portions also exhibit thin dark bands, or fringes, corresponding to locations where the retardation through the droplet is a multiple of 2π for some or all of the wavelengths. However, the experimental image is brighter in the center than our simulated image. We attribute this difference to the defect not being in the focal plane in the experimental image; our simulated image does not take into account focus effects. In addition, note how the bright portions of Figure 4.7(D) have a single, large, dark fringe where the retardation is a multiple of 2π . The fringe in this simulated texture appears larger than those in Figure 4.7(B) because the simulated droplet here has a smaller size, and because the simulation was done with a single wavelength.

For a bipolar director we use $\mathbf{n}^{bp} = \nabla\psi/|\nabla\psi|$, where

$$\begin{aligned}\psi = & \frac{1}{\sqrt{(x - p_x)^2 + (y - p_y)^2 + (z - p_z)^2}} \\ & - \frac{1}{\sqrt{(x + p_x)^2 + (y + p_y)^2 + (z + p_z)^2}},\end{aligned}\quad (4.18)$$

with $\mathbf{p} = R(\sin\theta_0 \cos\alpha_0, \sin\theta_0 \sin\alpha_0, \cos\theta_0)$, and R the sphere radius. The simulated bipolar OPM texture of a 40 μm diameter sphere for this director field using 20 evenly-spaced wavelengths between 400 nm and 700 nm for $\theta_0 = \pi/2$ and either $\alpha_0 = 0$ or $\alpha_0 = \pi/12$ are shown in Figure 4.7(G,K), respectively. Corresponding experimental images of a 40 μm diameter 5CB droplet in water with 1% polyvinyl alcohol to enforce tangential anchoring, as well as simulated images of a 40 μm diameter sphere from Ref. [187] are shown in Figure 4.7(H,L) and Figure 4.7(I,M), respectively. All six images exhibit excellent agreement. Note how Figure 4.7(G–I) all have four bright portions at the edge of the droplet and how the bright regions show a greater horizontal separation than a vertical separation. Note also how the central region is completely dark. When the droplet orientation changes by $\pi/12$ as seen in Figure 4.7(K–M), the central region in all three textures ceases being completely dark and begins to connect the upper-left and lower-right bright regions.

For a twisted bipolar director \mathbf{n}^{tb} , we follow Ref. [81] and use:

$$\mathbf{n}^{tb} = \mathbf{n}^{bp} \cos\tau + \mathbf{n}^{conc} \sin\tau,\quad (4.19)$$

where the concentric director is $\mathbf{n}^{conc} = (\sin\varphi, \cos\varphi, 0)$, with φ the polar angle measured off of the x-axis. \mathbf{n}^{bp} is the bipolar director derived from the normalized gradient of Eq. 4.18, and $\tau = \tau_0 \sqrt{x^2 + y^2}/\sqrt{R^2 - z^2}$ is a twist angle varying from $\tau = \tau_0$ at the surface of the sphere to $\tau = 0$ at the bipolar axis [see Figure 4.7(N,R)] [81]. Instead of generating OPM textures with different α_0 and a fixed polarizer and ana-

lyzer orientation as with the bipolar OPM textures, here we keep $\alpha_0 = 0$ and vary the polarizer and the analyzer orientations to generate different views. This makes the computation easier to perform. The simulated twisted bipolar OPM textures shown in Figure 4.7(O,S) were produced for a 50 μm diameter sphere with a single wavelength at $\lambda = 650$ nm. The simulated twisted bipolar images from Ref. [177] were also produced for a similar sphere with $\lambda = 650$ nm, as seen in Figure 4.7(Q,U). The experimental images of $\approx 40 \mu\text{m}$ diameter droplets imaged using $\lambda \approx 650$ nm from Ref. [177] are shown in Figure 4.7(P,T). As with the bipolar droplets, the six twisted bipolar textures also show remarkable agreement. Note how the number and position of the fringes in Figure 4.7(O–Q) and Figure 4.7(S–U) are the same. In addition, note that while the central region in the bipolar drops in Figure 4.7(G–I) is dark, the addition of a twist in the director field about the horizontal axis causes the central region in the twisted bipolar textures in Figure 4.7(O–Q) to be bright. Even though 20 wavelengths were used for the bipolar textures and only a single wavelength was used for the twisted bipolar textures, this is a valid comparison to make; using more or fewer wavelengths for the bipolar texture would not brighten the center, and using more wavelengths in the twisted bipolar texture would not darken the central region.

4.4.3 Planar-anchored nematic toroids

We first used simulated OPM textures in our previous work with NLC toroids under degenerate planar boundary conditions [37]. We observed the toroidal droplets from the top, shown in the OPM texture in Figure 4.8(A), and from the side, shown in the bright-field image in Figure 4.8(D) and the OPM textures in Figure 4.8(E,F). Note how the central region in the side-view OPM textures [red dashed line, Figure 4.8(E,F)] is always bright regardless of the PA orientation. The fact that this central region cannot be fully extinguished under crossed polarizers can be explained with the doubly-twisted director field ansatz in Eq. 4.4 [37]. Recall that the param-

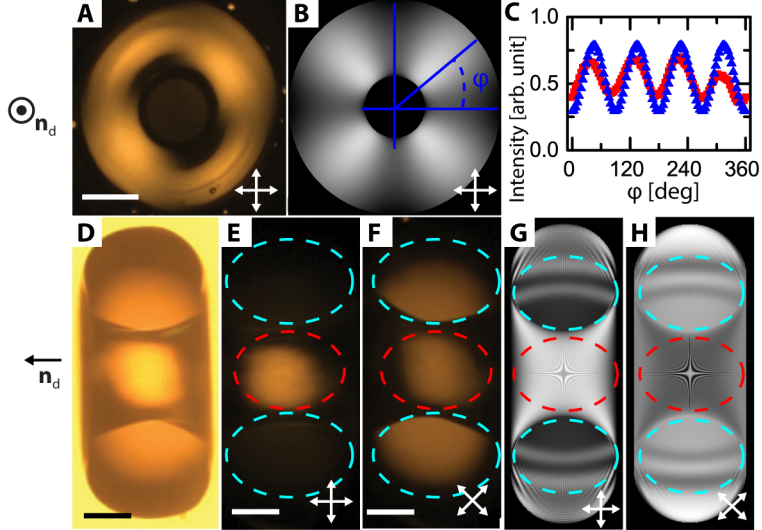


Figure 4.8: Simulated OPM textures of nematic tori and experimental images of nematic toroids. (A,D–F), Experimental images of a tangentially-anchored nematic toroid with $\xi \approx 1.8$ from Ref. [37]. (A), OPM view from the top, (D), bright field view from the side, and (E,F), OPM views from the side with PA oriented at 0° and 45° , respectively. (B,G,H), Simulated OPM textures for a torus of $\xi = 1.8$ using the ansatz from Eq. 4.4 with $\omega = 0.420$ and $g = 0.750$ from minimizing the free energy. The OPM textures are viewed from the (B) top and from the side with P and A oriented at (G) 0° and (H) 45° . The intensity along the central ring for (A) (■) and (B) (▲) is plotted in (C). Scale bar is 100 μm in (E,F) and 200 μm in (A).

eter ω determines the amount of twist in the director field and g allows the director field to splay; g also controls the θ -dependence of the director field. When $g = 0$, the θ -dependence vanishes and the director field is like that in a cylinder with $\xi = \infty$. As g increases, the twist measured along $\theta = 0, \pi$ becomes larger than τ , which is measured along $\theta = \pi/2, 3\pi/2$. Note that $g = 1$ corresponds to a splay-free configuration. From minimizing the Frank-Oseen free energy, including saddle splay, for different values of the toroidal aspect ratio, $\xi = R_0/a$, we obtained values of ω and g [37]. The values are plotted with the (●) symbols and the (■) symbols in Figure 4.9, respectively. As ξ decreases, ω increases and g decreases corresponding to an increase in the twist deformation. Note that $g = 1$ only for $\xi \approx 3$; the minimum energy configuration typically contains both splay and twist distortions.

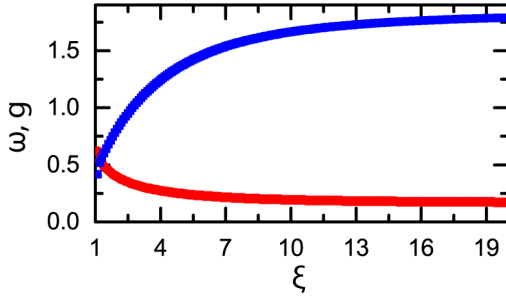


Figure 4.9: Values of (●) ω and (■) g as a function of ξ obtained by minimizing the Frank-Oseen free energy for the ansatz in Eq. 4.4.

Simulated textures

We simulate OPM textures for nematic tori under tangential anchoring using the ansatz in Eq 4.4 with values of ω and g provided from the free energy minimization [see Figure 4.9]. We produce textures using a weighted average over 200 wavelengths evenly-spaced between 400 nm and 700 nm. The normalized weights are provided by approximating the spectrum of the tungsten lamp in the microscope used to take the experimental OPM textures [188]. We use the functional form $weight(\lambda) = \sqrt{(\lambda - 375)/500}$, where λ is in nm; after calculating the individual weights, we normalize them so that the sum of all the weights must equal to 1. The normalized weights for 20 and 200 evenly-spaced wavelengths between 400 nm and 700 nm are plotted in Figure 4.10, respectively. We note that to better capture the output images, we could have also considered the spectral response of the camera in our experiments (The Imaging Source, DFK 41B02), plotted for the individual channels and the total luminance in Figure 4.11(A,B), respectively [189]. We simulate the side-view OPM texture by propagating the incident light perpendicular to \mathbf{n}_d , as seen in Figure 4.6(C), and we simulate the top-view OPM texture by propagating the light along \mathbf{n}_d , as seen in Figure 4.6(D).

Both the experimental top-view OPM texture in Figure 4.8(A) and the simulated top-view OPM texture in Figure 4.8(B) are predominantly bright with four brushes

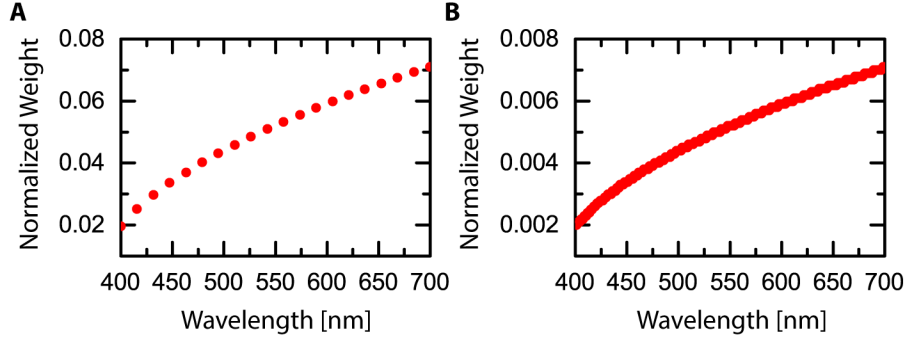


Figure 4.10: Normalized weights as a function of wavelength to approximate the spectrum of a tungsten lamp. (A,B), the weights for 20 and 200 evenly-spaced wavelengths between 400 nm and 700 nm, respectively.

exhibiting partial extinction aligned along the polarizer and analyzer. This can also be seen in 4 maxima and 4 minima in the intensity along the central ring from $\varphi = 0^\circ$ to $\varphi = 360^\circ$ as plotted in Figure 4.8(C) for the experimental OPM texture (■) and the simulated OPM texture (▲). In the simulations, the grayscale intensity goes from 0 to 1, corresponding to white and black in the simulated textures, respectively. Note that the incident intensity is always 1 in the simulations; for example, a value of 0.5 in Figure 4.8(C) corresponds to half the incident intensity. The two curves agree with respect to both the position of the minima and maxima and the relative height of the minima and maxima. Note that the lack of complete extinction in the brushes is reflected in the height of the minima in the intensity plot; this high minimum intensity is due to the doubly-twisted structure of the director field. As with the bipolar and twisted bipolar spherical droplets, the presence of twist raises the minimum intensity in the simulated OPM texture of the toroidal droplets.

The role of twist in preventing complete extinction is also present when looking at the brightness of the central region in both experimental side-view textures and the simulated side-view textures, as highlighted by the red dashed lines in Figure 4.8(E,F) and Figure 4.8(G,H), respectively. In addition, we see that the central region of both the experimental and simulated textures viewed with P and A aligned at 0° and 90° , respectively, measured with respect to \mathbf{n}_d [Figure 4.8(E,G)], is brighter than when P

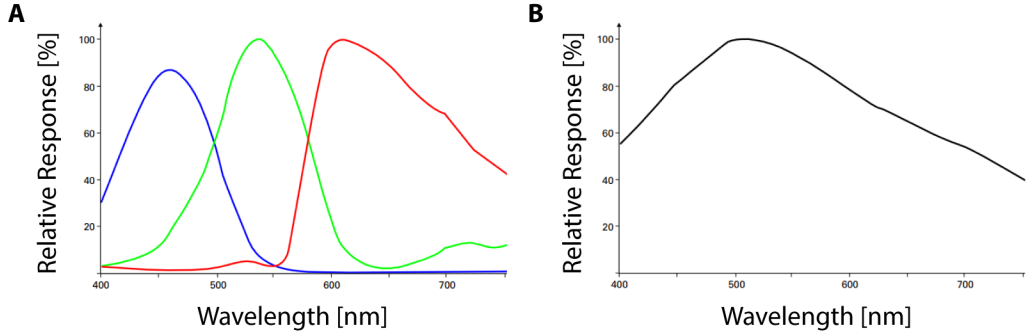


Figure 4.11: Relative response for the sensor in our color camera (DFK 41BU02). (A,B), the (A) individual R, G, and B channel and (B) total luminance relative response as a function of wavelength [189].

and A are aligned at 45° and 135° , measured with respect to \mathbf{n}_d [Figure 4.8(F,H)].

Now looking at the inner portion of the tubes, indicated by the cyan dashed lines in Figure 4.8(E–H), we see that again for both experiment and simulation with P and A at 0° and 90° [Figure 4.8(E,G)], the intensity is less than when P and A are at 45° and 135° [Figure 4.8(F,H)].

We quantify the difference between the brightness of the central region of a side-view OPM texture when P and A are aligned at 0° and 90° (I_0) versus when P and A are aligned at 45° and 135° (I_{45}), as seen in Figure 4.12(A), by taking the ratio of the two measurements I_0/I_{45} as a function of ξ . We find that for both the experimental and simulated OPM textures the intensity ratio decreases as ξ increases. In addition, I_0/I_{45} also passes through 1 around $\xi = 5$ for both the simulated and experimental textures, as seen in Figure 4.12(B,C). Physically, this corresponds to the aspect ratio where the entry director is oriented at approximately 67.5° with respect to \mathbf{n}_d . Thus the incident light at 0° for the I_0 measurement and the incident light at 45° for the I_{45} measurement have the same angular difference from the entry director, yielding similar output polarization states, reflected by the fact that $I_0/I_{45} \approx 1$. For $\xi \lesssim 5$, $I_0/I_{45} < 1$ and the entry director is closer to 90° measured from \mathbf{n}_d ; here the angular difference between the entry director and the P and A direction is greater when P and

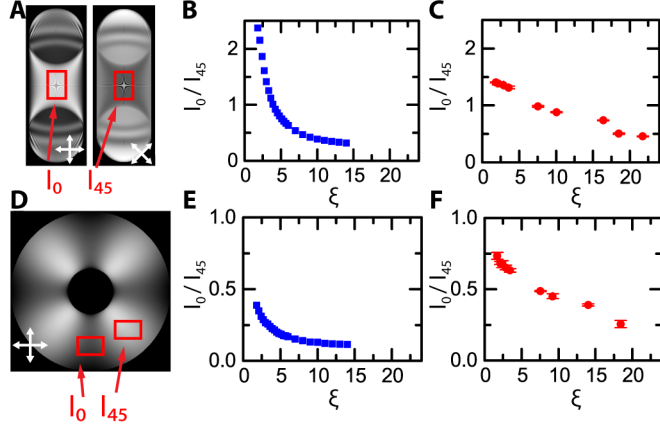


Figure 4.12: Intensity ratios for side-view and top-view simulated OPM textures of planar NLC toroids. (A), Schematic detailing the I_0 and I_{45} measurements from the side-view. (B,C), I_0/I_{45} versus ξ for (B) simulated and (C) experimental OPM textures from the side-view. (D) Schematic detailing the I_0 and I_{45} measurements from the top-view. (E,F), I_0/I_{45} versus ξ for (E) simulated and (F) experimental OPM textures from the top-view.

A are along 45° and 135° than when P and A are along 0° and 90° , corresponding to $I_{45} > I_0$. When $\xi \gtrsim 5$, the opposite is true; the entry director is closer to 45° measured from \mathbf{n}_d , leading to $I_0 > I_{45}$ and $I_0/I_{45} > 1$.

For I_0/I_{45} from the top-view OPM textures, we take the intensity in a region 0° measured from the polarizer axis for I_0 and the intensity in a region 45° measured from the polarizer axis for I_{45} , as seen in Figure 4.12(D). As with the intensity ratio for the side view, I_0/I_{45} for the top view also decreases with increasing ξ . However, $I_0/I_{45} < 1$ always for the top view. This is due to the fact that there is no aspect ratio where the entry director at 0° and at 45° possess the same angular difference from the incident direction of polarization. The angular difference between the director at 0° and the P and A orientation is always less than the angular difference between the director at 45° and the P and A orientation. This implies that $I_0 < I_{45}$ always, and is reflected in the fact that $I_0/I_{45} < 1$ always for the top view. For both the top view and the side view, the I_0/I_{45} from the experimental textures shows good qualitative agreement with the I_0/I_{45} from the simulated textures. The decrease in I_0/I_{45} as ξ

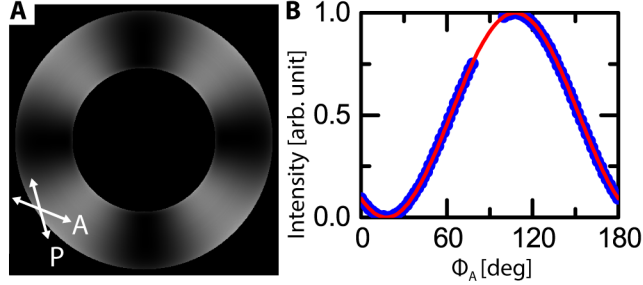


Figure 4.13: Predicted and measured twist angles for simulated OPM textures for planar NLC tori viewed from the top. (A) Simulated texture with the polarizer and analyzer aligned to extinguish both the e-mode (dark regions aligned vertically) and the o-mode (dark regions aligned horizontally). (B) Transmitted intensity as a function of analyzer angle with respect to the polarizer aligned along the entry director, with 1 corresponding to complete transmission and 0 to no transmission. The fit is to the theoretical transmitted intensity for a twisted nematic cell in the waveguiding limit [88].

increases can be explained with the decreasing value of ω . As ω decreases, the twist decreases and the entry director will be more aligned along P and A when P and A are at 0° and 90° than when P and A are at 45° and 135° . This causes I_0 to decrease and I_{45} to increase, such that I_0/I_{45} decreases.

We now validate the relation between ω and the twist angle in our simulations. Recall that the total twist angle of the director ansatz through the central ring viewed from the top can be written as $\tau = 2 \arcsin(\omega)$. As an example, for $\xi = 3.5$, minimizing the free energy yields $\omega = 0.294$ and $g = 1.162$, corresponding to a theoretical $\tau = 34.2^\circ$. We can confirm this by measuring the twist angle using simulated textures for $\xi = 3.5$ with various P and A orientations. We “rotate” the polarizer with a fixed A until the intensity at the central ring at $\varphi = 0^\circ$ is a minimum, signifying that we have matched the polarizer orientation with the entry director. We then fix P at this orientation and fit the intensity at $\varphi = 0^\circ$ at the central ring as a function of analyzer

angle to the expected transmission for a twisted nematic cell [88]:

$$T = \cos^2(\Phi_{\text{exit}} - \tau) - \frac{\tau}{2X} \sin(2X) \sin(2\Phi_{\text{exit}} - 2\tau) \\ - \tau^2 \frac{\sin^2(X)}{X^2} \cos(2\Phi_{\text{exit}} - 2\tau), \quad (4.20)$$

where $X = \sqrt{\tau^2 + (\pi(n_E - n_o)d/\lambda)^2}$, d is the sample thickness and Φ_{exit} is the angle of the analyzer measured with respect to the polarizer. This fit for the example torus in Figure 4.13(A) is shown in Figure 4.13(B) and results in $\tau = 33.61 \pm 0.01^\circ$. This is consistent with our expectations from the theoretical ansatz and supports our simulation procedure.

Experimentally, we measured $\tau \approx 50^\circ$ for a toroid with $\xi \approx 3.5$ [37]. Eq. 4.20 assumes that the Mauguin parameter $u = \pi(n_E - n_o)d/(\lambda\tau) \gg 1$ [88]. Physically, this corresponds to a regime where the phase difference introduced by the birefringence is much greater than τ such that the nematic acts as a waveguide. For our tori using 5CB with tube radius $\approx 100 \mu\text{m}$, $u \sim 10^2$, satisfying this limit. Provided the incident polarization is either parallel to the entry director (e-mode) or perpendicular to the entry director (o-mode), the incident polarization state will be propagated along the director twist and exit either parallel to (e-mode) or perpendicular to (o-mode) the exit director [88]. Thus, an analyzer oriented perpendicular to the exit director will extinguish the e-mode and pass the o-mode while an analyzer oriented parallel to the exit director will extinguish the o-mode while passing the e-mode. This can be seen in the simulated OPM texture in Figure 4.13(A), where the e-mode has been extinguished in the dark brushes aligned along the vertical and the o-mode has been extinguished in the dark brushes aligned along the horizontal.

Wavelength dependence of simulated OPM textures

Since the simulation algorithm only works for a single wavelength, an average of multiple single-wavelength OPM textures is needed to approximate a true white light source. To illustrate this effect, we will use the central section of a side view simulated OPM texture of a torus with $\xi = 1.8$, as seen highlighted in the red square in Figure 4.14(A). For the single-wavelength images shown in Figure 4.14(B–E), the output polarization state varies spatially, leading to spatial intensity variations in the final image once the output polarization state is passed through the analyzer. The symmetry of the ansatz found in Eq. 4.4 in a perfect torus results in the light and dark bands encroaching symmetrically to produce the star-like feature seen in the middle of each individual single-wavelength image. Note how the light and dark bands are smallest in the simulated texture for $\lambda = 400$ nm displayed in Figure 4.14(B) and largest in the simulated texture for $\lambda = 700$ nm displayed in Figure 4.14(E). This is because the retardation $\Gamma = 2\pi(n_E - n_o)d/\lambda \sim 1/\lambda$ [88]. Thus, as the light and dark bands are of different sizes and occur with different frequencies, averaging over multiple single-wavelength textures can wash out their appearance. Averaging over more wavelengths in the same range corresponds to a greater washing out of the light and dark bands. This is shown in Figure 4.14(F–I), where we average over 4, 8, 20, and 200 evenly-spaced wavelengths between 400 nm and 700 nm, respectively. Also note how the star-like feature does not average out as it is present in all the simulated single-wavelength images.

Effect of voxel size on simulated OPM textures

The voxel size is important, as a voxel size too large will fail to capture the director variation in the volume, while a voxel size too small will take unnecessary time and computation power to simulate. To capture the true effect of the given director field, the voxel must be small enough such that the director can be taken as a constant over

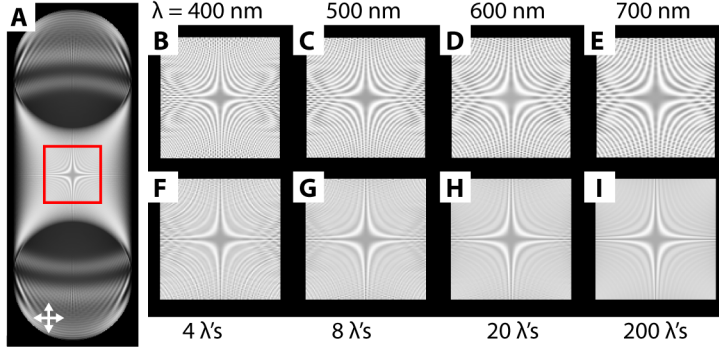


Figure 4.14: The effect of averaging over multiple wavelengths in a simulated OPM texture. (A) Side-view simulated OPM texture of a planar NLC torus averaging over 200 wavelengths. The red square highlights the central region shown in (B–I). (B–E), The central region shown for the single wavelengths 400 nm, 500 nm, 600 nm, and 700 nm, respectively. (F–I), The central region shown for an average of 4, 8, 20, and 200 wavelengths, respectively, over the interval $\lambda \in [400, 700]$ nm.

the voxel volume. Practically, this limit is found when simulating an OPM texture with a smaller voxel size produces no change in the output texture. To illustrate this, the central portion of a side-view simulated OPM texture of a torus averaging over 200 wavelengths are shown for P and A at 0° and 90° and at 45° and 135° in Figure 4.15(A–C) and Figure 4.15(D–F), respectively. Comparing $\Delta/a = 0.04$ in Figure 4.15(A,D) with $\Delta/a = 0.01$ in Figure 4.15(B,E), we see that both the star feature and the fringes are much smoother when $\Delta/a = 0.01$ than when $\Delta/a = 0.04$. In contrast, the difference between $\Delta/a = 0.01$ [Figure 4.15(B,E)] and the textures simulated for $\Delta/a = 0.001$ [see Figure 4.15(C,F)] is much less noticeable. Continuing to reduce the voxel size below $\Delta/a = 0.001$ produces no noticeable difference in the resulting textures.

While the individual textures show changes as Δ/a decreases towards $\Delta/a = 0.001$, the ratio I_0/I_{45} over the central region of the simulated side-view OPM textures does not change, as seen in Figure 4.15(G) for $\Delta/a = 0.04$ (□), $\Delta/a = 0.01$ (□), and $\Delta/a = 0.001$ (■). All three curves fall on top of each other. This is because I_0/I_{45} is taken using the average intensity over the central region.

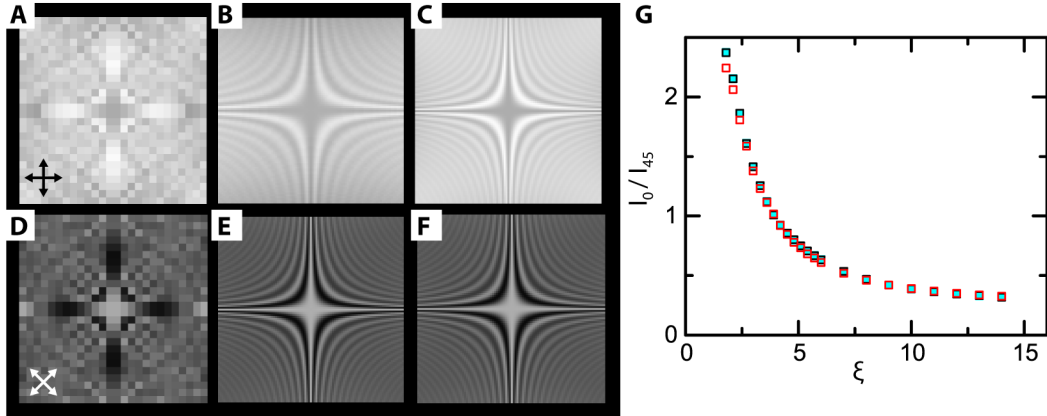


Figure 4.15: Effect of voxel size on individual OPM textures and on I_0/I_{45} for planar NLC tori. (A–F), The central region of a simulated side-view OPM texture with $\xi = 1.8$ with PA at 0° (A–C) and PA at 45° (D–F) for (A,D) $\Delta/a = 0.04$, (B,E) $\Delta/a = 0.01$, and (C,F) $\Delta/a = 0.001$. All textures use a 200 wavelength average with $a = 100 \mu\text{m}$. (G) Intensity ratio I_0/I_{45} as a function of ξ for simulated side-view OPM textures as seen schematically in Figure 4.12(A) for (□) $\Delta/a = 0.04$, (□) $\Delta/a = 0.01$, and (■) $\Delta/a = 0.001$.

Effect of refraction on OPM textures

Even though the simulated OPM textures do not take into account refraction, refraction effects are present in the experimental textures and they affect how the experimental and simulated OPM textures can be compared. First considering the experimental bright-field top view of an isotropic 5CB toroid with $n_{iso} \approx 1.6$ in a yield-stress fluid with $n \approx 1.33$ in Figure 4.16(A), the inner and outer edges of the torus are darker than the rest of the droplet. In contrast, the inner and outer edges of the bright-field top view of a toroid made with polydimethylsiloxane (PDMS) oil with $n \approx 1.4$ in Figure 4.16(B) are less prominent. These effects of refraction are supported by simulated images of isotropic tori with $n = 1.4$ and $n = 1.2$ in an outer medium with $n = 1$ seen in Figure 4.16(C,D), respectively. These images were generated by Ekapop Pairam using the 3D computer modeling software Autodesk Maya. As with the experimental images, the simulated image with the higher index contrast is darker overall with more prominent edges than the image simulated with

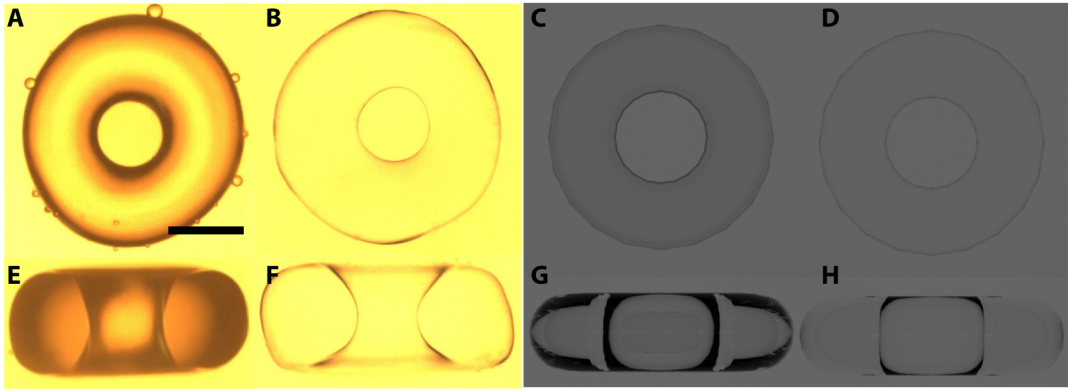


Figure 4.16: Effect of refraction of top and side view images of toroids. (A,B,E,F), Experimental bright-field images of toroidal droplets of 5CB with (A,E) $n_{iso} \approx 1.6$, and (B,F) PDMS oil with $n \approx 1.4$ in a yield-stress outer medium with $n \approx 1.33$ viewed from the top (A,B) and from the side (E,F). Scale bar for experimental images is 200 μm . (C,D,G,H), Simulated bright-field images of isotropic tori with (C,G) $n = 1.4$ and (D,H) $n = 1.2$ with outer index of refraction $n = 1$ viewed from the top (C,G) and from the side (D,H). Images simulated using Autodesk Maya.

a smaller index contrast. Thus, to minimize the effect of refraction on our data, we should only consider the region around the central ring when comparing simulated and experimental OPM textures for toroidal droplets viewed from the top.

We can also look at bright-field images of toroids viewed from the side made with either 5CB or PDMS oil immersed in a yield-stress medium, as seen in Figure 4.16(E,F), respectively. Viewed from the side, the central region and the inner portion of the tube of the 5CB toroid are bright, while the rest of the toroid is darker. In contrast, the PDMS toroid viewed from the side has a fairly homogeneous intensity, with only the edges exhibiting some darkening. As with the top view, these intensity trends are supported by simulated side-view images of tori with the higher index of refraction contrast shown in Figure 4.16(G) and the lower index of refraction contrast shown in Figure 4.16(H). From these images, we find that we can only compare the central region and the inner portions of the tube between the experimental and simulated OPM textures of toroids viewed from the side.

While the general intensity trends agree, the simulated side-view OPM textures possess a star-like feature in the center that is not present in the experimental side-view OPM textures. This feature does not affect the intensity measurements, as I_0/I_{45} is calculated using the average intensity in the central region. Given that the star feature is present in the single-wavelength images for $\lambda \in [400, 700]$ nm with even a small voxel size of $\Delta/a = 0.0001$, the star is a real consequence of the director ansatz from Eq. 4.4 confined to a perfect torus. We further confirm this by simulating side-view OPM textures from truncated tori, where we truncate a torus by slicing the torus perpendicular to \mathbf{k}_0 at a truncation length ℓ_t measured along \mathbf{k}_0 from the end of the torus closest to the analyzer, as schematically shown in Figure 4.17(D) for three truncation lengths.

For an example torus of $\xi = 1.8$ and $a = 100$ μm , we see that the star is present when simulating the OPM texture for the full torus with $\ell_t = 0$ μm [Figure 4.17(A)], almost nonexistent when taking $\ell_t = 10$ μm [Figure 4.17(B)], and is completely gone for $\ell_t = 30$ μm [Figure 4.17(C)]. Changing the geometry from that of a perfect torus causes the star-like feature to disappear. Since the experimental OPM textures come from toroids and not perfect tori, we believe that they do not have the symmetry required to exhibit a star-like feature in the center of their side-view OPM textures. This is likely why we never observe such a feature in our experimental toroids.

4.4.4 Comparison with homeotropically-anchored nematic toroids

We model a TER director field by coupling the doubly-twisted ansatz from our planar NLC toroids with the ER director field in the one-constant approximation:

$$\mathbf{n} = \hat{r} \sin(\Omega) + \hat{\theta} \cos(\Omega) \frac{\omega r}{a - g_\xi^r \cos \theta} + \hat{\varphi} \cos(\Omega) \sqrt{1 - \left(\frac{\omega r}{a - g_\xi^r \cos \theta} \right)^2}, \quad (4.21)$$

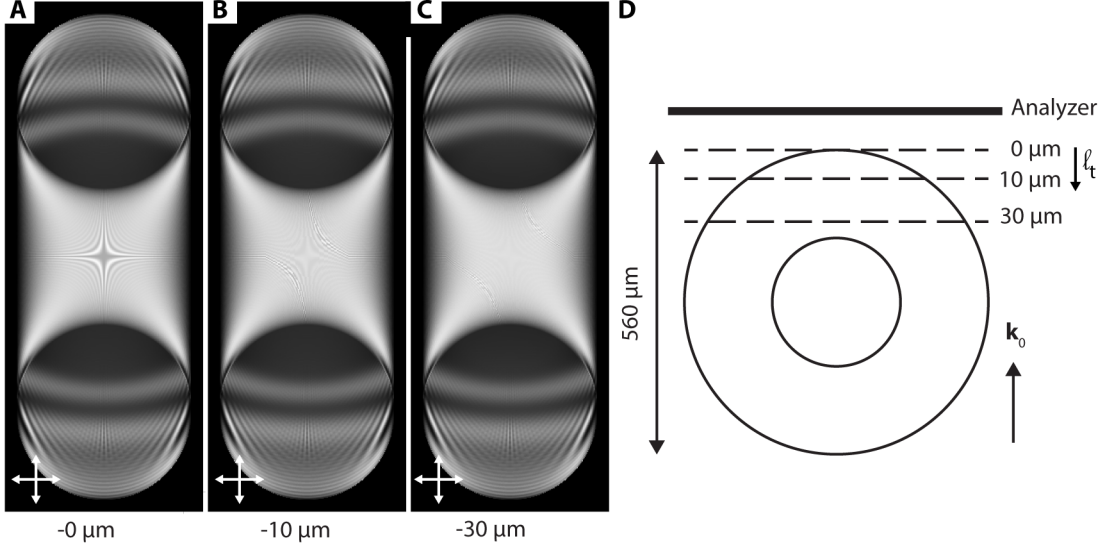


Figure 4.17: Effect of shape on the star feature in simulated OPM textures of planar NLC tori. (A–C), Simulated OPM textures with $\xi = 1.8$ and $\Delta/a = 0.001$ for $a = 100 \mu\text{m}$ viewed from the side of truncated tori, as described schematically in (D). All simulations performed averaging over 200 wavelengths.

where $\Omega = 2 \arctan(r/a)$. As with our simulated OPM textures of planar-anchored NLC toroids, we produce textures using a weighted average over 200 wavelengths evenly-spaced between 400 nm and 700 nm, where the weights are provided by the spectrum of the lamp in our microscope [see Figure 4.10]. Comparing the example experimental TER texture in Figure 4.5(B) with the partial example simulated ER and TER textures in Figure 4.18(A,B), respectively, we see that they share the same intensity features. Both of the simulated textures and the experimental texture exhibit the classic dark-bright-dark-bright-dark pattern when φ is aligned along the P and A directions. This gives credence to our hypothesis that the director field in a homeotropic nematic toroid is either escaped-radial or twisted escaped-radial.

To further confirm this, we simulate ER and TER capillaries, as shown in Figure 4.18(C,D), respectively. Here, we replace $\hat{\varphi}$ in Eq. 4.21 with \hat{z} , which we choose parallel to the capillary axis. From the top, we first see that our simulated ER and TER textures in a [Figure 4.18(A,B)] torus and simulated ER and TER textures in a [Figure 4.18(C,D)] capillary have the same alternating dark and bright intensity

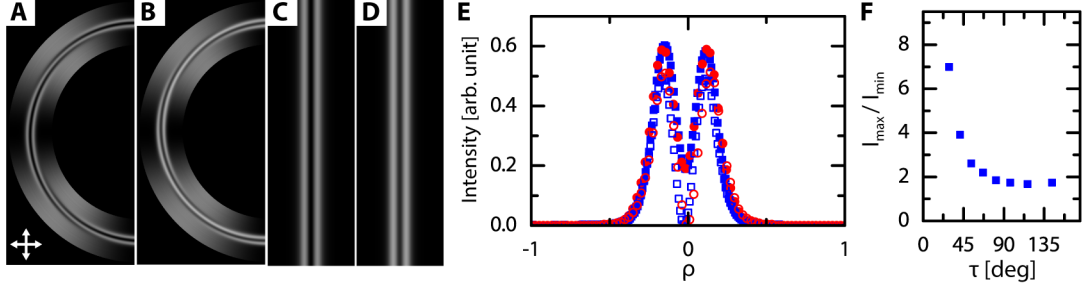


Figure 4.18: Simulated OPM textures, intensity profiles, and intensity ratios of TER configurations in tori and cylinders. (A–D), Simulated OPM textures of TER configurations in (A,B) tori and (C,D) cylinders. The textures are generated with twist angles (A,C) $\tau = 0^\circ$, (B,D) $\tau = 47.1^\circ$. (E), Intensity profiles from the simulated textures OPM textures in (A–D) corresponding to (\square , \blacksquare , \circ , \bullet), respectively. (F), Intensity ratio vs twist angle for simulated TER OPM textures.

features. We plot the intensity profiles in the simulated OPM textures of the tori (\square , \blacksquare) and the cylinders (\circ , \bullet) in Figure 4.18(E).

Second, from this plot we see that the intensity profiles are geometry independent; provided the $\hat{\varphi}$ and \hat{z} have the same τ and same orientation with respect to PA, the intensity profiles across the tube for the tori and the cylinders are identical. Thus, as expected, ER/TER configurations in a torus can be recognized by the classic alternating light and dark pattern associated with ER/TER capillaries. The TER configurations can further be distinguished from the ER configurations by the high central minimum in the TER intensity profiles [see Figure 4.18]. Third, we see that the intensity profiles of the simulated ER textures [(\square , \circ), Figure 4.18(E)] in the tori and the cylinders have $I_{\min} = 0$, in contrast to the experimental ER/TER textures in the capillaries; as mentioned earlier we believe that this is due to scattering from thermal fluctuations in the director orientation [22, 190]. Thus, while we cannot make a quantitative comparison between the intensity profiles in the experimental and simulated ER/TER toroidal textures, we can use our simulated OPM textures to investigate how the twist affects a TER texture.

4.4.5 Intensity ratio as a function of twist parameter

We simulate TER configurations for varying ω in tori, measure the intensity profiles, and plot I_{max}/I_{min} vs τ in Figure 4.18(F). We find I_{max}/I_{min} varies inversely and monotonically with τ . This confirms our expectations that adding twist raises the intensity of the central minimum in an OPM texture of a TER director configuration, causing I_{max}/I_{min} to decrease. In addition, the monotonic relationship between the intensity ratio and ω implies that we can use I_{max}/I_{min} as a proxy for twist. Thus, our observation that I_{max}/I_{min} increases with ξ [see Figure 4.5(G)] confirms that the amount of twist in a TER configuration in a toroid decreases with increasing ξ . This suggests that geometry is the driving factor in generating a TER structure. In addition, we argue that the twist in the TER structure results from bending the escape core, the central portion of the escape where $\mathbf{n} \sim \hat{\varphi}$. This is similar to straight capillaries filled with SSY, where the twist distortion also relieves a bend distortion. However, in SSY, $K_{11} \sim K_{33} \gg K_{22}$, such that it is energetically favorable to twist, even when the escape core is straight. In our case, we use 5CB with $K_{11} \sim K_{22} \sim K_{33}$. As a result, it seems that we need to introduce an extra bend distortion by bending the escape core to make the twist distortion energetically favorable in this case.

4.4.6 Intensity ratio as a function of escape rate

When we look closely at the escape core in the simulated TER textures in tori, we see that the escape core appears to spiral, similar to the experimental textures for NLC confined to toroids with low ξ . To test if we can obtain a spiral texture in our simulations similar to that in the experiments by changing the escape rate, we modify the ER and TER ansatzes from Eq. 4.21 by taking $\Omega = (\pi/2)(r/a)^\phi$. Recall that choosing $\phi = 1$ well approximates $2 \arctan(r/a)$, the one-constant solution [blue curve, Figure 4.3(D)]; choosing $\phi < 1$ yields a slower escape [red curves, Figure 4.3(D)]; and $\phi > 1$ yields a faster escape [red curves in Figure 4.3(D)].

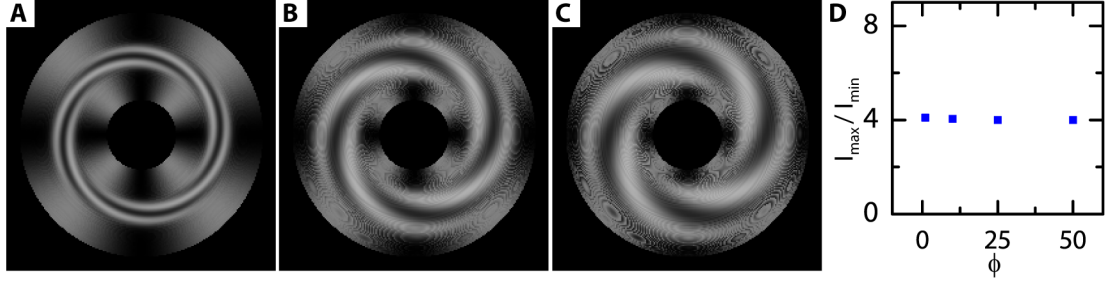


Figure 4.19: Simulated OPM textures and intensity ratios of TER configurations in tori with varying escape rates. (A–C), Simulated OPM textures of TER configurations with $\tau = 34^\circ$ and $\Omega = (\pi/2)(r/a)^\phi$, where (A) $\phi = 1$, (B) $\phi = 10$, and (C) $\phi = 25$. (D), Intensity ratio vs ϕ for OPM textures with $\tau = 34.9^\circ$.

Observing textures and the intensity profiles for $\phi = 1, 10, 25$ in Figure 4.19(A–C), respectively, we see $\phi > 1$ produces textures that qualitatively resemble those from our experimental toroids with the spiral textures. However, when we plot I_{\max}/I_{\min} vs ϕ for $\tau = 34.9^\circ$, we see that ϕ has no effect on the intensity ratio. This indicates that the intensity ratio in the spiral textures is still only determined by the twist in the texture.

4.5 Nematic liquid crystals in bent capillaries

To test whether geometry is the underlying cause for observing a TER texture in homeotropic NLC toroids, we consider 5CB under homeotropic anchoring in bent glass capillaries.

4.5.1 Making bent capillaries

We start with straight glass capillaries, heat the glass at a point with a blowtorch, and let gravity bend the capillary such that the capillary axis now forms a planar curve, as seen in the bright-field image of an example capillary in Figure 4.20(A). We apply the heat for as short of a duration as possible to minimize the change in the inner diameter of the capillary; applying the torch over a long duration melts the capillary.

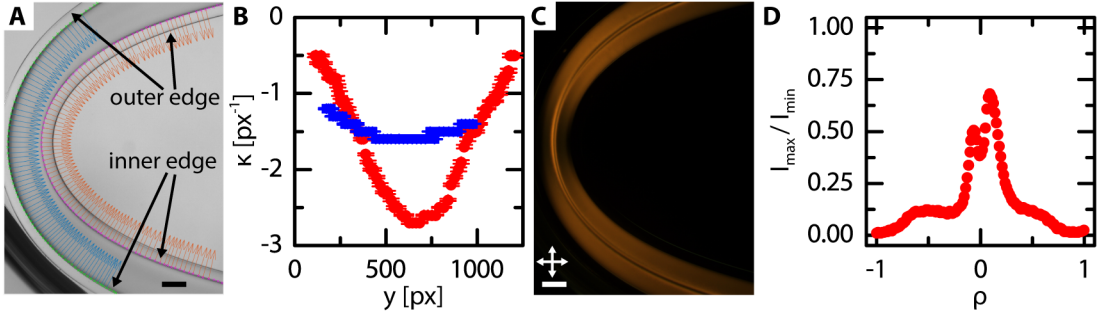


Figure 4.20: Measuring curvature and intensity profile in homeotropic NLC confined to bent capillaries. (A), Bright-field image of a bend capillary with points selected along the left and right contour. The normal vectors at each point are plotted on the image. (B), The measured curvature along the (■) left contour and (●) right contour of the image in (A). (C), OPM image of the capillary in (A). (D), Intensity profile from the OPM texture in (C). For this profile, $I_{max}/I_{min} = 1.8$ and $\xi^{cap} = 6.8$.

4.5.2 Measuring planar curvature

We measure the curvature of the capillary axis using a modified version of the IRLS routine we used in Chapter 3 to measure surface curvature. Here, instead of fitting to the extended Weingarten Matrix, we fit to the Frenet-Serret formula, $d\mathbf{k}/ds = -\kappa \cdot \mathbf{T}$, where s the arclength parameter, \mathbf{T} the unit tangent vector, \mathbf{k} the unit normal vector, and κ the curvature [19]. We then use:

$$\Delta \mathbf{k} \cdot \mathbf{T} = \kappa \Delta s, \quad (4.22)$$

with Δs the independent variable, $\Delta \mathbf{k} \cdot \mathbf{T}$ the dependent variable, and κ a fitting parameter. This approach is equivalent to fitting to the Weingarten Matrix for a surface with only one nonzero principal curvature everywhere, i.e. a surface with vanishing Gaussian curvature but nonzero mean curvature.

For a planar curve, we select points along the contour and then estimate \mathbf{T} and \mathbf{k} by calculating finite differences as in Chapter 3; these points and initial \mathbf{k} are plotted for the left and right contour on the image in Figure 4.20(A). We initially estimate κ for a point of interest by fitting Eq. 4.22 for all pairs of points within s_1

neighbors of the point of interest, where we take $\Delta\mathbf{k}_{[i,j]} = \mathbf{k}_{[i]} - \mathbf{k}_{[j]}$ and $\Delta s_{[i,j]} \approx \text{sign}\{(\mathbf{r}_{[i]} - \mathbf{r}_{[j]}) \cdot \mathbf{T}\}|\mathbf{r}_{[i]} - \mathbf{r}_{[j]}|$. We then use this initial estimate as the input for our IRLS routine and fit Eq. 4.22 considering all pairs of points within s_2 neighbors of the point of interest.

For the example image in Figure 4.20(A), we fit the left contour with $s_1 = 1$, $s_2 = 13$ and the right contour with $s_1 = 1$, $s_2 = 19$, plotting the output curvature [([■] left contour, (●) right contour] in Figure 4.20(B).

4.5.3 Measuring the intensity profile

To assign a local aspect ratio, we need the curvature along the central capillary axis. To find this, we start by selecting a point of interest in the capillary near the central axis. We then find the nearest point on the left and right contours, \mathbf{p}_{left} and \mathbf{p}_{right} , and take the intensity profile along the line connecting \mathbf{p}_{left} and \mathbf{p}_{right} . The central ring radius for the intensity profile is then given by $R_0^{cap} = (1/2)(\kappa(\mathbf{p}_{left})^{-1} + \kappa(\mathbf{p}_{right})^{-1})$, and the tube radius $a^{cap} = |\mathbf{p}_{left} - \mathbf{p}_{right}|/2$, such that we can calculate the local aspect ratio $\xi^{cap} = R_0^{cap}/a^{cap}$. Thus, we see that in a single bent capillary we can explore a variety of ξ simply by changing the crossed P and A to align with the capillary axis along different portions of the capillary. For the example OPM texture in Figure 4.20(C), we plot the intensity profile in Figure 4.20(D), where $\xi^{cap} = 6.8$. Note that similar to the toroids and to the straight TER capillaries, the maxima in the intensity profile of the bent capillaries generally have different intensity values. Since we observe no trend in which maximum is higher in the intensity profile, we employ the same strategy as earlier and take I_{max} to be the average of the two maxima in the intensity profile; for the example in profile in Figure 4.20(D), we find $I_{max}/I_{min} = 1.8$.

4.5.4 Comparison with toroids

We find that the intensity profiles for the $\xi^{cap} \rightarrow \infty$ regions of the bent capillary resemble the intensity profiles for the ER capillaries, while the intensity profiles with a finite ξ^{cap} [Figure 4.20(D)] have the raised central minimum indicative of a TER configuration, and similar to our TER toroids. Plotting I_{max}/I_{min} for the capillaries as a function of the local aspect ratio [(\blacktriangle), Figure 4.5(G)] on top of our data from the homeotropic toroids [(\circ), Figure 4.5(G)], we see that the data fall on top of each other, confirming that the amount of twist is determined solely by the local geometry. From this perspective, ξ can be seen as a dimensionless group locally comparing the relevant curvatures; a gives the radius of curvature in the bend distortion inherent to an escaped radial configuration, while R_0 is the radius of curvature of the additional bend distortion induced by bending the capillary. Bending the capillary breaks the cylindrical symmetry of the bend distortion in the ER configuration, introducing a dependence on θ . While for $\theta = 0$, the two bend distortions have the same sense, for $\theta = \pi$, they both have opposite sense. The aspect ratio details the magnitude of the asymmetry in the bend distortions: as ξ decreases, the asymmetry between the distortions grows, resulting in the twist distortion becoming more energetically favorable.

4.6 Conclusions

We have shown that geometry can affect the amount of twist in a homeotropic nematic confined to cylinders and toroidal droplets. In addition, we see that for NLC that do not twist when confined to a volume with $\xi = \infty$, making ξ finite can induce the nematic to twist, spontaneously breaking reflection symmetry in the process. While this is similar to results in degenerate-planar anchored NLC toroids, in this case there is no explicit curvature-coupling in the free energy driving the reflection-symmetry

breaking. To show this, we relied on simulated OPM textures to relate the effect of twist in the director fired to the corresponding OPM textures. We used planar-anchored toroids to demonstrate how the simulated textures responded to changing simulation parameters, and laid out a detailed methodology for simulating OPM textures in an arbitrary volume.

For NLC confined to a toroidal geometry with either homeotropic or degenerate planar boundary conditions, $\xi = R_0/a$ is the relevant geometrical parameter that controls the amount of twist in the system, comparing the scales of the relevant curvatures in the system. Under degenerate-planar anchoring, ξ is a measure of the difference between the principal curvatures, giving the strength of the saddle-splay distortion that drives the magnitude of the twist. When the anchoring is homeotropic, ξ instead gives the relative magnitudes of the bend distortions induced by the confinement; a sets the scale of the bend distortion inherent in an ER configuration, R_0 sets the scale of the additional bend distortion induced by curving the capillary axis. These distortions break the cylindrical symmetry of the bend distortion in the ER configuration, with the aspect ratio detailing the magnitude of the asymmetry: as ξ decreases, the asymmetry between the distortions grows, resulting in the twist distortion becoming more energetically favorable. Since the aspect ratio can be defined locally, the twist in both anchoring scenarios can be adjusted by locally tuning the aspect ratio. This demonstrates that confining NLC to toroidal-like geometries is a general strategy to tune chirality and investigate spontaneous symmetry breaking in an achiral material.

CHAPTER 5

HOMEOTROPIC NEMATIC BRIDGES

5.1 Introduction

The research presented so far has focused on nematic materials confined by toroidal surfaces. Here we consider a NLC confined under homeotropic anchoring to a volume topologically like a sphere. As established in Chapter 2, the volume must contain a total hedgehog charge $|d| = 1$, with the hedgehog charge defined in Eq. 2.8. Using a single defect, this condition can be satisfied by $d = -1$ hyperbolic point defects or hyperbolic ring defects, shown schematically from the side and top in Figure 2.6(B,D), and also by $d = +1$ radial point defects or radial ring defects, shown schematically from the side and top in Figure 2.6(A,C). The myriad of possible defect configurations satisfying the topological constraints gives the system a richness that has been well-explored for the spherical case, where the confinement can only be modified through changing the sphere radius [8, 11, 191–193]. However, the role of shape when confining NLC in geometries with more than one characteristic lengthscale is not completely understood.

Consider the case of a NLC under homeotropic anchoring in a cylindrical geometry of aspect ratio $\Gamma = 2R/H$, where R is the radius of the cylinder and H is its height. With this notation, the classic case of a cylindrical capillary corresponds to $\Gamma \ll 1$. The $\Gamma \gg 1$ situation corresponds to confinement between narrowly separated plates. When $\Gamma \sim \mathcal{O}(1)$, the equilibrium defect configuration undergoes a transition from a ring defect, found when $\Gamma \gg 1$, to a point defect, seen when $\Gamma \ll 1$. Prior experimental work on the defect structure in liquid crystal bridges focused on the transition between the ring and the point defect as a function of Γ [194, 195]. How-

ever, we note that Refs. [194, 195] only observed the bridge structures from above and thus were unable to determine how the bridge shape affects the defect transition. In addition, since the radial and hyperbolic defects appear the same when viewed from above, as seen in the lower row in Figure 2.6(A,B) and Figure 2.6(C,D) for ring defects and point defects, respectively, Refs. [194, 195] could not say whether the defects were radial or hyperbolic. Prior theoretical work used computational modeling to explore the defect configuration within a cylindrical bridge as a function of Γ and K_{11}/K_{33} [196, 197]. For 5CB, which has $K_{11}/K_{33} = 0.74$, they predicted that the bridge should transition between a radial ring defect [see Figure 2.6(C)] and a hyperbolic point defect [see Figure 2.6(B)]. However, as with the experimental work [194, 195], Refs. [196, 197] also do not investigate the role of the bridge shape. Thus, the role of shape in setting the defect structure (ring or point) and type (hyperbolic and radial) remains an open question.

In this Chapter, we address this open question and perform experiments pertaining to a confined NLC within a capillary bridge sandwiched between two parallel plates of adjustable separation and hence of varying Γ . By observing our experimental bridges from both the top and the side and comparing our observations with computations performed by our collaborators Shengnan Huang and Paul Goldbart, we find that the shape of the free surface controls whether the defect is radial or hyperbolic: waist-like bridges contain hyperbolic defects, and barrel-like bridges contain radial defects. To accomplish this, we develop polarized epifluorescent microscopy (PFM), an imaging technique allowing us to distinguish radial and hyperbolic defect structures in scenarios where common OPM techniques fail. In addition, we find good agreement between experiment and theory for the critical aspect ratio, Γ_c , at which the defect in the bridge undergoes a transition between a ring defect and a point defect. Finally, we see that this transition is hysteretic, due to the metastability of the point defect. Our results illustrate how shape and the nematic elasticity dictate defect structure in

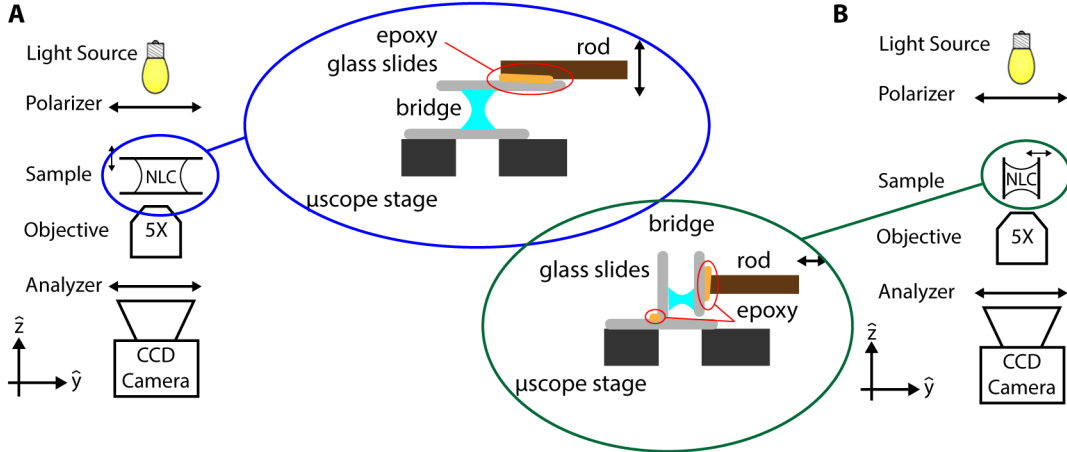


Figure 5.1: Experimental set-up. (A,B) Schematic from the side of the setup to view a bridge from the (A) top and (B) side. The zoomed-in portion of (A,B) highlights the setup to make and manipulate the bridge on the microscope stage.

confined homeotropic nematics.

5.2 Making capillary bridges

To make a capillary bridge, we confine 5CB between two parallel glass microscope slides. Prior to use, the slides were dip-coated with 0.1% w/w lecithin in hexane and left to dry to enforce homeotropic anchoring [82]. We set up an experiment to view a bridge from the top by first placing both microscope slides stacked on top of each other on the microscope stage. We then epoxy the top plate to a rod affixed to a micromanipulator such that we can adjust the distance between the slides. Note that this simple protocol ensures that the two microscope slides are parallel to each other and to the microscope stage. After the epoxy hardens, we raise the top slide and use a glass capillary to place a \sim nL-volume drop of 5CB onto the bottom plate. We then bring the top plate down until it makes contact with the sessile droplet and forms a capillary bridge. The final experimental setup is depicted schematically in Figure 5.1(A).

To set up an experiment to view a bridge from the side, we place an uncoated

glass slide on the microscope stage to act as a base, and then place a lecithin-coated glass slide vertically on the base and use a pair of blocks to hold it in place. We then epoxy the lecithin-coated slide to the base, applying epoxy to only one side of the joint between the base and the lecithin-coated slide. Once the epoxy has hardened, we remove the blocks and place the second lecithin-coated glass slide vertically on the base and against the previously-epoxied glass slide. We then use the rod attached to the micromanipulator to hold the two vertical slides together while we epoxy the second lecithin-coated glass slide to the rod. This protocol ensures that the two lecithin-coated glass slides are parallel to each other and perpendicular to the base. After the epoxy hardens, we use the micromanipulator to move the adjustable plate as far as possible from the fixed plate and place a \sim nl-volume drop of 5CB onto the fixed vertical plate as close to the base as we can. Finally, we bring the adjustable plate closer to the fixed plate until it makes contact with the sessile drop and forms a capillary bridge. The final experimental setup for a side view is depicted schematically in Figure 5.1(B).

As described, this procedure will yield a capillary bridge where the free-surface is in contact with air. To make a capillary bridge with the free surface in contact with water, we first make a bridge as described above and then pipette a drop of water near the edge of the parallel plates and let capillary action fill the gap between the plates. The water contains 8 mM SDS to enforce homeotropic anchoring.

5.3 Shape of capillary bridges

We begin by viewing the bridges from the side and characterizing their shapes. Bridges with air as an outer medium have a waist-like shape with negative Gaussian curvature everywhere on the free surface, as shown by the bright-field image of an example bridge in Figure 5.2(A). In contrast, as shown in the image of an example bridge in Figure 5.2(C), bridges with water and SDS as the outer medium have a

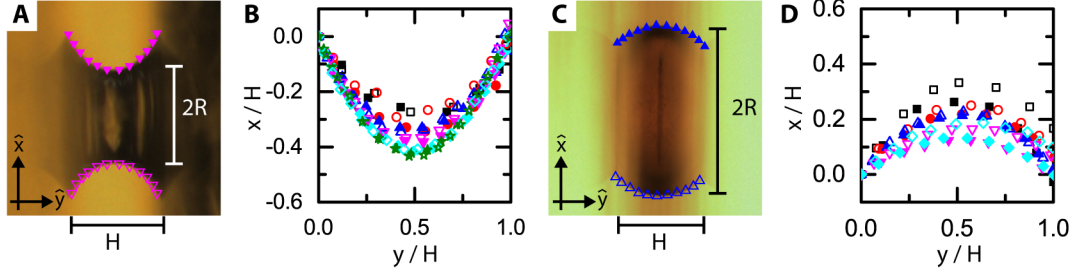


Figure 5.2: Measuring the shape of a bridge. (A,C), Bright-field images from the side of a (A) waist-shaped and a (C) barrel-shaped bridge, with the effective radius R and height H of each bridge defined in the image. The waist in (A) has $R = 180 \mu\text{m}$ and $H = 170 \mu\text{m}$, and the barrel in (C) has $R = 280 \mu\text{m}$ and $H = 300 \mu\text{m}$. (B,D), Contours of the bridge shown in (A,C), respectively, at different $\Gamma = 2R/H$, where the positions have been scaled by H and the (open symbols) lower contours have been reflected and shifted to line up with the (filled symbols) upper contours. The contours in (B) have (\blacksquare , \square) $\Gamma = 7.3$, (\bullet , \circ) $\Gamma = 4.6$, (\blacktriangle , \triangle) $\Gamma = 2.0$, (\blacktriangledown , \triangledown) $\Gamma = 1.0$, (\blacklozenge , \lozenge) $\Gamma = 0.6$, and (\star , \star) $\Gamma = 0.4$. The contours in (D) have (\blacksquare , \square) $\Gamma = 4.5$, (\bullet , \circ) $\Gamma = 3.9$, (\blacktriangle , \triangle) $\Gamma = 1.9$, (\blacktriangledown , \triangledown) $\Gamma = 1.5$, and (\blacklozenge , \lozenge) $\Gamma = 1.3$.

barrel-like shape with positive Gaussian curvature everywhere on the free surface.

5.3.1 Measuring the shape

As demonstrated on the example bridges in Figure 5.2(A,C), we record both the upper [closed symbols] and lower contours [open symbols] giving the shape of the bridge as a function of Γ , where we calculate an effective aspect ratio by taking R as the radius of the circular cross-section of the bridge midway between the two confining plates and taking H as the distance between the plates [see Figure 5.2(A,C)]. We then plot the contours normalized by the bridge height, with the lower contours reflected about the vertical axis, and all contours shifted so that their leftmost point corresponds to the origin, as shown in Figure 5.2(B,D) for the bridges in Figure 5.2(A,C), respectively. For both the barrels and the waists, the respective contours all approximately have the same shape regardless of Γ or experiment.

5.3.2 Constant mean curvature surfaces

To address the origin of the shape, we consider the relevant forces: the gravitational force $|\mathbf{F}_g| \sim \rho g R^2 H$; the surface tension force $|\mathbf{F}_\gamma| \sim \gamma H$; and the nematic elasticity force $|\mathbf{F}_K| \sim K$. The surface tension, density, and Frank elastic constant of 5CB are equal, respectively, to $\gamma \approx 30 \text{ mN/m}$, $\rho \approx 1 \text{ g/mL}$, and $K \approx 10^{-11} \text{ N}$. We compare these forces via two dimensionless groups: the Bond number $Bo = \frac{|\mathbf{F}_g|}{|\mathbf{F}_\gamma|} = \frac{\rho g R^2}{\gamma} \sim \mathcal{O}(10^{-2})$, and the elasticity group, $\frac{|\mathbf{F}_\gamma|}{|\mathbf{F}_K|} = \frac{\gamma H}{K} \sim \mathcal{O}(10^5)$, where we have taken $H = R = 100 \mu\text{m}$ as representative values. As $|\mathbf{F}_\gamma|$ is the dominant force, the mean curvature of the free surface of the bridge must be constant; otherwise, according to Eq. 3.8, there would be pressure gradients inside the bridge resulting in internal flow [47]. Thus, the surface must satisfy:

$$\Delta P = 2\gamma(-M) = -\gamma(\kappa_1 + \kappa_2) = \text{const}, \quad (5.1)$$

where ΔP is the Laplace pressure, $M = \text{tr}\{\mathbf{L}\}/2 = (\kappa_1 + \kappa_2)/2$ is the mean curvature of the surface, and γ is the surface tension. In addition, note that our capillary bridges are surfaces of revolution, where a planar curve is rotated about an axis to form a surface.

We can gain further insight into the shape of our bridges by writing Eq. 5.1 in terms of a contour of a surface of revolution. We can characterize such a contour in cylindrical coordinates $\{r, \varphi, z\}$, as schematically illustrated by the blue line in Figure 5.3(A), with the arclength parameter, s , and the angle between the r -axis and the tangent to the contour at s , θ , the elevation angle. The elevation angle naturally provides the contact angle for the surface, $\theta_0 = \theta(s = 0)$, with θ_0 the contact angle [blue circle, Figure 5.3(A)].

For a surface of revolution in cylindrical coordinates, the principal curvatures are

given by [29]:

$$\kappa_1 = \frac{z''(r)}{(1+z'(r))^{3/2}}, \quad \kappa_2 = -\frac{z'(r)}{r\sqrt{1+z'(r)^2}}. \quad (5.2)$$

We can easily write dr/ds and dz/ds in terms of the elevation angle, $dr/ds = \cos \theta$ and $dz/ds = \sin \theta$, implying that $z'(r) = \tan \theta$. Now, substituting this into Eqs. 5.2, we can write our principal curvatures in terms of θ :

$$\kappa_1 = \frac{1}{R_1} = \frac{\frac{d}{dr} \tan \theta}{(1 + \tan^2 \theta)^{(3/2)}}, \quad (5.3)$$

$$= \frac{\frac{d\theta}{dr} \frac{d}{d\theta} \tan \theta}{\sec^3 \theta}, \quad (5.4)$$

$$= \frac{d\theta}{ds} \frac{ds}{dr} \cos \theta, \quad (5.5)$$

$$= \frac{d\theta}{ds}. \quad (5.6)$$

$$\kappa_2 = \frac{1}{R_2} = -\frac{\tan \theta}{r\sqrt{1+\tan^2 \theta}} \quad (5.7)$$

$$= -\frac{\sin \theta}{r}. \quad (5.8)$$

From Eq. 5.6, we can write $ds = R_1 d\theta$, which makes sense considering that $\theta(s)$ is also the angle between \hat{z} and the normal to the curve at s ; the first principal curvature describes how the surface changes in the rz -plane. Similarly, from Eq. 5.8, we can write $R_2 = r/\sin \theta$, showing that the second radius of curvature is the distance from the contour to the z -axis along the normal to the contour. More importantly, this shows that R_2 always originates on the z -axis for a surface of revolution. Finally, if our bridges truly are surfaces of revolution with constant mean curvature, then the contours in Figure 5.2(B,D) must satisfy:

$$\frac{d\theta}{ds} = \frac{\sin \theta}{r} - \frac{\Delta P}{\gamma}, \quad (5.9)$$

$$\frac{dr}{ds} = \cos \theta, \quad (5.10)$$

$$\frac{dz}{ds} = \sin \theta. \quad (5.11)$$

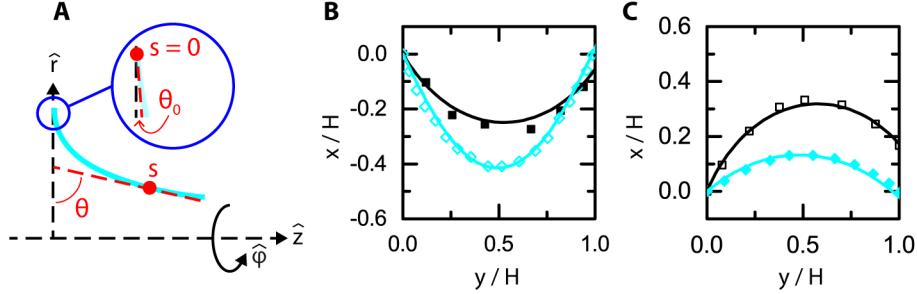


Figure 5.3: Constant mean curvature surfaces. (A), The elevation angle θ and arclength parameter s defined for a surface of revolution in cylindrical coordinates, $\{r, \varphi, z\}$, with a contour of the surface displayed in cyan. θ is the angle between the tangent of the cyan curve at s and \hat{r} . $\theta(s = 0) = \theta_0$, the contact angle, as shown in the magnified section in the blue circle. (B,C), Numerically calculated contours for a constant mean curvature surface of revolution plotted on experimentally measured contours for a (B) waist and a (C) barrel. The numerical solutions have contact angles (B) (black line) $\theta_0^{\text{waist}} = 37^\circ$, (cyan line) $\theta_0^{\text{waist}} = 35^\circ$ and (C) (black line) $\theta_0^{\text{barrel}} = 149^\circ$, (cyan line) $\theta_0^{\text{barrel}} = 120^\circ$. The measured contours in (B,C) are reproduced from Figure 5.2(B,D), respectively, and form the envelope of the measured contours in Figure 5.2(B,D).

These three equations can be solved with three initial conditions where $s = 0$. We control the height of the bridge in our experiments, determining $z(s = 0)$. As mentioned earlier, the contact angle is the initial condition on θ , $\theta_0 = \theta(s = 0)$. Finally, since the volume is fixed in our experiments, this determines the final condition $r(s = 0)$. However, since the contours in Figure 5.2(B,D) have all been scaled by H as well as all been shifted to all begin at $(0, 0)$, the actual values of $z(s = 0)$ and $r(s = 0)$ do not affect the shape. Accordingly, the difference between the contours for a waist [Figure 5.2(B)] and the contours for a barrel [Figure 5.2(D)] can only come from θ_0 . Thus, the contact angle between the lecithin-coated glass slide, the outer medium, and the 5CB determines the shape of our bridges [47].

To confirm this, we consider each bridge and numerically integrate Eqs. 5.9–5.11 to produce constant-mean curvature contours that capture the observed contours in Figure 5.2. We consider datasets in these figures representative of the spread observed, see Figure 5.3(B,C). To generate the numerical contours we start by making Eqs. 5.9–

5.11 dimensionless by dividing all lengths with H , such that $z(s = 0) = -1/2$ and $r(s = 0) = \Gamma/2$. Note that since Γ is measured in the middle of the two plates, $r(s = 0) = \Gamma/2$ is not accurate, but since the contours are shifted to all start at the same point, we emphasize again that $r(s = 0)$ doesn't affect the final shape. We then numerically integrate Eqs. 5.9–5.11 from $s = 0$ to $s = s_{lim}$, where $z(s = s_{lim}) = 1/2$, varying θ_0 and ΔP until the numerical contours capture the experimental data, see Figure 5.3(B,C). For an ideal bridge where $r(s = 0) = r(s = s_{lim})$ and $\theta(s_{lim}) = \pi - \theta_0$ [blue contour, Figure 5.3(B)], ΔP is not a free parameter but is determined by the constraints on $r(s = s_{lim})$ and $\theta(s_{lim})$. However, the contact areas on the plates are not always equal in our experiments, making $r(s = 0) \neq r(s = s_{lim})$ [black contour, Figure 5.3(C)]. Here, we vary ΔP for a given θ_0 to best fit the data, changing $r(s = s_{lim})$ and $\theta(s_{lim})$. We average the contact angles from the numerically-integrated contours for the waists and barrels to get $\theta_0^{waist} = 36^\circ \pm 8^\circ$ and $\theta_0^{barrel} = 127^\circ \pm 9^\circ$. We compare the contact angles determined from our calculated contours with contact angles measured from sessile droplets with both air and water as the outer medium, finding $\theta_0^{air} = 37^\circ \pm 5^\circ$ and $\theta_0^{water} = 123^\circ \pm 5^\circ$. This is in agreement with our data from the bridges, confirming that the contact angle is the main parameter determining the shape of our bridges.

5.4 Defect structure transitions

We view the bridge from the top to determine whether the defect is a ring or a point; examples of these situations are shown in the bright-field images of a waist-like bridge in Figure 5.4(A,C) and the corresponding crossed-polar images in Figure 5.4(B,D).

5.4.1 Defect transitions in a waist

We start at large Γ , where the equilibrium state has a ring defect, and determine the radius of the ring, R_{ring} , as we decrease Γ by increasing H in discrete steps. At each

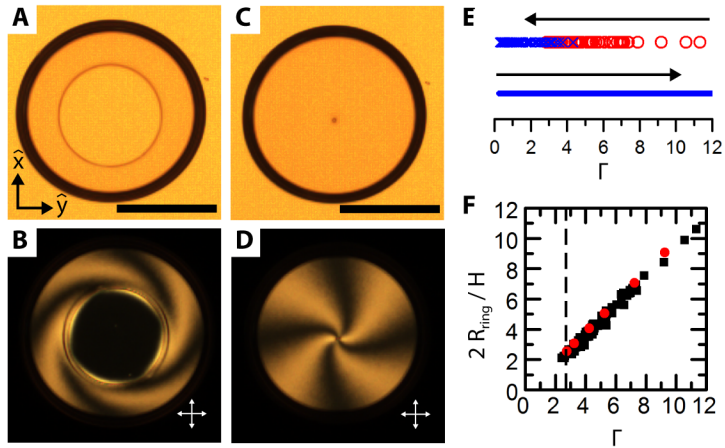


Figure 5.4: Data for bright-field and optical-polarized microscopy of waist-shaped NLC bridges viewed from the top. (A) Example bright-field image of a waist-shaped bridge with a ring defect. (B) Crossed-polar image of the bridge in (A). (C) Example bright-field image of a waist-shaped bridge with a point defect. This is the same bridge as in (A), but with an increased distance between the plates. (D) Crossed-polar image of the bridge in (C). (E) Experimental phase diagram for the defect state, demonstrating hysteresis at the transition. The arrows indicate the directions in which Γ is changed in the experiments. Starting at a large Γ in the ring-defect state (\circ) and decreasing Γ leads to a transition to a point defect (\times) at a value of $\Gamma = 2.7 \pm 0.3$, which we obtain by averaging the result for all bridges. In contrast, when starting at small Γ in a point-defect state and increasing Γ , the point-defect state persists; this is represented with a line. (F) The ring defect diameter in a waist-shaped bridge scaled by half the bridge height, plotted as a function of the bridge aspect ratio. A vanishing ring radius corresponds to a point defect. The (\blacksquare) are experimental measurements; the (\bullet) correspond to computations in a waist structure using the elastic constants for 5CB. Scale bars in (B,D): 250 μm .

H , we monitor the bridge over time to ensure that the defect state no longer changes and the system is in equilibrium. In addition, as we decrease Γ in each bridge, we also determine the effective aspect ratio for the defect transition, Γ_c . Using results for 21 different bridges, we find an average $\Gamma_c = 2.7 \pm 0.3$, as shown in the upper contour in Figure 5.4(E), where we have plotted each observation of a stable ring defect with a (○) symbol and each observation of a stable point defect with a (×) symbol. The ring diameter, scaled by the bridge height, varies linearly with Γ for $\Gamma > \Gamma_c$, as indicated by the squares in Figure 5.4(F), where we have again plotted every measurement we have performed. At Γ_c , the ring becomes unstable, and collapses to a point defect, yielding the discontinuity in R_{ring} shown with a dashed line in Figure 5.4(F), where the point defect is represented as having a vanishing R_{ring} .

However, when we start at $\Gamma < \Gamma_c$ in a point defect state and increase Γ , the point defect never transitions to a ring, as seen in the lower contour in Figure 5.4(E). Interestingly, if for $\Gamma > \Gamma_c$, we melt the nematic phase in a bridge containing a point defect, we always recover a ring defect state when we let the bridge cool back to the nematic phase. In contrast, when we do this for $\Gamma < \Gamma_c$, we still find a point defect when we let the bridge cool back to the nematic phase. This suggests that the point defect is metastable for $\Gamma > \Gamma_c$.

5.4.2 Defect transitions in a barrel

As with the waist structures, we start with a large Γ where the bridge contains a ring defect and decrease Γ in discrete steps, measuring the ring radius at each step, as shown in the bright field images of a barrel for four values of Γ in Figure 5.5(A,C,E,G), with the associated crossed-polar images in Figure 5.5(B,D,F,H). However, over time the SDS forms micelles in the 5CB that self-assemble onto the ring defect and form visible structures [see Figure 5.5(E,G)] in the NLC [198]. In addition, note how the area inside the ring defect in the OPM images in Figure 5.5(B,D,F,H) becomes pro-

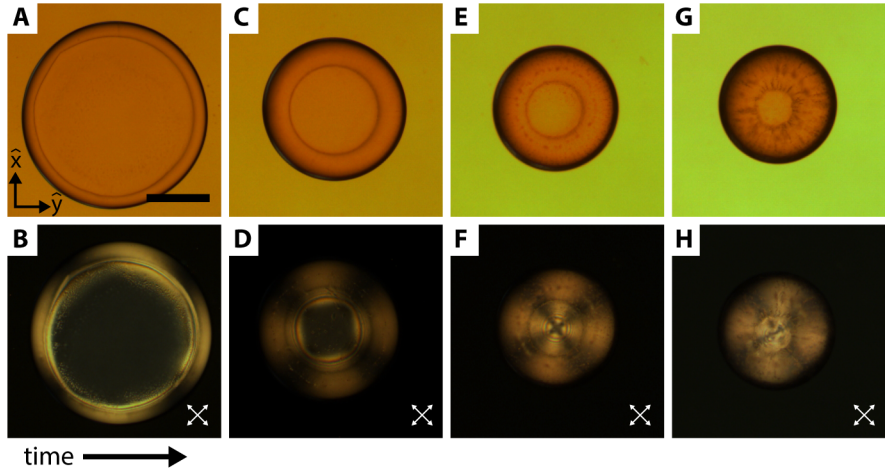


Figure 5.5: Bright-field and optical-polarized microscopy of barrel-shaped NLC bridges viewed from the top. (A,C,E,G), Bright-field images of a barrel-shaped bridge viewed from top with (A) $\Gamma = 5.0$, (C) $\Gamma = 2.6$, (E) $\Gamma = 1.4$, and (G) $\Gamma = 0.9$. Measurements were taken starting at (A) with $\Gamma = 5.0$ and decreasing Γ in discrete steps. (B,D,F,H), Corresponding crossed-polar images of the bridges in (A,C,E,G), respectively. Note how the sodium dodecyl sulfate (SDS) used to enforce homeotropic anchoring in the barrels forms micelles and disrupts the director in the bridge over time, from the initial measurement in (A,B) to the final measurement pictured in (G,H). The scale bar in (A) is 250 μm .

gressively brighter over time. Since the SDS micelles themselves are not birefringent, this brightening implies that the micelles are affecting the director field inside the bridge. Recall that the director field for a ring defect viewed from the top [see Figure 2.6(C,D)] indicates that the area bounded by the ring should be dark when the polarizer and analyzer are crossed. For a waist, where there is no SDS, this is always true [see Figure 5.4(B)]. In addition, we see that the self-assembled micelles can even stabilize non-circular ring shapes [see Figure 5.5(G)] and off-center rings [see Figure 5.6(B)], further indicating that the SDS can affect the director field in our bridges [198, 199].

To minimize the effect of the SDS micelles, we restrict our measurements to ring defects that are circular and centered in the bridge. We also make sure that the region within the ring in the crossed-polar images is dark, indicating that the SDS micelles have not yet significantly affected the NLC. For example, we exclude the data

in Figure 5.5(E-H) and in Figure 5.6(B,C). We then plot the ring diameter scaled by the bridge height as a function of Γ for each bridge, as seen in Figure 5.6(A). Here, the data are color coded by the measurement number for each bridge; the first measurement we make on a particular bridge is indicated by the (\blacksquare , \square) symbols. We then decrease Γ and make the second measurement for that bridge, plotting the data with the (\blacksquare , \square) symbols. Similarly, the third and fourth measurements on a bridge are indicated by the (\blacksquare , \square) and (\blacksquare , \square) symbols, respectively. The few magenta and blue points compared to the number of black and red points in Figure 5.6(A) indicate that the effect of the micelles grows in time; we, in fact, rarely have good data to make a fourth measurement and we never have good enough data to make a fifth measurement for a given bridge. Thus, even though we see that the scaled ring diameter varies linearly with Γ , [Figure 5.6(A)], we cannot make a quantitative prediction about a ring-to-point defect transition in our barrel-shaped bridges. This is true regardless of whether we make a barrel by adding the water + SDS to a waist with the 5CB in the nematic state [open squares, Figure 5.6(A)] or with the 5CB in the isotropic state [closed squares, Figure 5.6(A)]. In addition, note that the protocol used to make the barrel does not affect how the scaled ring diameter depends on Γ , indicating that the defect state in a barrel is not affected by the waist it was made from.

Even when we make barrels where the first measurement has low Γ , we do not see a clear collapse to a point defect; instead, we see a small ring defect with $0 < 2R_{ring}/H < 0.3$, as pictured in Figure 5.6(B,C) and Figure 5.6(D,E) for barrels made with $\Gamma = 2.4$ and $\Gamma = 2.8$, respectively. Since the ring in Figure 5.6(B) is off-center, we exclude this data. For the ring in Figure 5.6(D), we measure $2R_{ring}/H = 0.1$, and plot the data in Figure 5.6(A). We made ten barrels with an initial $\Gamma < 5$, we excluded seven of the barrels due to SDS effects. The remaining three barrels all have $0 < 2R_{ring}/H < 0.3$, as plotted in Figure 5.6(A).

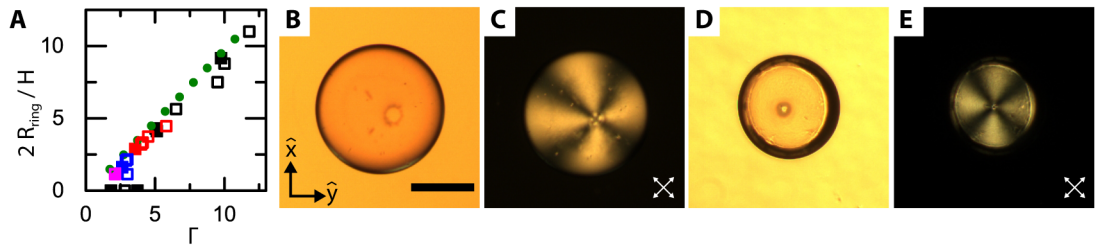


Figure 5.6: Ring defects in barrel-shaped NLC bridges viewed from the top. (A), The ring defect diameter in a barrel-shaped bridge scaled by height of the bridge divided by 2, plotted as a function of the bridge aspect ratio, Γ . The experimental points include barrels made with the 5CB in the [open squares] nematic phase and the 5CB in the [filled squares] isotropic phase. We label the experimental points with their measurement number, with (■, □) corresponding to the first measurement, (■, □) the second measurement, (■, □) the third measurement, and (■, □) the fourth measurement, where we start at a large Γ and decrease Γ with each subsequent measurement in a single barrel. The (●) correspond to computations in a barrel structure using the elastic constants for 5CB. (B–E), First measurement of a barrel with (B,C) $\Gamma = 2.4$ and (D,E) $\Gamma = 2.8$ made with the 5CB in the isotropic phase and viewed from the top just after the (B,D) bright field and (C,E) corresponding crossed-polar image indicate the director field has stopped changing. We exclude this bridge in (B,C) from the plot in (A) due to the presence of micelles; we cannot say if the micelles are preventing the ring from collapsing to a point defect or if the measured $2R_{ring}/H = 0.2$ is the equilibrium state. The defect structure in (D,E) is a ring with $2R_{ring}/H = 0.1$ and is plotted in (A) as such. The scale bar in (B) is 250 μm .

5.5 Measuring defect conformation using fluorescence microscopy

We return to viewing bridges from the side to determine if the defects are radial or hyperbolic. We start by viewing the bridges with OPM and rotating the crossed polarizer and analyzer; the texture for a radial defect rotates in the same direction as the polarizer and analyzer, while the texture for a hyperbolic defect rotates with the opposite sense [81]. However, due to the large curvature of the waist and barrel shapes, especially when Γ is large, we cannot clearly distinguish the rotation of the texture. This is demonstrated in Figure 5.7 for a bridge with small Γ [see Figure 5.7(A-C)] and a bridge with large Γ [see Figure 5.7(D-F)]. Changing the polarizer and analyzer (P and A) orientations by 45° for the bridge with small Γ [Figure 5.7(B,C)] produces a change in the texture, but it still does not clearly allow us to determine the brush rotation. Rotating PA by 45° for the bridge with large Γ [Figure 5.7(E,F)] produces an even smaller change in the texture. As an alternative approach, we develop and use polarized epifluorescent microscopy (PFM) to see whether the defect is radial or hyperbolic.

5.5.1 Theoretical overview of polarized epifluorescent microscopy

As mentioned earlier, fluorescence is an inelastic process where a material absorbs and then re-emits light. The realization that this process consists of both absorption and emission of light is attributed to Stokes, as is the name “fluorescence” itself. [200, 201]. However, the understanding that fluorescent emission could be polarized came from Weigert’s work with small fluorescent molecules, or fluorophores [202]. Individual fluorophores absorb and emit light like dipoles, with the absorption/excitation dipole and the emission dipole not necessarily parallel to each other [203]. Consequently, while an isotropic distribution of fluorophores will absorb and emit light isotropically, individual fluorophores are sensitive to the polarization of the excitation light and

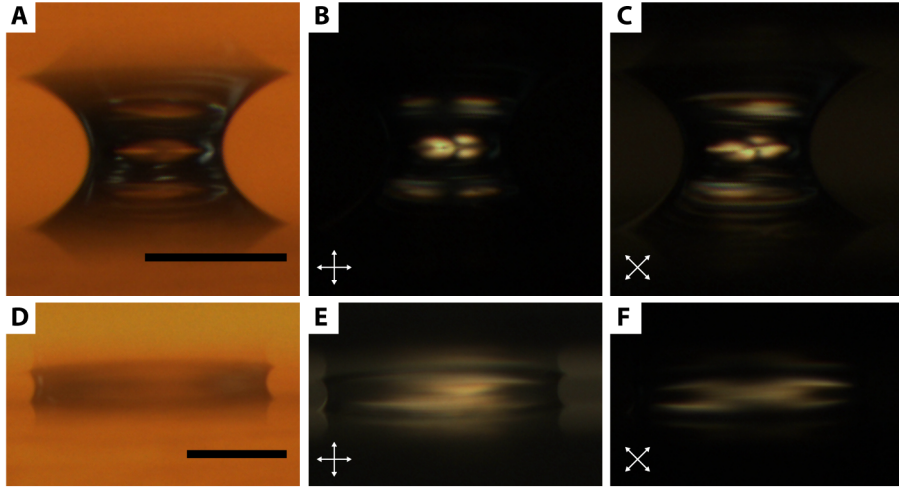


Figure 5.7: Rotating the polarizer and analyzer for a waist-shaped bridge viewed with optical-polarized microscopy from the side. (A-C), A waist-shaped bridge with $\Gamma = 1.2$ viewed from the side under (A) bright field and (B,C) with crossed polarizer and analyzer (PA), where the PA orientations are specified in each image. (D-F), A waist-shaped bridge with $\Gamma = 6.6$ viewed from the side under (D) bright field and (E,F) with crossed PA, where the PA orientations are specified in each image. The scale bars in (A,D) are 250 μm .

emit linearly polarized light along the emission dipole [203].

Polarized fluorescence has proven to be an incredibly effective tool in diagnostic imaging and the medical community; for example, it is commonly used to measure molecular or cellular mobility [203, 204]. Recently, the liquid crystal community has developed a renewed interest in polarized fluorescence, with techniques like Polarized Epifluorescent Confocal Microscopy (PCFM), enabling 3D resolution of a liquid-crystalline director [205, 206]. Here, we take inspiration from PCFM and develop Polarized Epifluorescent Microscopy (PFM), its wide-field cousin. At its core, PFM relies on anisotropic fluorophores whose emission axis is aligned along the long axis of the fluorophore. By introducing fluorophores in a NLC at low concentrations, the long axis of the fluorophores aligns along the nematic director without affecting the director configuration [205, 206]. Thus, the fluorescent emission of the mixed fluorophore and NLC system will be linearly polarized along the director. If we excite the sample with unpolarized light and place an analyzer in the emitted light path, as

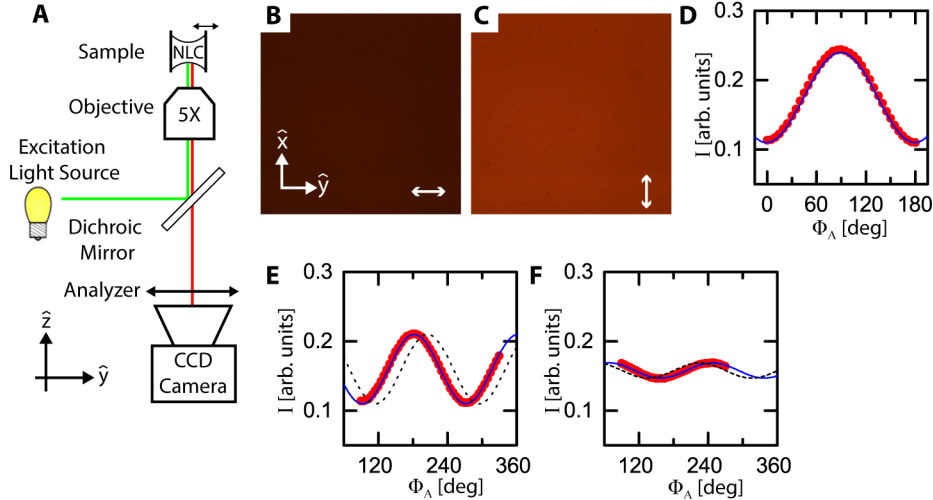


Figure 5.8: Polarized epifluorescent microscopy on a planar NLC cell filled with a mixture of 5CB and Nile Red. (A), Schematic from the side of the setup for polarized epifluorescent microscopy (PFM). (B–D), PFM (B,C) images and (D) recorded intensity as a function of Φ_A of the planar NLC cell with rubbing direction along \hat{x} . Φ_A is indicated in the images in (B,C), and is measured in (D) with respect to \hat{y} . The blue curve is a fit of the data to Eq. 5.12, returning $\delta' = 89^\circ$. (E,F), Recorded intensity as a function of Φ_A of the planar NLC cell with rubbing direction (E) 25° CCW from \hat{y} and (F) 45° CCW from \hat{y} . The blue curves are fits of the data to Eq. 5.12 and have $\delta' = 2^\circ$ and $\delta' = 67^\circ$, respectively. The black dashed lines correspond to theoretical curves for $\delta' = 25^\circ$ and $\delta' = 45^\circ$, respectively.

depicted schematically in Figure 5.8(A) then the emitted intensity from each point in the sample will be $\propto \cos^2(\Phi_A - \delta)$, where Φ_A is the orientation of the analyzer and δ is the orientation of \mathbf{n} in the plane of the output image [206]. However, as we use wide-field fluorescent microscopy, the recorded intensity at each point in the output image reflects an averaging of the director along the light path. Hence, we have sacrificed the three-dimensional spatial resolution of PCFM for the simplicity of PFM.

5.5.2 Experimental realization

We add 0.01 wt% Nile red to 5CB; at this concentration, Nile red does not affect the director configuration [207]. We image our sample using a standard epifluorescent setup with an analyzer in the emitted light path [Figure 5.8(A)] and a short-arc lamp

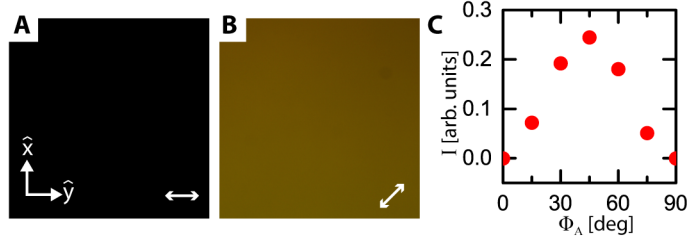


Figure 5.9: The dichroic mirror is birefringent. (A,B), Optical-polarized microscopy images with no sample, P and A crossed, and the dichroic mirror in the light path. Φ_A is indicated by the white arrow in the bottom-right of each image. (C), Transmitted intensity as a function of Φ_A for the same setup as in (A,B), with Φ_A measured CCW off of \hat{y} . The maximum at $\Phi_A = 45^\circ$ and minima at $\Phi_A = 0^\circ, 90^\circ$ implies that the optic axis of the mirror is along either \hat{x} or \hat{y} .

as our light source. We use filter set #20 from Zeiss, with a 534 nm – 558 nm bandpass excitation filter, a 560 nm longpass dichroic mirror, and a 575 – 640 nm emission filter [188]. For a sample, we record the output intensity $I(x, y)$ as a function of Φ_A and then fit the intensity at every pixel to the form:

$$I(x, y) = A + B \cos^2(\Phi_A - \delta'(x, y)), \quad (5.12)$$

where A , B and δ' are fitting parameters; A and B set the minimum value and range of I , respectively, and δ' reflects an average of the director orientation along the light path. Using the extracted δ' values, we can then plot the associated director field for a sample.

We initially test our analysis on planar cells (INSTECH LC2-9.0) that we fill with 5CB via capillary action. We image the cell with PFM and find that the fluorescence is much brighter when Φ_A is parallel to the rubbing direction than when Φ_A is perpendicular to the rubbing direction, as shown in Figure 5.8(B,C), respectively, for a rubbing direction oriented along \hat{x} . Plotting the average intensity in each image as a function of Φ_A with the (●) symbols in Figure 5.8(D), where Φ_A is measured off of \hat{y} , we see that the intensity varies as we would expect for such a rubbing direction: the

intensity is a maximum when $\Phi_A = 90^\circ$ and a minimum when $\Phi_A = 0^\circ, 180^\circ$. We fit the data in Figure 5.8(D) to the expression in Eq. 5.12 [blue curve] and find $\delta' = 89^\circ$, as expected.

We next change the rubbing direction to 25° measured from \hat{y} and plot the intensity as a function of Φ_A with the (●) symbols in Figure 5.8(E). However, when we fit the data to Eq. 5.12 [blue curve], we find $\delta' = 2^\circ$. Plotting the theoretical curve for $\delta' = 25^\circ$ [blue dashed line, Figure 5.8(E)], we see that the data are shifted to the left of the expected values. In addition, we see that the total intensity variation in the sample has decreased. Similarly, when we do the same for a rubbing direction of 45° [see Figure 5.8(F)], the fit returns $\delta' = 67^\circ$, with the data now shifted to the right of the expected values [blue dashed line, Figure 5.8(F)] and showing even less intensity variation. We hypothesize that there is another birefringent element in the light path with its optic axis along \hat{x} or \hat{y} ; the additional retardation changes the linearly polarized light to elliptically polarized light, shifting the I vs Φ_A curve and decreasing the variation in the light intensity as a function of Φ_A .

We confirm this by taking OPM images with no sample and just the dichroic mirror still in the light path, as seen for P and A at 0° and 90° and at 45° and 135° in Figure 5.9(A,B), respectively. The bright image in Figure 5.9(B) indicates the mirror is birefringent; plotting the transmitted intensity for crossed P and A as a function of Φ_A in Figure 5.9(C), we see that the optic axis of the mirror is indeed along either \hat{x} or \hat{y} . While the mirror affects the quantitative results, we see from our experiments with the planar cell that we can still distinguish between different rubbing directions. Finally, we also melt the 5CB in the cell to the isotropic to ensure that there is no appreciable intensity variation with changing Φ_A , as shown by the relatively flat transmitted intensity curve in Figure 5.8(J). With the 5CB in the isotropic, we measure the range in the intensity variation as a function of Φ_A to be 6% of the mean intensity. We compare this to the cell with the rubbing direction

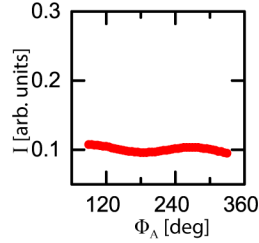


Figure 5.10: Recorded intensity as a function of Φ_A of a planar NLC cell filled with 5CB and melted to the isotropic. The rubbing direction is along 90° and the range in I is 6% of the mean.

along 45° , where our intensity variation with the 5CB in the nematic phase is the smallest, and find that the range in I is 25% of the mean. This indicates that the intensity variation is due to the 5CB and not to some property of the cell.

5.5.3 Validation in spherical droplets and cylindrical capillaries

We now turn to validating PFM using objects with a spatially varying director field. We start by considering spherical droplets of the Nile red-doped 5CB in water, with 8 mM SDS in the water to enforce homeotropic anchoring, shown in the bright-field image in Figure 5.11(A). We rotate the crossed P and A, as seen in Figure 5.11(B,C) for two different P and A orientations, and confirm that the droplets have the classic radial configuration [81], with a single radial hedgehog at the center of each droplet.

Importantly, we also notice that when rotating the analyzer the entire image appears to translate along a circular trajectory. Superimposing images of the spherical droplets with $\Phi_A = 0$ and $\Phi_A = \pi$ in Figure 5.11(D), we see that the images have been displaced. This displacement comes from the analyzer; it has a wedge angle to prevent specular reflections from affecting the final image quality,. However, this also serves to translate the image by $\Delta\rho$ along the orientation of the wedge angle, Φ_W , as illustrated schematically in Figure 5.12(A). Thus, rotating the analyzer by π translates the image in a semicircle with radius $\Delta\rho$ [see Figure 5.12(B)]. This means that to properly consider $\delta'(x, y)$ as a function of Φ_A , we have to correct this

displacement so that $I(x, y)$ comes from the same $\delta'(x, y)$ for all Φ_A .

We accomplish this by translating all the images along their respective Φ_W by a fixed magnitude $\Delta\rho$, removing the effect of the displacement due to the analyzer wedge angle for each image. Since $\Phi_W \in [0, \pi]$ while $\Phi_A \in [0, 2\pi]$, we use Φ_A to determine Φ_W up to a factor of π in each set of images; we translate an entire set by $\Delta\rho$ along both $\Phi_W = \Phi_A$ and along $\Phi_W = \Phi_A + \pi$ and keep the set where the displacement has been removed. Note that in our microscope, Φ_A and Φ_W also differ by 30° [see Figure 5.12(B)]. Our standard microscope setup with a $5\times$ objective and a $0.5\times$ adapter in front of the camera (The Imaging Source, DFK 41BU02) has $\Delta\rho = 6$ px.

Now superimposing the corrected versions of the images used in Figure 5.11(D), we see in Figure 5.11(E) that the displacement between the two images has disappeared. While in principle we could consider $\delta'(x, y)$ for every pixel, that is more information than we need and is susceptible to pixel-level noise. Instead, we blur each image with a mean filter to both remove noise and locally average the δ' , and then downsample each image to reduce the number of fits we need to perform. We illustrate this with the example PFM images in Figure 5.11(F–I), where the analyzer angle is indicated in each image. The original image is convolved with a mean filter of side length 7 px, yielding the blurred image in Figure 5.11(F) and then downsampled by a factor of 7, as displayed in Figure 5.11(G). Here, we focus on the highlighted pixel in the downsampled images in Figure 5.11(G–I) and plot the intensity in Figure 5.11(J). A fit of Eq 5.12 to the data in Figure 5.11(J) yields $\delta' = 88^\circ$. We do this for every pixel in the downsampled images and plot $\delta'(x, y)$ on top of the epifluorescent image in Figure 5.11(K). Indeed, we see that we qualitatively capture the radial texture. Note that we are unable to distinguish the actual point singularity due to the wide-field nature of our technique and the influence of the mirror; however, we clearly detect the presence of a radial defect in each droplet.

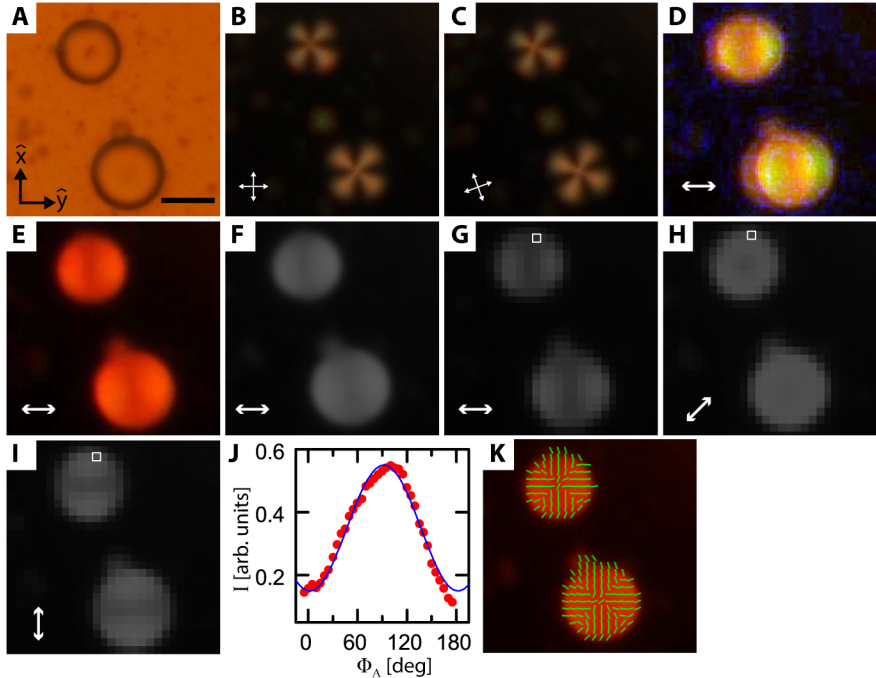


Figure 5.11: PFM analysis for radial droplets. (A), Bright field image of radial droplets made from a mixture of 5CB and Nile red dispersed in water and 8 mM SDS. (B,C), Corresponding crossed-polar images of the droplets in (A) with the P and A orientation indicated in each image. The texture rotates with P and A, indicating the hedgehog in each droplet is radial. (D), Superposition of two PFM images of the droplets in (A), where the images have the same Φ_A but opposite analyzer wedge-angle orientations. Note how the two images are displaced due to the effect of the analyzer wedge-angle, making the superposition blurry. (E), Superposition of the same images in (D) after shifting each image to correct for the displacement due to the analyzer wedge-angle. Here, the two droplets are clear and the superposition is no longer blurry. The analyzer angle in (D,E) is indicated schematically. (F), Grayscale intensity of a PFM image of the droplets in (A) after blurring with a square Gaussian filter with side length 7 px. The analyzer orientation is indicated schematically. (G-I), Downsampled PFM images after blurring, with the analyzer angle in each image indicated schematically. (J), PFM intensity as a function of Φ_A from the highlighted pixel in (G-I). The blue curve is a fit to Eq 5.12, returning $\delta' = 88^\circ$. (K), The δ' from a PFM analysis of every pixel in (G-I) plotted on top of an epifluorescent image of the droplets. The droplets are clearly radial, matching our observations in (B,C). The scale bar in (A) is 25 μm .

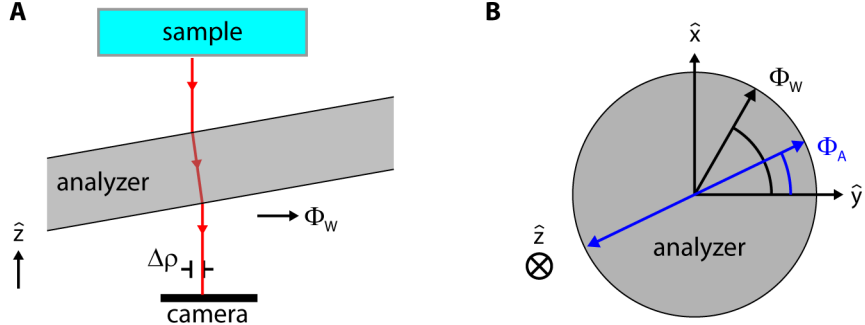


Figure 5.12: The analyzer shifts the image. (A), Schematic from the side showing how the wedge angle of the analyzer causes light from the sample to be translated by $\Delta\rho$ in the direction of the wedge, Φ_W . (B), The analyzer pass axis and the wedge angle are not parallel to each other. Rotating the analyzer by π will translate the image on the camera along a semicircle with radius $\Delta\rho$. Since $\Phi_A \in [0, \pi]$ while $\Phi_W \in [0, 2\pi]$, knowing Φ_A alone is not enough to know which direction the output image has been translated.

We next consider a cylindrical capillary filled with Nile red-doped 5CB. The capillary has a 600 μm inner diameter and is coated with lecithin to enforce homeotropic anchoring; it has a escaped-radial configuration with a point defect separating regions that escape in opposite directions [183], as seen in the crossed-polar images in Figure 5.13(A). We confirm that the defect is a radial point by rotating the crossed polarizer and analyzer and observing that the brushes follow the sense of rotation. We then image the capillary using PFM, where we have shifted, blurred, and down-sampled the images as with the radial droplets in Figure 5.11, and plot the output δ' on top of a bright-field image of the capillary in Figure 5.13(B).

As with the droplets, we see that we qualitatively capture the expected escaped-radial texture; we capture the radial character of the defect between the two escaped domains, but we do not resolve the singularity itself in our output. Since the escaped-radial director field for 5CB has been analytically solved [184, 185], with $\mathbf{n}(r, \varphi, z) = \{\sin(\Omega), 0, \cos(\Omega)\}$, where $\Omega = 2 \arctan(r/R)$, with R the capillary radius in cylindrical coordinates and \hat{z} along the capillary axis, we can compare the theoretical Ω with our measured δ' , as plotted in Figure 5.13(C). Even though there

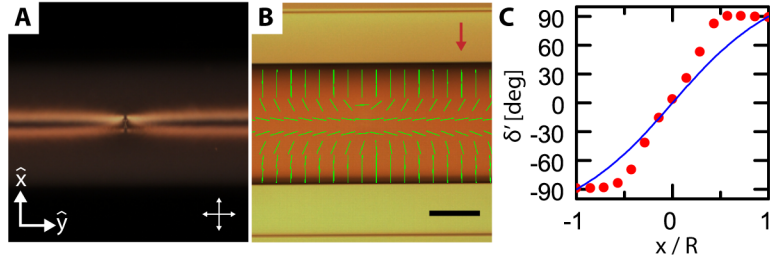


Figure 5.13: PFM in an escaped-radial capillary. (A), Crossed-polar image of a capillary filled with the Nile Red-Doped 5CB under homeotropic anchoring. (B), Bright-field image of the capillary in (A), with the director orientation from the PFM analysis plotted on top of the associated bright-field image. (C), δ' plotted versus the position across the capillary for the column indicated by the red arrow in (B). The blue curve is $2 \arctan(x/R)$, the theoretical director angles for an escaped-radial configuration in the one-constant approximation. Using the 5CB value of $K_{11}/K_{33} = 0.74$ would only slightly change the blue curve. The scale bar in (B) is 250 μm .

are quantitative differences, we can clearly see from both the plot of δ' vs x/R [Figure 5.13(B)] and the plotted δ' fields [Figure 5.13(C)] that we capture the different escape directions and thus can also resolve the radial character of defect between them.

5.5.4 Radial and hyperbolic defects in waists and barrels

We now use PFM on our waist-shaped bridges to determine if the defect is radial or hyperbolic. Since the output of PFM is biased due to the dichroic mirror, we orient the bridges with the plates along 45° , as seen in the bright-field image of a bridge in Figure 5.14(A), such that PFM will best distinguish the differences between a radial and a hyperbolic defect. We start with the waist-shaped bridges; for each bridge we perform a PFM analysis and plot the δ' on top of an epifluorescent image, as shown for an example bridge with large Γ in Figure 5.14(A,B) and an example bridge with small Γ in Figure 5.14(C,D). For both examples, we see that the defect structure is hyperbolic. We do this for waist-shaped bridges spanning $\Gamma \ll \Gamma_c$ to $\Gamma \gg \Gamma_c$, and find that the defect is always hyperbolic, implying that our waist-shaped bridges undergo transitions from a hyperbolic ring to a hyperbolic point as Γ decreases.

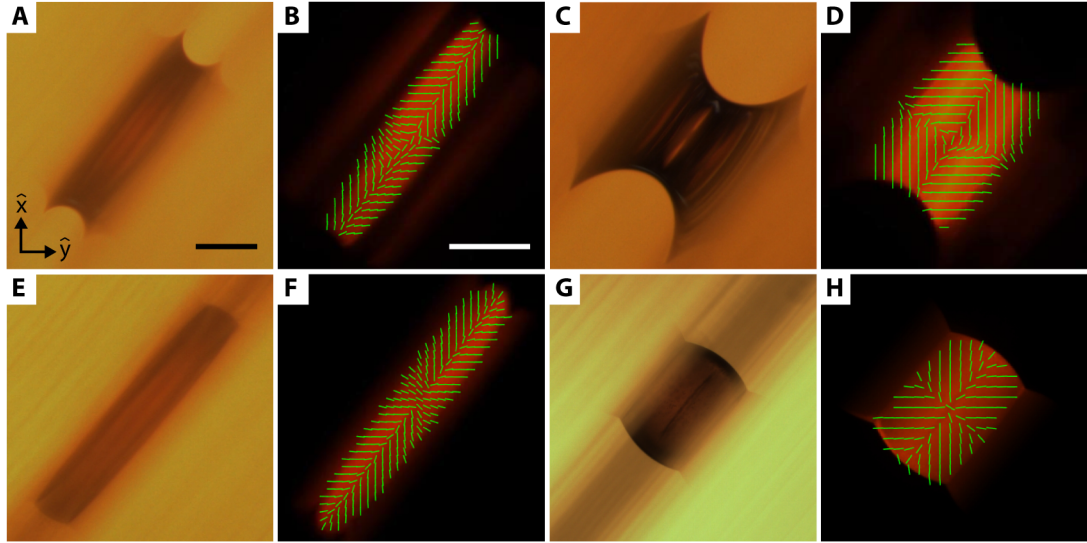


Figure 5.14: (A-D), PFM analysis on waist-shaped bridges with (A,B) $\Gamma = 4.0$ and (C,D) $\Gamma = 0.8$. The δ' are plotted on the epifluorescent images in (B,D) with the associated bright-field images in (A,C). (E-H), PFM analysis on barrel-shaped bridges with (E,F) $\Gamma = 6.6$ and (G,H) $\Gamma = 1.5$. The δ' are plotted on the epifluorescent images in (F,H) with the associated bright-field images in (E,G). The scale bars in (A,B) are $250 \mu\text{m}$, with the scale for all the (A,C,E,G) bright field images and all the (B,D,F,H) PFM images the same.

We now turn to barrel-shaped bridges, where we add the water and SDS mixture when the 5CB is in the isotropic phase, and we consider barrels made with both a large and a small initial Γ . As demonstrated in the plots of δ' on top of epifluorescent images of two example barrels with different Γ in Figure 5.14(E-H), the barrel-shaped bridges at all measured Γ have radial defects. Thus, we see that the shape of the bridge, driven by the contact angle, determines if the defect is radial or hyperbolic. This makes sense intuitively as the homeotropic boundary conditions cause the boundary to act as a level surface for the director.

Due to the ability of shape to bias the defect structure, the cylindrical bridge becomes an interestingly peculiar case, as the shape is neither a waist nor a barrel. While accomplishing this experimentally in our system would be technically difficult due to the requirement of maintaining $\Theta_0 = 90^\circ$, we can turn to numerical calculations to explore this scenario.

5.6 Comparison with numerical calculations: stable and metastable states

We compare our results with numerical calculations performed by Shengnan Huang and Paul Goldbart. These assume the problem is completely 2D; for a bridge parameterized in cylindrical coordinates, $\mathbf{n}(r, \varphi, z) = \{\sin(\Omega), 0, \cos(\Omega)\}$, where $\Omega = f(r, z)$ only. We then minimize the free-energy using a version of the finite difference method laid out in Ref. [197], modified as follows. Although the free energy in the algorithm presented there depends on the cut-off length of the defect core, the equilibrium defect configuration is independent of this length scale provided it is reasonably small. We modify the algorithm to treat the small region containing the defect separately from the remainder of the computation volume, such that the calculated free energy converges as the mesh size grows [208–210].

A cylindrical bridge is considered first. For the 5CB values of $K_{11}/K_{33} = 0.74$, a bridge should undergo a defect transition between a radial ring and a hyperbolic point, as highlighted by the dashed line in the phase diagram in Figure 5.15(A). This result is consistent with prior computational modeling [197], and highlights the peculiarity of the cylindrical case. However, the calculations find ring-to-point defect transitions at aspect ratios that are significantly smaller than previously reported [197]. In addition, in contrast to prior modeling, the calculations show no transition to a radial point structure [197]; only the hyperbolic point structure is stable [Figure 5.15(A)]. Instead, the numerical calculations predict that the radius of the radial ring should vary linearly with Γ for the entire range of Γ explored.

Next, the shape of the boundaries in the numerical calculations are changed. Consistent with our experiments, it is found that the radial defects in the phase diagram for a waist-shaped bridge disappear for all values of K_{11}/K_{33} used, as shown in Figure 5.15(B). Furthermore, the ring defect radius in Figure 5.4(F) predicted by the calculations (•) for a waist-like shape agrees very well with our experimental

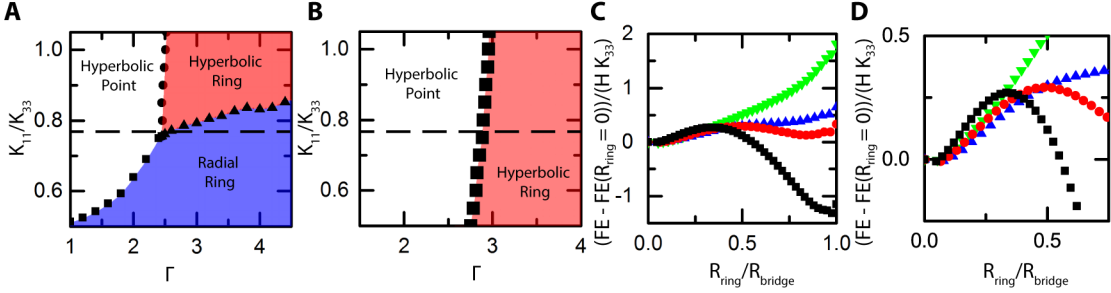


Figure 5.15: Results from the computational modeling of a nematic in a capillary bridge. (A), Phase diagram of the defect structure in a cylinder as a function of aspect ratio Γ and the ratio, K_{11}/K_{33} , of the splay and bend elastic constants. (B), Phase diagram of the defect structure in a waist-shaped bridge as a function of Γ and K_{11}/K_{33} . In (A,B), the minimum-energy state is indicated in each region, and the dashed line corresponds to K_{11}/K_{33} for 5CB. (C,D), Free energy of a director configuration in a waist-shaped bridge relative to the free energy in the presence of the point defect and normalized by HK_{33} , shown as a function of scaled ring radius R_{ring}/R_{bridge} . The curves correspond to (■) $\Gamma = 3.5$, (●) $\Gamma = 2.8$, (▲) $\Gamma = 2.5$, and (▼) $\Gamma = 2.0$.

data (■). In addition, the hyperbolic-ring to hyperbolic-point transition is found to happen at $\Gamma_c = 2.7$ for $K_{11}/K_{33} = 0.74$ [dashed line, Figure 5.15(B)], in agreement with our experimental measurement of $\Gamma_c = 2.7 \pm 0.3$ for decreasing Γ .

To investigate the hysteresis in our experimental hyperbolic ring to hyperbolic point transition, the energy landscape of a waist-shaped nematic bridge as a function of ring radius is calculated. Results for two bridges having $\Gamma > \Gamma_c$ and for two bridges having $\Gamma < \Gamma_c$ are shown in Figure 5.15(C,D), where we have taken $K_{11}/K_{33} = 0.74$; recall that the point defect is represented by the free energy for a vanishing ring radius. As the free energy exhibits a local minimum at $R_{ring} = 0$ [Figure 5.15(D)], we indeed see that the point defect is metastable for $\Gamma > \Gamma_c$, consistent with our interpretation of the experimental results. In addition, given a representative bridge height of $H = 100$ μm and $K_{33} \approx 10^{-11}$ N, we find that the height of the barrier is always $\mathcal{O}(10^4)$ $k_B T$, implying that a point defect will not spontaneously transform into a ring defect over the duration of our experiments, also consistent with our experimental observations. For $\Gamma < \Gamma_c$, this metastability disappears, and the hyperbolic point defect is the only

stable defect state.

Turning to barrel-shaped bridges, the calculations show that all hyperbolic defects disappear from the phase diagram, leaving the radial ring as the only equilibrium state for the range of Γ and K_{11}/K_{33} explored. This confirms that the shape of the free surface determines if the enclosed defect is radial or hyperbolic. Barrel-like shapes with positive Gaussian curvature favor radial defects and waist-like shapes with negative Gaussian curvature favor hyperbolic defects. We also see that the ring radius in Figure 5.6(A) predicted by the calculations (●) in a barrel-shaped bridge also agrees with our experimental results (squares), despite the influence of the SDS micelles in the experiments.

5.7 Conclusions

In conclusion, the equilibrium defect structure in a nematic capillary bridge under homeotropic boundary conditions is found to depend on both the shape of the bounding surface as well as the aspect ratio of the bridge. The aspect ratio determines whether the defect is a ring defect or a point defect, and the boundary shape determines whether the defect is radial or hyperbolic, with waist-like shapes containing hyperbolic defects and barrel-like shapes containing radial defects. In addition, we find that in a waist structure the point defect can be metastable, causing the transition between a ring defect and a point defect to exhibit hysteresis. Starting at $\Gamma > \Gamma_c$ and decreasing Γ to below Γ_c brings about the collapse of the ring defect to a point defect, with the collapse occurring at a nonzero value of the ring radius. However, starting with a point defect at $\Gamma < \Gamma_c$ and increasing Γ never yields a transition from a point defect to a ring defect.

Although prior computations with thin films [211] or perforated sheets [212] have been used to attribute the radial or hyperbolic character of defects to confinement shape, our work provides the first experimental evidence of this phenomenon. We

accomplish this by developing PFM, a simpler technique than its confocal counterpart that enables us, despite the influence of refraction from the surface of the bridge, to determine the director field when viewing the bridge from the side. Thus, our work confirms that curved geometries can be used to influence and control the equilibrium defect states in confined NLC under homeotropic boundary conditions.

As mentioned earlier, the cylindrical bridge with the predicted hyperbolic ring to radial point transition is a peculiar case. Specifically, we note that a hyperbolic ring can become a hyperbolic point and a radial ring can become a radial point simply by shrinking R_{ring} until $R_{ring} = 0$. However, the predicted transition between a radial ring and a hyperbolic point [see Figure 5.15(A)] requires the director field to reorient throughout the entire bridge at some point during the transition. The specific pathway for this transition is unclear and would be an interesting direction for future work. Similarly, the phase diagram [Figure 5.15(A)] also predicts an equally intriguing transition between a radial ring and a hyperbolic ring. Further interesting results would also be expected if the shape of the bridge is not fixed by surface tension, but can instead change and contribute to the free energy minimization [213]. Our work is thus one of many interesting studies that can be performed with nematic bridges to probe how shape and elasticity dictate the equilibrium defect structure of the liquid crystal.

CHAPTER 6

SUMMARY, CONCLUSIONS, AND FUTURE WORK

6.1 Summary and conclusions

Confining ordered materials can lead to interesting phenomenology due to the interplay between the order and the confinement geometry. For the nematic materials used in this Thesis, it is often the curvature of the confining volume or surface that affects the nematic order. This is a consequence of the fact that nematic materials possess only orientational order; with the order defined by the director \mathbf{n} , the free energy has order $|\nabla \mathbf{n}|^2$, indicating that curvature in the director field costs energy. The influence of curvature on a nematic material is even more explicit when considering a 2D nematic constrained to lie on a surface. In this situation, the free energy can be written to resemble that of a plasma, with defects in the nematic acting like discrete charges in the plasma and the Gaussian curvature of the surface as background charge in the plasma [see Eq 1.7]. Thus, if the surface has both positive and negative Gaussian curvature and the nematic has both positive and negative defects, the defects are predicted to segregate, with the positive defects migrating to the regions of positive Gaussian curvature and vice versa.

We explore this situation experimentally using an active polymeric nematic depleted to the surface of a toroidal droplet. Due to the activity, the nematic is filled with pairs of constantly creating and annihilating $s = \pm 1/2$ defects, with the $s = +1/2$ defects acting as self-propelled particles driving the nematic into a turbulent state. We measure the time-averaged topological charge in regions on the toroidal droplet and find that the average charge varies linearly with the integrated Gaussian curvature in the region. The slope of this relationship is positive, indicating

that our system exhibits defect unbinding. In contrast to predictions for a system at equilibrium, we find that the active unbinding depends only on the local geometry and is insensitive to the size and aspect ratio of our toroidal droplets. Comparing our experimental results to a numerical integration of the equations of motion of active nematic defects further illustrates that the defect unbinding also depends on the defect number density, and that the unbinding can even be suppressed in the limit of high activity. Finally, by using topological defects as micro-rheological tracers and quantitatively comparing our experimental and theoretical results, we are able to estimate the Frank elastic constant, the active stress, and the defect mobility of a microtubule-kinesin active NLC.

Overall, our results not only confirm the theory of topological defects on curved surfaces, but also demonstrate how adding activity to an ordered material changes and enriches equilibrium expectations. For example, because the active unbinding is driven solely by local interactions, we see that a combination of activity and curvature can be used to guide defects in ordered materials. In addition, our work introduces a new avenue for the quantitative mechanical characterization of active fluids.

So far we have only examined the behavior of the average topological charge $\bar{s}_\Theta = (\bar{N}_\Theta^+ - \bar{N}_\Theta^-)/2$, with \bar{N}_Θ^\pm the time-averaged number of $s = \pm 1/2$ defects in a region Θ on the active nematic toroid. This is only one of the things that our setup can explore. For example, we have preliminary data showing the time-averaged number density $\bar{N}_\Theta/A_\Theta = (\bar{N}_\Theta^+ + \bar{N}_\Theta^-)/A_\Theta$ depends on not only the local curvature, but also the aspect ratio of the toroid. It is not clear why the topological charge depends only on local interactions while the defect number density depends on the size and shape of the toroidal droplet. In addition, there is work with this active nematic system in flat space showing that the $s = +1/2$ defects can themselves assemble to form a nematic phase, where S associated to this higher-order nematic phase grows as \bar{N}_Θ grows. However, our preliminary data suggest that on a toroid, the $s = +1/2$ defects

do not form a nematic phase but instead a polar phase, and that the strength of this polar phase grows as the \bar{N}_Θ decreases. These are just two examples of future directions that we are currently working on that further explore the role of curvature and activity in partially ordered matter.

We also consider a NLC confined to toroidal droplets and bent capillaries under homeotropic boundary conditions. We observe spontaneous reflection symmetry breaking due to a twist distortion relieving the energetic cost of two competing bend distortions. The competition between the distortions is given by the local aspect ratio, ξ , comparing the radii of curvature of the two bend distortions. Thus, ξ also governs the amount of twist in the system, with the twist decreasing with increasing ξ . This geometrically-tuned chirality is similar to previous results in our group with NLC confined to toroidal droplets with degenerate planar anchoring, showing that tuning a ratio of curvatures to control chirality in NLC does not depend on the anchoring.

Lastly, we explore the equilibrium defect structure in NLC confined to capillary bridges under homeotropic boundary conditions. We find that the defect structure in our bridges depends on both the shape of the bounding surface as well as the aspect ratio of the bridge. The aspect ratio determines whether the bridge contains a ring defect or a point defect, and the boundary shape determines whether the defect is radial or hyperbolic, with waist-like shapes containing hyperbolic defects and barrel-like shapes containing radial defects. In addition, we find that in a waist structure the point defect can be metastable, causing the transition between a ring defect and a point defect to exhibit hysteresis. We compare with numerical calculations and find good agreement with our experiments. Our work thus shows that shape can be used to influence and control the equilibrium defect states in confined NLC under homeotropic boundary conditions. Interestingly, the numerical calculations predict that a cylinder-like structure can have defect transitions between radial rings and

hyperbolic points as well as between radial rings and hyperbolic rings. The specific pathways for these transitions are unclear and would be an interesting direction for future work.

6.2 Defect orientation on curved surfaces: current status

Prior work with a microtubule-kinesin active nematic on a flat surface demonstrated that the $s = +1/2$ defects self-organize into a higher-order nematic phase [15]. The orientation of each $s = +1/2$ defect is given by its velocity; calculating \mathbf{Q} for a collection of defect orientations uncovers long-range nematic order [15]. The strength of the order increases with increasing defect density and this higher-order nematic is typically defect-free, with a homogeneous director over the entire sample [15]. We are currently investigating how the $s = \pm 1/2$ defect orientations couple to the curvature of our toroidal droplets.

6.2.1 Theory

The velocity of the $s = +1/2$ defects is not the only way to assign an orientation to each defect. Recent work showed that the polar structure of the $s = +1/2$ defect can be characterized by a vector, and that the distortion free energy of a pair of $s = +1/2$ defects is minimized when the orientation vectors are antiparallel [214]. Thus, a dense collection of $s = +1/2$ defects would minimize its free energy by aligning antiparallel to each other, forming a higher-order nematic phase. For a single $s = +1/2$ defect, this orientation \mathbf{p} is calculated by:

$$p_i = \left\langle \partial_j Q_{ij}^{(\alpha)} \right\rangle_\alpha, \quad (6.1)$$

where Q_{ij} is the tensor order parameter and the average is taken along a closed contour encircling the defect. Reference [214] also proposed a method to characterize

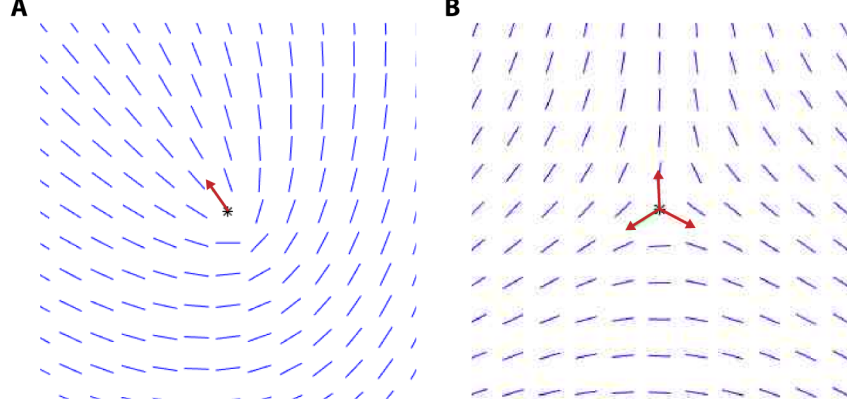


Figure 6.1: Example director fields and axes of symmetry for an (A) $s = +1/2$ and an (B) $s = -1/2$ defect. The axes of symmetry were calculated with Eqs. 6.2 and 6.3.

the orientation of $s = -1/2$ disclinations; however, their method requires a coordinate basis to be chosen.

Alternately, Ref. [215] has a method to calculate disclination orientation by constructing tensors of the appropriate rank. For example, the orientations of $s = +1/2$ and $s = -1/2$ disclinations are calculated via:

$$b_i = \left\langle \partial_j(n_i^{(\alpha)}n_j^{(\alpha)}) \right\rangle_\alpha, \quad (6.2)$$

$$T_{ijk} = \left\langle \partial_i(n_j^{(\alpha)}n_k^{(\alpha)}) + \partial_j(n_i^{(\alpha)}n_k^{(\alpha)}) + \partial_k(n_i^{(\alpha)}n_j^{(\alpha)}) \right\rangle_\alpha, \quad (6.3)$$

respectively, where the average is again taken over a path encircling the disclination. Importantly, the orientations of the $s = \pm 1/2$ disclinations calculated via Eqs. 6.2 and 6.3 are both tensors; they do not depend on the choice of a coordinate basis.

Comparing the two methods to calculate the orientation of an $s = +1/2$ disclina-

tion, we have:

$$\begin{aligned}
p_i &= \left\langle \partial_j Q_{ij}^{(\alpha)} \right\rangle_\alpha \\
&= \left\langle \partial_j \left(S^{(\alpha)} \left(n_i^{(\alpha)} n_j^{(\alpha)} - \frac{1}{2} \delta_{ij} \right) \right) \right\rangle_\alpha \\
&= \left\langle (\partial_j S^{(\alpha)}) \left(n_i^{(\alpha)} n_j^{(\alpha)} - \frac{1}{2} \delta_{ij} \right) \right\rangle_\alpha + \left\langle S^{(\alpha)} \partial_j (n_i^{(\alpha)} n_j^{(\alpha)}) \right\rangle_\alpha \\
&= \left\langle \frac{\partial_j S^{(\alpha)}}{S^{(\alpha)}} Q_{ij}^{(\alpha)} \right\rangle_\alpha + \left\langle S^{(\alpha)} \partial_j (n_i^{(\alpha)} n_j^{(\alpha)}) \right\rangle_\alpha.
\end{aligned} \tag{6.4}$$

If we choose a contour where S is constant, Eq. 6.4 becomes

$$p_i = S b_i. \tag{6.5}$$

Under this condition, both approaches give the same orientation. However, in general, Eq. 6.1 includes additional information about the spatial variation of S near the disclination. Since the methodology in Ref [215] produces a tensor for both $s = \pm 1/2$ disclinations, we will use Eqs. 6.2 and 6.3 to calculate our defect orientations.

6.2.2 Experiment

Our goal is to examine the defect orientations on the curved surface of our toroidal droplets. However, we project our data from the surface of the toroid onto a plane, forming a 2D image from which we determine the director and the defects. Thus, we will find the defect orientations in the 2D image and then project the defect orientations back onto our toroidal surface. In the plane of the image, we have the Cartesian coordinate system $\{\hat{x}, \hat{y}, \hat{z}\}$ with unit vectors $(1, 0, 0)$, $(0, 1, 0)$, and $(0, 0, 1)$, respectively. For an arbitrary unit surface normal $\mathbf{k} = (a, b, \sqrt{1 - a^2 - b^2})$, we define $\hat{v} = \hat{k} \times \hat{x}/|\hat{k} \times \hat{x}|$ and $\hat{u} = \hat{v} \times \hat{k}$, giving us an orthonormal coordinate frame on the surface $\{\hat{u}, \hat{v}, \hat{k}\}$.

Transforming between $\mathbf{r} \in \mathbb{R}^2$ to \mathbf{r}' on the surface of our toroid,

$$\mathbf{r}' = \begin{pmatrix} \frac{1}{\sqrt{1-a^2}} & 0 \\ \frac{ab}{\sqrt{(1-a^2)(1-a^2-b^2)}} & \sqrt{\frac{1-a^2}{1-a^2-b^2}} \end{pmatrix} \mathbf{r} = \mathbf{H}\mathbf{r}. \quad (6.6)$$

However, since $\{\hat{u}, \hat{v}\}$ depends on \hat{k} , $\{\hat{u}, \hat{v}\}$ will change over the surface of our droplet, making it difficult to compare defect orientations between different points on the surface. Instead, we will record our defect orientations on the surface of the torus in terms of a pair of curvilinear coordinate systems. The first coordinate system is the standard toroidal coordinate system, $\{\hat{\theta}, \hat{\varphi}, \hat{r}\}$, where $\hat{r} = \mathbf{k}$, the surface normal. The second coordinate system is $\{\hat{\theta}', \hat{\varphi}', \mathbf{k}\}$, with $\hat{\theta}' = (\nabla K)/|\nabla K|$, and $\hat{\varphi}' = \mathbf{k} \times \hat{\theta}'$. For a perfect toroid, the two coordinate systems are equivalent; however, in our case, the surface can be rough and our droplets are not perfectly axisymmetric. Thus, our two coordinate systems should allow us to distinguish between global effects driven by the toroidal geometry and local effects driven by K .

To calculate $\hat{\theta}$ and $\hat{\varphi}$, we start by finding the central circle from our data in \mathbb{R}^2 . We fit circles to the outer and inner contours in the 2D image of the toroidal droplet and average these contours to get an estimate of the central circle of our toroidal droplet. From the central circle, we can define a set of polar coordinates in the image $\{\hat{\rho}, \hat{\phi}\}$. We project $\hat{\phi}$ onto the surface of the torus to yield $\boldsymbol{\varphi} = \mathbf{H}\hat{\phi}$, and then normalize to get $\hat{\varphi} = \boldsymbol{\varphi}/|\boldsymbol{\varphi}|$. Finally, we calculate $\hat{\theta} = \hat{\varphi} \times \mathbf{k}$ to obtain the standard toroidal coordinate system on our toroidal droplet.

To calculate $\hat{\theta}'$ and $\hat{\varphi}'$, we start by computing ∇K in the 2D image and projecting it to the surface of the toroid to get:

$$\boldsymbol{\theta}' = \begin{pmatrix} \sqrt{1-a^2} & -\frac{ab}{\sqrt{1-a^2}} \\ 0 & \sqrt{\frac{1-a^2-b^2}{1-a^2}} \end{pmatrix} \nabla K = \mathbf{H}^{-1} \nabla K. \quad (6.7)$$

Normalizing, we get $\hat{\theta}' = \boldsymbol{\theta}'/|\boldsymbol{\theta}'|$, and then calculate $\hat{\phi}' = \mathbf{k} \times \hat{\theta}'$. Note that we project ∇K from the image to the surface of the toroid using \mathbf{H}^{-1} ; ∇K is a covector and thus the transformation matrix is the inverse of that for a vector.

As a first attempt, we will bin the surface by K and compute the order parameters in each bin. We will use overlapping bins of constant area in the 2D image.

We start by choosing a binsize N , in pixels. For a total area, A , in pixels, in the 2D image of the toroid, we consider a total of $A - N$ bins. With this protocol, two adjacent bins share all but a single pixel. We characterize each bin with $\langle K \rangle$, and then calculate the relevant order parameters in the bin using all $s = \pm 1/2$ defects in the bin over all time frames. For the $s = +1/2$ disclinations, we calculate the polar and nematic order parameters

$$S_{polar} \boldsymbol{\nu} = \frac{1}{n} \sum_{\alpha=1}^n \mathbf{b}^{(\alpha)}, \quad (6.8)$$

$$\mathbf{Q} = S_{nem} (\mathbf{n} \otimes \mathbf{n}) - \frac{1}{2} \mathbb{1} = \frac{1}{n} \sum_{\alpha=1}^n \mathbf{b}^{(\alpha)} \otimes \mathbf{b}^{(\alpha)} - \frac{1}{2} \mathbb{1}, \quad (6.9)$$

where S_{polar} and S_{nem} is the magnitude of the order and $\boldsymbol{\nu}$ and \mathbf{n} unit vectors describing the direction of the order, for polar order and nematic order, respectively. We note that Eq. 6.9 is equivalent to Eq. 2.1 and Eq. 2.4.

For the $s = -1/2$ disclinations, we take the orientation of T_{ijk} to be the angle $\phi_0 \in [-\pi/3, \pi/3]$, the orientation of one of the three axes of symmetry of an $s = -1/2$ disclination. Consider $\mathbf{n} = (n_x \hat{x}, n_y \hat{y})$ surrounding an $s = -1/2$ disclination, where $\theta = \arctan(y/x)$ is the polar angle describing the position. Then, if $\phi = \theta + \phi_0$ describes the director orientation, we can write the director field surrounding the disclination as $\mathbf{n} = (\cos(\phi/2) \hat{x}, -\sin(\phi/2) \hat{y})$. Computing T_{ijk} according to Eq. 6.3

and averaging over all θ , we have:

$$\begin{aligned}\langle T_{ij1}(\theta) \rangle_\theta &= \frac{3}{4} \begin{pmatrix} \cos \phi_0 & -\sin \phi_0 \\ -\sin \phi_0 & -\cos \phi_0 \end{pmatrix} \\ \langle T_{ij2}(\theta) \rangle_\theta &= \frac{3}{4} \begin{pmatrix} -\sin \phi_0 & -\cos \phi_0 \\ -\cos \phi_0 & \sin \phi_0 \end{pmatrix}\end{aligned}\quad (6.10)$$

From Eq. 6.10, we can now obtain ϕ_0 from $\langle T_{ijk}(\theta) \rangle_\theta$ via:

$$\phi_0 = \arctan \left(\frac{\langle T_{222}(\theta) - T_{121}(\theta) - T_{112}(\theta) - T_{211}(\theta) \rangle_\theta}{\langle T_{111}(\theta) - T_{221}(\theta) - T_{122}(\theta) - T_{212}(\theta) \rangle_\theta} \right). \quad (6.11)$$

Now, we use ϕ_0 to calculate the bond-angle order parameter for three-fold symmetry for the $s = -1/2$ disclinations in the bin

$$S_{bond} \exp(i3\Phi_o) = \frac{1}{n} \sum_{\alpha=1}^n \exp(i3\phi_o^{(\alpha)}), \quad (6.12)$$

where S_{bond} is the magnitude of the order and Φ_o is an angle giving the orientation of the order.

For an example toroid with $\xi = 2.4$, $a = 268 \mu\text{m}$, and an ATP concentration of $144 \mu\text{M}$, we plot the magnitude and orientation of the nematic and polar order for the $s = +1/2$ defects and the three-fold bond order for the $s = -1/2$ defects as a function of the mean Gaussian curvature in each bin in Figure 6.2(A–C), Figure 6.2(D–F), and Figure 6.2(H–J) respectively. We see that for both the $\{\Theta, \varphi\}$ [Figure 6.2(A,D,G)] and the $\{\nabla K = \theta', \varphi'\}$ [Figure 6.2(B,E,H)] coordinate systems, the $s = \pm 1/2$ defects exhibit order in the regions where the magnitude of K is larger. Interestingly, we note that the $s = +1/2$ defects exhibit polar order on our toroidal droplets, rather than nematic order seen in flat space [15]. Since we consider the defects at all time points when calculating the order, Figure 6.2 reflects a persistent

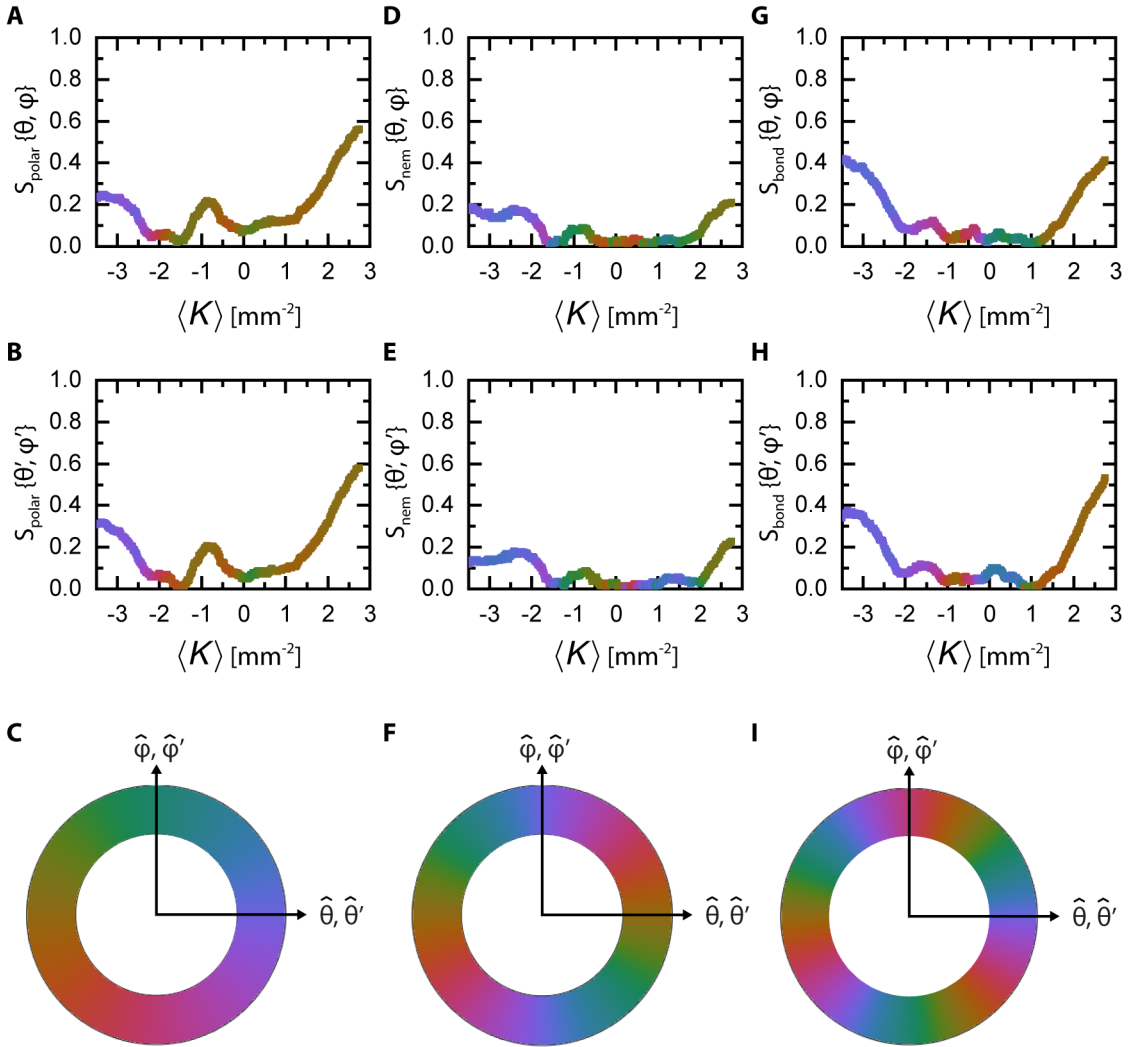


Figure 6.2: $s = \pm 1/2$ defect ordering on a toroid with $\xi = 2.4$, $a = 268 \mu\text{m}$, and an ATP concentration of $144 \mu\text{M}$. Magnitude and direction of (A–C) polar and (D–F) nematic order calculated for the $s = +1/2$ defects and (G–I) three-fold bond angle order calculated for the $s = -1/2$ defects. The order in (A,D,G) and (B,E,H) is calculated for the $\{\theta, \varphi\}$ and the $\{\nabla K = \theta', \varphi'\}$ coordinate systems, respectively, with (C,F,I) indicating the color scales used to denote orientation.

steady state. In addition, we see that the direction of the order is different in regions of negative and regions of positive Gaussian curvature. In regions where $K > 0$, the $s = +1/2$ defects align along $-\hat{\theta}$, consistent with the idea that the $s = +1/2$ defects migrate towards $\theta = \pi$ in order to minimize their contribution to the free energy. However, in regions where $K < 0$, the $s = +1/2$ defects align along $\hat{\theta}$, the opposite of what we expect; this indicates that on average, $s = +1/2$ defects in regions near the hole of the torus move further towards $\theta = 0$. We note that even if the $s = +1/2$ defects want to move towards the hole, this is still consistent with curvature-induced defect unbinding provided that the $s = -1/2$ defects migrate towards the hole at a higher rate than the $s = +1/2$ defects. Repeating this analysis for the remainder of our toroids, our preliminary results indicate that the $s = +1/2$ defects possess steady state polar order, the $s = -1/2$ defects possess steady state three-fold bond angle order, and that the magnitude of the order grows with increasing $|K|$ for both defect species.

To investigate the origin of this order, we plot the polar order for the $s = +1/2$ defects and the three-fold bond angle order for the $s = -1/2$ defects against the mean defect density and against the mean $|K|$ in each bin in Figure 6.3(A–D) and Figure 6.3(F–I), respectively. We see from the plotting the order against the mean defect density in each bin, that the magnitude of the order grows as the defect density decreases [polar order, Figure 6.3(A,C) and three-fold bond angle order, Figure 6.3(F,H)]; this is the opposite of the results in flat space [15]. We also see that the magnitude of the defect order grows with increasing $|K|$ [polar order, Figure 6.3(B,D) and three-fold bond angle order, Figure 6.3(G,I)]; this makes intuitive sense as the gradient of the Gaussian curvature reflects the change in the “background charge” influencing the defects.

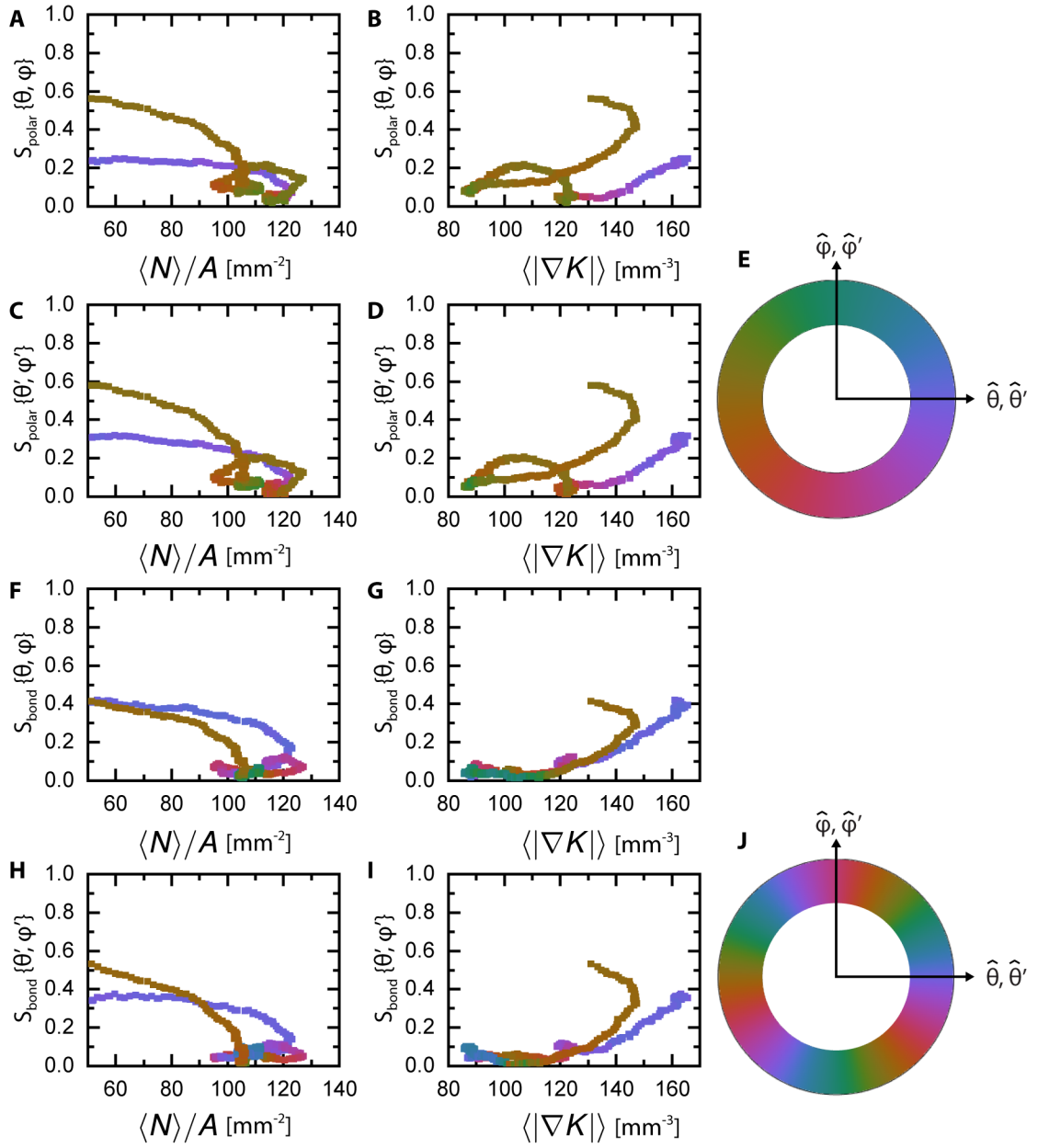


Figure 6.3: $s = \pm 1/2$ defect order plotted as a function of the mean defect density and of the magnitude of the gradient of the Gaussian curvature. Magnitude and direction of the (A–D) polar order for the $s = +1/2$ defects and the (F–I) three-fold bond angle order for the $s = -1/2$ defects. (A,B) and (F,G) are calculated in the $\{\theta, \varphi\}$ coordinate system, while (C,D) and (H,I) are calculated in the $\{\nabla K = \theta', \varphi'\}$ coordinate system. The magnitude and direction of the order are plotted in (A,C,F,H) and (B,D,G,I) as a function of the mean defect density and of the mean magnitude of the gradient of the Gaussian curvature, respectively. The polar and three-fold bond angle color scales are displayed in (E,J), respectively.

6.2.3 Future Work

To understand the nature of the ordering on the toroidal droplets, we need more data that focuses on the regions of the toroids that have a large Gaussian curvature magnitude. These regions are where we see the ordering arise and where we have the least amount of data. We are currently taking more data that looks specifically at these highly curved regions. In addition, we are currently taking data on cylindrical surfaces in order to better understand how the global properties of a surface affect the defect ordering. In addition, now that we see that there is a persistent steady-state in the defect orientations, we are analyzing smaller time windows to obtain the fluctuations in the orientation.

We also wish to understand defect orientation correlations in space at a given time. To do this, we need to be able to calculate discrete geodesics on the surface of the torus. We are currently working on implementing the algorithms in Refs. [216, 217].

6.3 Determining the saddle-splay elastic constant: current status

It is difficult to measure saddle-splay because it is difficult to achieve a pure saddle-splay distortion in a nematic volume [see Eq. 2.17]. In addition, since the saddle-splay distortion in the bulk is intimately connected with the director behavior on the boundary of the material, there is concern that anchoring and surface elastic terms could prevent an accurate measurement of K_{24} [56, 179, 218]. Finally, there are discrepancies concerning the coefficient associated with the saddle-splay distortion, with $-(1/2)(K_{22} + K_{24})\nabla \cdot (\mathbf{n}\nabla \cdot \mathbf{n} + \mathbf{n} \times \nabla \times \mathbf{n})$, $-(1/2)K_{24}\nabla \cdot (\mathbf{n}\nabla \cdot \mathbf{n} + \mathbf{n} \times \nabla \times \mathbf{n})$, and $-K_{24}\nabla \cdot (\mathbf{n}\nabla \cdot \mathbf{n} + \mathbf{n} \times \nabla \times \mathbf{n})$ all found in the literature. As a result, the published measurements of K_{24} often differ substantially. For example, the reported measurements of K_{24} for 5CB, the most common thermotropic NLC in the literature,

Table 6.1: Experimentally-obtained values for K_{24} using 5CB for four literature sources, both as reported and after recasting the saddle-splay distortion in the form: $-(1/2)(K_{22} + K_{24})\nabla \cdot (\mathbf{n}\nabla \cdot \mathbf{n} + \mathbf{n} \times \nabla \times \mathbf{n})$.

As reported		
Authors	K_{24}/K_{22}	Notes
Allender <i>et. al.</i> [219]	1.1 ± 0.9	Used 1-constant approximation
Polak <i>et. al.</i> [220]	3.1 ± 4.4	
Sparavigna <i>et. al.</i> [221]	0.994 ± 0.006	Used 1-constant approximation
Pairam <i>et. al.</i> [37]	$1.02 \pm .02$	
Corrected notation		
Authors	K_{24}/K_{22}	Notes
Allender <i>et. al.</i> [219]	1.2 ± 0.8	Used 1-constant approximation.
Polak <i>et. al.</i> [220]	2.5 ± 3.0	
Sparavigna <i>et. al.</i> [221]	0.994 ± 0.006	Used 1-constant approximation.
Pairam <i>et. al.</i> [37]	1.04 ± 0.04	

vary from $\approx K$ in a 1-constant approximation to $3.1K_{22}$ [see Table 6.1] [37, 219–221]. Even after correcting for notational differences and representing the saddle splay distortion as in Eq. 2.18, we see in Table 6.1 that the published measurements are in general imprecise due to either a large error or a reliance on a 1-constant approximation. Furthermore, the concerns in the literature that any measurement of K_{24} is always affected by interactions between the nematic and the confining volume cast further doubt on the measurements in Table 6.1 [56, 179, 218].

6.3.1 Prior estimates in tori

Recent work in NLC toroids with degenerate planar anchoring revealed the coupling between the saddle-splay distortion and the curvature of the bounding surface [see Eq. 2.52] [37, 39]. This coupling was used to make precise estimates of K_{24} not only in 5CB but also in the LCLCs SSY [40, 179] and DSCG [40] confined in cylindrical capillaries. To illustrate this estimate, we refer to the example illustrated in Section 4.1 of a linear twist ansatz in a torus where $\xi \rightarrow \infty$. Taking the values of the twist parameter, ω , that minimize the free energy [Eq. 4.6] and substituting into the

expression for the twist angle, τ [Eq. 4.7], we have:

$$K_{24} = K_{22} + \frac{K_{33}}{2} \sin^2\left(\frac{\tau}{2}\right). \quad (6.13)$$

Since the values of K_{22} and K_{33} are easy to establish independently, Eq. 6.13 provides a relation between a single measurement of a twist angle to the value of K_{24} for a given NLC. For example, using the value of K_{24} measured in Ref. [37], $K_{24} = (1.04 \pm 0.04)K_{22}$, we calculate that $\tau_{\xi \rightarrow \infty} = 19^\circ [+8^\circ, -19^\circ]$.

6.3.2 Results from spherical drops

Prior work with spherical emulsion droplets of 5CB in phosphate-buffered saline (PBS) with various ionic strengths found a size dependent configuration, with bipolar configurations observed for droplets with radius $R \gtrsim 1 \mu\text{m}$ and radial configurations for $R \lesssim 1 \mu\text{m}$ [222]. As a potential explanation, the authors considered the Frank-Oseen free energy for a radial droplet and a bipolar droplet in the presence of degenerate planar anchoring:

$$F_{radial} = 8\pi K_{11}R - 4\pi(K_{22} + K_{24})R + 2\pi WR^2 \quad (6.14)$$

$$F_{bipolar} = 5\pi K_{11}R - 2\pi(K_{22} + K_{24})R, \quad (6.15)$$

where $f_{anchoring}(\mathbf{r}) = (1/2)W(\mathbf{n}(\mathbf{r}) \times \mathbf{k}(\mathbf{r}))^2$ is the single-constant Rapini-Papoulier energy density for degenerate planar anchoring, with W the strength of the anchoring and \mathbf{k} the surface normal. Comparing these free energies, they subtract Eq. 6.15 from Eq. 6.14 with $2K_{22} = K_{11}$ for 5CB:

$$\Delta F_{trans} = 2\pi R(2K_{22} - K_{24} + WR). \quad (6.16)$$

If $K_{24} > 2K_{22}$, we see that bringing R small enough will eventually cause ΔF_{trans} to become negative, indicating that a radial structure has a lower free energy than a bipolar structure. From Eq. 6.16, Ref. [222] proposed saddle-splay as responsible for the size-dependent structures observed. While Table 6.1 has measurements of $K_{24} > 2K_{22}$, such a value of K_{24} also implies that cylindrical or toroidal confinement of 5CB would result in a highly twisted configuration, far more so than the values measured in Ref. [37].

Recently, we found that a similar bipolar-to-radial transition can be induced in 5CB emulsion droplets in water with 1% w/w PVA by bringing the temperature close to T_{NI} , the isotropic-nematic phase transition temperature. This transition is shown in Figure 6.4(A–C) for a sample with multiple droplets, and in Figure 6.5(A–E) for a single droplet [223]. We observe the transition at $\tilde{T} \gtrsim 0.995T_{NI}$, where $\tilde{T} = T/T_{NI}$ is the reduced temperature [223]. We use Jones Calculus to simulate bipolar droplets with varying ΔN , and compare the number of fringes in the simulated images with the number of fringes in our experimental images. This process is shown in Figures 6.5(A–C) for the experimental OPM images and Figure 6.5(F–H) for the simulated images as a function of increasing \tilde{T} . By matching the number of fringes, we can determine the birefringence, and therefore the scalar order parameter, S , in our experiments as a function of \tilde{T} [223]. We find that the relationship derived from the bipolar droplets agrees well with Raman scattering data on pure 5CB, as plotted in Figure 6.5(I), indicating that the bipolar-to-radial transformation occurs not only at a repeatable \tilde{T} , but also at a repeatable S [223]. However, from this data we cannot distinguish between an effect driven by the absolute temperature or an effect driven by the reduced temperature.

We test this by making 5CB emulsion droplets in mixtures of water and ethanol, where the concentration of PVA is always 1% w/w. The addition of ethanol to the continuous phase lowers T_{NI} ; at concentrations of ethanol greater than 30 % w/w,

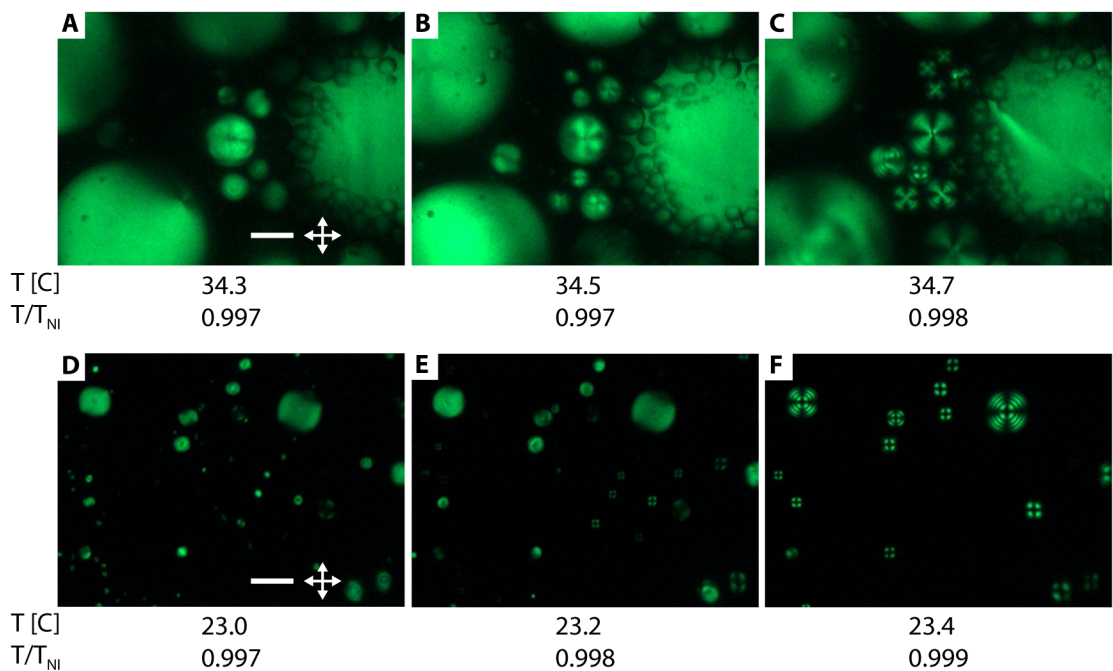


Figure 6.4: OPM textures of an emulsion of 5CB undergoing a bipolar-to-radial transformation. (A–C), The outer medium consists of 99% w/w Millipore water with 1% w/w PVA. (D–F), The outer medium consists of 69% w/w Millipore water, 30% w/w Ethanol, and 1% w/w PVA. In all images the absolute and reduced temperature are displayed below the image. The scale bar is: 50 μm .

we find that 5CB is isotropic at room temperature. Irrespective of the concentration of ethanol, we find that the transition occurs consistently at $\tilde{T} \gtrsim 0.995T_{NI}$, shown in Figure 6.4(D–F) for an outer medium of 1% w/w PVA, 30% w/w ethanol, and 69% w/w Millipore water. In addition, while we observe that small droplets tend to transform before large droplets, we do not have the sensitivity to quantitatively measure the transition as a function of size. This confirms that the transition is not a function of the absolute temperature, but depends on the reduced temperature through the scalar order parameter. Furthermore, the continuous phase here is very similar to that used in Ref. [37] to measure $K_{24} = (1.04 \pm 0.04)K_{22}$ for 5CB, indicating that it is not likely that saddle-splay is solely responsible for the bipolar-to-radial transition. However, we note that if saddle-splay truly cannot be measured without influence from the confining phase, then we would need to repeat these measurements in the identical outer phase to Ref [37]. When we do this, we find that regardless of the carbopol or ethanol concentration in the outer phase, all our spherical emulsions demonstrate a bipolar-to-radial transition at $\tilde{T} \gtrsim 0.995T_{NI}$. Finally, we note that while we generally assume that the ratios of the elastic constants do not change with temperature, Eqs. 2.69–2.72, indicate that there will be some variation, possibly reaching a regime where K_{24} could drive the bipolar-to-radial transition.

6.3.3 Distinguishing K_{24} and surface contributions using twist angle and temperature

To test whether the temperature scaling of K_{24} could result in $K_{24} > 2K_{22}$, we will measure the twist angle of 5CB confined under degenerate planar anchoring to cylindrical structures. We make cylindrical structures by inserting a 27 Ga (410 μm outer diameter) needle completely into a yield stress fluid and then slowly removing the needle as we pump 5CB into the void left by the withdrawing needle. The needle is ≈ 5 cm long, and we control the speed of withdrawal using a mechanical stage controlled by a MATLAB script. We set the volume flowrate of the 5CB between 0%

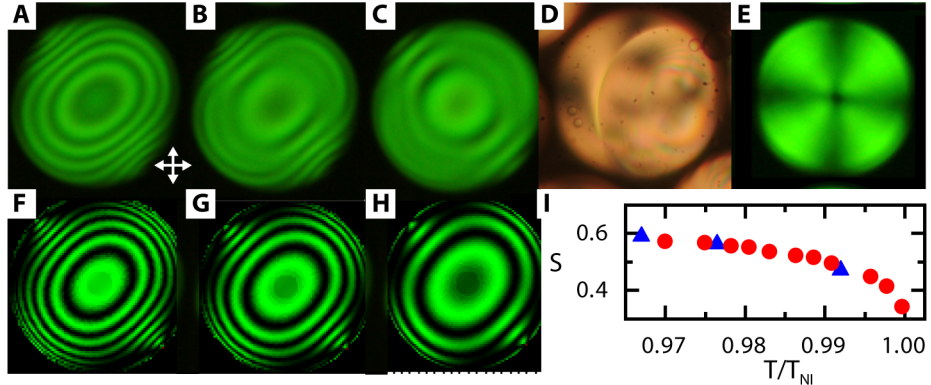


Figure 6.5: The transition from bipolar-to-radial happens as the order parameter decreases. (A–E), Experimental images showing how a 40 μm diameter bipolar droplet transforms into a radial droplet. As the reduced temperature increases, the number of fringes in the (A–C) bipolar OPM textures decrease. The saturn ring mediated the bipolar-to-radial transformation is clearly visible under bright-field illumination in (D), with the final radial structure visible in the OPM texture in (E). (F–H), Simulated OPM textures of bipolar droplets with varying Δn ; the Δn were chosen to match the number of fringes in the experimental OPM textures in (A–C), respectively. (I), Plot of the scalar order parameter vs. the reduced temperature with data from Raman scattering measurements (\bullet) and from matching the simulated and experimental OPM textures (\blacktriangle)

and 20% in excess of the volume/time vacated by the needle; flowrates in this range generally produce smooth, cylindrical structures, as shown in the example image in Figure 6.6(A). Currently, we have tested cylindrical structures in yield-stress media containing 1% w/w PVA, 3% w/w Glycerol, 0%–2% w/w carbopol, 0%–30% w/w ethanol, with the remaining percentage taken by Millipore water. Example OPM textures of the structure in Figure 6.6(A) are shown in Figures 6.6(B,C), while images for a structure made in a yield-stress medium with no ethanol are shown in Figures 6.6(D,E). We measure the twist angle by first varying both P and A until the minimum transmitted intensity is reached. We then fix P, measure the transmitted intensity every 5° in the A orientation, and fit the resulting data to the expected transmitted intensity for a twisted nematic cell [Eq. 4.20]. For the two examples in Figures 6.6(B,C) and Figures 6.6(D,E), we measure a twist angles of $\tau = 13^\circ \pm 1^\circ$ and $\tau = 7^\circ \pm 1^\circ$, respectively. Our preliminary data show twist angles consistent with

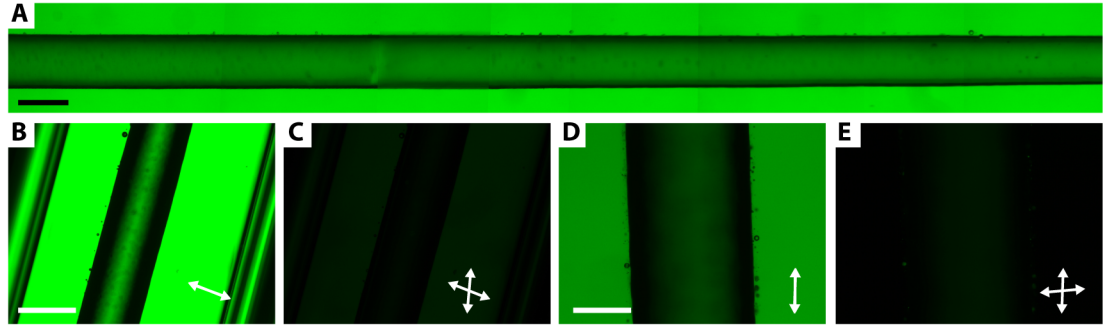


Figure 6.6: Cylindrical structures of 5CB in a yield-stress material. (A), Bright-field image of a cylindrical structure of 5CB in a yield-stress medium consisting of 1% w/w PVA, 1.5% w/w carbopol, 3% w/w glycerol, 30% w/w ethanol, 64.5 w/w % Millipore water. (B–E), OPM textures of cylindrical structures of 5CB with (B,D) having aligned P and A, and (C,E) having P and A oriented for minimum transmission through the 5CB structure. (B,C) are a section of the structure in (A), while (D,E) are a section from a structure in an outer medium consisting of 1% w/w PVA, 1.8% w/w carbopol, 3% w/w glycerol, 94.2 w/w % Millipore water. Scale bar for (A–C) is 500 μm ; for (D,E) the scale bar is 250 μm .

the value of K_{24} measured in Ref. [37], regardless of the concentration of carbopol or ethanol in the outer yield-stress medium. We are currently working on measurements of twist angle as a function of temperature. However, we note that our samples with higher concentrations of ethanol have a lower clearing point and thus the measurements corresponds to a higher \tilde{T} , indicating that it is not likely that increasing temperature for a given sample will cause $K_{24} \approx 2K_{22}$.

Appendices

APPENDIX A
EXPERIMENTAL PROTOCOL TO BOND POLYACRYLAMIDE
BRUSHES TO GLASS

Washing slides

1. Place glass into Alconox or Hellmanex solution (prepared per manufacturer specifications)
2. Sonicate the container for 5 – 10 minutes.
3. Rinse the glass with pure water until there are no bubbles (7 – 10 rinses)
4. Place glass into a \geq 70% solution of ethanol.
5. Sonicate the container for 5 – 10 minutes.
6. Rinse glass with pure water 5 – 7 times.
7. Ensure that water does not bead up on the cleaned glass. If it does, the glass must be washed again.
8. Place slides into 0.1 M NaOH solution
9. Sonicate the container for 5 – 10 minutes.
10. Rinse glass with pure water 5 – 7 times.
11. Store in pure water

Silane coating for acrylamide polymerization

1. Remove cleaned glass from water, dry with compressed air, and place in a dry container.

2. Determine the volume of solution needed to cover the glass
3. Prepare silane-coupling solution (**Solution is unstable. Prepare right before use**):
 - 98.5% v/v Ethanol (200 Proof)
 - 1.0% v/v Acetic Acid
 - 0.5% v/v 3-(trimethoxysilyl)propyl methacrylate
4. Cover the glass with the silane-coupling solution and leave it for 10 – 15 minutes.
5. Rinse with pure water 5 – 7 times

Acrylamide polymerization to silane-coated glass

1. Create or locate stock solution 10% w/v Potassium Persulfate (KPS) in water
2. Determine the volume of acrylamide solution needed to cover the glass
3. Create solution of 2% w/v acrylamide in water
4. Degass acrylamide solution under vacuum for 15 – 30 minutes
5. To the acrylamide solution add 10 μ L 10%KPS solution per 1 mL of acrylamide solution and gently mix.
6. To the acrylamide solution add 2.5 μ L TEMED per 1 mL of acrylamide solution and gently mix.
7. Pour acrylamide solution over coverslips immediately after mixing in the TEMED.
8. Wait 2 – 3 hours for polymerization.
9. Let sit in container until ready to use (**Use within weeks**).
10. To use, remove glass from container, rinse with pure water, and air dry.

REFERENCES

1. CHAIKIN, P. M. & LUBENSKY, T. C. *Principles of condensed matter physics* ISBN: 1139643053 (Cambridge university press, 2000) (Cited on pages 2–4, 9, 15, 20–24, 29, 32, 33, 47, 48, 142).
2. KOSTERLITZ, J. M. & THOULESS, D. J. Ordering, metastability and phase transitions in two-dimensional systems. *Journal of Physics C: Solid State Physics* **6**, 1181 (1973) (Cited on page 3).
3. YOUNG, A. P. Melting and the vector coulomb gas in two dimensions. *Physical Review B* **19**, 1855 (1979) (Cited on page 3).
4. HALPERIN, B. I. & NELSON, D. R. Theory of two-dimensional melting. *Physical Review Letters* **41**, 121 (1978) (Cited on page 3).
5. FRANK, F. I. Liquid crystals. On the theory of liquid crystals. *Discuss. Faraday Soc.* **25**, 19 (1958) (Cited on pages 4, 9, 33, 34, 36).
6. KLÉMAN, M. Defects in liquid crystals. *Reports on Progress in Physics* **52**, 555 (1989) (Cited on pages 4, 8, 27).
7. ČOPAR, S., TKALEC, U., MUŠEVIČ, I. & ŽUMER, S. Knot theory realizations in nematic colloids. *Proceedings of the National Academy of Sciences* **112**, 1675 (2015) (Cited on page 4).
8. ORLOVA, T., AHOFF, S. J., YAMAGUCHI, T., KATSONIS, N. & BRASSELET, E. Creation and manipulation of topological states in chiral nematic microspheres. *Nature* **6**, 7603 (2015) (Cited on pages 4, 186).
9. NELSON, D. R. Toward a tetravalent chemistry of colloids. *Nano Letters* **2**, 1125 (2002) (Cited on pages 4, 9).
10. DEVRIES, G. A. *et al.* Divalent metal nanoparticles. *Science* **315**, 358 (2007) (Cited on page 4).
11. POULIN, P., STARK, H., LUBENSKY, T. C. & WEITZ, D. A. Novel colloidal interactions in anisotropic fluids. *Science* **275**, 1770 (1997) (Cited on pages 4, 56, 186).

12. MUŠEVIČ, I., ŠKARABOT, M., TKALEC, U., RAVNIK, M. & ŽUMER, S. Two-dimensional nematic colloidal crystals self-assembled by topological defects. *Science* **313**, 954 (2006) (Cited on page 4).
13. ZAPOTOCKY, M., RAMOS, L., POULIN, P., LUBENSKY, T. C. & WEITZ, D. A. Particle-stabilized defect gel in cholesteric liquid crystals. *Science* **283**, 209 (1999) (Cited on page 4).
14. WOOD, T. A., LINTUVUORI, J. S., SCHOFIELD, A. B., MARENDOZZO, D. & POON, W. C. K. A self-quenched defect glass in a colloid-nematic liquid crystal composite. *Science* **334**, 79 (2011) (Cited on page 4).
15. DECAMP, S. J., REDNER, G. S., BASKARAN, A., HAGAN, M. F. & DOGIC, Z. Orientational order of motile defects in active nematics. *Nat Mater* **14**, 1110 (2015) (Cited on pages 4, 67, 72, 218, 223, 225).
16. ONSAGER, L. The effects of shape on the interaction of colloidal particles. *Annals of the New York Academy of Sciences* **51**, 627 (1949) (Cited on pages 5, 20).
17. POINCARÉ, H. Sur les courbes définies par les équations différentielles (iii). *Journal de mathématiques pures et appliquées* **1**, 167 (1885) (Cited on page 5).
18. ARMSTRONG, M. A. *Basic topology* ISBN: 1475717938 (Springer Science and Business Media, New York, 2013) (Cited on page 5).
19. KAMIEN, R. D. The geometry of soft materials: A primer. *Reviews of Modern Physics* **74**, 953 (2002) (Cited on pages 6, 8, 27, 46, 95, 105, 116, 182).
20. ALEXANDER, G. P., CHEN, B. G.-g., MATSUMOTO, E. A. & KAMIEN, R. D. Colloquium: Disclination loops, point defects, and all that in nematic liquid crystals. *Reviews of Modern Physics* **84**, 497 (2012) (Cited on pages 8, 17, 18, 24, 26–31).
21. For a single-valued scalar field $a(\mathbf{r})$ that is everywhere defined, $\nabla a(\mathbf{r})$ is conservative and has the following properties: (i) irrotational, (ii) the line integral is path independent, (iii) the line integral along a closed contour is 0. In the case of $\phi(\mathbf{r})$, it is not defined at the defect, hence $\nabla \phi(\mathbf{r})$ is no longer conservative. Note that integrating $\nabla \phi(\mathbf{r})$ along a contour now in general depends on the path taken. The exception is s , where the integral along any closed contour enclosing the defect will return the same value of s up to a sign indicating the direction of the integral along the contour. (Cited on page 8).

22. De GENNES, P. G. & PROST, J. *The physics of liquid crystals* ISBN: 9780198517856 (Oxford University Press, New York, 1995) (Cited on pages 9, 20–24, 29, 32, 42, 46–49, 52, 55–57, 151, 179).
23. LUBENSKY, T. C. & PROST, J. Orientational order and vesicle shape. *Journal de Physique II* **2**, 371 (1992) (Cited on pages 9, 15).
24. VITELLI, V. & NELSON, D. R. Nematic textures in spherical shells. *Physical Review E* **74**, 021711 (2006) (Cited on page 9).
25. UTADA, A. S. *et al.* Monodisperse double emulsions generated from a micro-capillary device. *Science* **308**, 537 (2005) (Cited on page 10).
26. FERNANDEZ-NIEVES, A. *et al.* Novel defect structures in nematic liquid crystal shells. *Physical review letters* **99**, 157801 (2007) (Cited on pages 10–12, 16, 57, 58).
27. LOPEZ-LEON, T., KONING, V., DEVAIAH, K. B. S., VITELLI, V. & FERNANDEZ-NIEVES, A. Frustrated nematic order in spherical geometries. *Nature Physics* **7**, 391 (2011) (Cited on pages 10, 16).
28. MERMIN, N. D. Games to play with 3he-a. *Physica B+ C* **90**, 1 (1977) (Cited on page 11).
29. KREYSZIG, E. *Differential geometry* ISBN: 9780486667218 (Dover Publications, New York, 1959) (Cited on pages 13, 46, 105, 110, 116, 122, 192).
30. BOWICK, M. J. & GIOMI, L. Two-dimensional matter: Order, curvature and defects. *Advances in Physics* **58**, 449 (2009) (Cited on pages 15, 68).
31. BOWICK, M. J., NELSON, D. R. & TRAVESSET, A. Interacting topological defects on frozen topographies. *Physical Review B* **62**, 8738 (2000) (Cited on page 16).
32. BAUSCH, A. R. *et al.* Grain boundary scars and spherical crystallography. *Science* **299**, 1716 (2003) (Cited on page 16).
33. LIPOWSKY, P., BOWICK, M. J., MEINKE, J. H., NELSON, D. R. & BAUSCH, A. R. Direct visualization of dislocation dynamics in grain-boundary scars. *Nature materials* **4**, 407 (2005) (Cited on page 16).
34. BROJAN, M., TERWAGNE, D., LAGRANGE, R. & REIS, P. M. Wrinkling crystallography on spherical surfaces. *Proceedings of the National Academy of Sciences* **112**, 14 (2015) (Cited on page 16).

35. DARMON, A. *et al.* Waltzing route toward double-helix formation in cholesteric shells. *Proceedings of the National Academy of Sciences* **113**, 9469 (2016) (Cited on page 16).
36. KELLEHER, C. P., GUERRA, R. E., HOLLINGSWORTH, A. D. & CHAIKIN, P. M. Phase behavior of charged colloids at a fluid interface. *Physical Review E* **95**, 022602 (2017) (Cited on page 16).
37. PAIRAM, E. *et al.* Stable nematic droplets with handles. *Proceedings of the National Academy of Sciences* **110**, 9295 (2013) (Cited on pages 16–18, 142, 144, 146, 153, 156, 165, 166, 172, 228–230, 232, 234).
38. PAIRAM, E., LE, H & FERNANDEZ-NIEVES, A. Stability of toroidal droplets inside yield stress materials. *Physical Review E* **90**, 021002 (2014) (Cited on pages 16, 79, 82, 153).
39. KONING, V., van ZUIDEN, B. C., KAMIEN, R. D. & VITELLI, V. Saddle-splay screening and chiral symmetry breaking in toroidal nematics. *Soft matter* **10**, 4192 (2014) (Cited on pages 17, 46, 144, 228).
40. NAYANI, K. *et al.* Spontaneous emergence of chirality in achiral lyotropic chromonic liquid crystals confined to cylinders. *Nature communications* **6** (2015) (Cited on pages 17, 142, 146, 150, 228).
41. TASINKEVYCH, M., CAMPBELL, M. G. & SMALYUKH, I. Splitting, linking, knotting, and solitonic escape of topological defects in nematic drops with handles. *Proceedings of the National Academy of Sciences of the United States of America* **111**, 16268 (2014) (Cited on pages 18, 147).
42. CAMPBELL, M. G., TASINKEVYCH, M. & SMALYUKH, I. I. Topological polymer dispersed liquid crystals with bulk nematic defect lines pinned to handlebody surfaces. *Physical Review Letters* **112**, 197801 (2014) (Cited on page 18).
43. FRIEDEL, G. *Les états mésomorphes de la matière* in *Annales de Physique* **9** (), 273. ISBN: 0003-4169 (Cited on page 20).
44. MERMIN, N. D. The topological theory of defects in ordered media. *Reviews of Modern Physics* **51**, 591 (1979) (Cited on pages 24, 26–30).
45. KURIK, M. V. & LAVRENTOVICH, O. Defects in liquid crystals: Homotopy theory and experimental studies. *Physics-Uspekhi* **31**, 196 (1988) (Cited on pages 24, 26–30).
46. ERICKSEN, J. L. Hydrostatic theory of liquid crystals. *Archive for Rational Mechanics and Analysis* **9**, 371 (1962) (Cited on page 32).

47. LAUTRUP, B. *Physics of continuous matter: Exotic and everyday phenomena in the macroscopic world* ISBN: 1439894205 (CRC press, 2011) (Cited on pages 33, 80, 191, 193).
48. OSEEN, C. The theory of liquid crystals. *Transactions of the Faraday Society* **29**, 883 (1933) (Cited on pages 37, 39).
49. NEHRING, J. & SAUPE, A. On the elastic theory of uniaxial liquid crystals. *The Journal of Chemical Physics* **54**, 337 (1971) (Cited on page 37).
50. OLDANO, C. & BARBERO, G. An ab initio analysis of the second-order elasticity effect on nematic configurations. *Physics Letters A* **110**, 213 (1985) (Cited on page 38).
51. OLDANO, C. & BARBERO, G. Possible boundary discontinuities of the tilt angle in nematic liquid crystals. *Journal de Physique Lettres* **46**, 451 (1985) (Cited on page 38).
52. BARBERO, G. & OLDANO, C. Derivative-dependent surface-energy terms in nematic liquid crystals. *Il Nuovo Cimento D* **6**, 479 (1985) (Cited on pages 38, 39).
53. STALLINGA, S & VERTOGEN, G. Solution of the oldano-barbero paradox. *Physical Review E* **53**, 1692 (1996) (Cited on pages 38, 39).
54. BARBERO, G., MADHUSUDANA, N. V. & OLDANO, C. Possibility of a deformed ground state in free standing nematic films. *Journal de Physique* **50**, 2263 (1989) (Cited on page 39).
55. PERGAMENSHCHIK, V. M. Phenomenological approach to the problem of the k13 surfacelike elastic term in the free energy of a nematic liquid crystal. *Physical Review E* **48**, 1254 (1993) (Cited on page 39).
56. YOKOYAMA, H. Density-functional theory of surfacelike elasticity of nematic liquid crystals. *Physical Review E* **55**, 2938 (1997) (Cited on pages 39–41, 43, 227, 228).
57. PONIEWIERSKI, A & STECKI, J. Statistical theory of the elastic constants of nematic liquid crystals. *Molecular Physics* **38**, 1931 (1979) (Cited on pages 39, 40).
58. STALLINGA, S., VAN HAAREN, J. A.M. M. & Van den EERENBEEMD, J. M. A. Influence of surface elasticity on the director profile of nontwisted nematic-liquid-crystal cells. *Physical Review E* **53**, 1701 (1996) (Cited on page 39).

59. FAETTI, S & RICCARDI, M. The phenomenological functions that characterize the surface free energy density of nematic liquid crystals: A microscopic analysis. *Journal de Physique II* **5**, 1165 (1995) (Cited on pages 39–41).
60. TEIXEIRA, P. I. C., PERGAMENSHCHIK, V. M. & SLUCKIN, T. J. A model calculation of the surface elastic constants of a nematic liquid crystal. *Molecular Physics* **80**, 1339 (1993) (Cited on pages 39, 40).
61. SOMOZA, A. M. & TARAZONA, P. Density functional approximation for hard-body liquid crystals. *The Journal of chemical physics* **91**, 517 (1989) (Cited on pages 39–41).
62. LIPKIN, M. D., RICE, S. A. & MOHANTY, U. The elastic constants of condensed matter: A directcorrelation function approach. *The Journal of chemical physics* **82**, 472 (1985) (Cited on pages 39, 40).
63. BARBERO, G., SPARAVIGNA, A & STRIGAZZI, A. The structure of the distortion free-energy density in nematics: Second-order elasticity and surface terms. *Il Nuovo Cimento D* **12**, 1259 (1990) (Cited on page 39).
64. EVANS, R. The nature of the liquid-vapour interface and other topics in the statistical mechanics of non-uniform, classical fluids. *Advances in Physics* **28**, 143 (1979) (Cited on page 39).
65. FAETTI, S. & VIRGA, E. G. On a curvature surface energy for nematic liquid crystals. *Archive for Rational Mechanics and Analysis* **140**, 31 (1997) (Cited on pages 41, 42).
66. STONE, M. & GOLDBART, P. *Mathematics for physics* (Cambridge University Press, New York, 2009) (Cited on page 42).
67. FRÉEDERICKSZ, V. & ZOLINA, V. Forces causing the orientation of an anisotropic liquid. *Transactions of the Faraday Society* **29**, 919 (1933) (Cited on page 42).
68. FRÉEDERIKSZ, V. & TSVETKOV, V. über die orientierung der anisotropen flüssigkeiten in dnnen schichten and die messung einiger die elastischen eenschaften charakterisierenden konstanten. *Physikalische Zeitschrift der Sowjetunion* **6**, 490 (1934) (Cited on page 42).
69. FAETTI, S., GATTI, M. & PALLESCHI, V. Measurements of surface elastic torques in liquid crystals : A method to measure elastic constants and anchoring energies. *Rev. Phys. Appl. (Paris)* **21**, 451 (1986) (Cited on page 42).

70. OLDANO, C., MIRALDI, E., STRIGAZZI, A., TAVERNA VALABREGA, P. & TROSSI, L. Optical study of the molecular alignment in a nematic liquid crystal in an oblique magnetic field. *J. Phys. France* **45**, 355 (1984) (Cited on page 42).
71. OLDANO, C., MIRALDI, E. & VALABREGA, P. T. Theoretical and experimental study of the static behaviour of a nematic liquid crystal near the freedericksz transition. *Journal de Physique* **45**, 755 (1984) (Cited on page 42).
72. ERICKSEN, J. L. Nilpotent energies in liquid crystal theory. *Archive for Rational Mechanics and Analysis* **10**, 189 (1962) (Cited on page 42).
73. CRAWFORD, G. P., ALLENDER, D. W. & DOANE, J. W. Surface elastic and molecular-anchoring properties of nematic liquid crystals confined to cylindrical cavities. *Physical Review A* **45**, 8693 (1992) (Cited on pages 42, 149).
74. ALEXE-IONESCU, A., BARBERO, G. & DURAND, G. Temperature dependence of surface orientation of nematic liquid crystals. *Journal de Physique II* **3**, 1247 (1993) (Cited on pages 42, 51).
75. KOS, Z. & RAVNIK, M. Relevance of saddle-splay elasticity in complex nematic geometries. *Soft Matter* **12**, 1313 (2016) (Cited on page 42).
76. LUBENSKY, T. C. Molecular description of nematic liquid crystals. *Physical Review A* **2**, 2497 (1970) (Cited on pages 47, 49–51).
77. SCHIELE, K & TRIMPER, S. On the elastic constants of a nematic liquid crystal. *Physica Status Solidi (B)* **118**, 267 (1983) (Cited on pages 47, 49–53).
78. WITTEBROOD, M. M., LUIJENDIJK, D. H., STALLINGA, S., RASING, T. H. & MUŠEVIČ, I. Thickness-dependent phase transition in thin nematic films. *Physical Review E* **54**, 5232 (1996) (Cited on page 49).
79. SHABNAM, S., DASGUPTA, S. & ROY, S. K. Existence of a line of critical points in a two-dimensional Lebwohl Lasher model. *Physics Letters A* **380**, 667 (2016) (Cited on pages 49, 131).
80. RAVNIK, M. & ŽUMER, S. Landau-de Gennes modelling of nematic liquid crystal colloids. *Liquid Crystals* **36**, 1201 (2009) (Cited on pages 51, 52).
81. DRZAIC, P. S. *Liquid crystal dispersions* ISBN: 9810217455 (World Scientific, 1995) (Cited on pages 53, 54, 61, 164, 200, 205).
82. HILTROP, K & STEGEMEYER, H. Contact angles and alignment of liquid crystals on lecithin monolayers. *Molecular Crystals and Liquid Crystals* **49**, 61 (1978) (Cited on pages 56, 188).

83. BRAKE, J. M. & ABBOTT, N. L. An experimental system for imaging the reversible adsorption of amphiphiles at aqueous liquid crystal interfaces. *Langmuir* **18**, 6101 (2002) (Cited on pages 56, 153).
84. MYSELS, K. J. Surface tension of solutions of pure sodium dodecyl sulfate. *Langmuir* **2**, 423 (1986) (Cited on pages 56, 57).
85. MCNAUGHT, A. D. *Compendium of chemical terminology* (Blackwell Science Oxford, 1997) (Cited on page 57).
86. SYED, I. M., CARBONE, G., ROSENBLATT, C. & WEN, B. Planar degenerate substrate for micro-and nanopatterned nematic liquid-crystal cells. *Journal of applied physics* **98**, 034303 (2005) (Cited on page 57).
87. CLARK, N. A. Surface memory effects in liquid crystals: Influence of surface composition. *Physical Review Letters* **55**, 292 (1985) (Cited on page 57).
88. YEH, P. & GU, C. *Optics of liquid crystal displays* ISBN: 0470181761 (John Wiley and Sons, 2010) (Cited on pages 57–61, 157, 159, 163, 171–173).
89. LOPEZ-LEON, T. & FERNANDEZ-NIEVES, A. Drops and shells of liquid crystal. *Colloid and Polymer Science* **289**, 345 (2011) (Cited on pages 57, 58).
90. STILLWELL, J. *Naive lie theory* (Springer Science, New York, New York, 2008) (Cited on page 62).
91. GALLIAN, J. *Contemporary abstract algebra* (Brooks and Cole, Boston, Massachusetts, 2013) (Cited on page 62).
92. RAMASWAMY, S. The mechanics and statistics of active matter (2010) (Cited on page 63).
93. MARCHETTI, M. C. *et al.* Hydrodynamics of soft active matter. *Reviews of Modern Physics* **85**, 1143 (2013) (Cited on page 63).
94. VICSEK, T. & ZAFEIRIS, A. Collective motion. *Physics Reports* **517**, 71 (2012) (Cited on page 63).
95. VICSEK, T., CZIRÓK, A., BEN-JACOB, E., COHEN, I. & SHOCET, O. Novel type of phase transition in a system of self-driven particles. *Physical review letters* **75**, 1226 (1995) (Cited on page 63).
96. BALLERINI, M. *et al.* Interaction ruling animal collective behavior depends on topological rather than metric distance: Evidence from a field study. *Proceedings of the national academy of sciences* **105**, 1232 (2008) (Cited on page 63).

97. TENNENBAUM, M., LIU, Z., HU, D. & FERNANDEZ-NIEVES, A. Mechanics of fire ant aggregations. *Nature materials* **15**, 54 (2016) (Cited on page 63).
98. LÓPEZ, H. M., GACHELIN, J., DOUARCHE, C., AURADOU, H. & CLÉMENT, E. Turning bacteria suspensions into superfluids. *Physical review letters* **115**, 028301 (2015) (Cited on page 63).
99. HATWALNE, Y., RAMASWAMY, S., RAO, M. & SIMHA, R. A. Rheology of active-particle suspensions. *Physical Review Letters* **92**, 118101 (2004) (Cited on page 63).
100. ZHOU, S., SOKOLOV, A., LAVRENTOVICH, O. D. & ARANSON, I. S. Living liquid crystals. *Proceedings of the National Academy of Sciences* **111**, 1265 (2014) (Cited on pages 64, 67, 140).
101. GIOMI, L., BOWICK, M. J., MA, X. & MARCHETTI, M. C. Defect annihilation and proliferation in active nematics. *Physical Review Letters* **110**, 228101 (2013) (Cited on pages 66, 67, 71, 74).
102. ADITI SIMHA, R. & RAMASWAMY, S. Hydrodynamic fluctuations and instabilities in ordered suspensions of self-propelled particles. *Physical Review Letters* **89**, 058101 (2002) (Cited on page 67).
103. EDWARDS, S. A. & YEOMANS, J. M. Spontaneous flow states in active nematics: A unified picture. *EPL* **85**, 18008 (2009) (Cited on page 67).
104. GREEN, R., TONER, J. & VITELLI, V. The geometry of threshold-less active flow in nematic microfluidics. *arXiv* (2016) (Cited on page 67).
105. GIOMI, L. Geometry and topology of turbulence in active nematics. *Physical Review X* **5**, 031003 (2015) (Cited on pages 67, 134).
106. GIOMI, L., BOWICK, M. J., MISHRA, P., SKNEPNEK, R. & MARCHETTI, M. C. Defect dynamics in active nematics. *Philosophical Transactions of the Royal Society a-Mathematical Physical and Engineering Sciences* **372**, 20130365 (2014) (Cited on pages 67, 71).
107. SANCHEZ, T., CHEN, D. T. N., DECAMP, S. J., HEYMANN, M. & DOGIC, Z. Spontaneous motion in hierarchically assembled active matter. *Nature* **491**, 431 (2012) (Cited on pages 67, 72, 74–79).
108. GUILLAMAT, P., IGNÉS-MULLOL, J., SHANKAR, S., MARCHETTI, M. C. & SAGUÉS, F. Probing the shear viscosity of an active nematic film. *Physical Review E* **94**, 060602 (2016) (Cited on pages 67, 72, 74, 75, 139).

109. KEBER, F. C. *et al.* Topology and dynamics of active nematic vesicles. *Science* **345**, 1135 (2014) (Cited on pages 67, 71, 72).
110. SAW, T. B. *et al.* Topological defects in epithelia govern cell death and extrusion. *Nature* **544**, 212 (2017) (Cited on page 68).
111. DOOSTMOHAMMADI, A., THAMPI, S. P. & YEOMANS, J. M. Defect-mediated morphologies in growing cell colonies. *Physical Review Letters* **117**, 048102 (2016) (Cited on page 68).
112. GIOMI, L. & DESIMONE, A. Spontaneous division and motility in active nematic droplets. *Physical Review Letters* **112**, 147802 (2014) (Cited on page 68).
113. BOWICK, M. J., GIOMI, L., SHIN, H. & THOMAS, C. K. Bubble-raft model for a paraboloidal crystal. *Physical Review E* **77**, 021602 (2008) (Cited on page 68).
114. IRVINE, W. T. M., VITELLI, V. & CHAIKIN, P. M. Pleats in crystals on curved surfaces. *Nature* **468**, 947 (2010) (Cited on page 68).
115. BURKE, C. J., MBANGA, B. L., WEI, Z., SPICER, P. T. & ATHERTON, T. J. The role of curvature anisotropy in the ordering of spheres on an ellipsoid. *Soft matter* **11**, 5872 (2015) (Cited on page 68).
116. MATSUMOTO, E. A. *et al.* Wrinkles and splay conspire to give positive disclinations negative curvature. *Proceedings of the National Academy of Sciences* **112**, 12639 (2015) (Cited on page 68).
117. GIOMI, L. & BOWICK, M. Elastic theory of defects in toroidal crystals. *European Physical Journal E* **27**, 275 (2008) (Cited on pages 68, 71, 129).
118. JESENEK, D., KRALJ, S., ROSSO, R. & VIRGA, E. G. Defect unbinding on a toroidal nematic shell. *Soft matter* **11**, 2434 (2015) (Cited on pages 68, 71, 129).
119. BOWICK, M., NELSON, D. R. & TRAVESSET, A. Curvature-induced defect unbinding in toroidal geometries. *Physical Review E* **69**, 041102 (2004) (Cited on pages 71, 129).
120. GIOMI, L. & BOWICK, M. J. Defective ground states of toroidal crystals. *Physical Review E* **78**, 010601 (2008) (Cited on pages 71, 129).
121. TRAVESSET, A. Structure of curved crystals in the thermodynamic limit and the perfect screening condition. *Physical Review E* **94**, 063001 (2016) (Cited on pages 71, 129).

122. GUILLAMAT, P., IGNÉS-MULLOL, J. & SAGUÉS, F. Control of active liquid crystals with a magnetic field. *Proceedings of the National Academy of Sciences* **113**, 5498 (2016) (Cited on pages 72, 74, 140).
123. WEISENBERG, R. C. Microtubule formation in vitro in solutions containing low calcium concentrations. *Science* **177**, 1104 (1972) (Cited on page 72).
124. CHRÉTIEN, D., METOZ, F., VERDE, F., KARSENTI, E. & WADE, R. Lattice defects in microtubules: Protofilament numbers vary within individual microtubules. *The Journal of cell biology* **117**, 1031 (1992) (Cited on page 72).
125. SCHNITZER, M. J. & BLOCK, S. M. Kinesin hydrolyses one atp per 8-nm step. *Nature* **388**, 386 (1997) (Cited on page 72).
126. SANCHEZ, T., WELCH, D., NICASTRO, D. & DOGIC, Z. Cilia-like beating of active microtubule bundles. *Science* **333**, 456 (2011) (Cited on pages 72, 74).
127. ASAOKA, S. & OOSAWA, F. On interaction between two bodies immersed in a solution of macromolecules. *The Journal of Chemical Physics* **22**, 1255 (1954) (Cited on page 74).
128. LAU, A. W., PRASAD, A. & DOGIC, Z. Condensation of isolated semi-flexible filaments driven by depletion interactions. *EPL* **87**, 48006 (2009) (Cited on page 74).
129. BRANGWYNNE, C. P. *et al.* Microtubules can bear enhanced compressive loads in living cells because of lateral reinforcement. *J Cell Biol* **173**, 733 (2006) (Cited on page 74).
130. HUANG, T.-G. & HACKNEY, D. D. Drosophila kinesin minimal motor domain expressed in escherichia coli. Purification and kinetic characterization. *Journal of Biological Chemistry* **269**, 16493 (1994) (Cited on page 75).
131. SCHMOLKA, I *Patent US* 3740421 (1973) (Cited on page 75).
132. CASTOLDI, M. & POPOV, A. V. Purification of brain tubulin through two cycles of polymerizationdepolymerization in a high-molarity buffer. *Protein expression and purification* **32**, 83 (2003) (Cited on page 76).
133. PAIRAM, E. & FERNANDEZ-NIEVES, A. Generation and stability of toroidal droplets in a viscous liquid. *Physical Review Letters* **102**, 234501 (2009) (Cited on pages 79, 82).

134. FRAGKOPOULOS, A. A., ELLIS, P. W. & FERNANDEZ-NIEVES, A. Teaching rayleigh-plateau instabilities in the laboratory. *European Journal of Physics* **36**, 055023 (2015) (Cited on page 79).
135. FRAGKOPOULOS, A. A. & FERNANDEZ-NIEVES, A. Toroidal-droplet instabilities in the presence of charge. *Physical Review E* **95**, 033122 (2017) (Cited on page 82).
136. FRAGKOPOULOS, A. A., PAIRAM, E., BERGER, E., SEGRE, P. N. & FERNANDEZ-NIEVES, A. Shrinking instability of toroidal droplets. *Proceedings of the National Academy of Sciences* **114**, 2871 (2017) (Cited on page 82).
137. FRAGKOPOULOS, A. A., AIZENMAN, A. & FERNANDEZ-NIEVES, A. Charge-induced saffman-taylor instabilities in toroidal droplets. *Physical Review Letters* **118**, 264501 (2017) (Cited on page 82).
138. CHANG, Y.-W. *et al.* Biofilm formation in geometries with different surface curvature and oxygen availability. *New Journal of Physics* **17**, 033017 (2015) (Cited on page 82).
139. WHITE, J. G., AMOS, W. B. & FORDHAM, M. An evaluation of confocal versus conventional imaging of biological structures by fluorescence light microscopy. *The Journal of Cell Biology* **105**, 41 (1987) (Cited on pages 85, 86).
140. MINSKY, M. Patent US 3013467 (1961) (Cited on page 85).
141. DAVIDOVITS, P. & EGGER, M. D. Scanning laser microscope. *Nature* **223**, 831 (1969) (Cited on page 85).
142. DAVIDOVITS, P. & EGGER, M. D. Scanning laser microscope for biological investigations. *Applied Optics* **10**, 1615 (1971) (Cited on page 85).
143. HECHT, E. & ZAJAC, A. *Optics* (Addison-Wesley, 1974) (Cited on pages 86, 87).
144. WILHELM, S., GROBLER, B., GLUCH, M. & HEINZ, H. *Confocal laser scanning microscopy. Principles* Website. 2003 (Cited on page 87).
145. Jackson immunoresearch laboratories Web Page. 2017 (Cited on pages 90, 91).
146. Nikon instruments Web Page. 2017 (Cited on pages 90, 91).
147. Olympus microscopy resource center Web Page. 2017 (Cited on page 92).

148. *Photomultiplier tubes: Basics and applications* (Hammamatsu Photonics, Ham-mamatsu City, Japan, 1999) (Cited on page 92).
149. *Open microscopy environment* Web Page. 2017 (Cited on page 94).
150. WEICKERT, J. Coherence-enhancing diffusion filtering. *International Journal of Computer Vision* **31**, 111 (1999) (Cited on page 96).
151. HODNELAND, E., KÖGEL, T., FREI, D. M., GERDES, H.-H. & LUNDERVOLD, A. Cellsegm - a matlab toolbox for high-throughput 3d cell segmentation. *Source Code for Biology and Medicine* **8**, 16 (2013) (Cited on page 96).
152. CROCKER, J. C. & GRIER, D. G. Methods of digital video microscopy for colloidal studies. *Journal of colloid and interface science* **179**, 298 (1996) (Cited on page 101).
153. The tracking minimizes $\sum_i \delta_i$, where δ_i is the distance between the i^{th} particle in one image and a candidate particle in the subsequent image. For N particles, this scales like $\mathcal{O}(N!)$; to reduce runtime, the algorithm has a cutoff length L , considering possible candidates only where $\delta_i < L$. (Cited on page 101).
154. JUBIN, B. A generalized poincaré-hopf index theorem. *arXiv* (2009) (Cited on page 103).
155. KALOGERAKIS, E., SIMARI, P., NOWROUZEZAHRAI, D. & SINGH, K. Robust statistical estimation of curvature on discretized surfaces. *Symposium on Geometry Processing*, 13 (2007) (Cited on pages 110, 114, 116, 118).
156. KALOGERAKIS, E., NOWROUZEZAHRAI, D., SIMARI, P. & SINGH, K. Extracting lines of curvature from noisy point clouds. *Computer-Aided Design* **41**, 282 (2009) (Cited on pages 110, 112, 116, 118, 122).
157. BISHOP, C. M. *Pattern recognition and machine learning* (Springer Science, New York, 2006) (Cited on pages 110, 111).
158. GEMAN, S. & MCCLURE, D. E. Statistical methods for tomographic image reconstruction. *Bulletin of the International Statistical Institute* **LII**, 5 (1987) (Cited on pages 112, 114, 123).
159. HUBER, P. J. & RONCHETTI, E. M. *Robust statistics* (John Wiley and Sons, New York, 1981) (Cited on pages 114, 123).
160. DELAUNAY, B. Sur la sphere vide. *Izv. Akad. Nauk SSSR, Otdelenie Matematicheskii i Estestvennyka Nauk* **7**, 1 (1934) (Cited on page 116).

161. PATHRIA, R. K. & BEALE, P. D. *Statistical mechanics* (Elsevier, Massachusetts, 2011) (Cited on page 132).
162. The probability distribution for the number of particles in an equilibrium system subject to number fluctuations can be approximated by a Gaussian distribution when N is large. In this limit, the fluctuations can be determined from the width of the distribution. (Cited on page 132).
163. At each timestep, a random acceleration, or kick, is added to the equations of motion; each kick is drawn independently from the same probability distribution. (Cited on page 133).
164. The turbulence in the flow is due to the vortices introduced by the $s = \pm 1/2$ defects [see Figure 3.3]. The large number of vortices span a range of length scales, and the resulting flow field leads to chaotic mixing. (Cited on page 134).
165. The viscosity of the active nematic in the turbulent regime is primarily determined by the surrounding medium. Since we keep the same outer medium, we use the same viscosity for both ATP concentrations. (Cited on page 139).
166. PASTEUR, L. *Recherches sur les relations qui peuvent exister entre la forme cristalline, la composition chimique et les sens de la polarisation rotatoire* (Impr. Bachelier, 1848) (Cited on page 142).
167. NEVILLE, A. & CAVENEY, S. Scarabaeid beetle exocuticle as an optical analogue of cholesteric liquid crystals. *Biological Reviews* **44**, 531 (1969) (Cited on page 142).
168. SHARMA, V., CRNE, M., PARK, J. O. & SRINIVASARAO, M. Structural origin of circularly polarized iridescence in jeweled beetles. *science* **325**, 449 (2009) (Cited on page 142).
169. SOUKOULIS, C. M. & WEGENER, M. Past achievements and future challenges in the development of three-dimensional photonic metamaterials. *Nature Photonics* **5**, 523 (2011) (Cited on page 142).
170. A material engineered to exhibit properties not found in nature. For example, a material engineered to have a negative index of refraction is a metamaterial. (Cited on page 142).
171. HOUGH, L. E. *et al.* Chiral isotropic liquids from achiral molecules. *Science* **325**, 452 (2009) (Cited on page 142).

172. WILLIAMS, R. D. Two transitions in tangentially anchored nematic droplets. *Journal of physics A: mathematical and general* **19**, 3211 (1986) (Cited on pages 142–144).
173. LAVRENTOVICH, O. & SERGAN, V. V. Parity-breaking phase transition in tangentially anchored nematic drops. *Il Nuovo Cimento D* **12**, 1219 (1990) (Cited on pages 142, 143).
174. PANG, J. & CLARK, N. A. Observation of a chiral-symmetry-breaking twist-bend instability in achiral freely suspended liquid-crystal films. *Physical review letters* **73**, 2332 (1994) (Cited on page 142).
175. DRZAIC, P. S. A case of mistaken identity: Spontaneous formation of twisted bipolar droplets from achiral nematic materials. *Liquid crystals* **26**, 623 (1999) (Cited on pages 142, 143).
176. PRINSEN, P. & van der SCHOOT, P. Parity breaking in nematic tactoids. *Journal of Physics: Condensed Matter* **16**, 8835 (2004) (Cited on page 142).
177. JEONG, J., DAVIDSON, Z. S., COLLINGS, P. J., LUBENSKY, T. C. & YODH, A. Chiral symmetry breaking and surface faceting in chromonic liquid crystal droplets with giant elastic anisotropy. *Proceedings of the National Academy of Sciences* **111**, 1742 (2014) (Cited on pages 142, 150, 162, 165).
178. JEONG, J. *et al.* Chiral structures from achiral liquid crystals in cylindrical capillaries. *Proceedings of the National Academy of Sciences* **112**, E1837 (2015) (Cited on pages 142, 147, 150, 151).
179. DAVIDSON, Z. S. *et al.* Chiral structures and defects of lyotropic chromonic liquid crystals induced by saddle-splay elasticity. *Physical Review E* **91**, 050501 (2015) (Cited on pages 142, 146, 150, 227, 228).
180. NAYANI, K., FU, J., CHANG, R., PARK, J. O. & SRINIVASARAO, M. Using chiral tactoids as optical probes to study the aggregation behavior of chromonics. *Proceedings of the National Academy of Sciences*, 201614620 (2017) (Cited on pages 142, 150).
181. The Williams criterion is found using a linear stability analysis on a twisted-bipolar ansatz considering small twist angles. (Cited on page 144).
182. HOROWITZ, V. R., JANOWITZ, L. A., MODIC, A. L., HEINEY, P. A. & COLLINGS, P. J. Aggregation behavior and chromonic liquid crystal properties of an anionic monoazo dye. *Physical Review E* **72**, 041710 (2005) (Cited on pages 147, 150).

183. WILLIAMS, C., PIERAŃSKI, P. & CLADIS, P. E. Nonsingular $s = +1$ screw disclination lines in nematics. *Physical Review Letters* **29**, 90 (1972) (Cited on pages 147, 149, 151, 208).
184. MEYER, R. B. On the existence of even indexed disclinations in nematic liquid crystals. *Philosophical Magazine* **27**, 405 (1973) (Cited on pages 149, 208).
185. CLADIS, P. & KLÉMAN, M. Non-singular disclinations of strength $s = +1$ in nematics. *Journal de Physique* **33**, 591 (1972) (Cited on pages 149, 208).
186. CRAWFORD, G., ALLENDER, D. W. & DOANE, J. Surface elastic and molecular-anchoring properties of nematic liquid crystals confined to cylindrical cavities. *Physical Review A* **45**, 8693 (1992) (Cited on page 149).
187. ONDRISCRAWFORD, R. *et al.* Microscope textures of nematic droplets in polymer dispersed liquid crystals. *Journal of applied physics* **69**, 6380 (1991) (Cited on pages 159, 162–164).
188. *Carl zeiss microscopy* Web Page. 2017 (Cited on pages 167, 203).
189. *Industrial Cameras: Spectral Sensitivity* The Imaging Source (2017), 17 (Cited on pages 167, 169).
190. CHATELAIN, P. Sur la diffusion, par les cristaux liquides du type nématic, de la lumière polarisée. *Acta Crystallographica* **1**, 315 (1948) (Cited on page 179).
191. POSNJAK, G., ČOPAR, S. & MUŠEVIČ, I. Points, skyrmions and torons in chiral nematic droplets. *Scientific Reports* **6**, 26361 (2016) (Cited on page 186).
192. MACHON, T. & ALEXANDER, G. P. Knotted defects in nematic liquid crystals. *Physical Review Letters* **113** (2014) (Cited on page 186).
193. SEČ, D., ČOPAR, S. & ŽUMER, S. Topological zoo of free-standing knots in confined chiral nematic fluids. *Liquid crystals* **5**, 3057 (2014) (Cited on page 186).
194. GILLI, J. M., THIBERGE, S., VIERHEILIG, A. & FRIED, F. Inversion walls in homeotropic nematic and cholesteric layers. *Liquid crystals* **23**, 619 (1997) (Cited on pages 186, 187).
195. THIBERGE, S., CHEVALLARD, C., GILLI, J. M. & BUKA, A. Critical radius of loop defects in homeotropic nematic liquid crystals. *Liquid crystals* **26**, 1225 (1999) (Cited on pages 186, 187).

196. CHEN, S.-H. & LIANG, B. J. Stability of a hedgehog nematic configuration in a small closed cylindrical cavity. *Applied physics letters* **59**, 1173 (1991) (Cited on page 187).
197. LIANG, B. J. & CHEN, S.-H. Directorconfiguration diagram for a closedcylinder nematic liquid crystal. *Journal of applied physics* **71**, 2189 (1992) (Cited on pages 187, 211).
198. WANG, X., MILLER, D. S., BUKUSOGLU, E., de PABLO, J. J. & ABBOTT, N. L. Topological defects in liquid crystals as templates for molecular self-assembly. *Nat Mater* **15**, 106 (2016) (Cited on pages 196, 197).
199. WANG, X. *et al.* Experimental insights into the nanostructure of the cores of topological defects in liquid crystals. *Physical Review Letters* **116**, 147801 (2016) (Cited on page 197).
200. STOKES, G. G. On the change of refrangibility of light. *Philosophical Transactions of the Royal Society of London* **142**, 463 (1852) (Cited on page 200).
201. STOKES, G. G. On the change of refrangibility of light. No. II. *Philosophical Transactions of the Royal Society of London* **143**, 385 (1853) (Cited on page 200).
202. WEIGERT, F. über polarisiertes fluoreszenzlicht. *Verh. d. D. Phys. Ges* **23**, 100 (1920) (Cited on page 200).
203. SAUER, M. & HOFKENS, J. *Handbook of fluorescence spectroscopy and imaging: From ensemble to single molecules* ISBN: 3527633529 (John Wiley and Sons, Singapore, 2010) (Cited on pages 200, 201).
204. JAMESON, D. M. & ROSS, J. A. Fluorescence polarization/anisotropy in diagnostics and imaging. *Chemical reviews* **110**, 2685 (2010) (Cited on page 201).
205. SMALYUKH, I. I., SHIYANOVSKII, S. V. & LAVRENTOVICH, O. D. Three-dimensional imaging of orientational order by fluorescence confocal polarizing microscopy. *Chemical Physics Letters* **336**, 88 (2001) (Cited on page 201).
206. SMALYUKH, I. I., SENYUK, B. I., GU, M. & LAVRENTOVICH, O. D. *Focused laser beams and liquid crystals: Fast three-dimensional imaging of structures and topological defects* in *Congress on Optics and Optoelectronics* (International Society for Optics and Photonics), 594707 (Cited on pages 201, 202).
207. SMALYUKH, I. I. *et al.* Ordered droplet structures at the liquid crystal surface and elastic-capillary colloidal interactions. *Physical review letters* **93**, 117801 (2004) (Cited on page 202).

208. DE LUCA, G. & REY, A. D. Ringlike cores of cylindrically confined nematic point defects. *The Journal of chemical physics* **126**, 094907 (2007) (Cited on page 211).
209. KRALJ, S., VIRGA, E. G. & ŽUMER, S. Biaxial torus around nematic point defects. *Physical Review E* **60**, 1858 (1999) (Cited on page 211).
210. PENZENSTADLER, E & TREBIN, H.-R. Fine structure of point defects and soliton decay in nematic liquid crystals. *Journal de Physique* **50**, 1027 (1989) (Cited on page 211).
211. IGNÉS-MULLOL, J., BAUDRY, J., LEJCEK, L. & OSWALD, P. Formation of disclination lines near a free nematic interface. *Physical Review E* **59**, 568 (1999) (Cited on page 213).
212. TRAN, L. *et al.* Lassoing saddle splay and the geometrical control of topological defects. *Proceedings of the National Academy of Sciences* **113**, 7106 (2016) (Cited on page 213).
213. GIOMI, L. Hyperbolic interfaces. *Physical Review Letters* **109** (2012) (Cited on page 214).
214. VROMANS, A. J. & GIOMI, L. Orientational properties of nematic disclinations. *Soft Matter* **12**, 6490 (2016) (Cited on page 218).
215. SELINGER, J. & TANG, X. private communication. Mar. 26, 2017 (Cited on pages 219, 220).
216. POLTHIER, K. & SCHMIES, M. *Straightest geodesics on polyhedral surfaces* in *SIGGRAPH'06* (ACM). ISBN: 1595933646 (Cited on page 227).
217. MARTINEZ, D., VELHO, L. & CARVALHO, P. C. *Geodesic paths on triangular meshes* in *SIBGRAPI'04* (IEEE), 210. ISBN: 0769522270 (Cited on page 227).
218. SIDKY, H., de PABLO, J. J. & WHITMER, J. K. In Silico Measurement of Elastic Moduli of Nematic Liquid Crystals. *Physical Review Letters* **120**, 107801 (2018) (Cited on pages 227, 228).
219. ALLENDER, D. W., CRAWFORD, G. & DOANE, J. Determination of the liquid-crystal surface elastic constant K 24. *Physical review letters* **67**, 1442 (1991) (Cited on page 228).
220. POLAK, R., CRAWFORD, G., KOSTIVAL, B., DOANE, J. & ŽUMER, S. Optical determination of the saddle-splay elastic constant K 24 in nematic liquid crystals. *Physical Review E* **49**, R978 (1994) (Cited on page 228).

221. SPARAVIGNA, A, LAVRENTOVICH, O. & STRIGAZZI, A. Periodic stripe domains and hybrid-alignment regime in nematic liquid crystals: Threshold analysis. *Physical Review E* **49**, 1344 (1994) (Cited on page 228).
222. MILLER, D. S. & ABBOTT, N. L. Influence of droplet size, pH and ionic strength on endotoxin-triggered ordering transitions in liquid crystalline droplets. *Soft Matter* **9**, 374–382 (2013) (Cited on pages 229, 230).
223. NAYANI, K. *ROLE OF SURFACE-LIKE ELASTIC CONSTANTS IN THE PHENOMENOLOGY OF CONFINED NEMATICS* PhD thesis (Georgia Institute of Technology, 2017) (Cited on page 230).

VITA

Born in 1988, Perry Ellis grew up in Orange County, California. He attended local public schools, finally landing himself at Harvey Mudd College and receiving his B.S. in physics in 2011. That same year he moved to Atlanta, Georgia to begin his graduate studies in the Georgia Tech School of Physics. When not pursuing higher education, Perry is an active person. He played water polo at a collegiate level and currently enjoys rock climbing and camping across the United States as well as practicing Brazilian Juijistu. At the time of writing, he is 29 years old, and in his 24th consecutive year as a student